LBL-18754 c.2
UC-13

Lawrence Berkeley Laboratory

UNIVERSITY OF CALIFORNIA

RECEIVED
LAWRENCE
BERKELEY LABORATORY

APR 17 1985

LIBRARY AND
DOCUMENTS SECTION

APPLIED SCIENCE DIVISION

FY 1984 Annual Report
ENVIRONMENTAL RESEARCH PROGRAM

March 1985

TWO-WEEK LOAN COPY
This is a Library Circulating Copy
which may be borrowed for two weeks.

APPLIED SCIENCE
DIVISION

Prepared for the U.S. Department of Energy under Contract DE-AC03-76SF00098

LBL-18754 c.2

DISCLAIMER

This document was prepared as an account of work sponsored by the United States Government. While this document is believed to contain correct information, neither the United States Government nor any agency thereof, nor the Regents of the University of California, nor any of their employees, makes any warranty, express or implied, or assumes any legal responsibility for the accuracy, completeness, or usefulness of any information, apparatus, product, or process disclosed, or represents that its use would not infringe privately owned rights. Reference herein to any specific commercial product, process, or service by its trade name, trademark, manufacturer, or otherwise, does not necessarily constitute or imply its endorsement, recommendation, or favoring by the United States Government or any agency thereof, or the Regents of the University of California. The views and opinions of authors expressed herein do not necessarily state or reflect those of the United States Government or any agency thereof or the Regents of the University of California.

LBL-18754

APPLIED SCIENCE DIVISION ANNUAL REPORT ENVIRONMENTAL RESEARCH PROGRAM FY 1984

Elton J. Cairns
Head, Applied Science Division
and
Associate Director, LBL

Tihomir Novakov
Program Leader, Environmental Research Program

Applied Science Division
Lawrence Berkeley Laboratory
University of California
Berkeley, California 94720

Prepared for the U.S. Department of Energy under Contract No. DE-AC03-76SF00098

CONTENTS

Environmental Research Program Staff List 4-vi

Introduction 4-1

ATMOSPHERIC AEROSOL RESEARCH

Oxidation of SO_2 in Fog Droplets by Primary Oxidants
W.H. Benner and T. Novakov 4-3

Temperature-Programmed Evolved Gas Analysis for Determining Pyrolyzable Oxygen
W.H. Benner and A.D.A. Hansen 4-5

The Role of Surface Oxygen in S(IV) Oxidation by Different Carbons
L.A. Gundel, W.H. Benner, and T. Novakov 4-8

Aerosol Characterization in Beijing, China, 1983–1984
R.L. Dod, R.D. Giauque, T. Novakov, and Su Wei-han 4-12

Role of Combustion-Generated Carbon Particles in the Absorption of Solar Radiation in the Arctic Haze
H. Rosen and A.D.A. Hansen 4-16

Vertical Distributions of Particulate Carbon, Sulfur, and Bromine in the Arctic Haze and Comparison with Ground-Level Measurements at Barrow, Alaska
A.D.A. Hansen and H. Rosen 4-20

Characterization of Respirable Coal Mine Dust
C.D. Parker, C.J. Pryor, J. Perkins, R.L. Dod, and T. Novakov 4-23

Determination of Black Carbon in Carbonaceous Particles by Evolved Gas Analysis and Optical Attenuation
L.A. Gundel, R.L. Dod, H. Rosen, and T. Novakov 4-28

Individual Microparticle Analysis and Characterization: Progress on New Techniques
R.J. Otto 4-32

APPLIED PHYSICS AND LASER SPECTROSCOPY RESEARCH

N.M. Amer, S.-H. Chen, H. Dersch, A. Frova, R.W. Gerlach, W. Imler, M. Olstead, A. Skumanich, D. Wei, and Z. Yasa

Laser Photothermal Measurements and Characterization 4-34

Surfaces and Interfaces 4-42

Amorphous Photovoltaic Semiconductors 4-45

Liquid Crystal Research 4-49

OIL SHALE RESEARCH

Rapid Estimation of Organic Nitrogen in Oil Shale Wastewaters
C.G. Daughton, B.M. Jones, R.H. Sakaji, and J.F. Thomas 4-51

Removal of Ammonia from Wastewaters Using Tubular Microporous Polytetrafluoroethene Membranes
R.H. Sakaji, J.F. Thomas, and C.G. Daughton 4-56

Identification and Correlation of Volatile Components in Retort Wastewaters
L. Hunter, P. Persoff, J.F. Thomas, and C.G. Daughton 4-60

Removal of Nitrogen Heterocycles from Water by Sorption to Spent Oil Shale
P. Persoff, L. Hunter, E.R. Blatchley, J.F. Thomas, and C.G. Daughton 4-63

COMBUSTION RESEARCH

Temporal and Spatial Scales in a Heated and in a Reacting Turbulent Boundary Layer
R.K. Cheng, L. Talbot, and F. Robben 4-66

Interpretation of Conditional Statistics in Open, Oblique Premixed Turbulent Flames
R.K. Cheng, I.G. Shepherd, L. Talbot, and F. Robben 4-68

Characterization of Density Fluctuations in a Premixed Turbulent V-Shaped Flame
M. Namazian, I.G. Shepherd, and L. Talbot 4-71

Premixed Flame Stabilization on a Bluff Body
J.R. Hertzberg, M. Namazian, L. Talbot, and F. Robben 4-74

Numerical Simulation of Turbulent Combustion
M. Pindera, F. Robben, and L. Talbot 4-77

Coal Slurry Ignition in a Diesel Engine Simulator
D.D. Brehob, F. Robben, R.F. Sawyer, and P.M. Sherman 4-78

Molecular Beam Studies of Ignition Chemistry
D. Lucas and N.J. Brown 4-82

The Measurement of Combustion-Generated Pollutants with TALMS
D. Lucas and N.J. Brown 4-83

Combustion Characteristics of Unvented Space Heaters
T. Lionel, R.J. Martin, and N.J. Brown 4-85

Theoretical Combustion Chemistry
N.J. Brown, O.M. Rashed, and A. Edlin 4-89

Lean Limit Combustion Processes
R.F. Sawyer and D. Dunn-Rankin 4-92

Fluid Mechanics of Combustion
C.-C. Hsaio, S.-L. Yuan, A.J. Chorin, and A.K. Oppenheim 4-95

Controlled Combustion
N.J. Brown, C.F. Edwards, M. Forsha, K. Hom, D. Lucas, A.K. Oppenheim, T. Parker, R.B. Peterson, R.F. Sawyer, and H.E. Stewart 4-98

Fire Modeling
P. Pagni and C. Okoh 4-103

The Use of High-Strength Concretes and Mortars in Combustion Environments
R.B. Williamson and A.I. Rashed 4-105

SCRUBBER CHEMISTRY RESEARCH

Reaction of Ferrous Nitrosyl Chelates with Sulfite and Bisulfite Ions
D. Littlejohn and S.G. Chang 4-110

Effect of Citrate Buffer Additive on Absorption of Nitric Oxide by Ferrous Chelates
E. Griffiths and S.G. Chang 4-113

Photoreduction of Ferric Chelates
S.G. Chang and E. Griffiths 4-116

Investigation of the Synergistic Effect of Metal Ions on S(IV) Oxidation by Laser Raman Spectroscopy, Using a High-Pressure, Rapid-Mixing Flow System
S. Wolfgang and S.G. Chang 4-118

A Study of Ferrous Ion on Chelex 100 for Nitric Oxide Absorption and Subsequent Reactivity with Oxygen
K. Brodbeck and S.G. Chang 4-121

Quantitative Determination of Nitrogen Sulfonates in Flue-Gas Liquors
D. Littlejohn and S.G. Chang 4-124

TOXICOLOGY STUDIES OF BIOLOGICAL SYSTEMS

Free Radicals in Mitochondrial Membranes
R. Mehlhorn, J. Maguire, and L. Packer 4-127

Lake Ecotoxicology Research
J. Harte, J. Oldfather, C. Blanchard, H. Michaels, M. Turner, and A. Bradman 4-132

TRACE ELEMENT ANALYSIS

Survey of Instrumentation for Environmental Monitoring
M. Quinby-Hunt, R. McLaughlin, G. Morton, and A. Quintanilha 4-134

Iridium Anomalies at the Cretaceous-Tertiary and Cambrian-Precambrian Boundaries
F. Asaro, H.V. Michel, W. Alvarez, and L.W. Alvarez 4-135

Determination of Hitherto Unknown Sources of New World Obsidians by Precise Elemental Analysis
F.H. Stross, F. Asaro, and H. Michel 4-137

ENVIRONMENTAL RESEARCH PROGRAM STAFF

ATMOSPHERIC AEROSOL RESEARCH

William Benner
Ray Dod
Lara Gundel
Anthony Hansen
Samuel Markowitz
Tihomir Novakov*†
Roland Otto
Cass Parker
Carolyn Pryor
Hal Rosen
Richard Schmidt
Linda Wroth

APPLIED PHYSICS AND LASER SPECTROSCOPY RESEARCH

Nabil Amer†
Shu-Hsia Chen
Helmut Dersch
Andrea Frova
Robert Gerlach
William Imler
Marjorie Olmstead
Andrew Skumanich
Diyonyuan Wei
Zafer Yasa

OIL SHALE RESEARCH

Ernest Blatchley
Christian Daughton‡
Gloria Harris
Joseph Healy, Jr.
Leon Hunter
Bonnie Jones
Fritz Jordan‡
Greg Langlois
Frank Mandola
Carl Martin
Peter Persoff
Rick Sakaji
Robert Selleck‡
Jerome Thomas†
Richard Watada

COMBUSTION RESEARCH

James Ang
Diana Brehob
Mark Brosmer
Nancy Brown†
Cam Carter
John Cavolowsky
Robert Cheng
Alexandre Chorin‡
John Daily
Edmund Dickson
Derek Dunn-Rankin
Christopher Edwards
Janet Ellzey
Debbie Fagin‡
Carlos Fernandez-Pello
Fred Fisher‡
Michael Forsha
Cecile Grant
Ralph Greif
Jean Hertzberg
Kenneth Hom
Wei-Ming Huang
Frank Hurlbut
Eileen Javar
Kwi Lee
Russell Lewis
Trudy Lionel
Donald Lucas
Richard Martin
Mehdi Namazian‡
Clement Okoh
Antoni Oppenheim
Patrick Pagni
Richard Peterson
William Pitz
David Propper
Ahmed Rashed
Ola Rashed
Frank Robben
Robert Sawyer
Ian Shepherd‡
Pauline Sherman§
Horton Stewart‡
Edward Stracke
Lawrence Talbot
Steve Vosen
Wayman Walker‡
R. Brady Williamson

SCRUBBER CHEMISTRY RESEARCH

Kevin Brodbeck‡
Shih-Ger Chang†
David Littlejohn
Elizabeth Griffiths
Steven Wolfgang

TOXICOLOGY STUDIES OF BIOLOGICAL SYSTEMS

Charles Blanchard
John Harte
Don Levy
John Maguire
Rolf Mehlhorn
Harvey Michaels
Joan Oldfather
Lester Packer
John Rees
Richard Schneider
Kathy Tonnessen

---

*Program Leader, †Group Leader, ‡University of California, Berkeley, §Participating Guest

TRACE ELEMENT ANALYSIS

Frank Asaro	Ralph McLaughlin	Cindy Polansky	Linda Sindelar
Jon Bechtel	Helen Michel	Mary Quinby-Hunt	Fred Stross[§]
Charles Case	Anthony Nero	Alexandre Quintanilha	Rafael Zamora
Robert Giauque	Amos Newton		

ADMINISTRATIVE SUPPORT

Cynthia Coolahan	Rachelle Edmond	Gloria Gill	Linda Maio

ENVIRONMENTAL RESEARCH PROGRAM

INTRODUCTION

The objective of the Environmental Research Program is to understand the formation, transformation, transport, and effects of energy-related pollutants on the environment. The effects studied include those on global, regional, and local scales and involve the atmosphere, hydrosphere, and biosphere.

This multidisciplinary research program includes fundamental and applied research in physics, chemistry, engineering, and biology, as well as research on the development of advanced methods of measurement and analysis. During FY 1984, research concentrated on atmospheric physics and chemistry, applied physics and laser spectroscopy, combustion theory and phenomena, environmental effects of oil shale processing, toxicology studies of biological systems, and trace element analysis for the investigation of present and historical environmental impacts.

Each of these areas is covered by a different research group or project. Atmospheric physics and chemistry, for example, is the province of the Atmospheric Aerosol Research Group, which has focused its studies on aerosol characterization, formation, and transformation, and on the effects of aerosols and gaseous species on precipitation, visibility, and climate. At present, the main research interests of the group concern the chemical processes that occur in haze, smog, clouds, and fogs, and the role of particulate carbon in global climate modification. To accomplish these research objectives, the group has developed novel analytical and research methods for the characterization of particles, dust, and aerosol species. A new effort is the development of a method for mass spectrometry of individual particles, and a microencapsulation technique for cloud and fog water characterization is being investigated.

The Applied Physics and Laser Spectroscopy Research Group applies advanced laser spectroscopy and condensed-matter physics to energy and environmental problems. Emphasis is on the development of physical methods, as opposed to conventional chemical analysis techniques. The ultrahigh sensitivity, narrow linewidth, and tunability of lasers and the minimal sample preparation required make it possible for team members to apply such techniques to energy production and to test novel methods for energy conversion, such as photovoltaic solar cells and superionic electrical energy storage devices and material characteristics in general.

The Oil Shale Project studies the environmental and waste-treatment problems that would arise from the tremendously large quantities of solid and liquid wastes that a commercial-scale shale oil industry would generate. A major task of the project is to delineate the potential problems of process and spent-shale wastewater codisposal, in particular the estimation of the types and quantities of uncontrollable air emissions that may result from such use of wastewaters (raw or treated). Its second major task is the development of economical approaches to the treatment of process wastewaters. Because of their turbidity and high concentrations of organic and inorganic solutes, they present tremendous difficulties to any water management scheme that entails reuse or discharge. This research effort is conducted in cooperation with the Sanitary Engineering and Environmental Health Research Laboratory of the University of California.

The Combustion Research Group studies complex combustion processes by acquiring a fundamental understanding of the chemical and physical processes that determine combustion efficiency, emissions, and safety. Development of suitable analytical techniques for measuring intermediate and product species formed during the oxidation of fossil fuels and for characterizing turbulence has been a major effort. The characterization and understanding of turbulence and high-temperature chemistry are of high priority in this program. Areas of application that dominate these studies are engine research, pollutant abatement in utilities, fire control, and ignition phenomena.

The Scrubber Chemistry Group has been investigating the chemical character of pollutants generated by the combustion of fossil fuels to develop new, efficient strategies for pollutant emission control. Current research has been directed toward understanding the kinetics and mechanisms of homogeneous and heterogeneous catalysis of the interactions of sulfur dioxide and nitrogen oxides,

both among themselves and with other compounds. When this fundamental chemistry is understood, it will be applied to the development of an efficient, cost-effective scrubber for simultaneous desulfurization and denitrification of flue gases. The same knowledge can also be applied to improving the performance of lime/limestone desulfurization scrubbing systems, currently the type of scrubber most widely used by utilities.

Toxic substances are generated not only in our environment as a result of man's activities, but also within our bodies as a result of normal metabolic processes. These substances can have important consequences for our ecosystems and for our health and well-being. The study of strongly chemically reactive compounds generated within cells during aerobic metabolism is of particular interest in attempting to understand cellular damage and repair. In particular, "active oxygen" species (including free radicals) that are generated during the normal life span of cells have been implicated in many processes that result in altered cellular metabolism. The study of free radicals in mitochondrial membranes focuses primarily on oxygen radicals generated by mitochondria (the energy-generating organelles within cells) during respiration and their effects on biological membranes. One aspect of this study attempts to clarify the correlation between irreversible cellular damage and aging. Ecotoxicology is the science that seeks to determine the pathways, fate, and effects of toxic substances in the natural environment. The projects of the Lake Ecotoxicology Research Group focus on one particular type of natural environment, freshwater lakes. Research has proceeded in two converging directions: the development of laboratory microcosms for lake ecotoxicology and the study of acid precipitation in the western United States. The group has demonstrated that lake microcosms can be designed and operated to provide realistic toxic-substance test systems and has applied microcosms to analyze the effects of acid precipitation. Field studies on acid precipitation and its effects in the Sierra Nevada and the Colorado Rockies have been another major focus of the group. Through a combination of microcosm technology and field work, it seeks to predict the chronology of acidification in the western United States.

The main emphasis of the Trace Element Analysis Group is the study of the relationship between massive repetitive life extinctions on the earth and asteroid (or other extraterrestrial) impacts. Studies of this relationship have concentrated on searches for unusually high iridium abundances in geochemical samples from rock layers known or expected to mark life-extinction horizons. Geochemical and other tests are made to determine if the iridium-rich rocks are of extraterrestrial origin and hence related to impacts. The nature of the sedimentation of the rocks, the worldwide extent of the extinction horizons, and the extent to which the extinctions are related to impacts are also studied.

The short reports that follow describe the program activities in FY 1984. In most cases, more detailed papers have been or will be published in appropriate scientific journals.

Oxidation of SO_2 in Fog Droplets by Primary Oxidants*†

W.H. Benner and T. Novakov

Specific catalysts and/or oxidants are required in aqueous sulfur dioxide oxidation pathways. The amount of SO_2 oxidized depends not only on the SO_2 concentration but also, under many circumstances, and perhaps critically so, on the availability and origin of the oxidants and catalysts.

Certain catalytic materials such as soot and transition metals are co-emitted into the atmosphere with SO_2 from the same combustion sources. Thus, the atmospheric concentrations of these catalysts are directly related to the source emissions and are therefore, in principle, controllable at the source. However, one of the most important oxidants for SO_2 is hydrogen peroxide (H_2O_2),[1–5] which has been believed to be produced entirely in the atmosphere by a series of photochemical reactions involving many reactants not emitted directly from combustion sources. The occurrence of H_2O_2 in the atmosphere has been assumed to be unrelated to source emissions and therefore uncontrollable. Recent work in our laboratory shows that incomplete combustion, besides being a source of particulate catalysts, is also a source of primary oxidants, which in the aqueous phase are mostly present as H_2O_2 and, to a lesser extent, organic peroxides.

The origin of these primary oxidants is the precombustion reactions between fuel molecules and oxygen, with reaction intermediates.[6–7] During perfect combustion, these species will be oxidized to CO_2 and H_2O. When the reacting mixture or some portions of it fail to ignite, the intermediate species produced by precombustion reactions will appear in the combustion effluent. These facts are known from combustion research but have not been fully appreciated by the atmospheric chemistry community. Emission of primary oxidants ties atmospheric chemistry to not only how much fuel is burned but also *how* it is burned, and this realization may have an effect on our understanding of the formation of acid precipitation, including acid fog and approaches to its control. The work reported here demonstrates the formation of acid fog from a reaction between SO_2 and primary oxidants.

ACCOMPLISHMENTS DURING FY 1984

The apparatus used in the fog chemistry experiments, schematically represented in Fig. 1, consists of two main parts: a glass chimney with a combustor, and the fog chamber itself. The chimney is the source of gaseous combustion effluents, water of combustion, and combustion-generated particles. These particles also serve as fog condensation nuclei. The fog chamber is a plexiglass cylinder through which cooled nitrogen is passed to provide a temperature below the dew point of the incoming combustion gases. The combustion products are fed through heated tubing (50°C) into the chamber through an opening in the center of the bottom flange of the chamber. The inlet itself is also slightly heated (50°C) to prevent water condensation. The flow rates of cold N_2 (6 L/min) and combustion gases (5 L/min) produce a fog at room temperature. The source of the water that condenses onto the combustion particles is principally from the flame

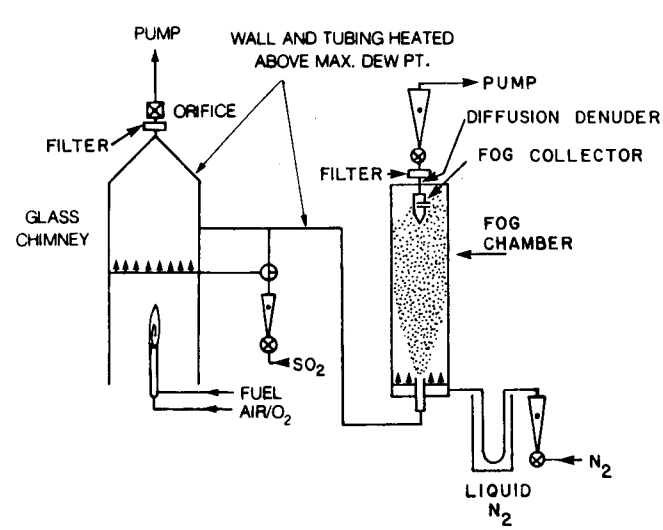

Figure 1. Apparatus for condensing combustion water onto combustion particles to produce fog droplets.
(XBL 844-1470)

*This work was supported by the Director, Office of Energy Research, Office of Health and Environmental Research, Physical and Technological Research Division of the U.S. Department of Energy under Contract No. DE-AC03-76SF00098 and by the National Science Foundation under Contract No. ATM 83-15442.

†Summary of paper accepted by *Atmospheric Environment*.

and, to a small degree, from water vapor in the room air that enters through the chimney. Fog droplets are collected with an impactor situated near the top of the chamber and designed to provide a cut-off size of about 7 μm.

Fog water was collected during runs having different flame conditions and with and without added SO_2. The SO_2 was introduced into the system at a point between the chimney and the chamber. The collected fog water was analyzed for anions (NO_3^-, SO_3^{2-}, SO_4^{2-}) by ion chromatogaphy. Hydrogen peroxide was determined by iodometric titration after ammonium molybdate was added to catalyze the reaction between I^- and H_2O_2.[6] A miniature pH electrode was used to measure $[H^+]$.

The apparatus shown in Fig. 1 was also used to study the formation of particulate sulfate. Sulfate particles were collected by quartz-fiber filters at two sampling points: at the top of the chimney and above a drying denuder on top of the fog chamber. Sampling from the fog chamber was performed with and without fog present in the chamber. The principal difference between sampling directly from the chimney and sampling from the fog chamber is in the gas temperature relative to the dew point of the combustion effluent. In the chimney, the gas temperature was 70°C, well above the 40°–45°C dew point, but in the fog chamber, the temperature was 20°C. In the chimney, the temperature was above the dew point and precluded formation of visible fog droplets, whereas in the fog chamber, because of additional cooling, the fog readily occurred. Propane (110 mL min^{-1}) was burned as a steady diffusion flame. The filter samples were collected for 10 minutes, and the water-soluble anions were extracted and analyzed by ion chromatography.

The results obtained with the fog chamber are summarized in Table 1 for three different flame conditions: intermittent diffusion flame, steady diffusion flame, and steady premixed (air) flame. Propane was used as the fuel in all these experiments. Table 1 shows that an intermittent flame of propane with minimal sulfur content produced fog with a pH of 2.7 and a trace of sulfate. This sulfate is due to the trace amounts of sulfur in the propane. The H_2O_2 concentration in this experiment was determined to be 21 mM. Adding about 20 ppm SO_2 (corresponding to propane with ~0.1% sulfur content) to the combustion effluent lowered the pH value from 2.7 to 1.9 and increased the sulfate concentration by a factor of 700 over the sulfate concentration without additional SO_2. No detectable H_2O_2 was found (detection limit of the method used is $\sim 1 \times 10^{-4}$ M) because it was consumed by reaction with dissolved SO_2. Analysis of fog water showed that ~10% of the available SO_2 was converted to sulfate nearly instantaneously, as the residence time in the fog chamber was less than 1 minute. The results in Table 1 show similar trends for other flame conditions; but, as expected, the droplets contain progressively smaller absolute concentrations as conditions are adjusted to produce more efficient combustion.

Table 1. Results of fog-water analysis (propane combustion).

Flame type	$[SO^2]$ (ppm)	pH	H^+ (mM)	H_2O_2 (mM)	NO_3^- (mM)	SO_4^{2-} (mM)	H^+ / $NO_3^- + SO_4^{2-}$
Intermittent	0	2.7	2.0	21	1.4	0.013	1.4
Intermittent	20	1.9	13.0	ND	1.3	9.1	1.3
Diffusion	0	3.0	1.0	0.48	0.36	0.013	2.7
Diffusion	4.7	2.7	2.0	ND	0.7	0.27	2.1
Premixed	0	2.8	1.6	ND	0.83	0.009	1.9
Premixed	4.7	2.8	1.6	ND	0.61	0.057	2.4

The following experiments indicate that liquid water is important for producing particulate sulfate from combustion products. As seen in Fig. 1, particulate sulfate could be sampled at two locations: from the chimney and from the fog chamber after the fog droplets were dried by passage through a diffusion drier. Reproducible flow rates of fuel and air through the system were used in all experimental runs. Entry of SO_2, when introduced, was between the chimney and the fog chamber. Effluent sampled at the top of the chimney contained 0.1 μg SO_4^{2-}(p)/liter of chimney gas. Passage of these combustion-generated particles through the fog chamber did not alter the concentration of particulate sulfate. However, when SO_2 (10 ppm) was introduced into the flowstream, the concentration of particulate sulfate in the effluent from the fog chamber increased to 1.2 μg SO_4^{2-}(p)/L of chimney gas. Samples collected from the effluent of the fog chamber, also with added SO_2 but without cold N_2 to suppress fog formation, showed 0.8 μg SO_4^{2-}(p)/L.

These experiments clearly demonstrate the role of liquid water in sulfate formation. The highest concentrations of particulate sulfate were produced when the conditions for aqueous reactions were present. The sulfate production was greatest when visible fog was observed; however, even in the absence of visible fog, sulfate was formed as long as the temperature was at or below the dew point. At this temperature, a relatively thin layer of water could condense on combustion particles, which was sufficient to enable the aqueous SO_2 oxidation reactions to occur.

At this time, we don't have solid direct evidence about the concentrations and role of primary oxi-

dants in polluted ambient atmospheres. However, data in the literature have shown that internal combustion engines[7,8] can be significant sources of primary oxidants.

PLANNED ACTIVITIES FOR FY 1985

We plan to do additional combustion emission studies and to assess the importance of primary oxidants in urban atmospheres.

REFERENCES

1. Penkett, S.A., Jones, B.M.R., Brice, K.A., and Eggleton A.E.S. (1979), "The Importance of Atmospheric Ozone and Hydrogen Peroxide in Oxidizing Sulfur Dioxide in Cloud and Rain Water," *Atmos. Environ. 13*, p. 123.
2. Martin, L.R., and Damschen, D.E. (1981), "Aqueous Oxidation of Sulfur Dioxide by Hydrogen Peroxide at Low pH," *Atmos. Environ. 15*, p. 1615.
3. Kunen, S.M., Lazrus, A.L., Kok, G.L., and Heikes, B.G. (1983), "Aqueous Oxidation of SO_2 by Hydrogen Peroxide," *J. Geophys. Res. 88*, p. 3671.
4. Schwartz, S.E. (1984), "Gas-Aqueous Reactions of Sulfur and Nitrogen Oxides in Liquid-Water Clouds," in *SO_2, NO, and NO_2 Oxidation Mechanisms: Atmospheric Considerations*, J.G. Calvert, Ed., Acid Precipitation Series, Vol. 3. Butterworth's, Boston.
5. Hoffmann, M.R., and Edwards, J.O. (1975), "Kinetics of the Oxidation of Sulfite by Hydrogen Peroxide in Acidic Solution," *J. Phys. Chem. 79*, p. 2096.
6. Johnson, R.M., and Siddiqi, I.W. (1970), *The Determination of Organic Peroxides*, Monographs in Organic Function Group Analysis, Vol. 4, Pergamon, Oxford.
7. Sturgis, M.M. (1955), "Knock and Antiknock Action," *SAE Trans. 63*, p. 253.
8. Heicklein, J. (1976), *Atmospheric Chemistry*, Academic Press, New York, p. 239.

Temperature-Programmed Evolved Gas Analysis for Determining Pyrolyzable Oxygen*†

W.H. Benner and A.D.A. Hansen

As a sample is heated in an inert gas, oxygen-containing decomposition products such as H_2O, CO, CO_2, C_xO_y, NO_x, and SO_x can be released. The oxygen in these products can be converted to CO by passage over hot carbon; the CO can then be detected by infrared spectrometry. The procedure for determining oxygen in a sample at a fixed pyrolysis temperature was recently reported.[1] This technique has now been expanded so that the amount of oxygen (detected as CO) that evolves as a function of sample temperature is quantitated. In this report, the development of a CO–evolved gas analysis (CO-EGA) technique is described.

*This work was supported by the Director, Office of Energy Research, Office of Health and Environmental Research, Physical and Technological Research Division of the U.S. Department of Energy under Contract No. DE-AC03-76SF00098 and by the National Science Foundation under Contract No. ATM 83-15442.

†Summary of paper published in *Anal. Chem. 56*, pp. 2876–2879 (1984).

ACCOMPLISHMENTS DURING FY 1984

The reagents and the major part of the EGA apparatus are shown in Fig. 1. A quartz pyrolysis tube (2 cm o.d., 0.25-cm-thick wall, 65 cm long) is packed with a 4-cm length of granular carbon and maintained at 1135°C in a tube furnace. The N_2 carrier gas flows at 40 mL/min and is purified by passage through drying tubes of $Mg(ClO_4)_2$ and P_2O_5-coated glass beads and an oxygen (O_2) scrubber tube that contains copper metal turnings at 325°C. A nondispersive infrared (NDIR) detector is used to measure the evolved CO and is calibrated with 40 ppm CO in N_2.

Samples are loaded into a small platinum boat and placed into the cool temperature-programmed oven while the system is backflushed with N_2. After the tube is sealed and any entrained air has been backflushed from the system, the multiport valve is switched, the CO detector is permitted to stabilize, and finally the temperature program heats the oven at 30°C/min from room temperature to 1100°C.

A platinum thermocouple inside the pyrolysis tube senses the temperature of the sample. A microcomputer compares this temperature with the desired temperature and controls power to the oven accordingly so that a linear temperature ramp from room temperature to 1100°C with less than 5°C

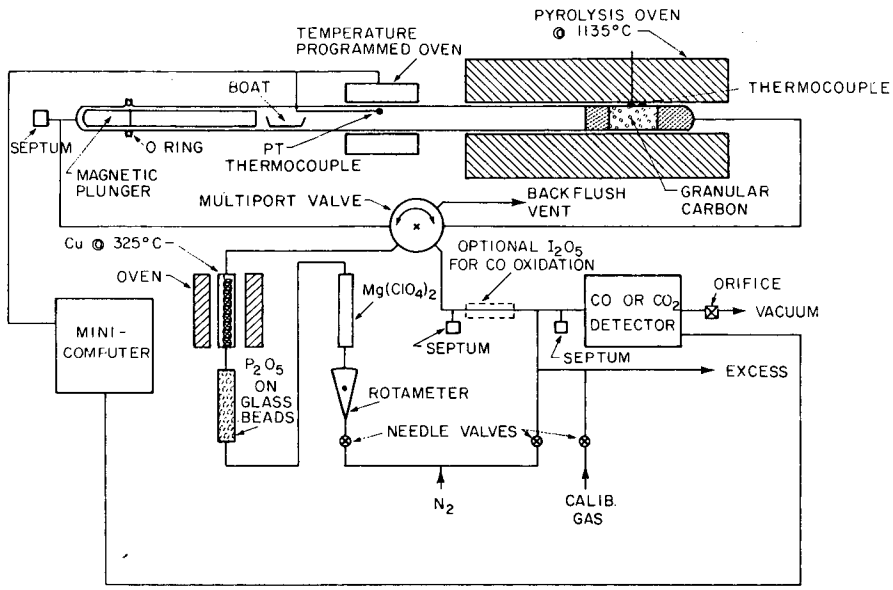

Figure 1. Experimental apparatus for temperature-programmed oxygen analysis. (XBL 833-126)

root-mean-square error is typically produced. The computer also records the CO concentration as averaged over 10-second intervals (5 C° interval). At the end of an analysis, an appropriate baseline, determined as the CO concentration at the start of analysis, is subtracted from each 10-second datum point. Knowledge of the flow rate through the detector allows the amount of oxygen evolved in selectable temperature intervals to be calculated from the area under the baseline-corrected thermogram.

The standard compounds analyzed were reagent grade and, except for pentanedioic acid and $CuSO_4$, were recrystallized before use. All were dessicated over P_2O_5 for 24 hours before being weighed and dissolved into HPLC-grade acetone (Fisher Scientific Co.). Solutions typically contained several micrograms oxygen per microliter. Aliquots (15–50 μL) of a solution were evaporated on 1-cm^2 discs of quartz-fiber filter material prefired at 800°C for 6 hours. The evaporated sample was again dessicated before analysis. The sample of $CuSO_4 \cdot H_2O$ was crystalline and was placed directly into the sample boat without prior dessication.

The amount of oxygen recovered from a sample was determined from the area under a thermogram. A relatively smooth and flat signal is a typical system blank (i.e., no sample in the system), which, after baseline correction, was 0 μg of oxygen.

The applicability of the technique is shown by the analysis of a series of standard compounds. Figure 2 shows oxygen thermograms for three dicarboxylic acids, all sharing two principal features. The first is a sharp low-temperature peak that evolves at increasingly higher temperatures as the molecular weight of the compound increases. The second is a much broader peak that shows a similar molecular-

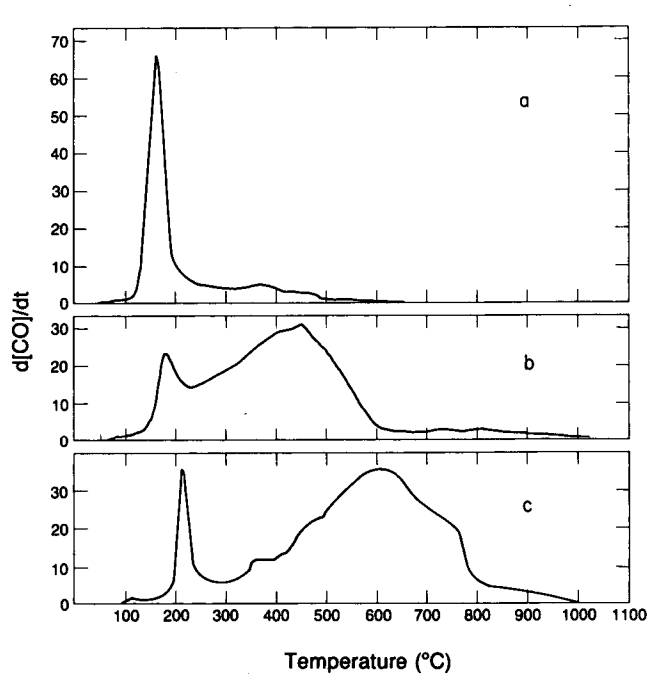

Figure 2. Thermograms of (a) 51.4 μg O in butanedioic acid, (b) 129.0 μg O in pentanedioic acid, and (c) 167.5 μg O in heptanedioic acid. (XBL 844-10462)

weight dependence for the dicarboxylic acids. The decomposition products that evolve during thermal analysis are unknown. A parallel analysis of succinic acid under N_2 flow but without use of the hot carbon converter was performed in our laboratory's H_2O/CO_2 EGA apparatus. These thermograms showed that the sharper peak was neither evolved water nor CO_2.[2] The broader peak may be the result of char (carbonization) formation, which traps some oxygen. The recovery of oxygen from the samples was (100.1 ± 3.3)% ($x \pm 1\sigma$), and a linear relationship between sample oxygen and the area under a thermogram was obtained. A linear regression equation for the data is: μg O detected = (0.986)(μg O in sample) + (1.02 μg O, $r^2 = 0.997$, $n = 6$).

The analysis of 153 μg $CuSO_4 \cdot H_2O$ is shown in Fig. 3. The peaks below 300°C describe the loss of water of hydration. Between 550°C and 725°C, $CuSO_4$ decomposes to CuO, and the peak at 775°C represents the conversion of CuO to Cu_2O.[3] The area under the thermogram from 50°C to 300°C represents 40.4 μg O from water, while 39.6 μg O was recovered from the conversion of $CuSO_4$ to Cu_2O. Therefore, the formula was calculated to be $CuSO_4 \cdot (3.6)H_2O$, and the recovery of oxygen from $CuSO_4 \cdot (3.6)H_2O$ was 103%. The position of the peaks in this thermogram corresponds very closely to the transformations observed in thermogravimetric[3] and differential thermogravimetric analyses of $CuSO_4 \cdot 5H_2O$.[4]

An additional application of this analytical technique is shown in Fig. 4, trace (a), which shows a number of peaks in the thermogram of the activated carbon RB-1. These peaks correspond to different physical and chemical states of oxygen present on the carbon due to activation or exposure to the ambient air. The peak below 100°C is primarily

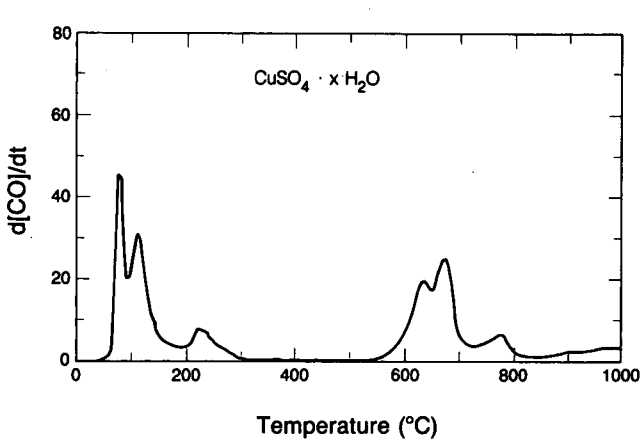

Figure 3. Thermogram of 153.0 μg $CuSO_4 \cdot xH_2O$.
(XBL 838-2990)

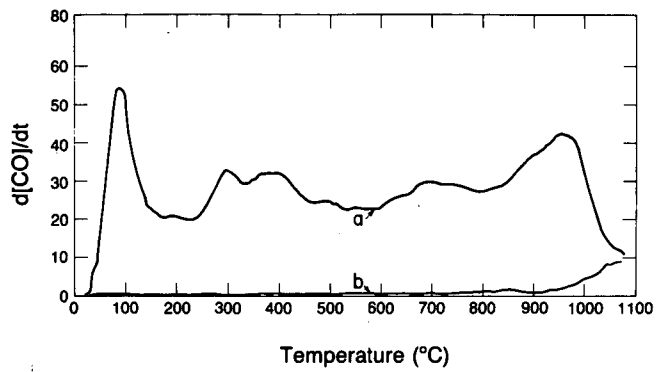

Figure 4. Thermograms of (a) activated carbon (RB-1) and (b) reanalysis of RB-1 without exposing it to air.
(XBL 844-10460)

adsorbed oxygen, of which less than 10% is H_2O.[2] This observation is consistent with the manufacturer's statement that RB-1 is hydrophobic. Activated carbon contains microcrystalline graphite and has many oxygen-functional groups on its surface.[5] These will all contribute to the structure of the thermogram, but the assignment of specific functional groups to particular peaks will require further investigation.

Figure 4, trace (b), indicates the ability of temperature-programmed analysis to remove oxygen from a sample. The sample of trace (a) was cooled to room temperature under N_2 at the end of the analysis and then reanalyzed without exposure to air. Except for a small amount of oxygen evolving above 950°C, the sample was completely stripped of oxygen. Programmed-temperature thermal analysis is a nonequilibrium process, the extent of which depends on the relationship of the heating rate to the equilibration time constant. The residual oxygen in the sample that evolved above 950°C during reanalysis is probably due to tightly bound oxygen that had not completely equilibrated at high temperatures during the first run.

PLANNED ACTIVITIES FOR FY 1985

We are in the process of obtaining samples of Los Angeles particulate matter. A comparison of O/C in samples collected at elevated levels of ozone concentration will be made with samples collected at low $[O_3]$.

REFERENCES

1. Benner, W.H. (1984), "The Determination of Pyrolyzable Oxygen in Ambient Particulate Matter," *Anal. Chem.* (in press).
2. Dod, R.L. (1984), unpublished data.

3. Wendlandt, W.W. (1974), *Thermal Methods of Analysis,* Wiley, New York, p. 11.
4. Buzas, I., Ed. (1975), "Thermal Analysis," in *Proceedings of the International Conference on Thermal Analysis,* Akademiai Kiado, Budapest, p. 1027.
5. Chang, S.G., Brodzinsky, R., Gundel, L.A., and Novakov, T. (1982), "Chemical and Catalytic Properties of Elemental Carbon," in *Particulate Carbon: Atmospheric Life Cycle,* G.T. Wolff, and R.L. Klimisch, Eds., Plenum, New York, p. 159.

The Role of Surface Oxygen in S(IV) Oxidation by Different Carbons*†

L.A. Gundel, W.H. Benner, and T. Novakov

Because of its potential significance for atmospheric chemistry, oxidation of sulfur dioxide by carbon particles has received considerable attention.[1–11] However, there is significant disagreement about the importance of soot-catalyzed SO_2 oxidation in the atmosphere. The principal reason for this disagreement is the extrapolation of laboratory studies, performed with different model carbons, to atmospheric conditions. Assessments of the importance of this process range from significant, under nonphotochemical conditions,[12] to negligible.[10] In this report we give data on SO_2 oxidation by a number of commercial carbons as well as by ambient carbon particles. These data show that the rates for different carbons may differ by two orders of magnitude, with the ambient carbon particles being the most active. We also show that the differences in catalytic activity can be ascribed to the capability of carbon surfaces to adsorb oxygen and that this surface oxygen is the actual oxidant of SO_2.

ACCOMPLISHMENTS DURING FY 1984

Commercially available activated carbons and carbon blacks were used in this study (Table 1). A sample of each carbon was ground overnight in an agate ball mill, washed in boiling distilled water, filtered, and dried overnight at 100°C. Black carbon was isolated from quartz filter samples of ambient particulate matter, using a digestion procedure based on the work of Smith *et al.*[13] To recover ~50 mg of black C, ~1500 cm_2 of heavily loaded high-volume filters collected at Berkeley between 1978 and 1983 were treated with HF, HCl, KOH, and H_2O_2. Total carbon was determined by combustion. Total or bulk oxygen was determined by temperature-programmed evolved gas analysis (EGA).[14] Surface oxygen to carbon atomic fractions were determined by electron spectroscopy for chemical analysis (ESCA), using an AEI-200 x-ray photoelectron spectrometer. Electron microscopy was performed using AM Ray model 1000 and International Scientific Instruments model DS 130 microscopes. Samples were prepared for electron microscopy by deposition of a few drops of aqueous slurries onto wet polycarbonate filters, followed by evaporation at room temperature. The density of the model carbons was measured by aqueous volume displacement.

The oxidation of S(IV) in aqueous slurries was measured using the procedures of Brodzinsky *et al.*[5] with minor modifications. The S(IV) was prepared from $Na_2S_2O_5$, which hydrolyzes to S(IV) in solution. For all experiments, the initial concentration of S(IV) was close to 5.0×11^{-4} *M*, and the concentration of particles was 1.00 g/L (total mass). [S(IV)] was determined by iodometric titration.[15]

Figure 1 shows the S(IV) concentration as a function of time for three commercial carbons: Vulcan 6, Nuchar S-N, and RB-1. The general behavior of S(IV) concentration after mixing together carbon and the S(IV) solution is qualitatively similar to

Table 1. Catalytic activity of various carbons.

Carbon	δ (m*M*/g)	Rate (*M*/g/s)	Surface O/C (atomic fraction)	A^* (m^2/g)	A_{geo} (m^2/g)	A_{BET}[a] (m^2/g)
Graphite	0	0	0.050			
Vulcan 6	0.016	5.0×10^{-9}	0.029	3	1.9	115
BP1300	0.045	3.2×10^{-8}	0.084			
Aktivkohle	0.068	1.1×10^{-7}	0.136			
Nuchar S-N	0.046	1.9×10^{-8}	0.136	8	8.0	1600
RB-1	0.075	3.9×10^{-7}	0.143	45	11.0	950
Poly C	0.060	$3.\times10^{-8}$	0.164			

[a]Manufacturer's data.

*This work was supported by the Director, Office of Energy Research, Office of Health and Environmental Research, Physical and Technological Research Division of the U.S. Department of Energy under Contract No. DE-AC03-76SF00098 and by the National Science Foundation under Contract No. ATM-83-15442.

†Abridged from a report to be submitted to *Atmospheric Environment.*

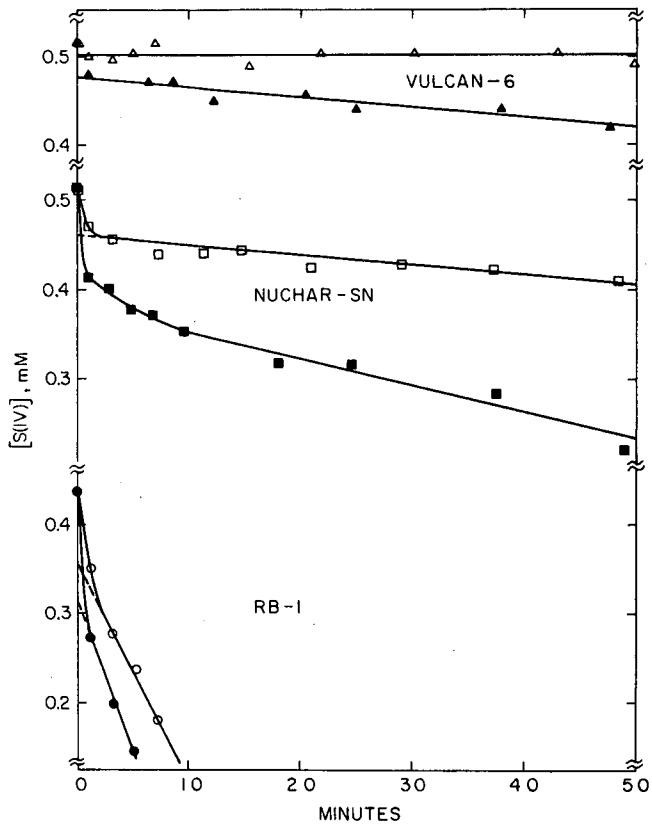

Figure 1. The effect of heat treatment on the catalytic activity [S(IV) concentration] of three model carbons. Open symbols, untreated carbons; closed symbols, carbons heated to 1000°C in N_2, cooled in N_2, and then exposed to room air for 6–18 hours. Model carbon concentrations were 1.0 g/L for all experiments. (XBL 845-1725)

observations reported before[5]; i.e., it is a two-stage process, consisting of a rapid initial depletion of S(IV) and a slower linear decrease in S(IV) concentration with time. Because the first step is very fast, its more detailed kinetics could not be studied by the analytical procedure used in these experiments; we therefore report only δ, the value of the initial decrease in S(IV) concentration. We obtained δ by extrapolating the linear portion of the curve to the start of the reaction and subtracting this extrapolated concentration from the initial concentration C_0 (Fig. 1).

It is clear from Table 1, where the δ values and the second-step rate constants for all carbons are tabulated, that different carbons have vastly different S(IV) catalytic activities. The rates for the second-stage oxidation differ by almost two orders of magnitude between the least active carbon (Vulcan 6) and the most active (RB-1). The δ values for these two carbons differ by about a factor of 5. Table 1 also shows that the higher the δ value for a particular carbon, the faster is the second-stage rate, i.e., the two processes are interrelated and possibly due to a common factor, such as surface oxygen. This hypothesis is supported by the fact that both δ and the second-stage rate increase with increasing surface O/C atomic fractions.

In order to study the role of surface oxygen, carbon samples were pretreated by heating to different temperatures in a nitrogen atmosphere, cooled to room temperature, exposed to air, and then used to catalyze S(IV) oxidation. The O/C atomic fractions were determined by ESCA and EGA after each treatment step. We found that both the surface and bulk O/C atomic fractions decreased with treatment temperature, but the δ value and the rate of the second-stage process increased with temperature for all three carbons. This demonstrates that not all the oxygen that was originally present in or on carbon particles participates in the S(IV) oxidation and that the small amount of oxygen present after heat treatment is more active than the oxygen that was originally present.

Temperature-programmed EGA has provided further insight into the identity of the oxygen responsible for the catalytic activity of carbons. Figure 2(a) shows the oxygen thermogram of RB-1 activated carbon that had not been heat-treated. The thermogram is complex, with peaks between 100° and 1000°C. These peaks, although not specifically identified, correspond to various forms of adsorbed oxygen, oxygen-containing functional groups, and water.

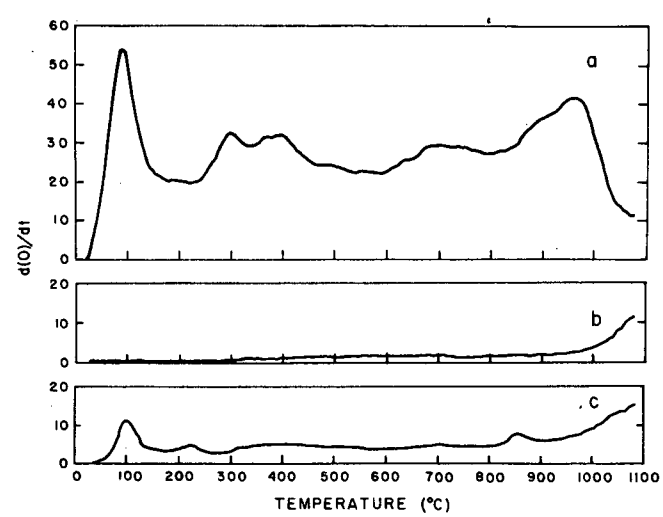

Figure 2. Oxygen thermograms for RB-1: (a) No heat treatment; (b) sample heated to 1000°C in N_2 and reanalyzed without exposure to air; (c) same (heat-treated) sample subsequently exposed to air at room temperature for 30 minutes, then reanalyzed. (XBL 845-1803)

Water accounted for 2% of the total oxygen, as measured in a separate EGA apparatus that has a water detector and a nitrogen atmosphere. Figure 2(b) is the thermogram of the same sample after it was heated in nitrogen to 1000°C and cooled to room temperature without exposure to air. Essentially no oxygen was detected in this sample, thus demonstrating that such heat treatment has removed all oxygen from the carbon. Finally, after this treated sample was exposed to room air for about 30 minutes, the thermogram shown in Fig. 2(c) was obtained. The peak at about 100°C is therefore due to adsorbed oxygen and water from the air, with the latter accounting for about 20% of the oxygen released in this peak. The remainder, i.e., adsorbed oxygen, is the active oxygen ($C_x \cdot O_2$). Most of the total oxygen that was originally present in the sample is not active, since carbons after heat treatment at 1000°C and subsequent exposure to air are more active than the original untreated carbons (Fig. 1). That the catalytic activity of untreated carbons follows the O/C atomic fractions is a reflection of more reactive surfaces in general. These would pick up more oxygen, both in the manufacturing process and during storage.

Of these carbons, the more reactive Nuchar S-N and RB-1 adsorbed much more oxygen after heating and re-exposure to air than did the least active Vulcan 6. This means that the surface of the inert carbon does not provide many suitable sites for oxygen chemisorption and consequently has few active sites for S(IV) oxidation. In contrast, both reactive carbons adsorbed considerable amounts of oxygen; however, the less reactive Nuchar S-N adsorbed more oxygen and water than the more reactive RB-1. This apparent contradiction may be understood by comparing the surface and bulk O/C fractions for carbons treated at 1000°C (Fig.3). The surface O/C for RB-1 is about 9 times higher than the bulk O/C, but the surface O/C is only about twice as high as the bulk O/C for Nuchar S-N. This result shows that the more active carbon is significantly enriched in surface oxygen. Furthermore, because both Nuchar S-N and RB-1 have similar surface O/C fractions but different δ values, it is possible that not all adsorbed oxygen participates in the S(IV) oxidation and that the oxygen on RB-1 may be more accessible to the S(IV) species at the solid-liquid interface.

Investigation of the microstructure of the model carbons provides further insight about the parameters that control the reaction rate. If the first step in S(IV) oxidation is caused by the reaction of sulfite with adsorbed oxygen, then δ can be used to estimate the active surface area, A^*, which equals mNa, where

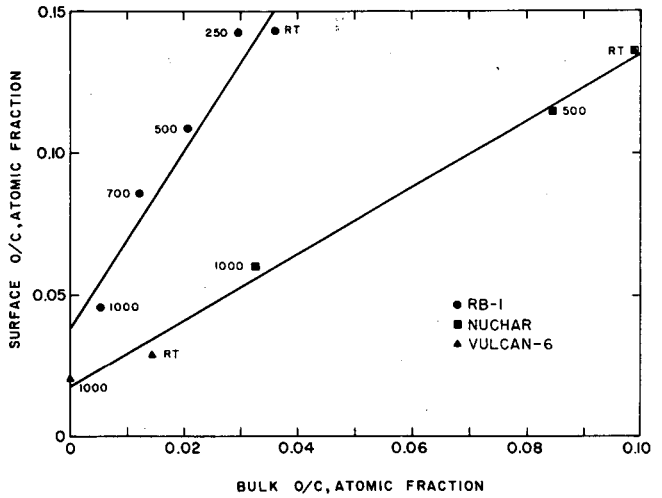

Figure 3. Surface oxygen vs. bulk oxygen for heat-treated carbons. Adjacent to the symbols are the temperatures of heat treatment in °C. Surface O/C was determined from ESCA; oxygen EGA provided bulk O/C fractions.
(XBL 845-1723)

m is the S/C mole fraction deduced from δ, N is Avogadro's number, and a is the cross-sectional area of an S(IV) ion. The area of S(IV) is estimated to be 30 Å^2, from the S-O bond lengths and angles in SO_3^{2-} and SO_4^{2-}.[16] The geometric surface areas, A_{geo}, are calculated from the observed median diameters of these particles (from SEM micrographs) and from the particle densities as measured in water. Results are given in Table 1. A^* corresponds reasonably well to A_{geo} for Vulcan 6 and Nuchar S-N and is roughly 5 times larger for RB-1. For all carbons, A^* is much smaller than the surface area as measured by nitrogen adsorption, A_{BET}. This is to be expected because A^* is the relevant surface area at the solid-liquid interface, which appears to be independent of the gas-solid surface area, A_{BET}.

The results of this study lead us to formulate the following model for the surface oxidation of S(IV). The oxidant is adsorbed oxygen, $C_x \cdot O_2^*$. The more $C_x \cdot O_2^*$ is available, the more S(VI) can be formed in the initial rapid step of the oxidation. The slower step involves the same sites but is limited by the diffusion of dissolved oxygen and S(IV) to the surface. The size and microstructure of the carbon surface also influence the accessibility of S(IV) to $C_x \cdot O_2^*$. The wide variation in measured oxidation rates for different carbons is due to variability in their capacities for chemisorbing oxygen. Removal of unreactive surface functional groups by heat treatment with subsequent re-exposure to air at room temperature allows for enhanced chemisorption because more sites are available, so the rates of both types of S(IV)

oxidation increase. Conversely, fresh combustion particles should be more reactive than aged particles, whose surfaces are covered with unreactive species.

We have not yet completed studies with fresh combustion particles, but we simulated them by use of black carbon digested from ambient particles collected in Berkeley. These particles were extremely reactive in oxidation of S(IV) (Fig. 4); heating in nitrogen at 1000°C did not change the reactivity. A larger δ was observed for these particles than for any of the model carbons: δ = 0.30 m*M*/g, compared to 0.23 for RB-1 (1000°C), the most reactive model carbon in this study. These results help clarify part of the controversy about the importance of soot as an atmospheric catalyst for SO_2 oxidation. For model carbons and ambient carbon, the rapid first step accounts for most of the total conversion. Since the second-stage process is much slower than the first step, extrapolation of the rate of the second process to atmospheric conditions may seriously underestimate the ability of a fresh carbon particle to oxidize S(IV). Earlier neglect of the importance of the rapid first step and the wide variation among different carbons in measured rates for the second-stage process account for the range of predicted rates of soot-catalyzed atmospheric SO_2 oxidation.

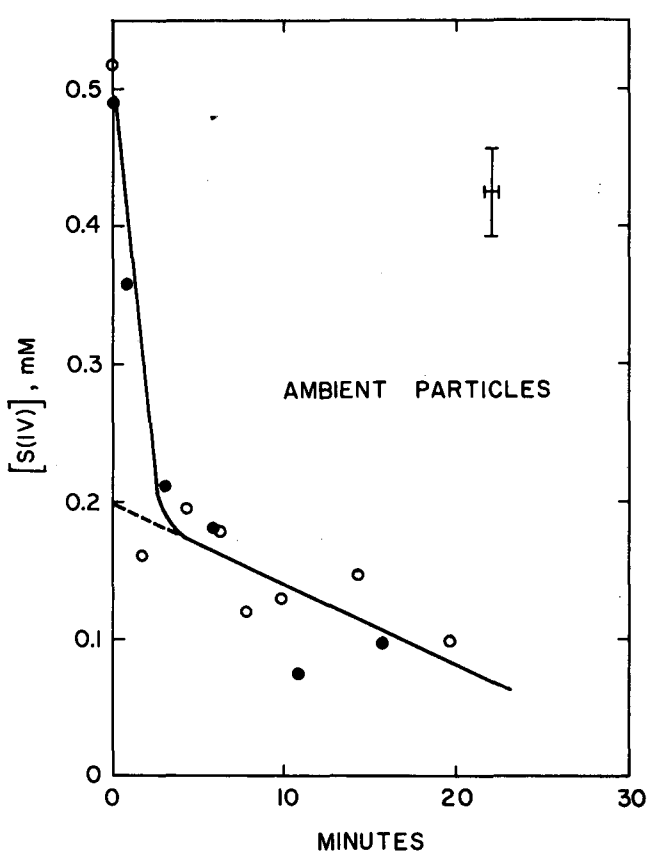

Figure 4. Catalytic activity of digested ambient particulate matter from Berkeley, California. Concentration of particles was 1.0 g/L. Open circles, untreated; filled circles, heated to 1000°C in N_2, cooled in N_2, then exposed to air for 3 hours. (XBL 845-1728)

PLANNED ACTIVITIES FOR FY 1985

We plan to expand this project by measuring the rate of the fast first step. This will be done by quenching the reaction with formaldehyde and measuring [S(IV)] and [S(VI)] by ion chromatography. We will also use the results of this study to estimate what fraction of ambient particulate sulfur is produced by heterogeneous oxidation of dissolved SO_2.

REFERENCES

1. Novakov, T., Chang, S.-G., and Harker, A.B. (1974), "Sulfates as Pollution Particulates: Catalytic Formation on Carbon (Soot) Particles," *Science 186*, p. 259.
2. Liberti, A., Brocco, D., and Possanzini, M. (1978), "Absorption and Oxidation of Sulfur Dioxide on Particles," *Atmos. Environ. 12*, p. 255.
3. Judeikis, H.S., Stewart, T.B., and Wren, A.G. (1978), "Laboratory Studies of Heterogeneous Reactions of SO_2," *Atmos. Environ. 12*, p. 1633.
4. Britton, L. G., and Clarke, A.G. (1980), "Heterogeneous Reactions of Sulfur Dioxide and SO_2/NO_2 Mixtures with a Carbon Soot Aerosol," *Atmos. Environ. 14*, p. 829.
5. Brodzinsky, R., Chang, S.-G., Markowitz, S.S., and Novakov, T. (1980), "Kinetics and Mechanism for the Catalytic Oxidation of Sulfur Dioxide on Carbon in Aqueous Suspensions," *J. Phys. Chem. 84*, p. 3354.
6. Cofer III, W.R., Schryer, D.R., and Rogowski, R.S. (1980), "The Enhanced Oxidation of SO_2 by NO_2 on Carbon Particulates," *Atmos. Environ. 14*, p. 571.
7. Cofer III, W.R., Schryer, D.R., and Rogowski, R.S. (1981), "The Oxidation of SO_2 on Particles in the Presence of O_3, NO_2, and N_2O," *Atmos. Environ. 15*, p. 1281.
8. Baldwin, A.C. (1982), "Heterogeneous Reactions of Sulfur Dioxide with Carbonaceous Particles," *Int. J. Chem. Kinetics 14*, p. 269.
9. Benner, W.H., Brodzinsky, R., and Novakov T. (1982), "Oxidation of SO_2 in Droplets Which Contain Soot Particles," *Atmos. Environ. 16*, p. 1333.

10. Harrison, R.M., and Pio, C.A. (1983), "Kinetics of SO_2 Oxidation over Carbonaceous Particles in the Presence of H_2O, NO_2, NH_3 and O_3," *Atmos. Environ. 17*, p. 1261.

11. Cofer III, W.R., Schryer, D.R., and Rogowski, R.S. (1984), "Oxidation of SO_2 by NO^2 and O_3 on Carbon: Implications to Tropospheric Chemistry," *Atmos. Environ. 18*, p. 243.

12. Middleton, P., and Kiang, C.S. (1979), "The Relative Importance of Nitrate and Sulfate Aerosol Production Mechanisms in Urban Atmospheres," in *Nitrogenous Air Pollutants: Chemical and Biological Implications*, D. Grosjean, Ed., Ann Arbor Science, Ann Arbor, p. 269.

13. Smith, D.M., Griffin, J.J., and Goldberg, E.D. (1975), "Spectrometric Method for the Quantitative Determination of Elemental Carbon," *Anal. Chem. 47*, p. 233.

14. Benner, W.H., and Hansen, A.D.A. (1984), "Temperature-Programmed Evolved Gas Analysis for Determining Pyrolyzable Oxygen," accepted by *Anal. Chem.*.

15. Skoog, D.A., and West, D.M. (1969), "Volumetric Methods Involving Iodine," in *Fundamentals of Analytical Chemistry*, 2nd ed., Holt, Rinehart and Winston, New York, p. 445.

16. Bailar, J.C., Ed. (1973), *Comprehensive Inorganic Chemistry*, vol. 2., Pergamon, Oxford, p. 879.

Aerosol Characterization in Beijing, China, 1983–1984*

R.L. Dod, R.D. Giauque, T. Novakov, and Su Wei-han[†]

Studies of the conversion of sulfur dioxide to particulate sulfates in the atmosphere have led to ambiguous and/or contradictory conclusions regarding reaction mechanisms and rates. A variety of mechanisms have been proposed that have potential import under ambient conditions, but verifying the contributions of these mechanisms to the sulfate burden in the atmosphere of the United States has been complicated by the relatively low concentrations of pollutants and the great variety of fuels and combustion sources used. In order to increase our data base on this subject, we have established a sampling site in Beijing, China, a location that is subject to a large pollutant impact from a limited variety of combustion sources whose emissions are not so tightly regulated as those in the United States.

ACCOMPLISHMENTS DURING FY 1984

Daily 24-hour aerosol samples were collected during 1983 and part of 1984. The sampling sequence was arranged to cover approximately three seasons—spring, summer, and winter. The spring samples were collected from March through the beginning of May, 1983; summer samples, during July 1983; and winter samples, from the end of October 1983 through February 1984.

Total carbon and particulate sulfur were determined for every sample collected. Total carbon was determined by a combustion method[1]; particulate sulfur was measured with a low-energy dispersive x-ray fluorescence spectrometer.[2] The concentrations of these two elements constitute the minimal data set that was used for preliminary data analysis. On the basis of the results of this analysis, samples from March, July, and December 1983 were selected for a complete x-ray fluorescence analysis for all trace elements. Most samples from these three months were also analyzed by thermal evolved gas analysis[3] to determine their primary carbon or soot content. The results obtained for these months, together with rudimentary meteorological information and SO_2 concentrations, constitute the complete data base. An evaluation of this data base has enabled us to make certain conclusions about the SO_2 to SO_4^{2-} conversion processes operating during the three sampling seasons.

Figure 1(a) shows the 24-hour total carbon concentrations in micrograms per cubic meter for each sampling day. It is evident that the total carbon concentrations are relatively low and approximately constant during April, May, and July. The average concentrations during this period are $\sim 30\ \mu g/m^3$. Starting in October, however, large variations in carbon concentrations are seen. The maximum carbon con-

*This work was supported by the Director, Office of Energy Research, Office of Health and Environmental Research, Physical and Technological Research Division of the U.S. Department of Energy under Contract No. DE-AC03-76SF00098.

[†]Institute of Environmental Chemistry, Academia Sinica, Beijing, China.

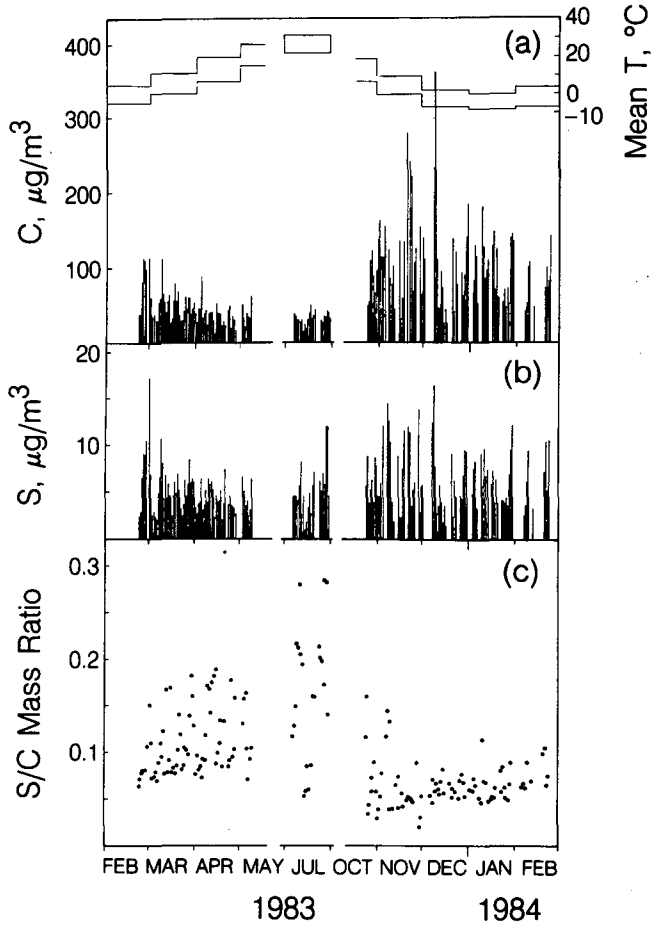

Figure 1. Daily average particulate carbon (a) and sulfur (b) loadings near the Institute for Environmental Chemistry, Beijing, China; (c) the daily S/C mass ratios.
(XBL 8411-4760)

centration reached about 360 $\mu g/m^3$ in the beginning of December. During the winter, carbon concentrations greater than 100 $\mu g/m^3$ were frequently measured.

Representative samples from different months were also analyzed by evolved gas analysis. The single most distinctive feature of the EGA thermograms is the black carbon, composing about 40% to 50% of the total noncarbonate carbon. Such a feature is characteristic of combustion-produced soot particles, as demonstrated elsewhere.[4] (A small fraction, usually less than 15%, of total carbon was present as carbonate carbon.) On the basis of such evidence, we conclude that most of the particulate carbon is soot and that the total carbon concentrations are approximately equivalent to the soot concentration. Further justification of this conclusion will be presented later in this article, using an analysis of the ratios of total carbon to combustion-related trace metals.

An examination of the average temperatures during the winter sampling period suggests that the wintertime soot is related to space heating. The average monthly maximum and minimum temperatures for 1983–84 (compiled from international weather reports) are indicated in Fig. 1(a). It is evident that the increase in ambient soot concentrations corresponds to lower temperatures, suggesting that space heating is a significant source of ambient soot during cold periods. Stagnant air conditions occurring during cold days would, of course, result in maximum soot concentrations.

Particulate sulfur concentrations for the entire set of samples are displayed in Fig. 1(b). These concentrations indicate, as well, the corresponding sulfate concentrations, if it is assumed that all particulate sulfur is in the form of sulfate. It is of interest that the sulfate concentrations, like the carbon concentrations, are relatively constant during April, May, and July. However, starting in November, large sulfate concentration peaks are observed on many days. The maximum 24-hour average concentrations are about 15 $\mu g/m^3$ of sulfur (or 45 $\mu g/m^3$ of sulfate). The average sulfur concentrations are not very different for summer and winter days because of alternating high and low sulfur days during winter.

Soot is a primary combustion-generated pollutant and can be used as a conservative tracer for the products of incomplete combustion. In contrast, suspended sulfates are secondary species produced by oxidation of SO_2 in the atmosphere. The ratio of particulate sulfur (or sulfate) to soot can be used to infer the relationship between sulfates and source emissions. This approach is illustrated in Fig. 1(c), where the particulate sulfur-to-carbon ratios are shown. The most striking feature is the difference in these ratios for different periods of the year. During July, large scatter in the data is seen, but overall, during the rest of the year, the S/C ratios are lower than in the summer. The summer aerosol is therefore enriched in sulfate with respect to the soot tracer, whereas the winter aerosol, in contrast, seems to be directly related to emissions from, most likely, local sources.

One interpretation of the differences in these ratios could be the existence of two different SO_2 conversion processes, one being dominant in the summer and the other in the winter. For example, the dominant summertime mechanism could be photochemical, while in the winter a nonphotochemical mechanism might predominate. The wintertime mechanism is either less efficient, involves shorter residence times, or is in some way limited by the available reactants so that a lower but constant S/C ratio results.

In order to gain further insight into the processes suggested by the analyses described above, samples from March, July, and December were chosen for complete x-ray fluorescence analysis for trace elements. The average concentrations were computed for the first and second half of each month. Table 1 lists the semimonthly average C/Pb, C/V, C/Se, Se/V, S/C, S/Se, and S/V concentration ratios. In the following analysis, it was assumed that Se and V are tracer elements for coal and fuel oil, respectively. Several conclusions about the sources of particulate matter can be reached from an examination of these ratios.

Carbon/selenium ratios are essentially the same for all three months, suggesting that the principal source of particulate carbon is coal combustion. Carbon/vanadium ratios are equal during March and July but noticeably higher in December. Such behavior is to be expected if fuel-oil usage is approximately constant throughout the year. The higher C/V ratio in December reflects increased coal use in December. A similar conclusion is suggested by the Se/V ratios. The C/Pb ratio is about an order of magnitude higher than that in countries with a much higher automotive source component. Because the absolute Pb concentrations are low and the C/Pb ratio is similar for all three seasons, we conclude that the atmospheric lead is related to coal combustion.

We have already mentioned that the seasonal behavior of the S/C ratio suggests different SO_2 oxidation mechanisms in summer and in winter. This conclusion is strengthened by the ratios of S to other tracer elements such as Se and V. The standard deviations of these ratios are greater than those for the S/C ratio, mainly because of the greater analytical error in Se and V determination. Nevertheless, both the S/Se and S/V ratios are statistically significantly higher in July than in December. The values for these ratios in March are generally between those for July and December.

The differences in these ratios could be interpreted as a result of a photochemical SO_2 oxidation mechanism that predominates during the summer, possibly occurring during long-range transport, while a less efficient mechanism predominates during the winter. Nevertheless, the absolute concentrations of sulfate are lower during the summer because the concentration of SO_2 available for oxidation is also low. Conversely, a relatively inefficient wintertime mechanism, presumably nonphotochemical, can produce high sulfate concentrations because the SO_2 concentrations are high.

That the winter sulfates are derived from local sources is evident from the excellent correlation with soot. This correlation is poor or nonexistent during summer. These correlations are shown graphically in Fig. 2.

A thorough examination of the data from this location also suggests that the winter sulfate is formed rapidly, a conclusion reached by examining periods of air stagnation that can last for several days. It is plausible, therefore, that during such episodes the average residence time of pollutants in the air must differ from day to day, allowing more sulfate to be formed during stagnant periods. This should result in a systematically increasing ratio of sulfate to a primary particulate tracer; however, this did not happen. The sulfate-to-soot ratios, for example, remained approximately constant during the entire winter sampling period, including the stagnant periods.

The causes of, and the mechanisms responsible for, this apparent rapid formation are unknown at present. However, several processes potentially capable of explaining these wintertime observations can be identified. The obvious possibility is that local sulfates are primary, that is, produced by SO_2 oxidation to SO_3 in flames. Such SO_3 will react with water and ammonia to form suspended sulfate. This explanation agrees with the observed correlations between

Table 1. Semimonthly elemental ratios (±).

	March		July		December	
Ratio	1–15	16–31	1–15	16–31	1–15	16–31
S/C	0.11(0.09)	0.11(0.05)	0.15(0.09)	0.18(0.09)	0.06(0.05)	0.06(0.04)
S/Se	380(321)	382(218)	407(247)	518(306)	158(160)	212(158)
S/V	64(53)	56(30)	95(67)	129(89)	90(79)	69(52)
C/Pb	184(138)	198(108)	193(103)	156(65)	216(296)	244(182)
C/V	587(419)	511(265)	623(362)	728(407)	1606(1960)	1148(860)
C/Se	3506(2554)	3511(1929)	2680(1193)	2910(1259)	2818(3717)	3513(2623)
Se/V	0.17(0.13)	0.15(0.09)	0.23(0.14)	0.25(0.15)	0.57(0.72)	0.33(0.26)

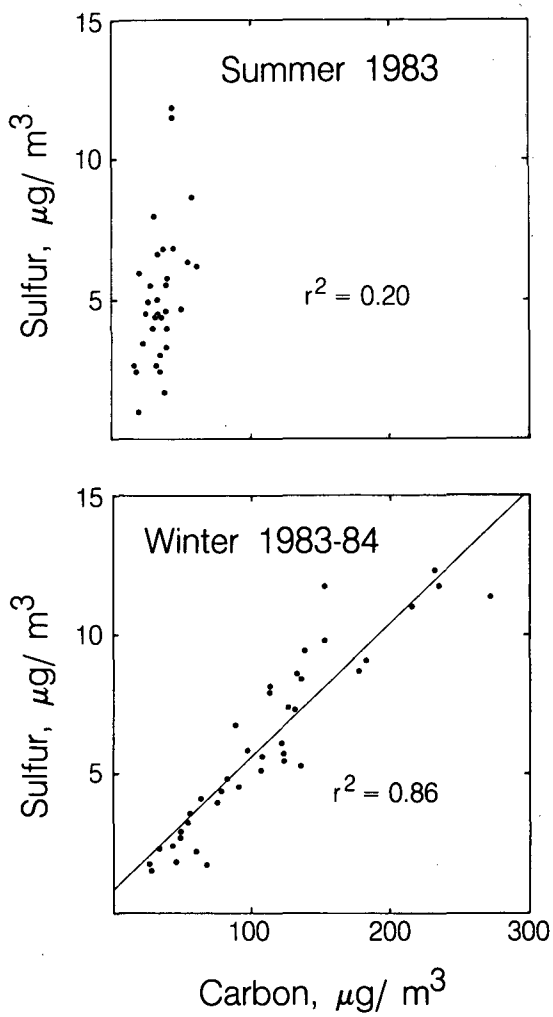

Figure 2. Summer and winter correlation plots of particulate sulfur with particulate carbon. The correlation coefficients, r^2, for linear least-squares fits are shown.
(XBL 8411-8927)

sulfate and primary combustion-generated species. However, sulfate composes on the average 15% of total airborne sulfur. This value is too high to be accounted for by primary sulfates because it is known that only about 1% of fuel sulfur is converted to SO_3 in the combustion process.[5]

Other candidate mechanisms are heterogeneous processes involving aqueous systems in the form of liquid water droplets and/or wetted particle surfaces and include catalytic oxidation by water-soluble transition-metal ions,[5,6] reactions on fly-ash surfaces,[7] catalytic oxidation on soot surfaces,[8] and oxidation by primary oxidants, such as peroxides.[9]

We have already demonstrated the existence of excellent sulfur-carbon correlations in the winter. However, no significant correlations were observed with manganese or iron, the transition metals believed to be important in aqueous SO_2 oxidation. On the basis of the information presented, the winter sulfate appears to be either primary or quasi-primary, produced in the vicinity of sources by a process limited by the available surface and/or catalyst or oxidant availability.

Recently obtained daily average humidity data show a pattern that tracks that of the ratio of sulfur to particulate carbon in Fig. 1(c). This agreement implies that particulate carbon in the presence of water provides an efficient mechanism for the oxidation of SO_2 to sulfate.

PLANNED ACTIVITIES FOR FY 1985

We intend to further analyze recently acquired meteorological data and to obtain data regarding ionic species present in the samples collected. We will also use the resulting information to plan further sample collection and analysis to more explicitly determine the role of particulate carbon in atmospheric SO_2 oxidation. It is intended that this will complement and extend our studies in Europe.

REFERENCES

1. Huffman, E.W.D., Jr. (1977), "Performance of a New Automatic Carbon Dioxide Coulometer," *Microchem. J. 22*, p. 567.
2. Giauque, R.D., Garrett, R.B., and Goda, L.Y. (1979), "Determination of Trace Elements in Light Element Matrices by X-Ray Fluorescence Spectrometry with Incoherent Scattered Radiation as an Internal Standard," *Anal. Chem. 51*, p. 511.
3. Dod, R.L., and Novakov, T. (1982), "Application of Thermal Analysis and Photoelectron Spectroscopy for the Characterization of Particulate Matter," in *Industrial Applications of Surface Analysis*, L.A. Casper, and C.J. Powell, Eds., American Chemical Society, Washington, D.C.
4. Gundel, L.A., Dod, R.L., Rosen, H., and Novakov, T. (1984), "The Relationship Between Optical Attenuation and Black Carbon Concentration for Ambient and Source Particles," *Sci. Total Environ. 36*, p. 197.
5. Freiberg, J. (1974), "The Mechanism for Iron Catalyzed Oxidation of Sulfur Dioxide by Aerosols of Manganese Sulfate," *Atmos. Environ. 9*, p. 661.
6. Matteson, M.J., Stober, W., and Luther, H. (1974), "Kinetics of the Oxidation of Sulfur Dioxide by Aerosols of Manganese Sulfate," *I&EC Fund. 8*, p. 667.

7. Cohen, S., Chang, S.G., Markowitz, S.S., and Novakov, T. (1981), "Role of Fly Ash in Catalytic Oxidation of S(IV) Slurries," *Environ. Sci. Technol. 15*, p. 1498.
8. Brodzinsky, R., Chang, S.G., Markowitz, S.S., and Novakov, T. (1980), "Kinetics and Mechanism for the Catalytic Oxidation of Sulfur Dioxide on Carbon in Aqueous Suspensions," *J. Phys. Chem. 84*, p. 3354.
9. McKinney, P.M., Benner, W.H., and Novakov, T. (1984), "Primary Peroxides from Hydrocarbon Flames," in *Applied Science Division FY 1983 Annual Report: Atmospheric Aerosol Research*, LBL-17073, p. 4-10.

Role of Combustion-Generated Carbon Particles in the Absorption of Solar Radiation in the Arctic Haze*†

H. Rosen and A.D.A. Hansen

The phenomenon of Arctic haze, first reported by Mitchell,[1] is due to small aerosol particles that scatter[2] and absorb[3] solar radiation,[4,5] leading to substantial optical depths.[6] From both trace element analysis[7,8] and direct identification of large concentrations of combustion-generated graphitic particles[3,9] in the Arctic atmosphere, it is known that the Arctic haze has a major combustion-derived component. This component could lead to significant heating effects over the high-surface-albedo polar icecap.[6,10,11] A major uncertainty in modeling the effects of the Arctic haze on the solar radiation balance has been our limited knowledge of the vertical distribution of graphitic carbon particles and their associated absorption coefficients. Here and in a companion paper,[12] we report on the first measurements of such distributions in the Arctic atmosphere and, to the best of our knowledge, in the atmosphere in general.

ACCOMPLISHMENTS DURING FY 1984

During March and April, 1983, a series of flights called AGASP organized by the National Oceanic and Atmospheric Administration (NOAA) explored the vertical and horizontal distributions of the Arctic haze. One instrument used in this program was the aethalometer,[13] which was developed at Lawrence Berkeley Laboratory and has the capability of determining graphitic carbon concentrations[9] on a real-time basis, using the calibration of Gundel *et al.*[14]

Vertical profiles were obtained by dividing the atmosphere into altitude bins and determining the average aethalometer response in each of these bins over the particular time periods of interest. The bin size was chosen so that the errors due to the minimum detection limit of the aethalometer were small compared with the average aethalometer response in the altitude bin. Error bars shown in the first two figures are based on three times the minimum detectable limit of the aethalometer and correspond to a change in the transmission of the filter deposit of 0.075%. The error bars are different at different altitudes because they are inversely proportional to the volume of air sampled in a given altitude bin. Particles were also collected in parallel on Millipore filters (1.2-μm nominal pore size, type RATF) for x-ray fluorescence analysis of elements with $Z > 11$.

In Figs. 1 and 2, vertical profiles of graphitic carbon concentrations versus altitude are shown for AGASP flights 8 and 10 in the Norwegian Arctic. Flight 8 was essentially in a northerly direction over Bear Island to northern Spitzbergen at 80°N 15°E and then returned to Bodo. The flight profile included a slow descent from 7 km to 0.1 km at 74°N 25°E near Bear Island. The graphitic carbon concentrations as a function of altitude are shown for this descent in Fig. 1. Also shown for comparison are the average ground-level concentrations found at the NOAA-GMCC‡ observatory near Barrow, Alaska, for April, 1982, and the annual average ground-level concentrations found in various urban areas in the United States. It is clear from this figure that the vertical profile has considerable structure with at least three layers at approximately 1 km, 2.5 km, and 4.5 km altitude, and what appears to be a very narrow layer at 1.7 km. The haze layers can have sharp boundaries with dramatic changes in con-

*This work was supported by the Director, Office of Energy Research, Office of Basic Energy Sciences, Carbon Dioxide Research Division of the U.S. Department of Energy under Contract No. DE-AC03-76SF00098. The AGASP project was organized, funded, and operated by the National Oceanic and Atmospheric Administration.

†Summary of paper published in *Geophys. Res. Lett. 11*, pp. 461–464 (1984).

‡Global Monitoring for Climatic Change.

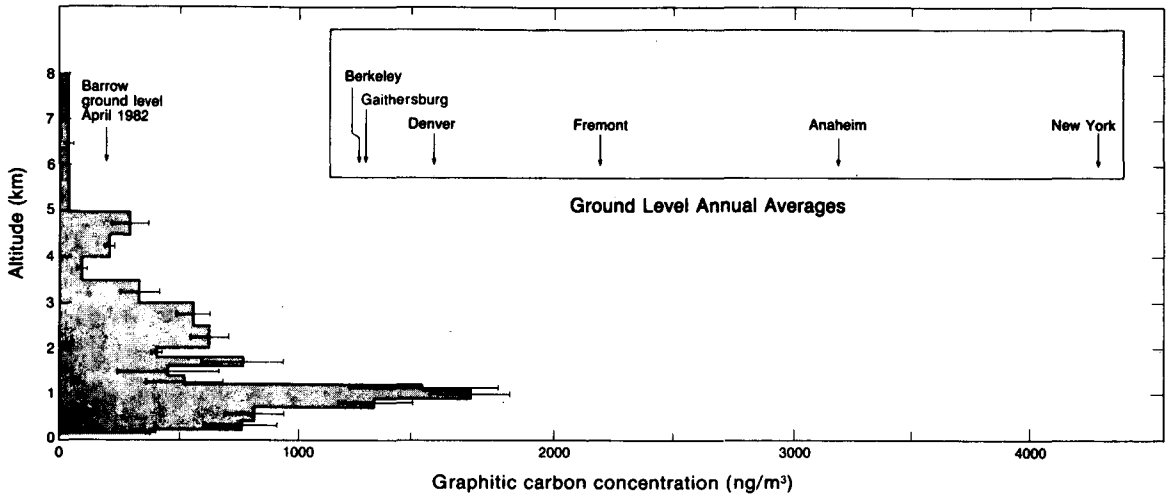

Figure 1. Vertical profile of graphitic carbon concentrations expressed as nanograms per cubic meter on March 31, 1983, at ~74°N 25°E. Shown for comparison are the annual average ground-level graphitic carbon concentrations at various urban locations in the United States and the average April, 1982, ground-level values at the NOAA-GMCC observatory near Barrow, Alaska. (XBL 8312-4319A)

centration over distances of less than 100 m. The concentrations within these layers are large, with the peak concentrations at 1 km altitude as large as some typical ground-level concentrations in the United States (Berkeley, Denver, Gaithersburg) and only about a factor of 2.5 lower than those in New York City. The concentrations in this band are about a factor of 10 higher than the 0.15-$\mu g/m^3$ ground-level concentration at Barrow, Alaska in April 1982. The flight profile also indicates a relatively clean region

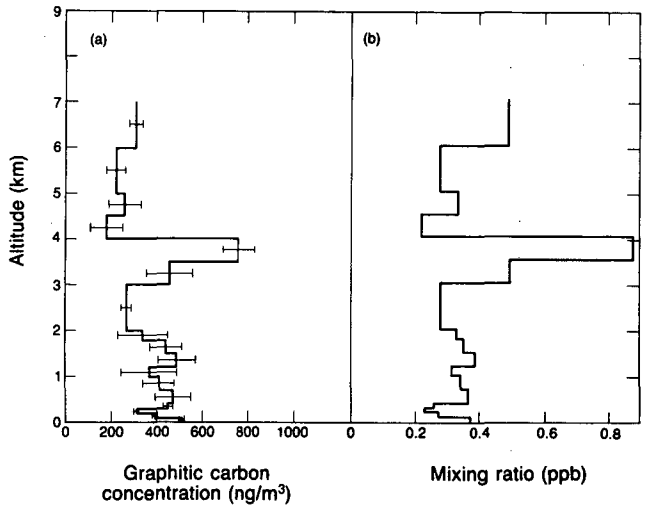

Figure 2. (a) Vertical profile of graphitic carbon concentrations expressed in nanograms per cubic meter on April 5, 1983, at ~70°N 0°E. (b) Same as (a), but with graphitic carbon concentrations expressed as a mixing ratio. (XBL 8312-6879A)

at low altitudes, which is consistent with the Barrow results[12] and the limited ground-level measurements made in the Norwegian Arctic.

Flight 10 also originated in Bodo, Norway, but flew west across the Norwegian sea on April 5, 1983, to an area near 70°N 0°E over the open ocean and then returned to Bodo. The plane remained within 70° ± 2°N latitude and ranged from 5°E to 5°W in longitude between 0914 Greenwich mean time and 1604 GMT. The average vertical profile of graphitic carbon concentrations for this period is shown in Fig. 2(a). This profile is quite distinct from that shown in Fig. 1: it has much less structure, with only one sharp band at 3.75 km altitude superimposed over an almost uniform haze layer that decreases only slightly with altitude even close to the top of the troposphere. If this profile is plotted versus the mixing ratio, as in Fig. 2(b), we see that it is essentially flat to the top of the troposphere except for the very intense band located at 3.75 km. This profile could indicate significant transport at high altitudes above the planetary boundary layer. However, it may also indicate changes in the vertical distribution that occurred after the air mass reached the Arctic.

Recent modeling studies of the possible effects of the Arctic haze on the radiation budget of the Arctic indicate rather substantial changes in the heat balance if the optical depth due to absorption is sufficiently large.[10,11] One can calculate absorption coefficients and optical depth from the results shown in Figs. 1 and 2 for various models of the Arctic aero-

sol. In these models, it is important to distinguish between graphitic particles mixed internally or externally with nonabsorbing components. Ackerman and Toon[15] showed that such differences can lead to significant changes in aerosol absorption. We will consider three examples:

- *Model 1.* Graphitic carbon particles internally mixed with all the major submicron aerosol components (i.e., sulfates, organics).
- *Model 2.* Graphitic carbon particles internally mixed with only submicron organic aerosol components.
- *Model 3.* Graphitic carbon particles externally mixed with the other aerosol components.

Of these three, the first two are the most likely combinations. For these, we treat the particles as homogeneous spheres and mix in the various components by volume mixing of dielectric constants. In these Mie calculations, the indices of refraction of graphitic carbon were chosen to be 1.94–0.66 i,[15] with a density of 1.5, and the index of refraction of the nonabsorbing components was taken to be 1.5. The relative concentrations of graphitic carbon and sulfates were determined from chemical analyses of filters collected on the flights over the time periods of the vertical profiles, while the relative concentrations of the organic component were obtained from ground-level measurements in April at Barrow, Alaska. The particle size distribution for the submicron aerosol is assumed to be log-normal with r_{gv} = 0.2 μm and σg = 2, which are obtained for the urban aerosol. For the external mixture (model 3), we use the photoacoustic measurements of Roessler and Faxvog[16] and Szkarlat and Japar,[17] who obtain an average value of 8.3 m^2/g for a wavelength of 0.5 μm.

For the vertical profile in flight 8, the three models yield specific absorption coefficients of, respectively, 19.1 m^2, 12.0 m^2, and 8.3 m^2 per gram of graphitic carbon. The corresponding results for flight 10 are 14.6 m^2, 12.0 m^2, and 8.3 m^2 per gram of graphitic carbon. The sulfur-to-graphitic-carbon ratios used in these calculations were, for models 1 and 2 respectively, 2.8 and 0.7, while the graphitic-to-total-carbon ratio was 0.2. Vertical profiles of the absorption coefficient using aerosol model 1 are shown for flights 8 and 10 in Figs. 3 and 4. The absorption coefficients can be integrated over altitude to determine absorption optical depths for the various flights and aerosol models. For flight 8, the three aerosol models yield optical depths of 0.053, 0.035, and 0.024 at 0.5 μm wavelength; for flight 10, the corresponding optical depths are 0.036, 0.029,

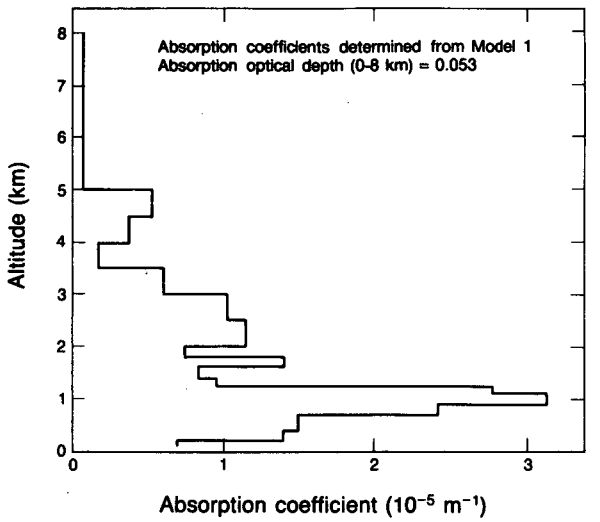

Figure 3. Vertical distribution of absorption coefficients obtained from the graphitic carbon profile shown in Fig. 1, using aerosol model 1. The corresponding absorption coefficients for models 2 and 3 can be obtained by multiplying the distribution by factors of 0.66 and 0.46, respectively.
(XBL 8312-4317A)

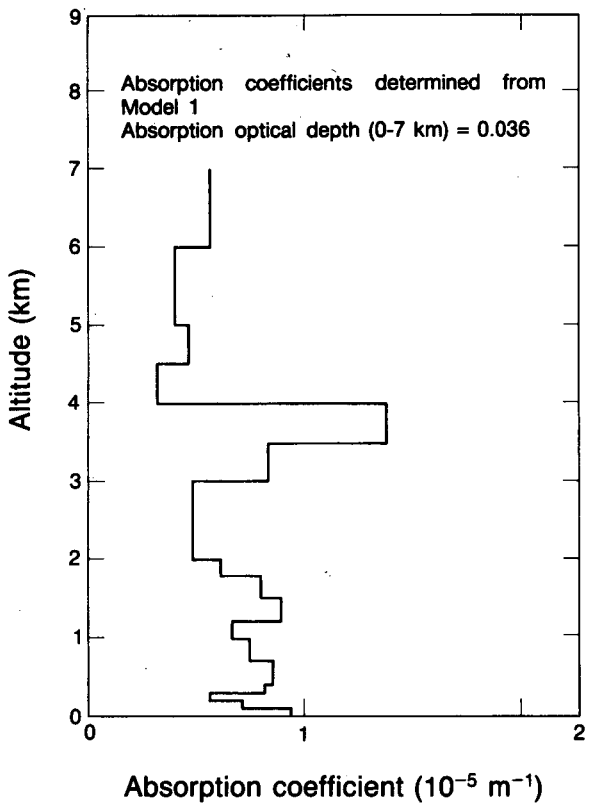

Figure 4. Vertical distribution of absorption coefficients obtained from graphitic carbon profile shown in Fig. 2, using aerosol model 1. The corresponding absorption coefficients for models 2 and 3 can be obtained by multiplying the distribution by factors of 0.82 and 0.57, respectively.
(XBL 8312-4318A)

and 0.020. It is interesting to compare these optical depths with those obtained by Valero *et al.*,[18] using a net-flux radiometer. Such a comparison can be made for the vertical profile from flight 8 shown in Fig. 1, where Valero *et al.*[18] have completed their analyses. They obtain a best-fit optical depth due to absorption of 0.06, which is very close to the largest value we report and could suggest that the aerosol may be completely internally mixed as represented in model 1.

The optical depths reported here are large enough to produce significant changes in the radiation balance over a highly reflecting surface.[10,11] This is illustrated by the calculations of Porch and MacCracken[10] and of Cess,[11] who have modeled the Arctic aerosol for an absorption optical depth of 0.021 (close to our minimum estimate), cloud-free conditions, a zenith angle of 72°, and a surface albedo of 0.8. For these parameters, they obtain a change in the noontime solar radiation balance at the top of the troposphere of about 20 W/m^2. When averaged over the day for March 15 and 70°N, the surface-atmosphere energy absorption would increase by about 7 W/m^2.[10,11] These changes are substantial and would correspond to an increase in the energy absorbed by the earth-atmosphere system of approximately 5% of the incident solar flux at the top of the troposphere.

PLANNED ACTIVITIES FOR FY 1985

The data presented here represent only a small fraction of the total data base obtained in the AGASP program. During the next fiscal year, these data will be analyzed to gain a better understanding of the vertical and horizontal distributions of the Arctic haze and its implications for radiative transfer and source regions.

REFERENCES

1. Mitchell, J.M. (1957), "Visual Range in the Polar Regions with Particular Reference to the Alaskan Arctic," *J. Atmos. Terr. Phys., Spec. Supp.*, p. 195.
2. Bodhaine, B.A., Harris, J.M., and Herbert, G.A. (1981), "Aerosol Light Scattering and Condensation Nuclei Measurements at Barrow, Alaska," *Atmos. Environ. 15*, p. 1375.
3. Rosen, H., Novakov, T., and Bodhaine, B.A. (1981), "Soot in the Arctic," *Atmos. Environ. 15*, p. 1371.
4. Heintzenberg, J. (1982), "Size-Segregated Measurements of Particulate Elemental Carbon and Aerosol Light Absorption at Remote Arctic Locations," *Atmos. Environ. 16*, p. 2461.
5. Patterson, E.M., Marshall, B.T., and Rahn, K.A. (1982), "Radiative Properties of Arctic Aerosol," *Atmos. Environ. 12*, p. 2967.
6. from the Mid-Latitudes: A Preliminary Model," *Atmos. Environ. 15*, p. 1483.
7. Rahn, K.A., and McCaffrey, R.J. (1980), "On the Origin and Transport of the Winter Arctic Aerosol," *Ann. N.Y. Acad. Sci. 338*, p. 486.
8. Barrie, L.A., Hoff, R.M., and Daggupaty, S.M. (1981), "The Influence of Mid-Latitudinal Pollution Sources on Haze in the Canadian Arctic," *Atmos. Environ. 15*, p. 1407.
9. Rosen, H., and Novakov, T. (1983), "Combustion-Generated Carbon Particles in the Arctic Atmosphere," *Nature 306*, p. 768.
10. Porch, W.M., and MacCracken, M.C. (1982), "Parametric Study of the Effects of Arctic Soot on Solar Radiation," *Atmos. Environ. 16*, p. 1365.
11. Cess, R.D. (1983), "Arctic Aerosols: Model Estimates of Interactive Influences Upon the Surface-Troposphere Radiation Budget," *Atmos. Environ. 17*, p. 2555.
12. Hansen, A.D.A., and Rosen, H., (1984), "Vertical Distributions of Particulate Carbon, Sulfur, and Bromine in the Arctic Haze and Comparison with Ground-Level Measurements at Barrow, Alaska," *Geophys. Res. Lett. 11*, p. 381.
13. Hansen, A.D.A., Rosen, H., and Novakov, T. (1982), "Real-Time Measurement of the Absorption Coefficient of Aerosol Particles," *Appl. Opt. 21*, p. 3060.
14. Gundel, L.A., Dod, R.L., Rosen, H., and Novakov, T. (1984), "The Relationship Between Optical Attenuation and Black Carbon Concentration for Ambient and Source Particles," *Sci. Total Environ. 36*, p. 197.
15. Ackerman, T.P., and Toon, O.B. (1981), "Absorption of Visible Radiation in an Atmosphere Containing Mixtures of Absorbing and Nonabsorbing Particles," *Appl. Opt. 21*, p. 3661.
16. Roessler, D.M., and Faxvog, F.R. (1979), "Optoacoustic Measurement of Optical Absorption in Acetylene Smoke," *J. Opt. Soc. Amer. 69*, p. 1699.
17. Szkarlat, A.C., and Japar, S.M. (1981), "Light Absorption by Airborne Aerosols: Comparison of Integrating Plate and Spectrophone Techniques," *Appl. Opt. 20*, p. 1151.
18. Valero, F.P.J., Ackerman, T.P., and Gore, W.J. Y. (1983), "Radiative Effects of the Arctic Haze," *Geophys. Res. Lett. 10*, p. 1184.

Vertical Distributions of Particulate Carbon, Sulfur, and Bromine in the Arctic Haze and Comparison with Ground-Level Measurements at Barrow, Alaska*†

A.D.A. Hansen and H. Rosen

The Arctic haze appears to have a large combustion-derived component, containing particulate carbon in both organic and microcrystalline graphitic forms.[1,2] The latter species is often termed "black carbon"; its only source is incomplete combustion, and its presence in polluted atmospheres is a tracer for combustion emissions, usually of anthropogenic origin. In the Arctic, the optical absorption of this material could be large enough to cause a significant perturbation of the solar radiation balance.[3–5] The haze also includes trace metals and sulfur species.[6–8] To study the distributions and to link airborne measurements with the considerable data base obtained from ground stations, the 1983 AGASP experiment, organized by the National Oceanic and Atmospheric Administration (NOAA), included aircraft flights taking vertical and horizontal samplings of the atmosphere upwind of Barrow, Alaska. Aerosol filter samples are routinely collected there at the NOAA Global Monitoring for Climatic Change ground station, and this activity was intensified during the AGASP program so that 24-hour samples were taken for each day of the overflights.[9]

ACCOMPLISHMENTS DURING FY 1984

On board the aircraft during the AGASP program, we operated the aethalometer, an instrument recently developed at LBL that responds in real time to the concentration of black carbon.[10] Vertical distributions of black carbon concentration are determined by grouping the data taken during slow descents into ranges of altitude and calculating the average. The measurement accuracy is proportional to the total data acquisition time in the range, so the range boundaries are chosen for each flight profile to optimize the balance between accuracy and vertical resolution.

We also used two filter sampling lines to collect a large number of total aerosol samples on cellulose filters (Millipore, type RATF) and prefired quartz fiber filters (Pallflex, type QAO 2500). Analyses included the measurement of major and minor elements by x-ray fluorescence. By appropriately timing the filter changes relative to the flight plan, we collected samples whose air flows were taken primarily from particular altitude ranges. In the method we use here to present these data (Figs. 3 and 4), the extent of each solid line parallel to the altitude axis indicates the range encompassing 70% of the total air volume sampled by a particular filter, with adjacent broken lines accounting for the next 20% of the air volume. The 24-hour aerosol samples collected at the NOAA–GMCC ground station were analyzed using the techniques mentioned above.

Figure 1 shows the vertical distribution of black carbon obtained near Barrow during AGASP flight 1. There is a very pronounced layer below 1 km altitude, with peak concentrations at 400–500 m altitude; substantial concentrations on the order of 100

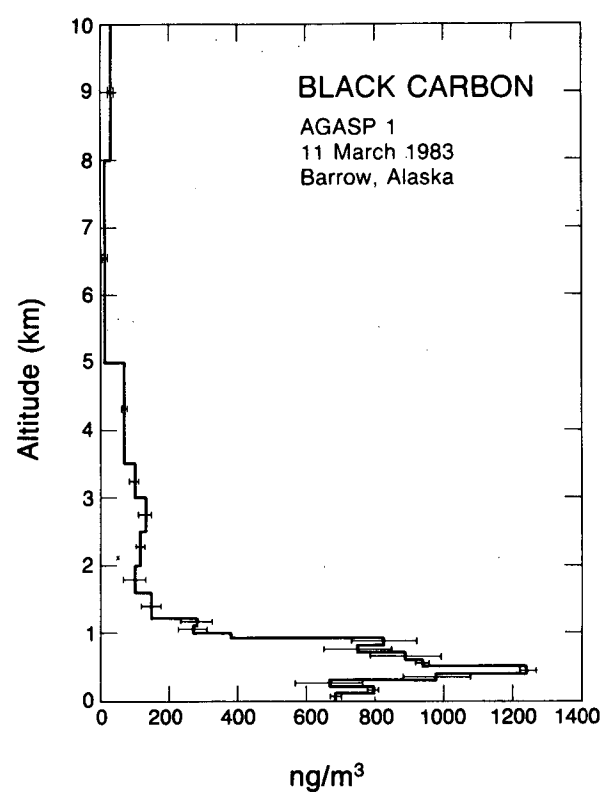

Figure 1. Vertical profile of black carbon concentrations obtained during AGASP flight 1 on March 11, 1983, near Barrow, Alaska. Arrow on ordinate indicates the 24-hour average black carbon concentration measured that day at the NOAA–GMCC ground station at Barrow. Units are nanograms per geometric cubic meter. (XBL 8312-6876A)

*This work was supported by the Director, Office of Energy Research, Office of Basic Energy Sciences, Carbon Dioxide Research Division of the U.S. Department of Energy under Contract No. DE-AC03-76SF00098.

†Summary of paper published in *Geophys. Res. Lett. 11*, pp. 381–384 (1984).

ng/m^3 are present up to 5 km altitude. Figure 2 shows data obtained during flight 3. We detected a lower layer extending from ground level to 800 m altitude, then a region of relatively clean air, and then a broad upper layer having a maximum at approximately 1.5 km altitude and extending to 5 km. Although the peak concentration was less than one-half that measured on flight 1, the total air column burdens were similar: 130 ($\pm$10) ng/cm^2 for flight 1, 0–10 km altitude, and 135 ($\pm$15) ng/cm^2 for flight 3, 0–9 km. Flights 2 and 4 showed less pronounced vertical structure but comparable extent and intensity of black carbon concentration. In all profiles, the vertical distributions show a reduction in concentration at the lowest levels relative to the peaks observed at altitudes of a few hundred meters, and the 24-hour average concentrations of black carbon observed at the ground station were lower still. Table 1 shows some of the results from the analyses of the 24-hour ground-level samples taken at Barrow on the AGASP flight days. To reproduce the air column burdens derived from the airborne measurements on flights 1 and 3, it would be necessary to multiply those days' ground-level concentrations by column lengths of 5.4 and 6.4 km.

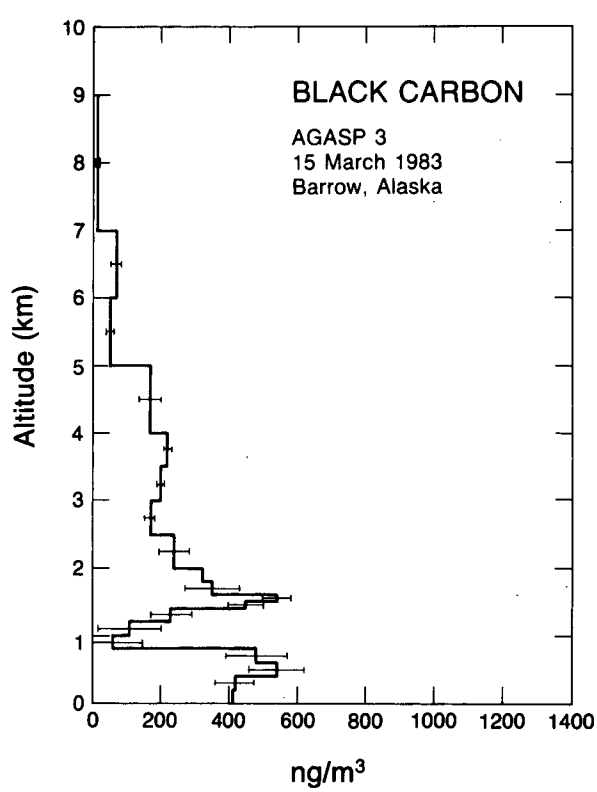

Figure 2. Vertical profile of black carbon concentration obtained during AGASP flight 3, March 15, 1983; arrow on ordinate is same-day reading at Barrow ground station. (XBL 8312-6877A)

Table 1. Analysis of 24-hour aerosol samples collected at Barrow.

AGASP flight no.	Concentration, ng/m^3				
	Black Carbon	S	Br	Si	K
1	241	940	63	65	41
2	295	980	37	58	29
3	206	1170	25	64	22
4	253	1030	30	68	29
Mean	249	1030	39	64	30

Figures 3 and 4 show results from the sulfur and bromine analysis of the Millipore filter samples collected on flights 1–4 compared with the 24-hour average values measured on the ground. The sulfur data show concentrations of the order of 200–300 ng/m^3 at high altitudes, increasing considerably at lower levels with the suggestion of a peak somewhat above the ground. The peak concentration measured during flight 1 on the filter operated mainly at 1 km altitude is about 50% higher than the corresponding average ground measurement that day. Figure 4 shows the bromine data in the same format; not all filters yielded significant analyses, so less data are represented. The highest bromine concentrations on the ground and aloft were also measured on the day of flight 1.

The intensity and vertical extent of the aerosol components are remarkable. During AGASP flight 1 near Barrow, Alaska, the peak black carbon concentration detected at 500 m altitude was more than 5 times greater than that day's ground-level average and was greater than the annual average concentration measured at Lawrence Berkeley Laboratory. When expressed as a mass mixing ratio, the black carbon concentration measured during flight 3 between 4 km and 5 km altitude was 50% greater than the average ground-level measurement that day. Air masses at different altitudes may have passed over different source regions, and the presence of substantial quantities of black carbon at these altitudes could suggest a distant origin.

The sulfur data shown in Fig. 3 present some evidence of a peak in concentration at low altitudes but also show that we measured substantial concentrations of filterable aerosol sulfur throughout the Arctic troposphere to 10 km altitude. The downward diffusion of sulfuric acid droplets present in the stratosphere as a result of recent volcanic activity[11] could

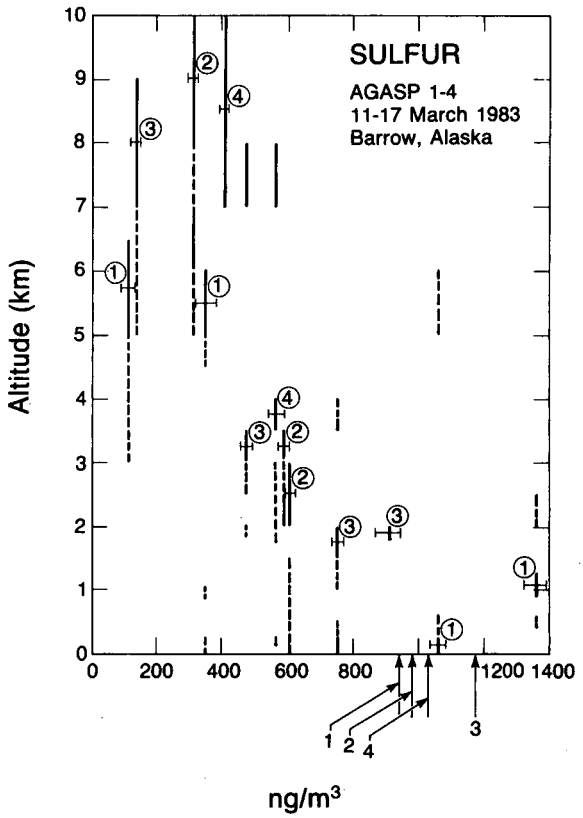

Figure 3. Results of analysis for sulfur on Millipore filter samples collected during AGASP flights 1 through 4 near Barrow, Alaska, from March 11 to 17, 1983. Solid lines parallel to altitude axis represent range within which first 70% of volumetric air flow was sampled; broken lines encompass next 20%. Error bars, representing 3 σ limits, are placed at center of range covering majority air flow, and adjacent numeral indicates AGASP flight number. Numbered arrows on ordinate indicate 24-hour average sulfur concentrations measured at NOAA/GMCC ground station on those flight days. Units are nanograms per geometric cubic meter. (XBL 8312-6875A)

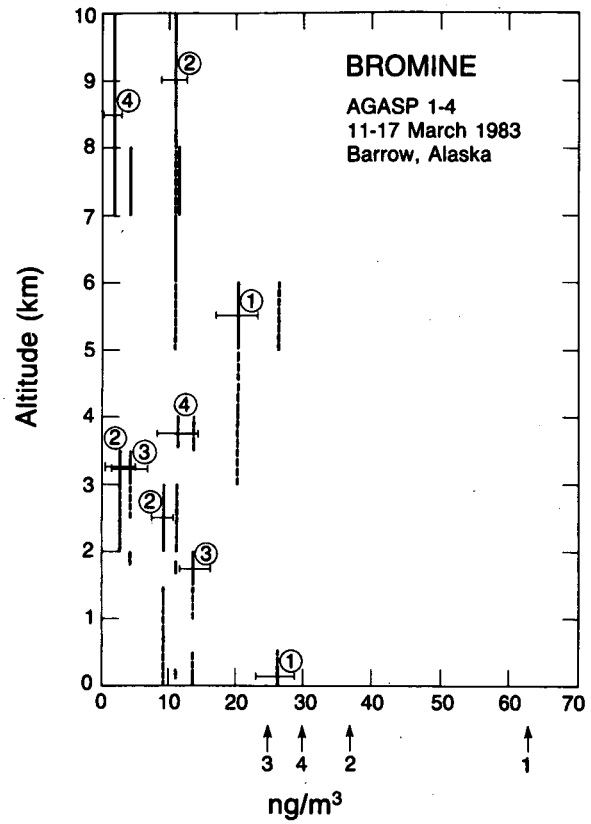

Figure 4. Results of analysis for bromine on Millipore filter samples collected during AGASP flights 1 to 4, in same format as Fig. 3. (XBL 8312-6878A)

be one contributor to this latter observation. The ground-level concentrations of aerosol sulfur were comparable to those measured in the lower troposphere.

The results shown in Fig. 4 for the concentrations of filterable aerosol bromine show no discernible vertical structure but do show that the ground-level concentrations were always substantially larger than those measured aloft. These observations would be consistent with a ground-level natural source.[12]

PLANNED ACTIVITIES FOR FY 1985

The AGASP aircraft experiment demonstrated the value of an instrument that can measure aerosol black carbon concentrations in *real time*. Preliminary examination of the minute-by-minute data base in correlation with the aircraft tapes of meteorological measurements has shown that the aethalometer can reveal horizontal inhomogeneities of aerosol black carbon concentration within the layers shown in this report. In addition, data from a few flight segments that were in the form of vertical loops may allow for the contour mapping of this combustion effluent tracer. This data analysis will continue during FY 1985. We will also design and construct the next version of the aethalometer for aircraft studies, with the objectives of improving sensitivity, incorporating real-time data analysis and display, and reducing the instrument's weight and power requirements.

REFERENCES

1. Rosen, H., Novakov, T., and Bodhaine, B.A. (1981), "Soot in the Arctic," *Atmos. Environ. 15*, p. 1371.
2. Rosen, H., and Novakov, T. (1983), "Combustion-Generated Carbon Particles in the Arctic Atmosphere," *Nature 306*, p. 768.

3. Porch, W.M., and MacCracken, M.C. (1982), "Parametric Study of the Effects of Arctic Soot on Solar Radiation," *Atmos. Environ. 16*, p. 1365.
4. Cess, R.D. (1983), "Arctic Aerosols: Model Estimates of Interactive Influences Upon the Surface-Troposphere Radiation Budget," *Atmos. Environ. 17*, p. 2555.
5. Rosen, H., and Hansen, A.D.A. (1984), "Role of Combustion-Generated Carbon Particles in the Absorption of Solar Radiation in the Arctic Haze," *Geophys. Res. Lett. 11*, p. 461.
6. Rahn, K.A., and McCaffrey, R.J. (1980), "On the Origin and Transport of the Winter Arctic Aerosol," *Ann. N.Y. Acad. Sci. 338*, p. 486.
7. Barrie, L.A., Hoff, R.M., and Daggupaty, S.M. (1981), "The Influence of Mid-Latitudinal Pollution Sources on Haze in the Canadian Arctic," *Atmos. Environ. 15*, p. 1407.
8. Ottar, B. (1981), "The Transfer of Airborne Pollutants to the Arctic Region," *Atmos. Environ. 15*, p. 1439.
9. Bodhaine, B.A., Dutton, E.G., and DeLuisi, J.J. (1984), "Surface Aerosol Measurements at Barrow During AGASP," *Geophys. Res. Lett. 11*, p. 377.
10. Hansen, A.D.A., Rosen, H., and Novakov, T. (1982), "Real-Time Measurement of the Absorption Coefficient of Aerosol Particles," *Appl. Opt. 21*, p. 3060.
11. Gandrud, B.W., Kritz, M.A., and Lazrus, A.L. (1983), "Balloon and Aircraft Measurements of Stratospheric Sulfate Mixing Ratio Following the El Chicon Eruption," *Geophys. Res. Lett. 11*, p. 1037.
12. Berg, W.W., Sperry, P.D., Rahn, K.A., and Gladney, E.S. (1983), "Atmospheric Bromine in the Arctic," *J. Geophys. Res. 88*, p. 6719.

Characterization of Respirable Coal Mine Dust*

C.D. Parker,† C.J. Pryor,†, J. Perkins,† R.L. Dod, and T. Novakov

Chemical and physical characterization of coal dust is needed to understand its formation and transport. Formation is probably related to several factors, including overall chemical and physical characteristics of the coal and mining equipment and conditions.[1] Certain materials are more apt to become airborne than others; it is known that approximately 10% of all dust in mines becomes airborne.[2] This study was undertaken to characterize coal dust chemically and physically.

To characterize coal dust, several analytical methods are being applied: (a) thermal evolved gas analysis (EGA), (b) electron spectroscopy for chemical analysis (ESCA), (c) scanning electron microscopy (SEM) and light microscopy, and (d) electron probe microanalysis (EPMA). Each technique yields information that, when examined together, gives a whole picture of coal mine dust. The most promising technique used to date is EGA; however, we will use each technique to obtain an accurate description of coal dust.

Evolved gas analysis has been used extensively to study atmospheric particulates[3–6] and has proven to be a very useful technique in the analysis of laboratory-generated coal dust. This method simultaneously gives carbon, hydrogen, and nitrogen contents of a collected coal-dust sample. Oxygen content can also be determined in a separate analysis.[6] In addition, an optical transmission value can be obtained[5] that may prove applicable to determining diesel exhaust particulates in the presence of coal dust. Characterization of coal dust is essential to determine if a window exists whereby diesel particulates can be measured in conjunction with coal mine dust, individually or concurrently.

ACCOMPLISHMENTS DURING FY 1984

A large number of reports and journal articles exist that describe coal-related research, including mining equipment and coal production, dust, and workers' health.[7] Most of the papers immediately available on the subject of coal-dust analysis were based on mineral analysis, e.g., silica content, which is considered a major problem in mining health safety.[8–11] Methods of analysis were x-ray fluorescence, atomic absorption, neutron activation, infrared analysis, and x-ray analysis. In many

*This work was supported by the U.S. Bureau of Mines under Contract No. J0134056 with Jackson State University and by the U.S. Department of Energy under Contract No. DE-AC03-76SF00098 under the auspices of the Jackson State University–Lawrence Berkeley Laboratory collaborative program.
†Jackson State University researcher.

instances, organic matter was removed by combustion or pyrolysis prior to analysis.[8–17] Of interest to our research were reports that detailed analysis of organic material in addition to inorganic (mineral) materials in coals. For instance, Schultz *et al.* used high-resolution mass spectrometry to analyze dust samples.[18] Dust samples from the same coal seam differed for several reasons: (a) particle size and (b) coal rank and generation (mine- or laboratory-generated). Variations were based on molecular-weight distribution of major compounds observed in the mass spectra of the different samples. In a similar manner, Artemov *et al.* have begun a study of dust formation based on mechanical and chemical properties of coal[19]; however, no final report of their results is available. They are using paramagnetic and spectroscopic methods of analysis.

Lacking suitable readily available mine-dust samples, we collected simulated dust from a dust chamber. The dust chamber was a 7.3-ft^3 enclosure in which finely ground coal was dispersed. Collection was done using a four-stage Lundgren impactor to exclude nonrespirable particles. Flow rates were adjusted to 2.5 ft^3/min. Collected particles were usually less than 6 μm. All samples were collected on prefired quartz filters. A personal respirable dust sampler gave similar particle sizes.

Evolved gas analysis was done on an in-house (Lawrence Berkeley Laboratory) system, as shown in Fig. 1. Samples for analysis, either sections of the quartz filters or bulk samples, are inserted into the combustion tube.[3–5] Analyte gas concentrations are monitored as a function of temperature; the resulting thermograms are a plot of concentration temperature with the integrated area of the curves being proportional to the carbon, hydrogen, or nitrogen content of the sample. Quantitation is determined by combustion of known quantities of pure compounds. For filter samples, transmission of a He-Ne laser beam (6328 nm) is monitored simultaneously. This provides a concomitant measurement of absorptivity and CO_2 evolution. An examination of the CO_2 evolution and light transmission enables the assignment of peaks in the thermogram corresponding to light-absorptive types of carbon.[3,4]

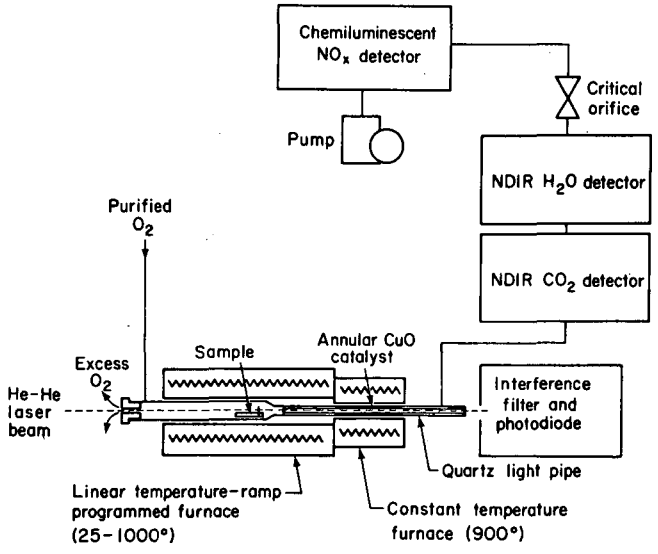

Figure 1. Schematic diagram of apparatus for thermal evolved gas analysis. (XBL 8412-5169)

Oxygen analysis of coal is done with similar EGA equipment; however, it involves pyrolysis in a nitrogen atmosphere and conversion of evolved oxygen species to CO with a heated graphite catalyst.[6] ESCA data were collected with a modified AEI ES-200A spectrometer equipped with a Surface Science Laboratories position-sensitive detector. SEM was done with a JEOL scanning electron microscope equipped with a Kevex x-ray emission detector. Coals were obtained through DOE from Bruceton, Pennsylvania, and the North American Coal Company in Powhatan, Ohio.

The characterization of dust to date has been on several ground coals. Attempts to remove dust from standard U.S. Bureau of Mines filters for analysis has proved ineffectual. Grinding coal to achieve a fine powder the size of mine dust is done in an agate ball mill. This has the disadvantage that certain coals have their surfaces modified by grinding, altering their EGA or ESCA results.

Evolved gas analysis has been used extensively in characterizing these coal dusts. The information obtained involves hydrogen-to-carbon and nitrogen-to-carbon ratios; percentages of different carbon, hydrogen, or nitrogen types; and the specific light attenuation of coals. Table 1 gives the H/C and N/C ratios, totals and fractional, for coals studied. From the table, we see that H_{total}/C_{total} (H_T/C_T) ranges from 0.74 to 1.58 for various coals. These values are to some extent a measure of hydrogenation and can be used for identification and differentiation of coal dusts. They also denote when gross changes occur in a sample. For example, the H_T/C_T ratio for Black Creek coal changes when the sample is ground in a ball mill rather than in an electrical grinder—from 0.74 in a grinder to 1.17 in a mill. This increase in total H is due to a change in the hydrogen content of what we refer to as the aliphatic fraction, i.e., C_1. The H_1/C_1 ratio for the ball mill sample is a factor of 2 greater, as can be seen from Table 1. Such variations are used to determine changes; in addition, peak shift is also used.

Table 1. Elemental ratios detected by thermal evolved gas analysis.

Sample	H_T/C_T	H_1/C_1	H_2/C_2	N/C_T	N/C_2
L25956	0.87	5.04	0.26	0.04	0.05
Bruceton coal (ball mill) April sample	0.84	2.70	0.28	0.02	0.02
Black Creek (hand grinder)	0.74	2.26	0.18	0.01	0.02
Black Creek (ball mill)	1.17	5.74	0.22	0.01	0.02
Bruceton coal 30 sec. coll.	1.26	2.57	0.39	0.01	0.02
Bruceton coal 60 sec. coll.	0.86	2.09	0.34	0.01	0.02
NACCO JSU-LBL Q1 Powhatan #6 Pitt #8	1.09	3.17	0.51	0.01	0.01
L25144	1.26	4.13	0.58	0.03	0.04
NACCO 53 μg Powhatan #6 Pitt #8	0.95	2.58	0.39	0.01	0.02
NACCO (ball mill) 51 μg Powhatan #6 Pitt #8	0.71	3.13	0.12	0.01	0.01
NACCO (ball mill) 75 μg Powhatan #6 Pitt #6	0.83	2.62	0.31	0.02	0.02
NACCO (ball mill) Powhatan #6 Pitt #8 30 sec. coll.	1.0	2.74	0.42	0.02	0.02
NACCO JSU-LBL Q2 Powhatan #6 Pitt #8	1.27	3.15	0.52	0.02	0.02
NACCO (ball mill) Powhatan #6 Pitt #8	1.58	4.33	0.52	0.02	0.02

In evaluating the ability of EGA to differentiate samples, we have been able to compare the EGA data obtained for bulk coal, laboratory-generated coal dust, and coal dust collected from a mine site. Figures 2, 3, and 4 show, respectively, the CO_2, H_2O, and NO_x thermograms for a laboratory-generated dust sample (A), an actual mine-source sample (B), and a bulk coal sample from the same mine (C). The first two are samples collected on quartz filters, and the bulk sample is 75 μg of coal in a platinum boat. The thermograms of A and B differ from the bulk sample, C, and from each other. Samples A and B show evidence of a very volatile fraction being evolved, starting at 130°C. This highly volatile fraction is not detected in the bulk sample. All three samples do show that the majority of the carbon is associated with two peaks: C_1, considered aliphatic, and C_2, considered fixed, highly aromatic, or black carbon. C_2 has always been found to be the most abundant. As previously mentioned, the black carbon peak is the peak assigned to the absorptive character of the sample. In Fig. 2, for samples A and B, the laser transmission trace shows that the high-temperature carbon (C_2) is the absorptive species.

The carbon thermograms of A and B (Fig. 2) differ in that CO_2 evolution is not detected at 620°C for A. The 620°C peak in thermogram B is thought

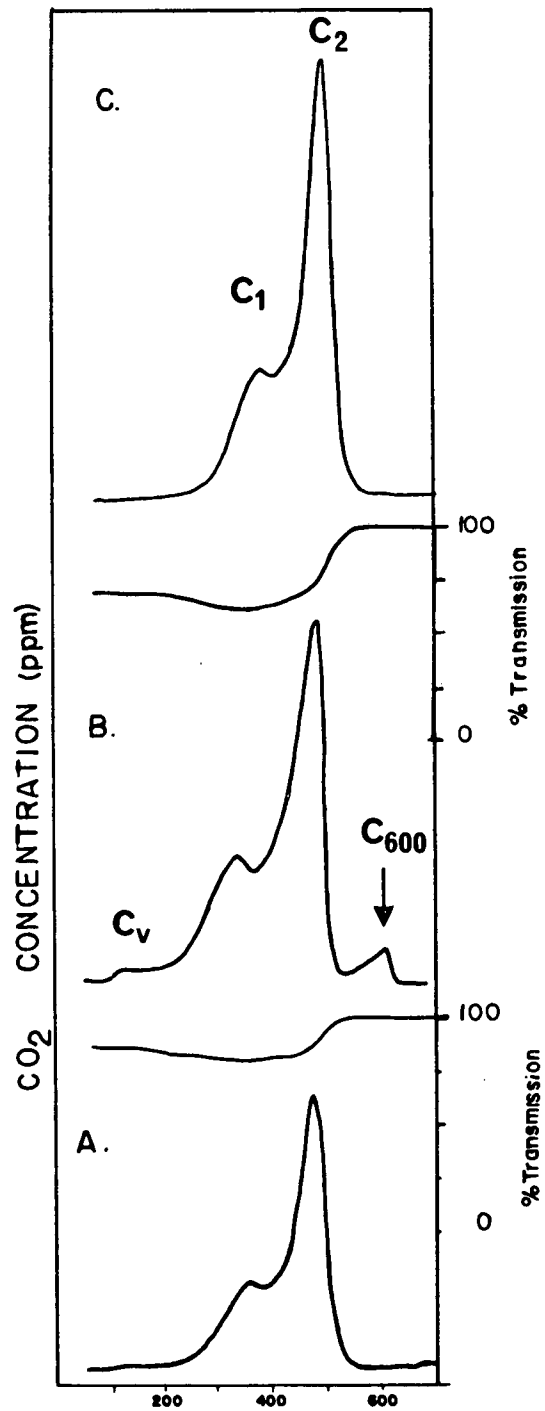

Figure 2. Evolved CO_2 thermogram of (A) laboratory-generated coal dust, (B) coal mine dust, and (C) bulk coal samples. (XBL 8412-5168)

to arise from limestone (calcium carbonate). This peak at 620°C is not hydrogenous as there was no hydrogen evolution at that temperature.

The hydrogen thermogram, Fig. 3, shows that hydrogen evolution parallels CO_2 evolution, i.e., we see two distinct water peaks. In addition, we see that the majority of the hydrogen is associated with C_1, the low-temperature carbon. The average ratio for H_1/C_1 is 3, which suggests that C_1 is highly hydrogenated. The average H_2/C_2 ratio is 0.36, which allows us to conclude that C_2 is very unsaturated.

The nitrogen thermogram for the three samples shows that only one major nitrogen species exists. However, as seen in Fig. 4 (A and B) the dust samples show low volatile nitrogen species. This accounts for only a very small percentage of total nitrogen. Differences in the CO_2, H_2O, and NO_x thermograms of the three samples allow for differentiation and identification. We have obtained very low values for specific attenuation of coal dust samples; this suggests that diesel particulates may be detected in their presence. The specific attenuation of diesel particulates is ~25, with coal samples ranging from 1.0 to 2.0. This means that diesel particulates are at least a factor of 10 more absorbing than coal dust. However, since we presently obtain inconsistent results for the specific attenuation values, it must be determined whether these discrepancies are due to size-distribution differences. Most diesel particulates are of submicron size; the average size of collected dust particles is about 4 μm. If we have very large particles (8 μm or larger), we seriously degrade the absorption characteristic of the particles. This is true for combustion-generated particles; however, we do not know if it will hold true for coal-dust particles.

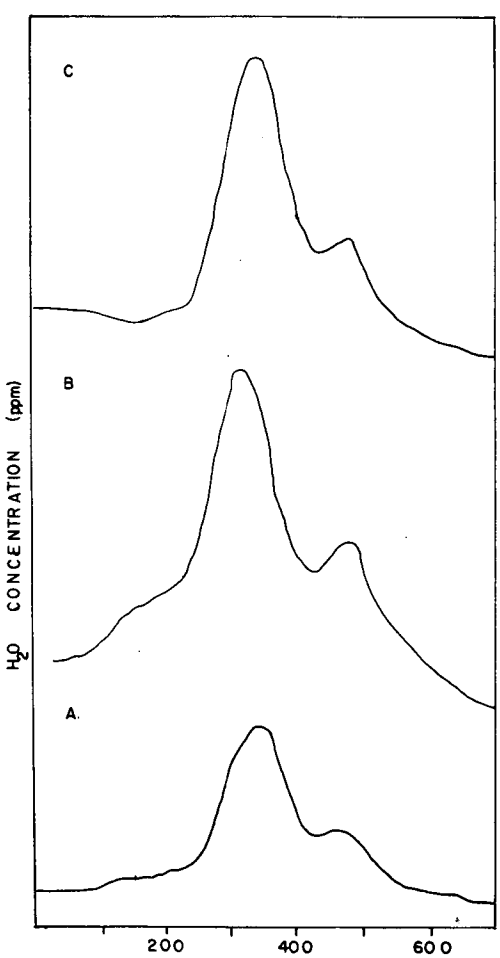

Figure 3. Evolved H_2O thermogram of (A) laboratory-generated coal dust, (B) coal mine dust, and (C) bulk coal samples. (XBL 8412-5167)

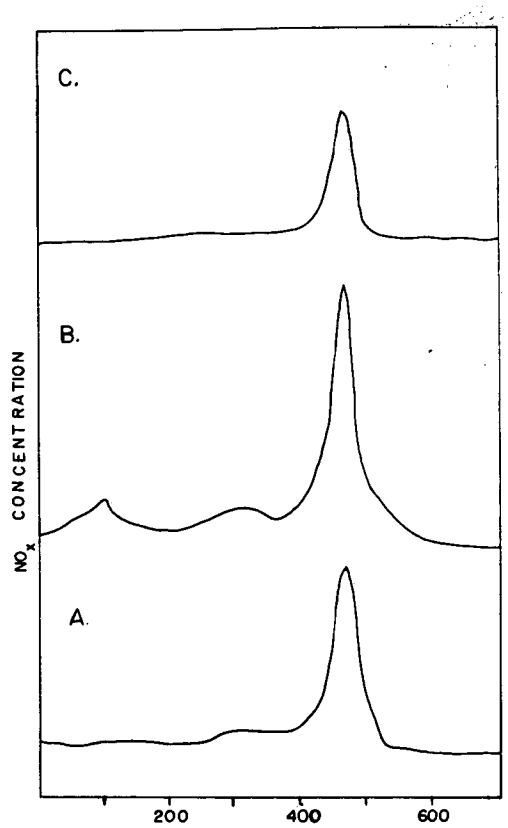

Figure 4. Evolved NO_x thermogram of (A) laboratory-generated coal dust, (B) coal mine dust, and (C) bulk coal samples. (XBL 8412-5167)

ESCA results for samples studied to date show that collected coal dust particles contain C, O, N, Si, and some S. These results are not tabulated because we question the amount of signal in the Si and O peaks that is due to background support. The ESCA results of a bulk coal sample indicate that a fair amount of silicates is present in coals. In addition, ESCA analysis of the mine-source dust sample indi-

cates that there are three surface species of carbon, two of silicon, and two of oxygen. Nitrogen and sulfur were not detected, which may be due to surface coverage of the additional species detected. In comparison, the ESCA results of a coal slice from the mine (bulk sample) shows only one carbon; possibly two types of oxygen; and one each of silicon, nitrogen, and sulfur. These ESCA results indicate surface differences between dust and bulk samples.

Scanning electron microscopy and light microscopy have been used mainly to determine size distribution. Light microscopy is used for a quick measure of approximate size. Samples are considered suitable if the average particle size is less than 6 microns.

PLANNED ACTIVITIES FOR FY 1985

Preliminary results show that the proposed methods for coal dust characterization are indeed viable in answering questions concerning the chemical and physical characteristics of coal dust. EGA has proved to be the quickest method for evaluating the chemical characteristics of coal. EGA quickly shows the different types of C, H, N, and O and their relationships to each other. ESCA is beginning to prove that surface characteristics are indeed different when we compare a bulk sample to a dust sample.

The research for FY 1985 will proceed on several points:

(1) Deconvolution computer programs for better data handling and more precise results.
(2) Continued evaluation of EGA data of bulk and actual dust samples.
(3) Analysis of actual mine-site samples.
(4) Determination of the effect of coal-particle size on the specific attenuation of coals; this will lead to (a) the question whether diesel particulates may be detected in the presence of coal dust and (b) the possibility of developing a real-time dust measurement technique.
(5) Travel to the U.S. Bureau of Mines Library in Pittsburgh, Pennsylvania, to obtain unreleased USBM reports.

REFERENCES

1. National Academy of Sciences (1980), "Measurement and Control of Respirable Dust in Mines," U.S. Bureau of Mines report OFR 118-80.
2. Chang, L., and Zulcovich, P.P. (1973), "Respirable Dust Adhering to Run-of-Face Bituminous Coals," U.S. Bureau of Mines report P1 7765.
3. Dod, R.L., Rosen, H., and Novakov, T. (1978), "Optico-Thermal Analysis of the Carbonaceous Fraction of Aerosol Particles," LBL-8696, p. 2.
4. Gundel, L.A., Dod, R.L., Rosen, H., and Novakov, T. (1984), "The Relationship Between Optical Attenuation and Black Carbon Concentration for Ambient and Source Particles," *Sci. Total Environ. 336*, p. 197.
5. Dod, R.L., Gundel, L.A., Benner, W.H., and Novakov, T. (1984), "Non-Ammonium Reduced Nitrogen Species in Atmospheric Aerosol Particles," *Sci. Total Environ. 336*, p. 277.
6. Benner, W.H., Hansen, A.D.A., Gundel, L.A., and Novakov, T. (1984), "Determination of Organic Oxygen in Ambient Particulate Matter," *Sci. Total Environ. 336*, p. 271.
7. Approximately 117,000 abstracts on coal are in the Department of Energy's Energy Data Base (EDB) for the years 1974–1984.
8. Sweet, D.V., Crouse, W.E., Crable, J.V., Carlberg, J.R., and Lainhart, W.S. (1984), "The Relationship of Total Dust, Free Silica, and Trace Metal Concentrations to the Occupational Respiratory Disease of Bituminous Coal Mines," *Amer. Indus. Hyg. Assoc. J.*, p. 479.
9. Hamilton, R.J., French, A.G., and Spence, A.C. (1976), "Developments in Dust Control in Coal Mines," *Min. Eng. 135*, p. 317.
10. Freedman, R.W. (1978), "Procedures for Analysis of Respirable Dust as Related to Coal Workers' Pneumoconiosis," in *Analytical Methods for Coal and Coal Products,* Vol. II, C. Karr, Jr., Ed., Academic Press, New York, p. 315.
11. Crawford, N.P., Bodsworth, P.L., Hadden, G.G., and Dodsson, J. (1981), "An Investigation of Dust Composition and Other Factors at Collieries Where the Pneumoconiosis Progression Index Appears to Be Anomalous in Relation to Dust Concentration," Commission of the European Community report EUR-6527.
12. Anderson, C.C. (1983), "Collaborative Tests of Two Methods for Determining Free Silica in Airborne Dust," National Technical Information Service PC A08/MF A01.
13. Freedman, R.W., Toma, S.Z., and Lang, H.W. (1984), "On-Filter Analysis of Quartz in Respirable Coal Dust by Infrared Absorption and X-Ray Diffraction," *Amer. Indus. Hyg. Assoc. J.*, p. 411.
14. Vitak, J. (1977), "Respirable Dust Sampling in Czechoslovak Coal Mines, *Amer. Indus. Hyg. Assoc. J. 38*, p. 247.

15. Kessler, T., Sharkey, Jr., A.G., and Friedel, R.A. (1971), "Spark-Source Mass Spectrometer Investigation of Coal Particles and Coal Ash," U.S. Bureau of Mines report BM-TPR-42.

16. Wesson, T.C., and Armstrong, F.E. (1972), "Report of Investigation: Elemental Composition of Coal Mine Dust," U.S. Bureau of Mines report BM-RI-7992.

17. Rawat, N.S., Sinha, J.K., and Sahvo, B. (1982), "Atomic Absorption Spectrophotometric and X-Ray Studies of Respirable Dusts in Indian Coal Mines," *Arch. Environ. Health 37*, p. 32.

18. Schultz, J.L., Friedel, R.A., and Sharkey, Jr., A.G. (1972), "Detection of Organic Compounds in Respiratory Coal Dust by High-Resolution Mass Spectrometry," U.S. Bureau of Mines report RM-TPR-61.

19. Artemov, A.V., Reznik, L.A., and Shilenkov, V.N. (1982), "Mechanical and Chemical Properties of Dust Formation from Coal from Donets and Kuznets Coal Basins" (in Russian), *Izvestiya Vysshikh Uchebnykh Zavedenii Gornyi Zhurnal 2*, p. 1.

Determination of Black Carbon in Carbonaceous Particles by Evolved Gas Analysis and Optical Attenuation*

L.A. Gundel, R.L. Dod, H. Rosen, and T. Novakov

Particulate material collected on filters from ambient air and combustion sources usually appears black because of the presence of light-absorbing graphitic or black carbon (BC).[1] In the atmosphere, the light absorption by these particles can degrade visibility[2] and perturb the tropospheric radiation balance.[3,4] The major climatological changes that have been predicted as a consequence of large-scale urban fires (e.g., nuclear winter) are due primarily to light absorption by black carbon.[5] Black carbon may also play a role in atmospheric chemical reactions such as heterogeneous oxidation of SO_2.[6,7] Development of accurate and rapid experimental techniques for determination of BC is essential to continue these studies.

Most methods for determining of black carbon[8] rely on separation of organic carbon (OC) from black carbon by pyrolysis, oxidation, or solvent extraction before determination of BC as CO_2 or CH_4. In this study, we describe a technique based on temperature-programmed combustion–evolved gas analysis (EGA) of filter samples of carbonaceous particles. This approach is unique in the following features: since light transmission is monitored continuously during EGA, black carbon can be distinguished from organic carbon by observing which peaks in the thermograms correspond to increases in light transmission during combustion of black carbon. If pyrolysis occurs during EGA, it is observed because it leads to increases in light absorption as BC is produced by charring of organic species. If accurate separation of BC from organic carbon is difficult because of the nature of the particulate sample, the soluble organic species can be removed by extraction before analysis. This procedure leads to thermograms in which determination of the black carbon is easy. To illustrate the method, we have determined black carbon in particulate matter collected from several locations in the United States and Europe. In previous work, we used EGA to calibrate the laser transmission method (LTM), which measures the attenuation (ATN) of visible light as it passes through a particulate sample on a filter.[9] This fast and nondestructive method for BC is based on the absorption of visible light by black carbon.[1,10] In that study, we found that the relationship between ATN and [BC] is the same for particles from a variety of sources and seven sampling locations and that

$$\mathrm{ATN} = \sigma[\mathrm{BC}] \quad , \tag{1}$$

where $\sigma = 25.4 \pm 1.7$ for ATN $\leqslant 200$.

$$\mathrm{ATN} = -100 \ln I/I_0 \quad , \tag{2}$$

with I_0 and I as transmitted light intensities for blank and loaded filters, respectively.

The appropriate method for determining BC depends on the type of sample and on the required levels of accuracy and precision, since EGA and

*This work was supported by the Director, Office of Energy Research, Office of Health and Environmental Research, Physical and Technological Research Division of the U.S. Department of Energy, under Contract No. DE-AC03-76SF00098 and by the National Science Foundation under Contract No. ATM 83-15442.

LTM can provide independent measurements of [BC], with different strengths and drawbacks. In this study, we extend and unify our earlier work by evaluating and applying these methods for various types of particulate samples.

ACCOMPLISHMENTS DURING FY 1984

Samples of aerosol particles were collected on quartz fiber filters (Pallflex 2500 QAS) that had been prefired at 800°C for 12 hours. Ambient samples were collected at two sites in Berkeley, one near the Laboratory, the other 100 m from a heavily traveled freeway. Other samples originated in Anaheim, California; Warren, Michigan (provided by Groblicki[8]); and Vienna, Austria (Technical University of Vienna). A variety of combustion sources were studied. Average motor vehicle populations were sampled in the exhaust vents of the uphill bore of a highway tunnel and in a parking garage. In these locations, diesel vehicles represented 3 and 0.5% of the traffic, respectively. Propane soot was collected during an extensive intercomparison study.[11] A natural gas boiler (input of 290,000 BTU hr^{-1}) was sampled in its chimney.

Before determining BC, some filter samples were sequentially extracted by benzene and a methanol-chloroform mixture (1:2,v:v) in two 6-hour steps as suggested by Appel *et al.*,[12] and modified by Gundel *et al.*[13] Temperature-programmed evolved gas analysis in oxygen was used to identify and quantitate BC. The heating rate was 10 C°/min. During EGA, the intensity of light (He-Ne laser) transmitted through the sample (1.69 cm^2) was continuously monitored. The apparatus has been described elsewhere.[14] [BC] was determined from the area of the thermogram peak that corresponded to the increase in light transmission during EGA. The black peak's shape corresponded well to the shape predicted from the derivative of the light transmission trace, as illustrated below. The limits of detection and quantitation for blank corrected samples are 0.6 and 2.0 μg BC/cm^2, respectively. These are defined as 3 and 10 times the standard deviation for replicate determinations, as suggested by McDougall *et al.*[15] This method of determination of BC was validated by an extensive 11-laboratory round-robin comparison.[8] Our results were indistinguishable from the mean values obtained in that study for three filter samples of ambient particulate matter from Warren, Michigan.

Four typical thermograms are shown in Fig. 1. The sample of auto exhaust from a parking garage is similar to many combustion-source thermograms, with the high-temperature BC peak well separated

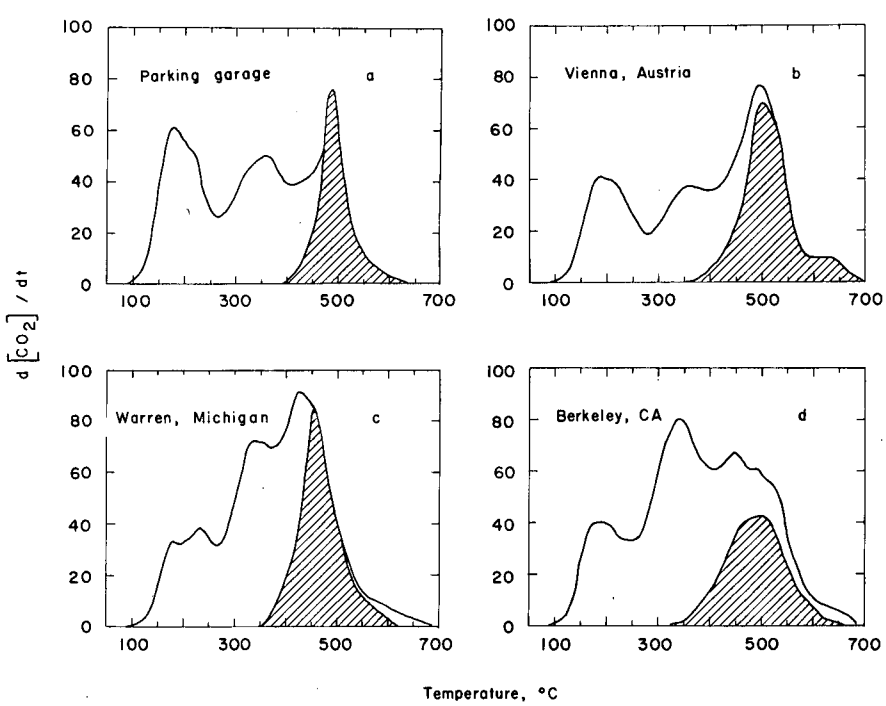

Figure 1. Thermograms of source and urban particles. The shaded area corresponds to black carbon, as determined from extracted filter samples.
(XBL 8412-5490)

from the organic carbon peaks. Particles collected in Vienna, Austria, and Warren, Michigan, also have clearly identifiable black peaks and show source-like thermograms. For these sample types, the high-temperature peaks for the untreated sample correspond well to the high-temperature peak for extracted samples. Here, no extraction is necessary, and EGA alone provides good estimates of [BC], even when the light transmission is not measured. This procedure has been applied successfully for samples collected in southern California.[16] Some improvement in accuracy occurs when the LTM is applied because the shape of the low-temperature side of the BC trace can be found from the derivative of the optical attenuation with respect to temperature. See Table 1 for a summary of the results for [BC] as determined using EGA alone and ATN alone, with $\sigma = 25$ for various types of samples. All results have been normalized to [BC] for extracted portions of the same samples.

Some urban particles have thermograms for which the black carbon peak is obscured somewhat by organic C. Difficult samples such as these tend to show common features: the peak at around 350°C has a higher peak height than the high-temperature peak at ~450°C. Figure 1(d) gives such an example for particles collected near LBL. If time and facilities permit, the most reliable measure of [BC] will come from thermograms of extracted samples. Two simpler alternatives exist: we can estimate [BC] from the high-temperature peak or construct the BC peak from the derivative of ATN and use Eq. (1) to find the peak height and area. The latter approach is equivalent to use of ATN alone, for which the coefficient of variance is 8%.[9] For five samples with similar thermograms, the former approach overestimates [BC] by an average of 65%, as shown in Table 1. It is important to note that even for untreated complex samples, EGA provides an upper limit for [BC], even when light transmission information is unavailable.

This study is part of a larger project whose aim has been development of chemical methods for determination of BC and calibration of the LTM.[9] The most important results obtained so far can be summarized as follows:

Regardless of their origin and source, ambient particles follow the same relationship between ATN and [BC] (Eq. (1)); thus, good predictions of [BC] can be made from measurements of ATN alone as an alternative to EGA. EGA provides useful characterization of organic as well as black carbon and can be performed on samples such as metal foils or solids for which the LTM is impossible. For all source samples and most urban particulate samples, EGA, supplemented by LTM when possible, is sufficient for determination of BC within about 15%. For complex samples, this method provides upper limits to [BC]; further accuracy requires extraction before thermal analysis.

Table 1. Black carbon concentrations from EGA and ATN.

Sample type	Number of samples	Complexity[a]	$[BC]_{high\ T}/[BC]_{ext}$[b]	$[BC]_{ATN}/[BC]_{ext}$[c]
Combustion sources[d]	10	Simple	1.05 ± 0.09	0.98 ± 0.12
Source-influenced urban particles[e]	12	Intermediate	1.10 ± 0.10	1.02 ± 0.17
Urban particles[f]	12	Complex	1.65 ± 0.62	0.98 ± 0.24

[a]Complexity refers to the degree to which the black carbon peak is obscured by organic carbon in EGA.

[b]BC concentrations were estimated from the area of the high-temperature peak of thermograms of untreated samples, normalized to [BC] from thermograms of extracted samples.

[c]BC concentrations were estimated by using ATN values to predict [BC] from Eq. (1).

[d]Propane soot, highway tunnel, parking garage, natural gas soot.

[e]Particles from Vienna, Austria; Denver, CO; Warren, MI; Berkeley, CA; and Ljubljana, Yugoslavia.

[f]Particles from Berkeley, CA; Anaheim, CA; and Riverside, CA.

PLANNED ACTIVITIES FOR FY 1985

We plan to use EGA for determination of [BC] in soot from combustion of common building materials. We also plan to study the relationship between ATN and [BC] as a function of particle size.

REFERENCES

1. Rosen, H., Hansen, A.D.A., Gundel, L., and Novakov, T. (1978), "Identification of the Optically Absorbing Component in Urban Aerosols," *Appl. Opt. 17*, p. 3859.
2. Weiss, R.E., Waggoner, A.P., and Charlson, R.J. (1979), "Studies of the Optical, Physical and Chemical Properties of Light Absorbing Aerosols," in *Proceedings, Conference on Carbonaceous Particles in the Atmosphere*, LBL-9037, p. 257.
3. Porch, W.M., and MacCracken, M.C. (1982), "Parametric Study of the Effects of Arctic Soot on Solar Radiation," *Atmos. Environ. 16*, p. 1365.
4. Cess, R.D. (1983), "Arctic Aerosols: Model Estimates of Interactive Influences Upon the Surface-Troposphere Clear-Sky Radiation Budget," *Atmos. Environ. 17*, p. 2555.
5. Turco, R.P., Toon, O.B., Ackerman, T.P., Pollack, J.B., and Sagan, C. (1983), "Nuclear Winter: Global Consequences of Multiple Nuclear Explosions," *Science 222*, p. 1283.
6. Brodzinsky, R., Chang, S.G., Markowitz, S.S., and Novakov, T. (1980), "Kinetics and Mechanism for the Catalytic Oxidation of Sulfur Dioxide on Carbon in Aqueous Suspensions," *J. Phys. Chem. 84*, p. 3354.
7. Benner, W.H., Brodzinsky, R., and Novakov, T. (1982), "Oxidation of SO_2 in Particles Which Contain Soot Particles," *Atmos. Environ. 16*, p. 1333.
8. Groblicki, P.J., Cadle, S.H., Ang, C.C., and Mulawa, P.A. (1983), "Interlaboratory Comparison of Methods for the Analysis of Organic and Elemental Carbon in Atmospheric Particulate Matter," General Motors Laboratories report GMR-4054.
9. Gundel, L.A., Dod, R.L., and Novakov, T. (1984), "The Relationship Between Optical Attenuation and Black Carbon Concentration for Ambient and Black Carbon Concentration for Ambient and Source Particles," *Sci. Total Environ. 36*, p. 197.
10. Yasa, Z., Amer, N.M., Rosen, H., Hansen, A.D.A., and Novakov, T. (1979), "Photoacoustic Investigations of Urban Aerosol Particles," *Appl. Opt. 18*, p. 2528.
11. Gerber, H.E., and Hindman, E.E., Eds. (1982), *Light Absorption by Aerosol Particles*, Spectrum Press, Hampton, VA.
12. Appel, B.R., Hoffer, E.M., Kothny, E.L., Wall S.M., Haik, M., and Knights, R.L. (1979), "Analysis of Carbonaceous Material in Southern California Atmospheric Aerosols—2," *Environ. Sci. Technol. 13*, p. 98.
13. Gundel, L.A., and Novakov, T. (1984), "Characterization of Particles from Several Sources and Three Urban Areas by Solvent Extraction," *Atmos. Environ. 18*, p. 273.
14. Dod, R.L., Rosen, H., and Novakov, T. (1979), "Optico-Thermal Analysis of the Carbonaceous Fraction of Aerosol Particles," in *Atmospheric Aerosol Research Annual Report, 1977–78*, LBL-8696, p. 2.
15. McDougall, D., *et al.*, ACS Committee on Environmental Improvement (1980), "Guidelines for Data Acquisition and Data Quality Evaluation in Environmental Chemistry," *Anal. Chem. 52*, p. 2242.
16. Ellis, E.C., and Novakov, T. (1982), "Application of Thermal Analysis to the Characterization of Organic Aerosol Particles," *Sci. Total Environ. 23*, p. 227.

Individual Microparticle Analysis and Characterization: Progress on New Techniques*

R.J. Otto

Microencapsulation of micrometer- and submicrometer-size aerosols, fog, and cloud particles is being investigated. The goal of the project is to develop advanced methods for characterization of heterogeneous-phase aerosol particles. Microencapsulation using organic polymers is a potential method for rapidly fixing and preserving the size and chemical composition of both liquid and solid particles. Particles preserved by encapsulation could be collected without the occurrence of sampling artifacts or loss of volatile components in the vacuum of an analysis system. A number of microprobe techniques already exist for the analysis of individual particles greater than 0.5 μm in diameter.[1] In addition, a method for individual microparticle mass spectrometry based on electrostatic acceleration of charged particles ranging in size from 0.01 μm to 10 μm is being considered. The system has been given the acronym MACA (Microparticle Acceleration for Composition Analysis). Microencapsulation would play a key role in the uniform charging and release of the particles for acceleration.

ACCOMPLISHMENTS DURING FY 1984

Encapsulation Experiments with Fog on Soot Condensation Nuclei

The encapsulation procedure reported in the literature for cigarette smoke[2] was successfully repeated with cigarette smoke and used in an attempt to encapsulate fog produced at 25°C, using soot as the condensation nuclei. On the basis of the visibility of the soot-induced fog, the density and particle size were estimated to be in the ranges 0.1 to 1.0 g/m^3 and 1 to 10 μm diameter, respectively. The fog was drawn into the remaining volume of a 100-cc syringe containing 50 cc of methyl-2-cyanoacrylate monomer at 70°C. The full 100-cc volume was then drawn past a 9-μm diameter graphitic carbon fiber at a flow rate of 1 L/min. The efficiency for collection of particles as a function of particle size had been calculated as well as experimentally measured for polystyrene latex spheres.

Figures 1(a) and (b) show two electron micrographs of the carbon fiber following the experiment. Spherical droplets in the size range of 1 to 10 μm would have been seen if encapsulation of the fog had been accomplished, consistent with previous results obtained with cigarette smoke. What is seen in these pictures are agglomerated chains of 50-nm soot spheres. Based on previous encapsulation experiments of diesel exhaust, the agglomerated soot chains appear to have been wetted at the time of

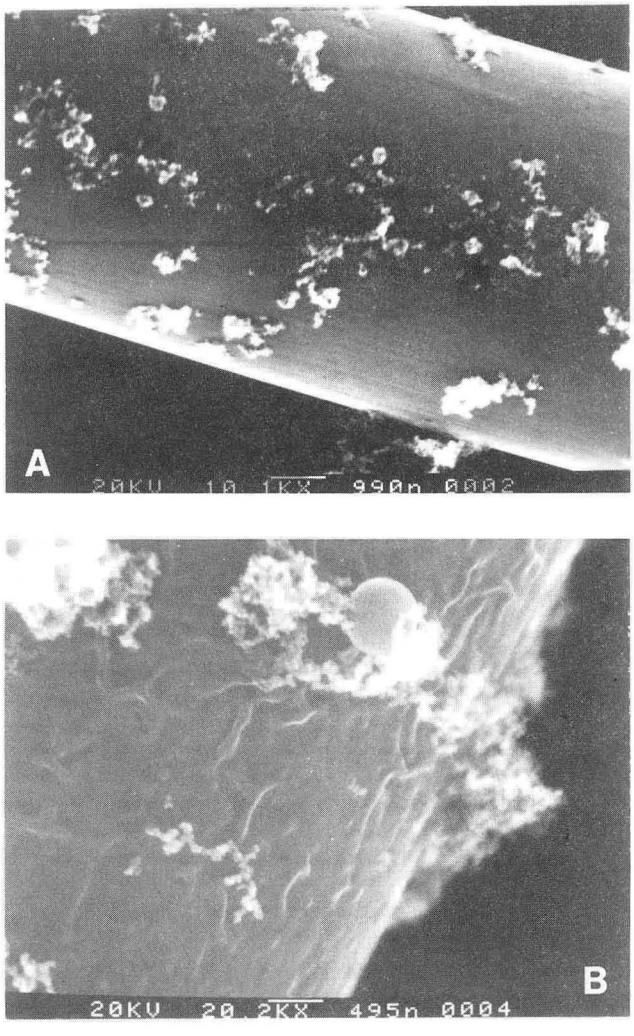

Figure 1. Scanning electron micrographs of graphitic carbon fibers with residual soot particles on the surface [20 keV electrons, bar = 990 nm in (A) and 495 nm in (B)]. (A) Agglomerated chains of soot particles with methyl-2-cyanoacrylate polymer coating. (B) Fiber surface showing typical soot chain (lower left), agglomerated soot chains, encapsulated 0.5-μm sphere, and condensed polymer seen as ripples on fiber surface. (XBB 8412-9541)

*This work was funded by the LBL Director's Program Development Fund and the U.S. Department of Energy under Contract No. DE-AC03-76SF00098.

encapsulation. In these experiments, the relatively high temperature in the sampling syringe resulted in evaporation of the fog prior to encapsulation. The point in time and the process leading to agglomeration of the chains cannot be determined from the experimental results and could have occurred prior to, during, or after polymerization of the condensed monomer on the particles' surface. Note the presence of a 0.5-μm encapsulated sphere in Fig. 1(b).

Encapsulation of a Warm Fog

A system capable of producing fog droplets at temperatures above 60°C was built and used in a series of encapsulation experiments. The rate of polymerization is rapid above this temperature, and microencapsulation requires less than a few seconds. Experiments were carried out using the syringe procedure, with the addition of particle collection by a 0.2-μm pore size Nuclepore filter placed behind the carbon fiber. The electron micrographs showed hollow shell remnants of the encapsulated fog droplets in the size range of 15 to 20 μm. The experiments were plagued by a large amount of water vapor in the aerosol, which tended to condense on the collecting fiber and filter, along with excess monomer vapor, and to produce an irregular, thick, polymer-coated surface.

Electron Probe Microanalysis of Encapsulated Particles

A bursting bubble particle generator was used to produce aerosol particles in the 1 to 10 μm region containing known concentrations of $MnSO_4$. These particles were subsequently analyzed by electron probe microanalysis. The characteristic x-rays for S and Mn were not seen. However, the sensitivity of the probe was greatly reduced by the Au-K_α peak and bremsstrahlung background resulting from the Au coating used to make the sample electrically conducting. Two of the encapsulated spheres analyzed during the course of the experiments showed primary detectable components corresponding to NaCl and KCl. The source of these salt particles is unknown. Elements such as oxygen and carbon have characteristic x-rays too low in energy to be detected by the microprobe system, so that the polymer and any encapsulated water are not detected, although they clearly constitute most of the mass of the particles.

PLANNED ACTIVITIES FOR FY 1985

Further work on the encapsulation process requires the development of a reliable method for the controlled encapsulation of aerosols, fogs, and cloud droplets. The basic criteria for a successful encapsulation method are:

(1) The procedure should preserve the size and heterogeneous-phase composition of the particles during encapsulation.
(2) The system should be capable of encapsulating particles over a wide range of temperatures, relative humidities, and particle sizes and densities.
(3) The encapsulation process should be relatively rapid with respect to the time scale for meteorological changes.

The focus of the research project for the coming year will be on the development of a staged diffusion tube system that will sequentially encapsulate the aerosol or fog and remove unwanted water vapor prior to filtering. The development of a controlled encapsulation procedure will allow further research on mass spectrometric analysis of individual microparticles as well as the physical and chemical characterization of fog and cloud droplets, which are recognized as playing a significant role in the transformation of SO_2 and NO_x to sulfate and nitrate.[3]

REFERENCES

1. Weiser, P., Wurster, R., and Seiler, H. (1980), "Identification of Airborne Particles by Laser Induced Mass Spectroscopy," *Atmos. Environ. 14*, p. 485.
2. Holmberg, R.W. (1979), "Determination of Particle Size in Tobacco Smoke Inhalation Exposure Devices Using Methylcyanoacrylate Fixation and Scanning Microscopy," in *Tobacco Smoke Inhalation Bioassay Chemistry.* Oak Ridge National Laboratory report ORNL-5424, p. 103.
3. Jacob, D.J., Wang, R.-F.T., and Flagan, R.C. (1984), "Fog Water Collector Design and Characterization," *Environ. Sci. Technol. 18*, p. 817.

Applied Physics and Laser Spectroscopy Research*

N.M. Amer,† S.-H. Chen, H. Dersch, A. Frova, R.W. Gerlach, W. Imler, M. Olmstead, A. Skumanich, D. Wei, and Z. Yasa

The research philosophy of our group is to develop and apply advanced laser spectroscopy and condensed-matter physics to energy-related problems. Lasers, with their high spectral purity and tunability, constitute an excellent probe of matter, and the advanced state of our knowledge of condensed-matter physics makes it possible to apply such knowledge to energy research. Areas of investigation that we are interested in include the development of novel laser spectroscopic techniques, the physics of photovoltaic semiconductors, semiconductor surfaces and interfaces, liquid crystals and their applications, and the detection of molecular and atomic species at the ultratrace level.

ACCOMPLISHMENTS DURING FY 1984

Laser Photothermal Measurements and Characterization

Laser photothermal spectroscopy employs the heating concomitant with the absorption of electromagnetic radiation to measure minute optical absorption coefficients (10^{-8}), to characterize nonradiative processes quantitatively, and to measure thermal properties of matter. This type of spectroscopy has been developed largely by our group here at LBL.

Spatially Resolved Photothermal Technique for the Investigation of Transport and Recombination in Semiconductors‡

The development of spatially resolved probes for the investigation of transport processes in semiconductors is of increasing interest. In principle, these methods should enable the study of such important phenomena as the interaction between macroscopic defects (e.g., dislocations) and carrier transport, as well as the fate of these carriers near interfaces. Typically, conventional methods integrate the measurement over the entire distance between the electrodes. Furthermore, the electrodes themselves may influence the results unless care is taken in configuring the experimental setup.

These limitations have motivated us to develop a noncontact, spatially resolved *in situ* probe of transport properties in semiconductors. The basic premise of the technique is the use of the heat associated with nonradiative processes (e.g., recombination of carriers) to deflect a focused laser probe beam (subgap energy) propagating *through* the semiconductor. The deflection of the probe beam is caused by a change in the refractive index of the sample, which is in turn governed by carrier diffusion and recombination (Fig. 1). A quantitative theory was developed to account for the observed signal.

The experimental setup employs the method of transverse photothermal deflection shown in Fig. 2. The sample used for our experiment was a *p*-doped Si ($\rho \approx 6\Omega\cdot$cm). One face of the crystal was mechanically polished and its surface treated with methanol to minimize surface recombination. The photocarriers were generated by an Ar^+ ion laser beam (5145

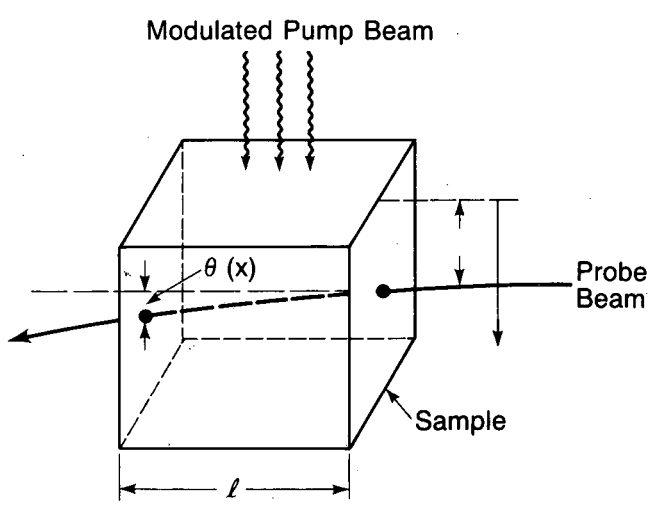

Figure 1. Principle of the scheme for spatially resolved photothermal detection of carrier transport and recombination in semiconductors. Such carrier processes govern the refractive index of semiconductors. A focused laser probe passing through a semiconductor sample will therefore be deflected by an angle, $\theta(x)$, that is governed by these processes. (XBL 8410-10944)

*Supported by the Director, Office of Energy Research, Office of Basic Energy Sciences, Materials Sciences Division of the U.S. Department of Energy under Contract No. DE-AC03-76SF00098, and by the Defense Advanced Research Projects Agency, Department of Defense under DARPA Contract No. 3343.

†Group Leader.

‡Complete version submitted to *Journal of Applied Physics*.

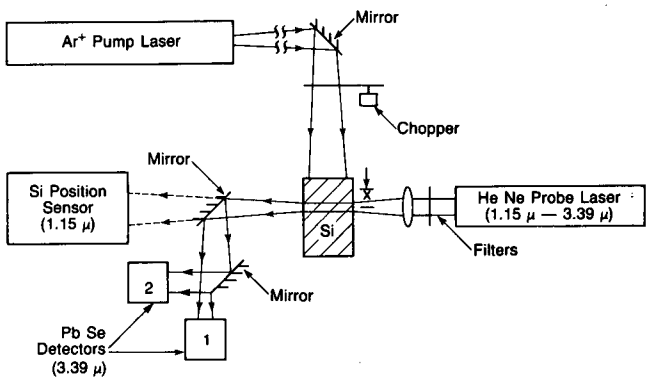

Figure 2. Experimental arrangement for deflection measurements. Two detection schemes are shown: for the 1.15 μ wavelength, a silicon position sensor was used; for the 3.39 μ wavelength, a mirror cutting the beam in two equal parts and two well-matched PbSe detectors were used. The signal was processed by a differential-phase-sensitive detector. (XBL 8410-10945)

Å), the maximum power density on the sample being ~500 mW/cm^2. This corresponds to a minority carrier density one order of magnitude smaller than that of the majority carriers. To probe the index of refraction gradient within the crystal, we used two different wavelengths (1.15 μ and 3.39 μ) from a HeNe laser focused to 30 μ. In the case of the 1.15 μ probe beam, the deflection was measured with a position-sensitive detector, while for the 3.39 μ beam two PbSe detectors were used, as shown in the figure. It should be pointed out that it is important to use an actual position-sensitive detector that gives good rejection of probe-beam intensity fluctuations. This is crucial for the 3.39 μ case where free-carrier absorption is significant.

The measurements were made at two probe-beam wavelengths: 1.15 μ and 3.39 μ. Before proceeding to describe the results, we note that the power dependence of the signal in the range of 30–500 mW/cm^2 was found to be linear within the experimental error.

Figure 3 shows the results obtained when the polished, methanol-treated face of the Si crystal was illuminated and the carrier transport probed at 1.15 μ. At this wavelength, the free-carrier dispersion is negligible, and one expects the $\partial T/\partial n$ term to be dominant. As can be seen, the two regions predicted by the theory are evident, and agreement with the theory is satisfactory.

It is interesting to note that by using the same set of parameters and varying the surface conditions of the Ar$^+$-illuminated surface (i.e., varying the surface recombination velocity s), we obtain good agreement between the theoretical predictions and the experimental results when the opposite unpolished and untreated face was illuminated (Fig. 4).

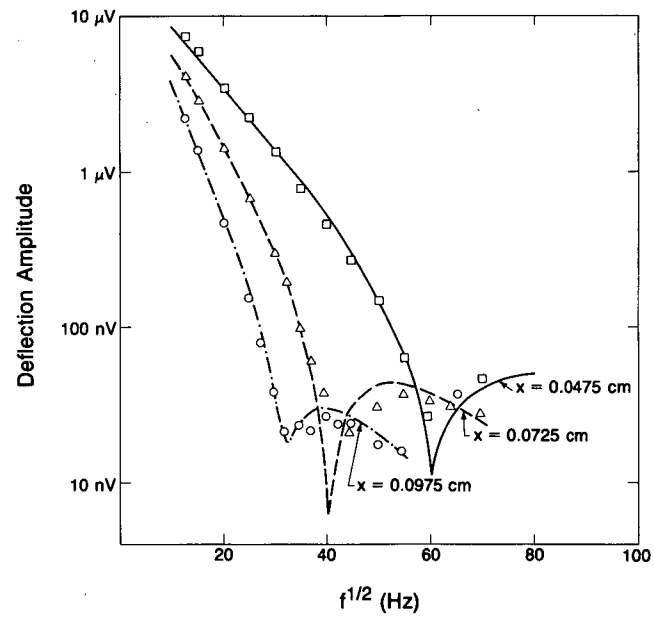

Figure 3. Comparison of the experimental measurements (points) with the theory (lines) for a well-polished treated surface of silicon crystal and a laser probe of 1.15 μ wavelength. (XBL 8410-10927)

To further test the theory, we probed the carrier transport with a 3.39 μ beam. At this wavelength,

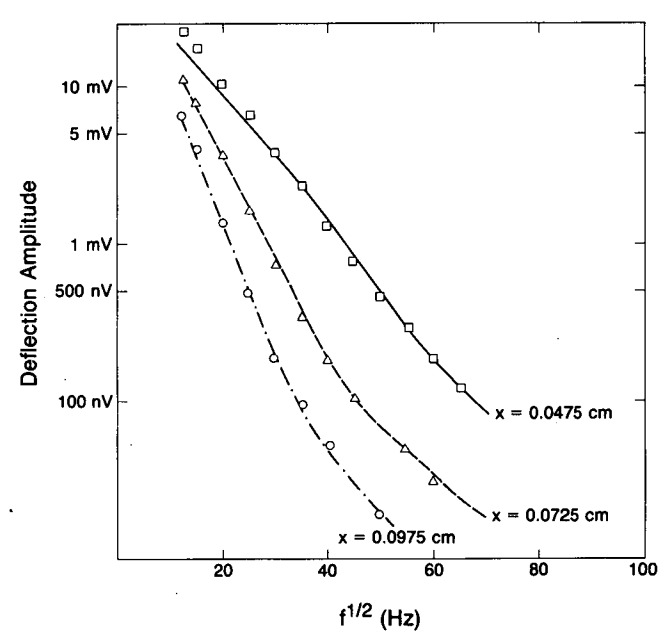

Figure 4. Comparison of the experimental measurements (points) with the theory (lines) for the unpolished surface of the Si crystal and a 1.15 μ laser probe. (XBL 8410-10924)

the free-carrier dispersion is not negligible. The free-carrier contribution (high frequency range) and the thermal contribution (low frequency range) are observed simultaneously. By using the preceding set of parameters to characterize the bulk and the illuminated surface, we obtain good agreement, as shown in Fig. 5.

*Photothermal Spectroscopy and Imaging of Gallium Arsenide**

The small rise in temperature associated with the absorption of electromagnetic radiation has provided the basis for a new spectroscopic tool generally known as photothermal spectroscopy. The advantages of this type of spectroscopy are its sensitivity and the relative ease with which it can be implemented.

The heating causes a change in the index of refraction of the medium surrounding the sample. This change is probed with a weak laser beam that is deflected as the index of refraction changes. Using phase-sensitive methods, the amplitude and the phase of the deflection can be readily measured with a position-sensitive detector (Fig. 6). Thus, by varying the wavelength of the optically exciting (pump) beam, the deflection of the probe beam is a measure

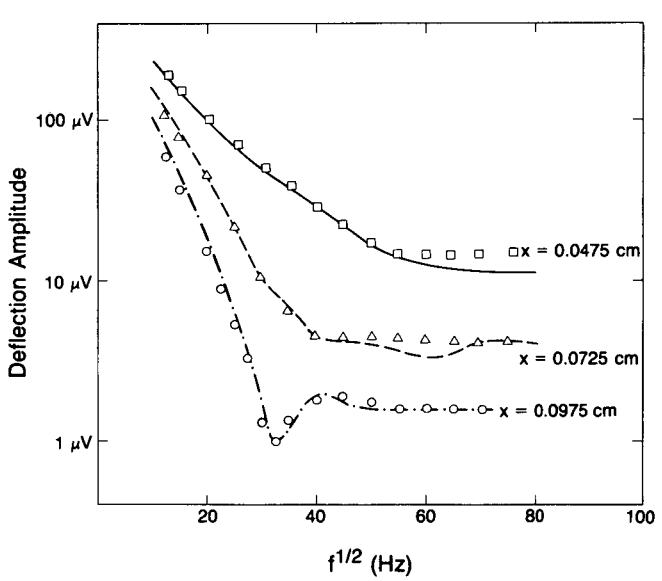

Figure 5. Comparison of the experimental measurements (points) with the theory (lines) for a well-polished treated surface and a 3.39 μ probe. (XBL 8410-10942)

*Complete version appeared in the *Proceedings of Third Conference on Semi-Insulating III–V Materials*, 1984.

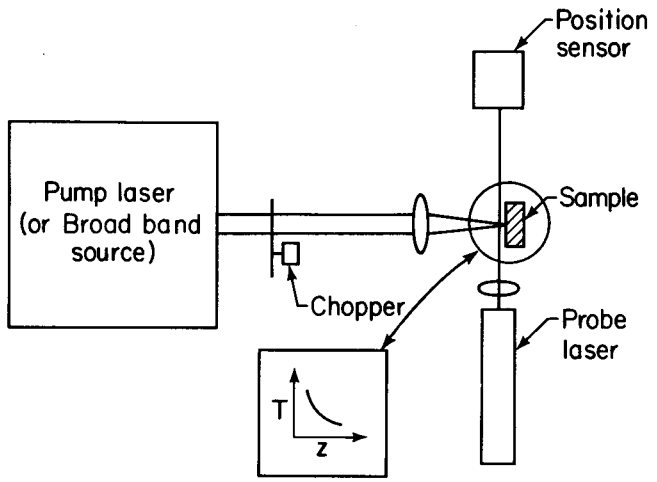

Figure 6. Schematic of experimental setup for photothermal deflection spectroscopy. (XBL 836-2666)

of the optical absorption. This type of spectroscopy is known as *photothermal deflection spectroscopy.*

The photothermal signal S is quantitatively related to the optical absorption coefficient in the following manner:

$$S = A[1 - \exp(-\alpha\ell)] \quad , \qquad (1)$$

where A is a constant that can be determined empirically, α is the optical absorption coefficient, and ℓ is the sample thickness.

Sensitivities of $\alpha\ell \approx 10^{-7}$ have been achieved, and the superiority of this technique in terms of sensitivity and flexibility has been demonstrated in a recent study of the optical properties of defects in amorphous semiconductors.

There exists a class of experimental conditions, however, for which photothermal deflection techniques are not suited in studying the optical and thermal properties of matter. Examples of such experiments are those that require vacuum and/or cryogenic temperatures. Such conditions are encountered in the study of surfaces and interfaces. Similar requirements exist for *in situ* and real-time characterization of thin-film semiconductors. These conditions motivated the use of optical heating in yet another manner. Since heating results in the expansion and buckling of the illuminated surface, a measurement of the surface displacement is a means of determining the optical and thermal properties of the illuminated solid. This small displacement can be detected in a variety of ways, the simplest of which is by reflecting a weak laser beam off the illuminated surface. As the surface is displaced upon being optically heated, the probe beam will be deflected from

its original reflection direction. This deflection is then detected with a position-sensitive detector (Fig. 7). Typically, $\alpha\ell$ of 10^{-6} are readily achievable. This version of photothermal spectroscopy is called *photothermal displacement spectroscopy.*

An important and characteristic parameter in photothermal spectroscopy is the thermal diffusion length L_{th}, which defines the depth from which the photothermal signal originates. L_{th}, which is also called the thermal wavelength, is given by:

$$L_{th} = (K_{th}/\omega\rho\, C)^{1/2} \quad , \qquad (2)$$

where K_{th} is the thermal conductivity of the sample, ω is the modulation frequency of the light, ρ is the density, and C is the heat capacity.

The modulation dependence of the thermal diffusion length is what is exploited to perform nondestructive depth profiling and imaging of solids. The higher the modulation frequency, the shorter the thermal length, and the closer to the surface the information is derived from. On the other hand, for low modulation frequencies, the photothermal signal is a probe of the bulk. Furthermore, by focusing the pump and probe beams, scanning microscopy can be performed. The achieved spatial resolution is a function of the size of the focal spot of the pump beam as well as the thermal diffusion length. Resolution to 1 micrometer has been attained.

We have performed scanning photothermal microscopy of semi-insulating LEC undoped GaAs wafers. The pump beam was an argon-ion laser focused to 1 micron on the wafer. The probe beam was a 0.5 mW HeNe laser. Both the deflection and the displacement schemes were used and yielded identical results. As can be seen (Fig. 8), both the phase and the amplitude of the photothermal signal exhibit small features that are due to the scattering of the thermal wave by thermal inhomogeneities in the wafer. By varying the modulation frequency, we were able to determine that these features lie on and near the surface. By analyzing the photothermal signal, using the theory we developed earlier, we were able to deduce that the inhomogeneities are arsenic-high inclusions. Our preliminary estimate of the degree of arsenic enhancement in these inclusions is approximately 14%, averaged over the 1-micron pump-beam diameter. To test the validity of our conclusion, scanned Auger spectroscopy (2-micron resolution) was performed on these inclusions. The Auger spectra verified our conclusion and gave an arsenic enhancement of 12%. Upon heating the wafers in a nitrogen atmosphere at 250°C, the arsenic-rich inclusions were no longer observed in the photothermal scans. This could be due to the arsenic diffusing into the matrix or evaporating out of the wafer.

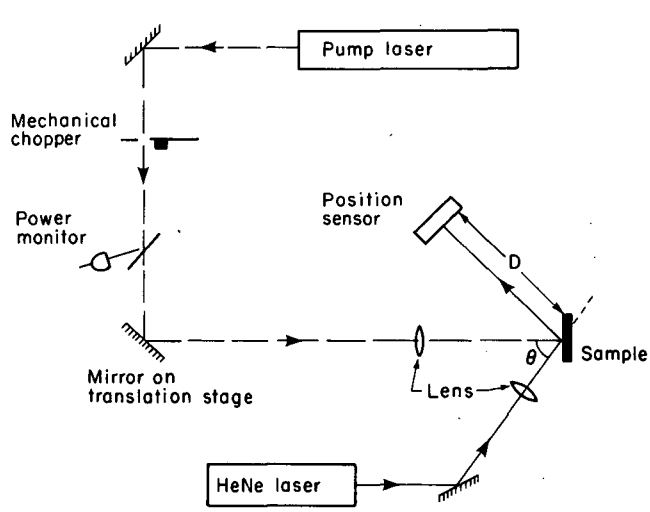

Figure 7. Schematic of experimental arrangement for photothermal displacement spectroscopy. (XBL 831-22)

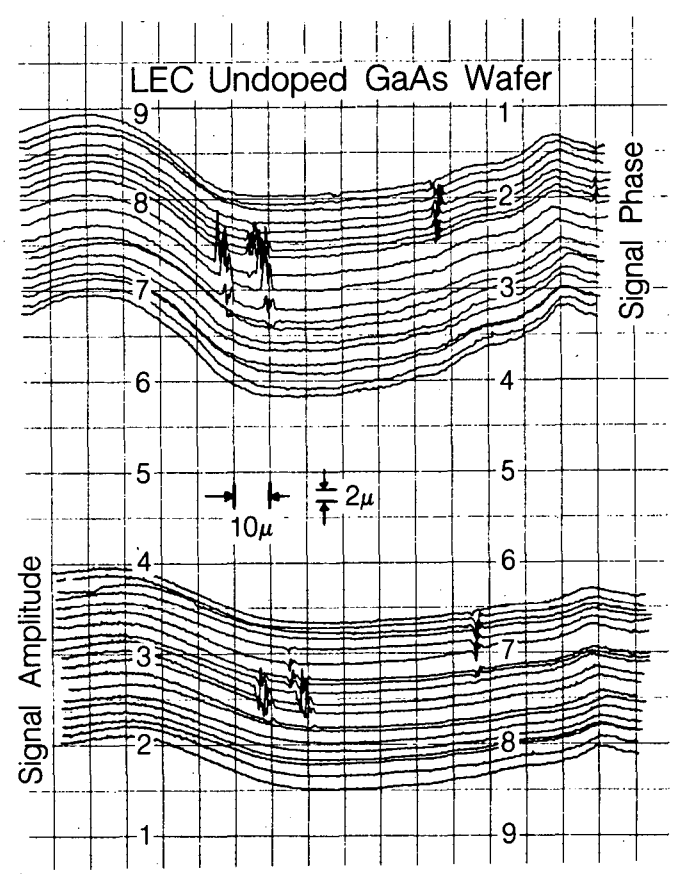

Figure 8. Spatially resolved photothermal scans of LEC undoped GaAs wafer. (XBL 845-1701)

We have also investigated the optical absorption spectra of undoped, chromium-doped, and silicon-doped GaAs crystals in the 0.5–1.5 eV range. In Fig. 9, we compare the photothermal deflection spectra of Cr- and Si-doped materials. As can be seen, the semi-insulating Cr-doped sample reproduces the main features obtained using conventional techniques. In addition, we observe a small peak at 0.5–0.6 eV, which we tentatively attribute to Fe impurities. The Si-doped sample exhibits a qualitatively different spectrum. The absorption coefficient does not drop at photon energies lower than 0.9 eV as is the case for the Cr-doped material. The spectra of two Si-doped n-GaAs samples are shown in Fig. 9. While both are from the same boule, sample A is from near the top of the boule, and sample B is from near the center. The larger thermal gradients and stresses expected near the top of the boule may account for the increased defect density in sample A.

In Fig. 10, we show the spectra of semi-insulating LEC GaAs and of the same material after being plastically deformed at 400°C. It is clear that the deformation increases the deep-level defect density. This is in agreement with results obtained by other methods such as electron spin resonance (ESR) and conventional infrared absorption.

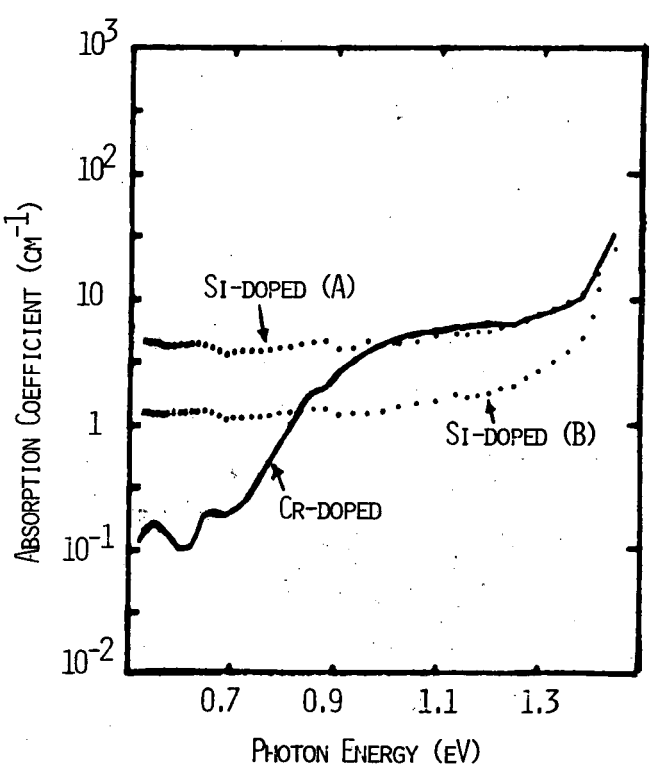

Figure 9. Photothermal absorption spectra of Cr- and Si-doped GaAs. (XBL 845-1702)

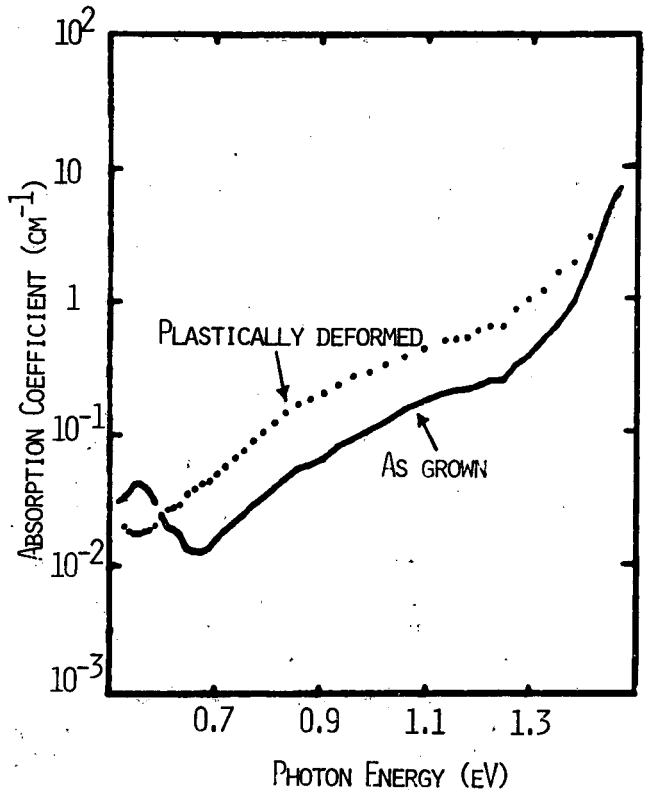

Figure 10. Photothermal absorption spectra of LEC semi-insulating as-grown and plastically deformed (at 400°C) GaAs. (XBL 845-1703)

*An Optical Approach to Thermopower and Conductivity Measurements in Thin-Film Semiconductors**

Conductivity and thermopower measurements are widely used to study the transport properties of semiconductors. The thermopower S is related to the Peltier coefficient Π, which, for conduction above a mobility edge E_c, may be written as:

$$ST = \Pi = \frac{kT}{e}\left(A + \ln\frac{N_0}{n}\right) . \qquad (3)$$

Since the quantities A and N_0 do not contain the mobility μ, the thermopower provides a measure of the carrier density n alone and is often applied to separate the product $n\mu$ in the conductivity $\sigma = en\mu$. Moreover, the sign of S directly gives the charge of the majority carriers.

A common problem with transport experiments is that properties of the metal contacts may influence the results. A current-voltage measurement reflects the conductivity only if the contact resistance is

*Complete version appeared in *Appl. Phys. Lett. 45*, p. 272 (1984).

much lower than the sample resistance. In the thermopower experiment, the metal contacts serve as reference for the thermovoltage, and contact properties are generally not considered to be a problem in the thermal equilibrium case, i.e., dark transport. In studying photoconductivity, however, thermopower measurements are much more difficult to perform because of the photovoltage, which may exceed the small thermovoltage. To understand the steady-state photoconductivity, it is essential to be able to distinguish between the effects due to change in carrier density and those due to changes in mobility. Photothermopower measurements are of particular importance in the case of hydrogenated amorphous silicon, since Hall effect data fail to give even the correct sign of the charge carriers. We have developed a technique to study transport properties that is based on the photothermal detection of Joule and Peltier heat generated by electrical currents. The method gives a spatially resolved profile of the conductivity along the film surface, thus allowing the detection of σ away from any metal contacts. The measurement of the Peltier heat rather than the thermovoltage avoids the influence of photovoltages on the signal. Preliminary results for the photo-Peltier coefficient of doped *a*-Si:H are presented.

All measurements were done on 1-micron-thick *a*-Si:H films deposited onto quartz substrates. An oscillating voltage, $U = U_0 \cos\omega t$ with frequency $f = 5$ to 10 Hz, is applied between two evaporated Al contacts in gap configuration with a spacing of 1 to 1.5 mm (Fig. 11). The heat generated by the current creates a temperature gradient perpendicular to the sample surface, which changes the index of refraction in the surrounding medium. This change is probed by a laser beam skimming the surface of the sample perpendicular to the current direction. To prevent changes in conductivity caused by the probe laser, an IR-laser ($\lambda = 3.39\ \mu$) is used, and the deflection is measured by a position-sensitive PbSe-detector. Both signals appearing at the reference frequency ($1f$ signal) and at twice the reference frequency ($2f$ signal) are monitored as the probe beam is scanned along the direction of the electric current (x direction). It has been demonstrated that the deflection is directly proportional to the heat generated within the interaction region between the probe laser and the sample. The Joule heat U^2/R (R = sample resistance) has a component oscillating at twice the reference frequency with amplitude $U_0^2/2R$. The differential Joule heat per unit length in the x direction is given by:

$$\frac{1}{\sigma}\left(\frac{U_0^2}{2R^2Q}\right),$$

where Q is a cross section of the sample. The $2f$ signal, therefore, provides a profile of the resistivity $1/\sigma$ along the x direction with a resolution determined by the beam diameter and the thermal diffusion length. Both quantities are on the order of 0.2 mm. The Peltier heat Π oscillates at the reference frequency with amplitude $\Pi \frac{U_0}{R}$ and appears centered and with opposite sign at each of the contacts.

In Fig. 12(a), the $2f$ signal, plotted as a function of x, is shown for a heavily phosphorous-doped sample. Both amplitude and phase are nearly constant, indicating that the conductivity is uniform throughout the sample. The strong decrease of the signal at both contacts shows that the contact resistance is negligible compared to the sample resistance. Furthermore, the time delay of the signal at the contacts, exhibited as a decreasing phase angle, indicates that the tail of the signal is caused by diffusing heat from the gap region rather than by contact properties. We found that the $2f$ signal is linear in the Joule heat over more than 3 orders of magnitude. This was verified both by varying the voltage at fixed resistance and by varying the resistance in photoconductive samples illuminated with different light intensities at fixed voltages. The minimum detectable signal corresponds to a total Joule heat of 10^{-5} W, which, for the given geometry and an electric field of 10^3 V/cm, corresponds to a lower limit of $10^{-6}\ \Omega^{-1}\text{cm}^{-1}$ for the conductivity.

The flat conductivity profile shown in Fig. 12(a) is not obtained in all samples. In Fig. 13, results for a sample with lower doping concentration are shown. It can be clearly seen that the major part of the Joule heat is generated at the contacts. It follows that the resistance of the film is much lower than indicated by a current-voltage measurement.

The magnitude and phase of the $1f$ signal of the heavily phosphorus-doped sample are plotted in Fig.

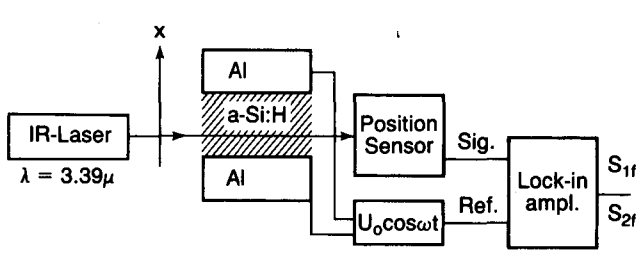

Figure 11. Experimental setup for thermopower and conductivity measurements on *a*-Si:H semiconducting thin film. (XBL 843-10190)

12(b). The signal has the predicted shape for the Peltier heat, with approximately symmetric peaks appearing at the contacts. The phase of the signal at the peak positions differs by 180°, indicating that the deposited heat has opposite signs at the contacts. Also shown is the phase of the $1f$ signal measured in a boron-doped sample, which at each contact is shifted by 180° with respect to the phosphorus-doped

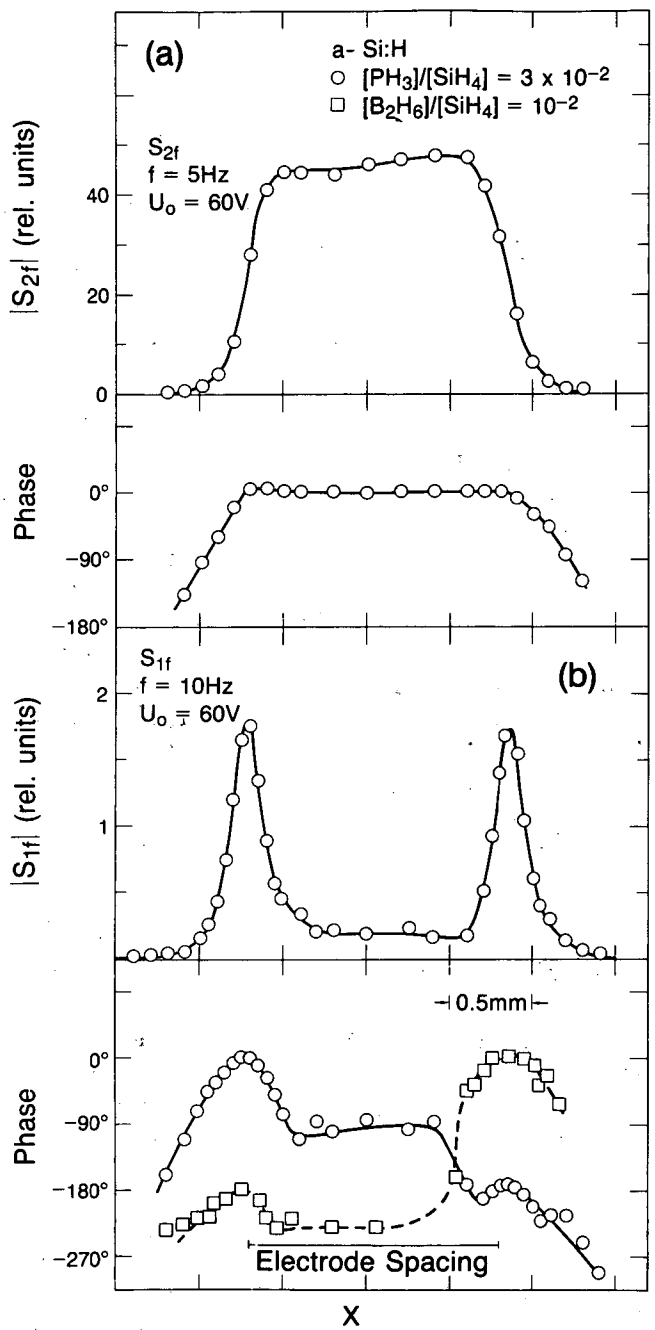

Figure 12. Magnitude and relative phase angle of (a) the $2f$ and (b) $1f$ signals for a heavily phosphorus-doped sample.
(XBL 843-10187)

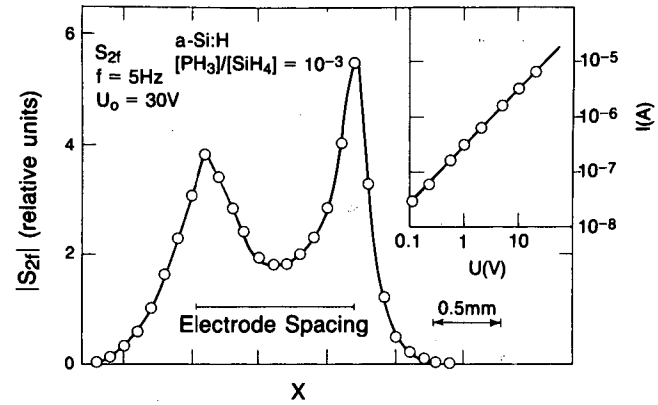

Figure 13. The $2f$ signal for a sample with non-ohmic contacts. Inset shows current-voltage characteristics.
(XBL 843-10184)

sample. This behavior reflects the change in sign of the Peltier coefficient as the conductivity is changed from n to p type. As in the case of the $2f$ signal, the phase decreases in the tails, which is attributed to heat diffusing from the peak position, leading to a time delay in the signal. The Peltier heat was found to be proportional to the current through the sample over more than 2 orders of magnitude. The Peltier coefficient Π can be calculated directly from the integrated $2f$ and $1f$ signals (S_{2f} and S_{1f}). These quantities are proportional to the total Joule heat $\left(\frac{U_0^2}{2R}\right)$ and Peltier heat $\left(\Pi \frac{U_0}{R}\right)$, respectively. To compare the signals quantitatively, we have chosen twice the frequency for S_{1f} than in the case of S_{2f} making sure that both quantities experience the same thermal relaxation. Dividing S_{1f} through S_{2f} and solving the equation for Π, we are left with:

$$\Pi = \frac{U_0}{2} \times \frac{S_{1f}}{S_{2f}} \quad . \tag{4}$$

Determining the sign of Π is equivalent to determining the phase angle, which corresponds to heating in phase with the applied voltage. This can easily be done by adding a dc-offset U_1 to the oscillating voltage $U_0 \cos\omega t$. Then, besides the signal from the Peltier heat, a second $1f$ signal due to the Joule heat appears with amplitude proportional to $(2U_1U_0)/R$. Comparing the phases of these two signals allows the determination of the sign of Π.

We have shown that the photothermal detection of electronic transport yields information about contact influences, macroscopic sample homogeneity, and Peltier coefficients of thin-film samples. Possible extensions of the method that are currently under

investigation include an ability to provide two-dimensional conductivity images of device structures and the separation of surface from bulk contributions to the conductivity.

*Heat Diffusion Solutions for the Nonresonant Spectrophone**

Most theoretical treatments of the nonresonant spectrophone have used as their starting point the standard inhomogeneous heat diffusion equation:

$$\rho_0 C_v \frac{\partial T'}{\partial t} = \kappa \nabla^2 T' + H \tag{5}$$

where T' is the temperature disturbance, H is the heat released due to collisional deactivation of the optically excited molecules, ρ_0 is the density, C_v is the specific heat per unit mass at constant volume, and κ is the thermal conductivity. This equation neglects the work done on or by the gas in compression or expansion, respectively, and treats it as if it were a solid. A more proper equation of energy conservation for a gas, taking expansion and compression into account, is given by:

$$\rho_0 C_p \frac{\partial T'}{\partial t} = \kappa \nabla^2 T' + H + \frac{\partial p'}{\partial t} \tag{6}$$

where p' is the pressure disturbance. When the cell dimensions are small compared to the acoustical wavelength, p' is constant throughout the cell, and, if one uses the ideal gas equation of state and the fact that the total mass of gas is conserved, one finds that p' is proportional to the volume integral of the temperature disturbance T'; if one assumes an $e^{-i\omega t}$ time dependence, one obtains the equation

$$\nabla^2 T' + \frac{i\omega\rho_0 C_p}{\kappa} T' - \frac{i\omega(\gamma - 1)\rho_0 C_p}{\gamma\kappa\pi R^2} \times \int_0^R T'(r')\, 2\pi r'\, dr' = -\frac{H}{\kappa}, \tag{7}$$

where we have assumed an infinitely long cylindrical cell of radius R and assumed that H depends only on r, the radical coordinate, and neglected the microphone impedance correction.

*Complete version submitted for publication in *Journal of Applied Physics.*

We present here a general solution by a Green's function method and show that the pressure amplitude one obtains by integrating the temperature solution is:

$$p' = \frac{i(\gamma - 1)}{\pi R^2 \omega} \times \frac{\int_0^R H(r')\left[1 - \frac{I_0(kr')}{I_0(kR)}\right] 2\pi r'\, dr'}{1 + \left(\frac{2(\gamma - 1)}{\gamma kR}\right)\left(\frac{I_1(kR)}{I_0(kR)}\right)}, \tag{8}$$

where $k = (-i\,\omega\rho_0 C_p/\kappa)^{1/2}$ and I_0 and I_l are modified Bessel functions. We have also solved the heat diffusion Eq. (5) in the frequency domain for arbitrary $H(r)$ and obtained for the pressure:

$$p' = \frac{i(\gamma - 1)}{\pi R^2 \omega} \times \int_0^R H(r')\left[1 - \frac{I_0(k'r')}{I_0(k'R)}\right] 2\pi r' dr', \tag{9}$$

where $k' = (-i\omega\rho_0 C_v/\kappa)^{1/2} = k/\sqrt{\gamma}$. The heat diffusion Eq. (5) tends to overestimate the temperature disturbance near the center of the cell and underestimate it near the walls, but these effects tend to cancel out in integrating to obtain the pressure, and thus it gives an excellent approximation for the pressure. In particular, both expressions (8) and (9) have identical limiting behavior at high and low frequencies. At low frequencies ($\omega << \kappa/\rho_0 C_p R^2$), both give

$$p' = \frac{p_0}{4\pi\kappa T_0} \int_0^R H(r')\left(1 - \frac{r'^2}{R^2}\right) 2\pi r'\, dr'. \tag{10}$$

At high frequencies ($\kappa/\rho_0 C_p R^2 << \omega << 3.83\, c/R$), both give

$$p' = \frac{i(\gamma - 1)}{\pi R^2 \omega} \int_0^R H(r')\, 2\pi r'\, dr'. \tag{11}$$

Thus, the use of the heat diffusion equation for the photoacoustic effect in the nonresonant spectrophone is well justified; however, where the temperature and/or density solutions are needed, as in thermal lensing, photothermal deflection, etc., in finite-radius cells, the solution of Eq. (7) may be more appropriate.

*Photothermal Spectroscopy in Turbulent Media**

In the atmosphere, a propagating laser beam wanders due to the effect of turbulence. The larger turbulent eddies deflect the beam as a whole, and the smaller (<< beam diameter) turbulent eddies broaden the beam. Hence, after propagating in the atmosphere over a sufficient distance, a laser beam appears to have a long-term averaged diameter significantly greater than the short-term averaged beam spot that randomly wanders about a mean position with a frequency spectrum $\leqslant$ 1000 Hz.

In the application of photothermal deflection spectroscopy (PDS) for the measurement of small absorptions in the atmosphere, this turbulence-induced beam wander is the dominant source of noise because of the inherent sensitivity of the technique to variations in the beam position. A modulation scheme that minimizes this component of noise is considered to be the most effective solution. The following pulsed technique proved to be most effective with an $\alpha\ell \sim 10^{-4}$ detection level: In the typical geometry of a PDS experiment, a pulsed pump beam and a cw probe beam are used. The advantage of the high power of pulsed lasers is therefore available. The rapid thermalization following the pump absorption and the consequent stepwise deflection of the probe beam is detected by a lateral position sensor (LPS) with a bandwidth of $\sim$100 Hz. Since the high-frequency signal from the LPS is independent of the low-frequency position of the probe beam, there is negligible influence from beam wandering on the signal detection process. Two samples are detected from the transient signal, at a separation of $\lesssim$10 μsec, one before and one after the pump pulse, and the process is repeated at the rate of the pump pulses for signal averaging. For times less than 100 μsec, turbulence is essentially stationary, so one can assume that there is no noise due to turbulence in the difference signal between the two samples. Note that the samples of the short-term-averaged probe beam are taken as it wanders on the LPS at low frequencies.

After each pump pulse, the imposed thermal gradient decays by heat diffusion. A pump repetition rate of $\leqslant$10 Hz allows sufficient diffusion. The primary effect of turbulence is to be observed in the overlap of the pump and probe beams. At each repetition of this process, the pump and probe beams have wandered to different positions (depending on the conditions of turbulence along the pathlength to the interaction region). Hence, the signal detected (the difference between the samples) is directly affected. However, the initial sample (before the pump pulse) yields information about the probe-beam position at the interaction region. Correlating this signal to the relative positions of the pump and probe at the interaction region, a normalization can be carried out. Since the pump beam also wanders, full correction is possible only if the pump-beam position is also monitored by a position sensor.

This technique accounts for the turbulence-induced beam wandering *before* the interaction region. The random deflections of the beam *after* the interaction region results in the loss of beam position information. The signal level before the pump pulse can only be correlated to the probe beam position at the interaction region probabilistically. This can be an important source of noise. An additional source of turbulence-induced noise is the variations in the beam diameters, which directly affect the signal. An analysis of these contributions of noise has been carried out in order to determine the smallest absorptions measurable under typical atmospheric conditions. Figure 14 shows a setup for a laboratory simulation. Experimental results have yielded a sensitivity of $\alpha\ell \sim 10^{-4}$.

Surfaces and Interfaces

Surfaces and interfaces play an increasingly important role in various technological applications.

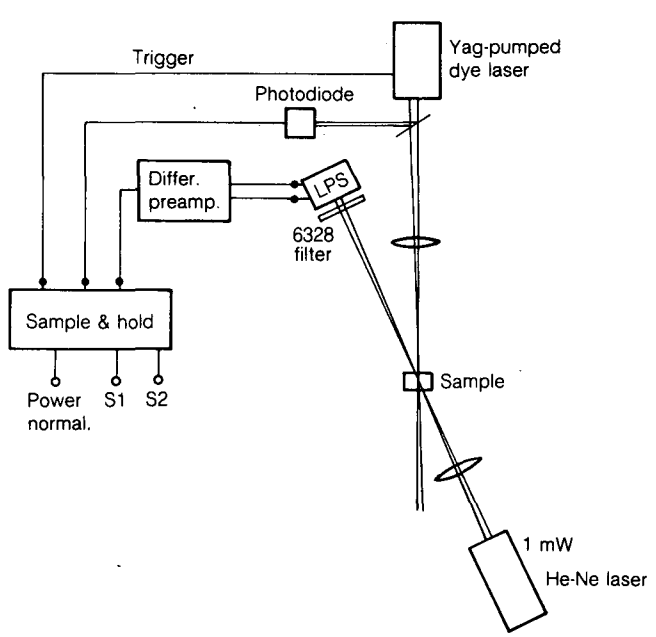

Figure 14. Experimental arrangement for a modulation scheme to minimize "noise" from atmosphere-caused beam wandering in photothermal deflection spectroscopy; LPS, lateral position sensor. (XBL 852-8815)

*Complete version to be submitted to *Applied Optics*.

Although the reactive nature of surfaces has been exploited for some time in processes such as catalysis, the exact nature and mechanisms responsible for their unique behavior remain to be ascertained. In this area of research, we employ photothermal spectroscopy to probe semiconductor surfaces and interfaces. Initially, our emphasis is on gaining a better understanding of the electronic properties of surface states through the investigation of their optical properties.

*Polarization and Temperature Dependence of Surface State Absorption in Si and Ge(111)**

The room temperature (111) cleavage faces of silicon and germanium are known to reconstruct to a metastable 2 × 1 unit cell, with period doubling along one of the three equivalent $<1\bar{1}2>$ directions on the surface. The mechanism behind this doubling of the unit cell has been the subject of much inquiry, with numerous models proposed to explain the various experimental results. The polarization dependence of the surface optical absorption is a consequence of the overall symmetry of the dangling-bond orbitals and does not require exact knowledge of the atomic positions to allow comparison with a class of models. The angular dependence of the dipole matrix element is different for the various models, making the polarization-dependent dangling-bond absorption a crucial test of these models.

We have studied the (111)2×1 surface state absorption of both Si and Ge, using polarization-dependent photothermal displacement spectroscopy. In addition to investigating the room temperature cleaved surface, we have also monitored the temperature dependence of the surface absorption as it is changed during annealing of the Ge(111) surface from the 2×1 to the *c*-2×8 structure.

Polarization Dependence. The polarization-dependent dangling-bond absorption was measured using photothermal displacement spectroscopy. In brief, this involves the optical detection of the thermal expansion of a sample as it is heated by absorption of light. The change in slope of the surface due to local thermal expansion is detected through the deflection of a HeNe probe beam reflected from the sample. Among the advantages of this technique is the ability to measure surface absorption directly, without requiring a difference measurement between a clean and an oxidized surface.

Both Si and Ge (111)2×1 surfaces exhibit ~2% absorption of $[\bar{1}10]$ polarized light, peaked at ~0.46 eV for Si and ~0.50 eV for Ge. The polarization dependence of the absorption peaks for Si and Ge in single-domain regions are shown in Fig. 15. A $\cos^2\theta$ dependence with a maximum along $[\bar{1}10]$ can be seen for both Si and Ge. The silicon results are in agreement with recent polarization-dependent reflectivity measurements. There is no significant rotation of the pattern, with all measurements being within the experimental alignment error of $\sim \pm 5°$. The pattern was observed to change when areas of different or mixed domains were examined. It could always be fitted by:

$$\sum_{\beta_i=-1,0,1} a_i \cos^2\left(\theta + \beta_i \frac{2\pi}{3}\right) ,$$

with the a_i correlating to the observed LEED intensities of the different domains. Of the various models discussed below, this is consistent only with the π-bonded chain model for both materials. The surface absorption disappeared upon oxidation, as can be seen in Fig. 15.

Temperature Dependence. The Ge(111) surface converts from 2×1 to a *c*-2×8 structure upon mild annealing, and preliminary results of observing this phase transition via the polarization-dependent absorption as an order parameter are shown in Fig. 16. This particular cleave was not a single domain, but, by fitting the polarization dependence, it was determined that, at the measurement point, two domains were present in the ratio of ~12:1, with the primary absorption occurring for vertical polarization. The polarization of the incident light ($\kappa\omega$ = 0.48 eV) was alternated between vertical and horizontal during the annealing process, and the photothermal signal at the two polarizations is shown in Fig. 16(a). The spectrum and polarization dependence when half of the signal had been annealed away was indistinguishable from the original except in magnitude. The sample was then heated to 135°C, and as can be seen in Fig. 16, above ~105°C there was no significant polarization dependence. In the first cycle, the sample temperature was greater than 60°C, where the surface signal starts to diminish, for 40 minutes. In the second cycle, the time between the data points at 60°C and 105°C was 37 minutes.

Free carrier absorption can be seen contributing to the signal above room temperature. The surface

*Complete versions of this work appeared in *Phys. Rev. Lett. 52*, p. 1148 (1984); *Phys. Rev. B. 29*, p. 7048 (1984); and the *Proceedings of the 17th International Conference on the Physics of Semiconductors*, J.D. Chadi and W.A. Harrison, Eds. (Springer-Verlag, 1985).

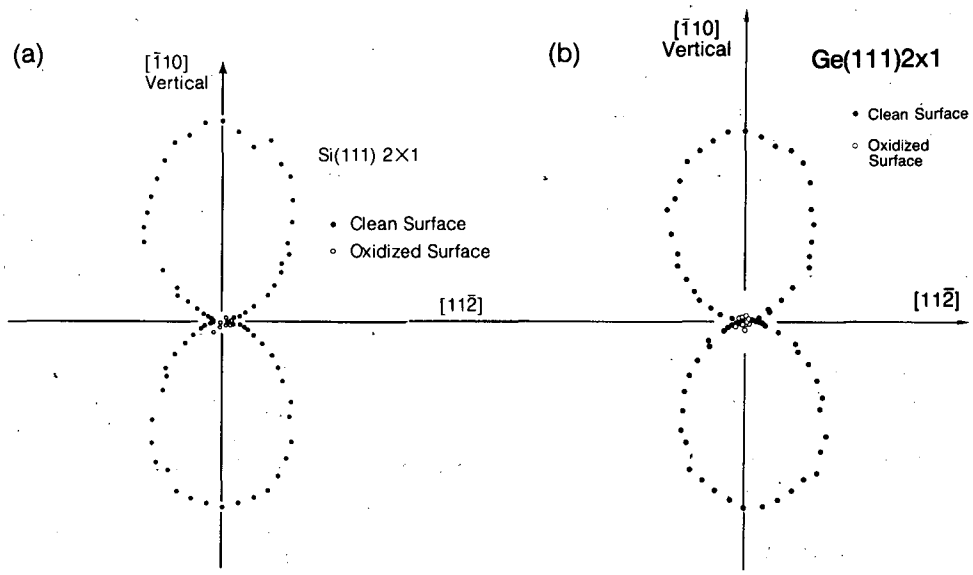

Figure 15. Polarization dependence of (111)2×1 peak absorption for (a) Si (0.46 eV) and (b) Ge (0.50 eV). [(a) XBL 8312-6936; (b) XBL 843-10183]

signal can be extracted as the difference between the absorption of light polarized parallel and perpendicular to [$\bar{1}$10], since the isotropic free carrier absorption adds equally to both polarizations [Fig. 16(b)]. It is also possible to separate surface and bulk contributions through the phase of the photothermal signal. The phase was observed to change smoothly from that of a surface absorption to the later arrival of the bulk signal between 60°C and 100°C. A vector separation of the two components was found to be consistent with the polarization data in Fig. 16.

The 135°C anneal resulted in a diffuse, "weak 8" LEED superstructure, and a subsequent 210°C anneal resulted in a sharp *c*-2×8 pattern. After the 210°C anneal, a small absorption at room temperature was detected at 0.48 eV. This absorption had a magnitude of ~0.06% and no polarization dependence. Although the signal-to-noise ratio was low, the phase seemed to indicate surface origin. If so, it would indicate that the *c*-2×8 structure has a small absorption at this energy. This is consistent with surface photovoltage (SPV) and photoconductivity (SPC) measurements, which find a signal at similar energies for the *c*-2×8 structure. The precise temperature dependence varies among cleaves, but the signal usually decays between 60°C and 130°C when the sample has been annealed just before cleavage. If the sample is not preannealed, the signal occasionally decays at 35°–60°C, and the resulting LEED pattern is 1×1, probably due to contamination.

The polarization-dependent optical absorption of cleaved Si and Ge (111)2×1 surfaces exhibit similar spectra, peaking at ~0.47 eV in Si and ~0.50 eV in Ge. This peak absorption has a strength of about 2-1/2% on flat, single-domain cleaves and is weaker on less homogeneous surfaces. The absorption is intrinsic to the 2×1 reconstruction and is the same as that previously seen with reflectivity, surface photovoltage, surface photoconductivity, and electron energy loss spectroscopies. The polarization dependence of this absorption was seen to follow $\sin^2\phi$, with maximum absorption parallel to [1$\bar{1}$0], and no absorption for light polarized along the period doubling [11$\bar{2}$] direction. This result was found to be consistent with only one of the many models proposed for these surfaces: a rebonded chain exhibiting a (1$\bar{1}$0) mirror plane. The size of the optical gap indicates a probable buckling of the π-bonded chain. This structural assignment is in agreement with data from a variety of other techniques as reported in the literature.

The polarization-dependent absorption is characteristic of the (111)2×1 surface and was used to probe the extent of the 2×1 phase during annealing and chemisorption. Monitoring of the absorption during a heating cycle similar to that in the stepwise annealing experiments showed additional decay in the 2×1 concentration upon reheating to a lower temperature than previously attained. This leads to the conclusion that the proximity of annealed

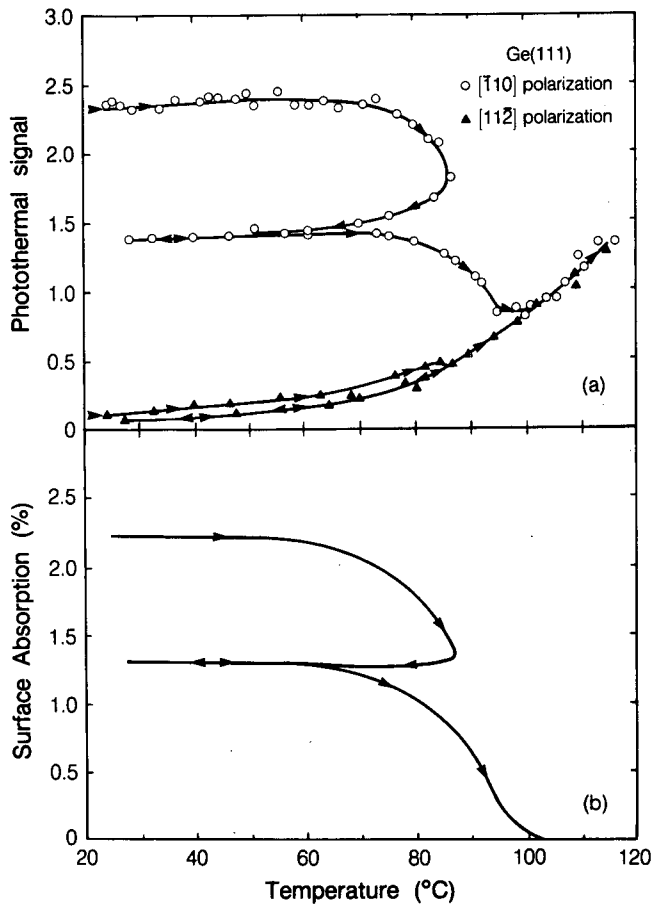

Figure 16. (a) Temperature dependence of photothermal signal from cleaved Ge(111). Sample is heated, cooled, and heated again. (b) Surface absorption. Difference between $[\bar{1}10]$ and $[11\bar{2}]$ signals in (a). (XBL 846-8488)

regions can lower the transition temperature of a given region of the surface. Preliminary experiments probing the temperature dependence of the surface optical energy gap showed little or no temperature dependence in the range of 300–450 K, contrary to the bulk gap dependence. This appears to support the buckled nature of the π-bonded chains, which would result in a strong interaction between the surface phonon and the dangling-bond states. Finally, these results have shown photothermal displacement spectroscopy to be a powerful new tool for surface studies, as well as for other applications that require remote sensing.

Amorphous Photovoltaic Semiconductors

Amorphous photovoltaic semiconductors, such as hydrogenated amorphous silicon (*a*-Si:H), hold promise for meeting Department of Energy cost and efficiency goals for thin-film solar cells prior to 1990. To achieve the higher conservation efficiencies required, it is necessary to better characterize the unique optical and transport properties of these materials. Photothermal spectroscopy can be used to elucidate the optical and electronic properties of *a*-Si:H. Of particular interest is the investigation of the optical properties near the so-called bandgap. By combining luminescence studies, photoconductivity, and optical absorption, a full and accurate characterization of the de-excitation of these photoexcited amorphous semiconductors can be achieved.

*The Effects of Dopants and Defects on Light-Induced Metastable States in Hydrogenated Amorphous Silicon**

An intriguing property of many amorphous semiconductors is that they exhibit metastable defect states. For both the chalcogenide glasses and *a*-Si:H, prolonged illumination creates defect states that disappear upon annealing. In the case of *a*-Si:H, these metastable states (Staebler-Wronski effect) alter various properties such as conductivity and luminescence. Yet, despite extensive research, they are still not well understood. Although silicon dangling-bond defects have been implicated, the question remains whether the apparent increase in the number of these defects is due to a shift in the Fermi level or to the creation of new defects upon illumination. Another significant issue is the connection between already existing (annealed-state) defects and dopants, and those defects induced by illumination. Using photothermal deflection spectroscopy (PDS), we have studied the optical absorption of the light-induced defects in *a*-Si:H. Since the measurement is insensitive to the position of the Fermi level, both the change in defect density due to illumination and the energy level of the defect can be determined.

Figure 17 shows that exposure to light enhances the gap-state absorption, whereas annealing restores the absorption to its original dark value. The enhancement is consistently reproducible when the illumination-anneal cycle is repeated several times. Previous work has demonstrated that the magnitude of gap-state absorption in *a*-Si:H provides a direct measure of the silicon dangling-bond-defect density, N_s. Using the same procedure for the change in optical absorption, we quantitatively determine the change in the defect density between the annealed and illuminated state, ΔN_s. For undoped material, ΔN_s is approximately $10^{16}\,\mathrm{cm}^{-3}$. By comparing the experimental absorption spectra with calculated spectra generated from density-of-states models, the defect energy level is determined to be ~1.25 eV

*Complete version to appear in *Physical Review B.*

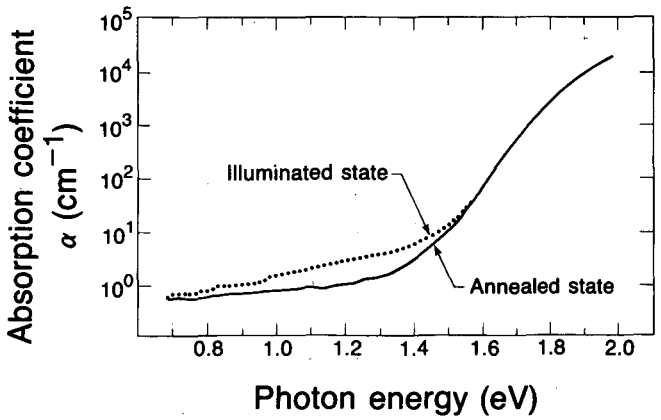

Figure 17. Effect of illumination on gap-state absorption of undoped *a*-Si:H. (XBL 847-10700)

below the conduction band. Since the energy of the defect and its cross section are identical to those measured for silicon dangling-bond defects, we conclude that the change in subgap absorption is due to silicon dangling-bond defects. Little or no change is seen in the exponential absorption (Urbach) edge.

Figure 18 shows that the light-induced defects scale with dopant concentration over a wide range of doping levels. The ratio $\Delta N_s/N_s$ is found to be independent of doping level to within a factor of 2. Thus, the effect is largest for high doping, unlike the case of conductivity changes. The fully compensated sample exhibited the least enhancement, $\lesssim 10^{15}$ cm^{-3} defects, which is an order of magnitude smaller than for the undoped material. For undoped material, the increase in defect density, ΔN_s, is constant to within a factor of 2 or 3, independent of the initial defect density, N_s, as seen in Fig. 19.

The results unambiguously show that the increase in defect density is not due simply to a shift in the Fermi level toward midgap upon illumination. A shift in the Fermi level, without any change in dangling bond defect density, results in less subgap absorption rather than the observed increase. Further, by successively increasing the dopant concentration, the Fermi level moves into the band tails so that after illumination it is still in a region of *smaller* dangling-bond density. Consequently, the effect should increase with increased doping, which is the opposite of what we observe. Since Fermi-level motion alone cannot account for the observed changes, we conclude that illumination creates new dangling-bond defects.

In terms of the mechanism for creating the dangling bonds, the results imply that the light-induced

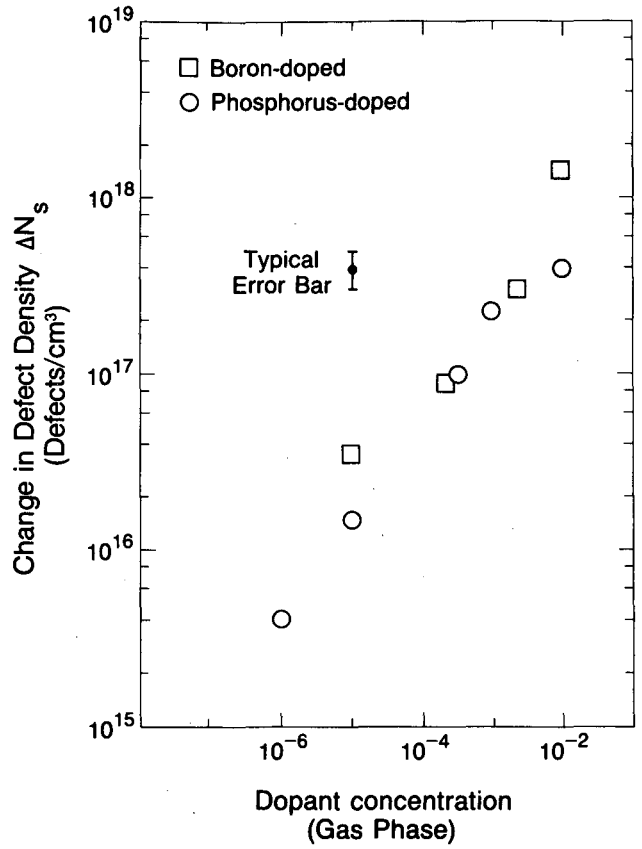

Figure 18. Dependence of the light-induced increase in defect density, ΔN_s, on dopant concentration. (XBL 836-2671)

defects do not result from breaking weak Si-Si bonds. One would expect ΔN_s to be relatively large for high-defect-density undoped material, which has substantial strain disorder (as evidenced by a broad Urbach edge) and consequently a large number of weak Si-Si bonds. Yet, for undoped material, ΔN_s is constant, *independent of disorder.*

Finally, there are several implications for solar cell fabrication. When air is let into the chamber during preparation, the cell exhibits an even larger efficiency drop after prolonged illumination, which again can be annealed away. The conclusion that light-induced defects are impurity-related is consistent with this observation. In addition, for *p-i-n* solar cells, illumination results in a fall-off in the blue response. Here, the doped outer layer will have the largest density of light-induced defects. Consequently, photons with short penetration depths will be strongly affected.

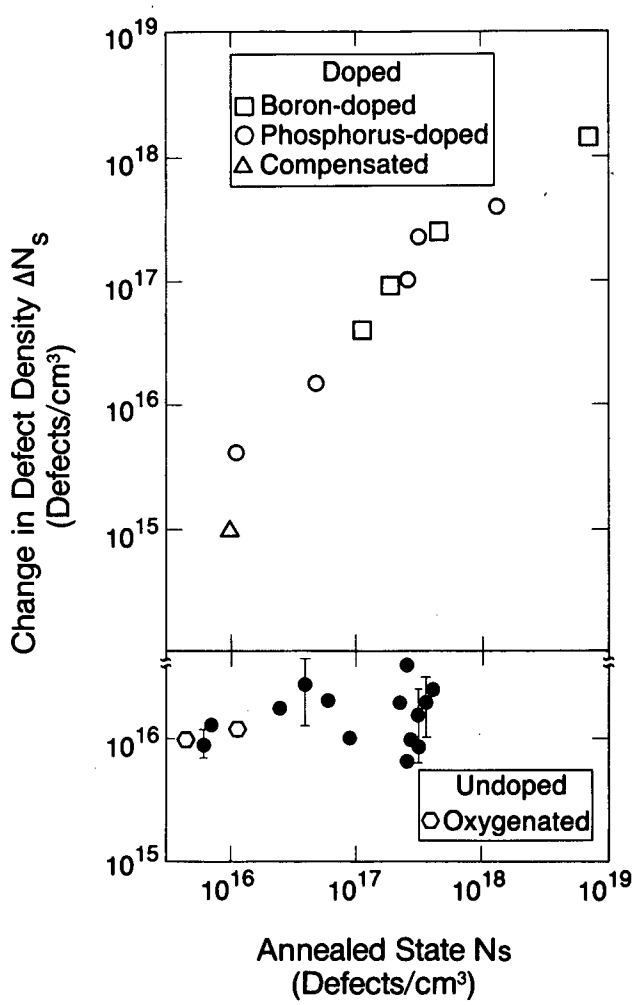

Figure 19. Dependence of the light-induced increase in defect density, ΔN_s on the initial defect density, N_s, for doped and undoped material. (XBL 847-10703)

*Urbach Edge and Gap States in Hydrogenated a-SiC and a-SiGe Alloys**

Considerable interest has developed recently in amorphous alloys based on hydrogenated amorphous silicon. Alloys with gaps smaller than *a*-Si:H—such as *a*-SiGe:H—are of interest in photovoltaic devices since they offer a better match to the solar spectrum (e.g., stacked cells). Alloys with gaps wider than *a*-Si:H—such as *a*-SiC:H or *a*-SiN:H—are also important in the construction of solar cells because they provide suitable window-layer materials. Moreover, *a*-SiC:H is promising for large-area white luminescence devices. Further interest in these alloys has resulted from the development of amorphous superstructures, which are developing into a major field of interest.

*Complete version to appear in *Solid State Communications.*

Most of these alloy phenomena are critically dependent on the spectral distribution of localized states—i.e., band tails and defect levels—inside the pseudogap of the alloy. For instance, the best SiGe alloys available to date have a density of dangling-bond defects that are a few times 10^{17} cm^{-3}. This results in a very poor photoconductive and luminescent behavior. Also, the SiC alloy, although exhibiting good room-temperature luminescence efficiency, shows a rapid drop in photoconductivity as the amount of carbon in the solid is gradually increased. Possible mechanisms behind this behavior include (1) the added compositional disorder of the alloy, which is reflected by a larger localized state density, and (2) the different energies and bond lengths of the elements, differences that can influence the formation of structural defects.

We investigated such effects when undoped *a*-Si:H, produced by glow discharge in silane, is increasingly mixed with either carbon or germanium.

The spectral distribution of the subgap states was determined by photothermal deflection spectroscopy (PDS), which allows detection of very weak optical absorption levels. The above-gap absorption was measured by direct transmission, using a Cary spectrophotometer. Typical absorption curves of the *a*-Si_xC_{1-x}:H alloys are shown in Fig. 20 for values of x between 1 and 0.77.

A remarkable result is that there is no appreciable variation in the density of defect states throughout the concentration range explored. This leads to two important conclusions: first, the presence of carbon has little effect on the existing structural defects, or on the bond passivation due to hydrogen; second, one can rule out the possibility that tail states are involved in the low-energy absorp-

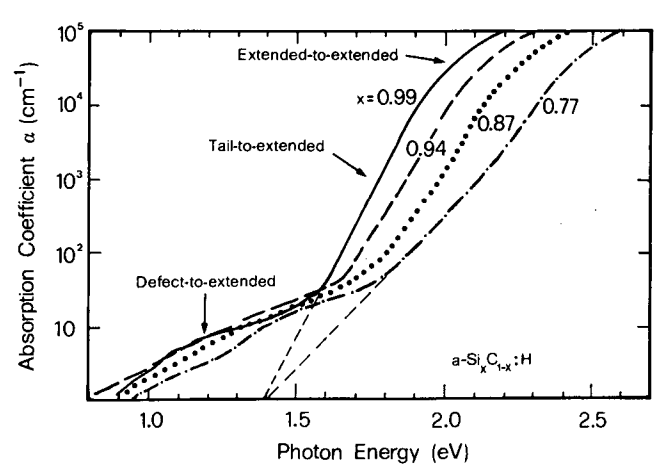

Figure 20. Absorption spectra of *a*-Si_xC_{1-x}:H alloys of different composition. (XBL 851-9704)

tion region because their increased density for larger C content would be reflected in stronger transition rates at those energies. The integrated absorption in the low-energy region is therefore a true measure of defect density.

Corresponding experimental results for the a-Si_xGe_{1-x}:H alloy are reported in Fig. 21. We shall stress only the significant differences. (1) The Urbach characteristic energy E_o increases with germanium content, but not as effectively as in a-SiC:H. Moreover, the tail is soon ill-defined for the reason discussed in (2) below, so that E_o is almost certainly overestimated. (2) The defect state density is higher than in a-SiC:H. It can be measured with some accuracy only for the lowest Ge content sample; its determination is otherwise made difficult by serious overlap with the Urbach tail. The values found are consistent with the silicon dangling-bond density found in the same samples by ESR. However, for $x \lesssim 0.60$, ESR predicts a higher density of Ge-related dangling bonds—10^{18} cm^{-3} and above. These states apparently are not optically active in the same energy range as Si dangling bonds but are closer to the gap. Figure 22 has been obtained by additively superimposing the Si and Ge dangling-bond spectra and the alloy bands. Because of their position in the upper half of the bandgap, above Fermi level, Ge dangling bonds can only be final states for transitions from the valence continuum. The minimum energy for these is about 1.1 eV, which already falls over the Urbach tail. This explains why in a-SiGe the latter is ill-defined for $x \leqslant 0.60$.

We now proceed to account for the Urbach tail broadening observed in the alloys in terms of compositional disorder. The appearance of an exponential tail below the fundamental threshold is due to

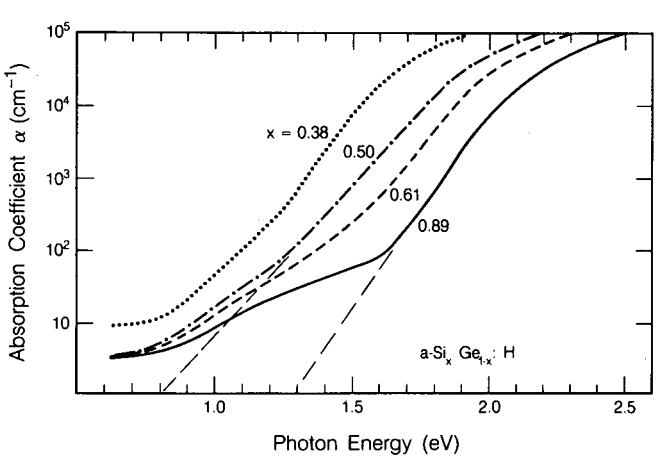

Figure 21. Absorption spectra of a-Si_xGe_{1-x}:H alloys.
(XBL 851-9705)

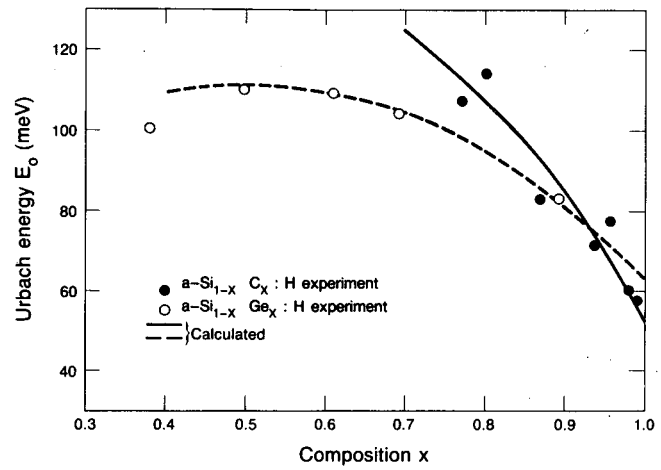

Figure 22. Urbach characteristic energy as deduced from PDS spectra and as calculated by a model assuming a Gaussian bandgap due to compositional disorder.
(XBL 8412-6457A)

the definition of local gap values over regions comparable to the phonon coherence length. The tail states are in a sense "pulled out" of the band continua. We extend the model to the alloys by taking a characteristic Urbach energy E_o that results from the sum of three contributions:

$$E_o = E_T + E_X + E_c$$

$$= K[\langle U^2\rangle_T + \langle U^2\rangle_X] + E_c \quad , \qquad (12)$$

where K is an appropriate quadratic deformation potential of the bandgap and the $\langle U^2\rangle$'s are the mean-square deviations of atoms from an ideally ordered configuration, respectively due to thermal and structural disorder. E_c is the added term from compositional disorder, due to potential fluctuations associated with the heterobonds. We take the $\langle U^2\rangle_T$ and $\langle U^2\rangle_X$ terms as constants; in other words, we assume that structural disorder and phonon effects are comparatively unaffected by the inclusion of carbon or germanium. A measure of the third term in Eq. (12) is then given by the gap spreading which stems from local fluctuations in the alloy composition. If these are Gaussian, as in the case of a-Si_xC_{1-x}:H, where the Si and C atoms are randomly distributed throughout the film without chemical ordering, Urbach tailing is expected. The probability of finding the local composition y in a cell containing n atoms for an alloy of given x, is:

$$P(y) \propto e^{-\frac{n(y-x)^2}{2x(1-x)}} \quad , \qquad (13)$$

whose full width at half maximum is:

$$\Delta = 2\,\frac{2\ln 2x(1-x)^{1/2}}{n} \quad . \tag{14}$$

A measure of the bandgap spreading around $E_g(x)$ is given by:

$$\Delta E_g = \frac{dE_g}{dx}\,\Delta \quad ,$$

where (dE_g/dx) is the experimental x range. We assume $E \approx f\,\Delta\,E_g$, where f is a suitable coupling factor. We collect the prefactors into a single constant:

$$A = \frac{8\ln 2^{1/2}}{n} \quad ,$$

and try to fit the experimental data (Fig. 22) by means of the equation:

$$E_o = E_T + E_X + A[x(1-x)]^{1/2}\,\frac{dE_g}{dx} \quad . \tag{15}$$

The best fitting is obtained for $A = 0.106$ for a-SiC and 0.192 for a-SiGe, and $E_T + E_X = 34$ meV in both cases. If we take $f \approx 1$, i.e., the gap spreading does directly add to the Urbach energy, the A value gives $n \approx 150$ for the number of the sampled atoms in SiGe and $n \approx 490$ in SiC, which fit respectively in spheres of radii approximately 8 and 12 Å. These values are probably closer to the average localization length of the tail states than, for instance, to excitonic radii. The agreement of this model with the experimental data is particularly good.

Liquid Crystal Research

The liquid-crystalline state of matter is characterized by a spontaneous anisotropic order and by fluidity. The anisotropic order leads to anisotropy in the physical properties of the medium, and the fluidity makes it easily susceptible to external perturbations in the form of electric or magnetic fields, temperature, or pressure. In addition, we have demonstrated that certain gaseous organic pollutants change the liquid-crystalline structure. This change, which is readily detectable, was the basis for the development of a sensitive (10^{-6}) personal dosimeter for exposure to organic chemicals. Our current research focuses on the basic physics of the liquid-crystalline state to lay the groundwork for further applications of this class of materials.

*Two-Dimensional Phase Transition in Lyotropic Liquid Crystals**

The nature of phase transition in a monolayer of lecithin (DPPC) at the water-oil interface has been investigated using photon correlation spectroscopy (Fig. 23). We observe the following results:

Main Transition (LE/LC). The "main transition" is the large flat region shown in Fig. 24. We believe this region represents either a weak first-order or first-order phase transition. There clearly seems to be only one slope discontinuity, so the weak first-order transition seems more likely. This would be driven by chain melting and should not be of the Halperin-Nelson type because of the large entropy involved in the chain's degrees of freedom. The nearly zero slope is also consistent with a weak first-order transition. Presumably, the difference between air-water and oil-water isotherms is due to the size of the cooperative domains.

Second Phase Transition. We believe that we have also seen evidence of a second phase transition at lower areas. This may be related to the "pretransition" observed in bilayer stacks. This transition could possibly correspond to the elimination of a chain tilt in the region between the two transitions. It is also not likely to be of the Halperin-Nelson type since large viscosities are observed for pressures above the main (LE/LC) transition in lecithin monolayers.

We believe this is a real effect, since the flat region, the increase in transversal viscosity, and the decrease in slope all occur at the same region of the isotherm. Since the photon correlation is a local probe, a leak would not explain the increase in instrumental linewidth. Film collapse is unlikely because the size of the hysteresis indicates collapse did not occur until much later. Also, no evidence of a leak was observed during the course of the experiment. At very high pressures, above the second flat region, the high signal-to-noise ratio allowed rapid measurements, but total times of 5 minutes between points were still maintained since one could easily see that the film took ~3 minutes to "relax" to its final value.

*Complete version to be submitted to *Physical Review Letters.*

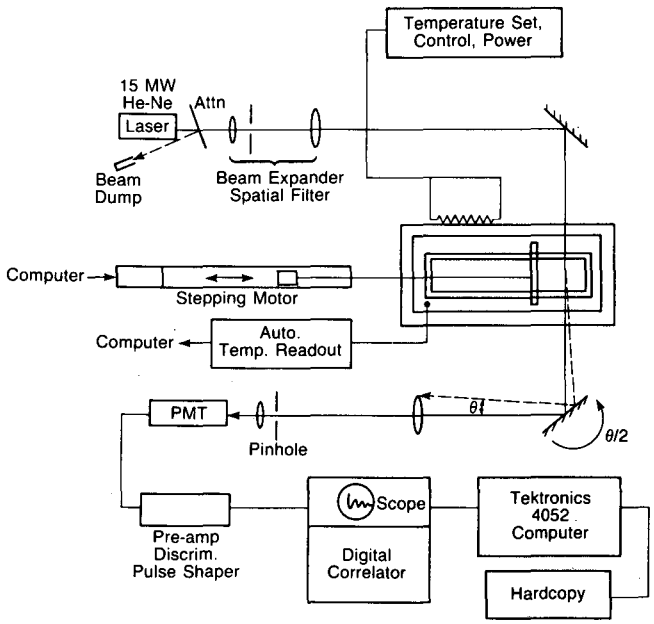

Figure 23. Experimental setup for a investigation of phase transition in a liquid-crystal monolayer (lecithin), using photon correlation spectroscopy. (XBL 846-10616)

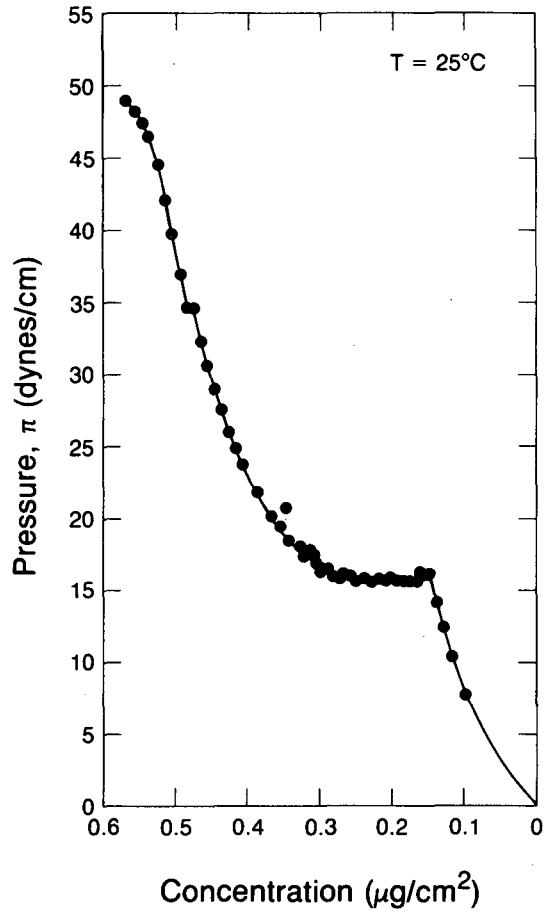

Figure 24. Lecithin (DPPC) isotherm at water-dodecane interface. (XBL 846-10640)

PLANNED ACTIVITIES FOR FY 1985

In laser spectroscopy, our goals will be to develop novel techniques and to exploit advanced applied physics concepts to the ultrasensitive measurements of minute optical absorption and vibrational spectra of gases, liquids, and solids. The emphasis will continue to be on unambiguous remote sensing of atmospheric constituents of laser photothermal spectroscopy and detection. Pulsed photothermal displacement spectroscopy will continue to be studied, and extensions of this technique for the study of liquids will be devised. Nonlinear photoacoustic and photothermal spectroscopy of gases will be initiated.

Research on amorphous semiconductors will focus on the physics of defects in hydrogenated amorphous silicon and germanium. The elucidation of the nature of the metastable photoinduced defects in amorphous silicon will continue to be of interest. A new research direction is the physics of photovoltaic devices.

Another relatively new activity is the investigation of the properties of semiconductor surfaces and interfaces. Processes at the liquid-semiconductor and gas-semiconductor interfaces will also be studied.

Finally, we will continue our research on laser physics and technology, with the goal of achieving widely tunable, high-average-power pulses a few femtoseconds wide. Another goal is to continue exploiting the waveguide laser configuration we have developed.

Rapid Estimation of Organic Nitrogen in Oil Shale Wastewaters*

C.G. Daughton,[†] *B.M. Jones, R.H. Sakaji, and J.F. Thomas*

Organonitrogen compounds (ONCs) are a predominant class of organic solutes in oil shale process wastewaters.[1–7] These waters also usually contain high concentrations of ammonia, often an order of magnitude greater than the organic-N concentrations.[8] A rapid method for quantifying organic-N within this ammonia matrix would be useful to regulatory agencies for setting monitoring standards, to the synfuels industry for routine monitoring, and to researchers studying waste treatment processes.

Quantitation of total nitrogen in aqueous solutions is usually done by the time-consuming, wet-chemical Kjeldahl method.[9] For organic-N, however, a predistillation step is required to remove endogenous, free ammonia from the sample. In addition, the problems with determining organic-N by the Kjeldahl method include (1) hydrolysis of primary amines in the distilland (caused by use of high pH and temperature), (2) unavoidable distillation of volatile ONCs, (3) lengthy analysis time, and (4) incomplete recovery of nitrogen from certain classes of ONCs.

A new method for total-N, one that uses combustion/chemiluminescence (C/CL), has been validated for oil shale wastewaters.[9,10] This method is extremely rapid, with analysis times of about 90 seconds. It has no current use, however, in directly determining organic-N, because a rapid method for selectively removing endogenous ammonia is not available. The disparity of ammoniac-N and organic-N concentrations and the lack of specificity of ammoniac-N assays precludes the indirect determination of organic-N by subtracting ammoniac-N values (obtained by a rapid method such as phenate colorimetry) from total-N values.

We present here two methods, one based on chromatographic "reverse-phase" fractionation (RPF)[11] and the other relying on nonosmotic dissolved gas dialysis (NOGD),[12] for separating ammonia from various fractions of ONCs in oil shale wastewaters. The ammonia-free sample can then be directly analyzed by C/CL, yielding a rapid estimate of organic-N. Both separation methods are more rapid and selective than distillation and do not subject the sample to high temperature.

The organic-N content of nine oil shale retort waters was determined using these two separation methods with C/CL detection; the resulting values were compared with the respective values for organic Kjeldahl nitrogen (OKN). The sequential application of these two separation methods recovered a more complete spectrum of organic-N compounds than either method separately. These data also were used to estimate the minimum percentage of organic carbon in these wastewaters that was associated with nitrogen.

ACCOMPLISHMENTS DURING FY 1984

The major advantage of C/CL in analyzing waters for total-N is speed. A method for removing endogenous ammonia from an aqueous sample so that C/CL can be used to quantify the remaining total-N as an estimate of organic-N should likewise be rapid. For the Kjeldahl method, removal of endogenous ammonia from aqueous samples is accomplished by distillation. This is not a selective process, nor is it rapid. High temperature and pH are required, and the distilland, which contains the ONCs, is not amenable to C/CL analysis because of the extremely high salt and alkali content.

The ammonia-removal methods reported here use two alternative means of separation: reverse-phase partitioning and nonosmotic dialysis. These methods are more rapid than distillation, their selectivity is different, and the products are amenable to C/CL analysis.

Reverse-Phase Fractionation (RPF)

The reverse-phase fractionation protocol is summarized in Fig. 1. Polar solutes (hydrophilic fraction, HpF) remain in the aqueous effluent, while nonpolar solutes (lipophilic fraction, LpF) are retained by the stationary phase. Distribution of

*This work was supported by the Assistant Secretary for Fossil Energy, Office of Oil Shale, Division of Oil, Gas, and Shale Technology of the U.S. Department of Energy under Contract No. DE-AC03-76SF00098.

[†]Sanitary Engineering and Environmental Health Research Laboratory, University of California (Berkeley), Richmond, CA.

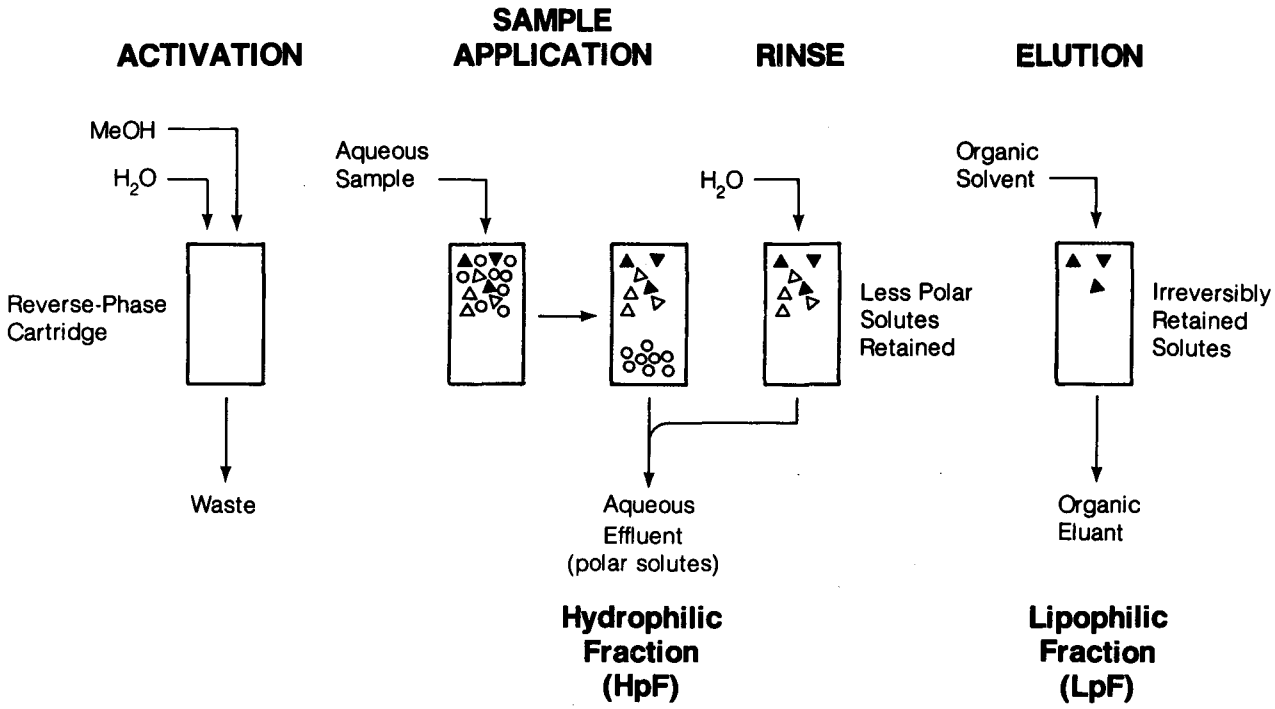

Figure 1. Reverse-phase fractionation scheme for separation of aqueous-waste solutes into hydrophilic (HpF) and lipophilic (LpF) fractions. Solutes belonging to the HpF are represented by open circles. Solutes belonging to the LpF are represented by triangles; filled triangles represent those LpF solutes that are irreversibly retained. (XBL 843-1090)

nitrogenous compounds between the HpF and LpF is determined by their relative polarities. Inorganic nitrogenous compounds (e.g., ammonia) would remain exclusively in the HpF; certain ONCs that contain polar functionalities also pass through in the aqueous effluent. Of the ONCs found in retort waters, those that would remain in the HpF include only lower aliphatic amines and nitriles and oxygenated and hydroxylated aromatic amines. Most N-heterocycles and aromatic amines (the major ONCs that have been identified in retort waters) are retained by the stationary phase.

Analysis of the LpF for total-N by C/CL yields a direct measure of nonpolar organic-N (NPON). These data are listed in Table 1 for each of the nine retort waters and a composite water,[‡] along with the respective values for organic Kjeldahl nitrogen (OKN). For all but two of the waters (Paraho and Oxy-6 gas condensate), the NPON values ranged from 46% to 150% of the respective OKN values, with relative standard deviation (rsd) values less than 4% (excluding Paraho). The average NPON value for the waters (excluding Paraho) was 147 mg/L compared with 311 mg/L for the composite water. The average OKN value was 218 mg/L. Correlation analysis of these NPON and OKN values gave a correlation coefficient of 0.934.

The same RPF procedure has been used for determining the polarity distribution of organic carbon in these waters.[11,13] On the basis of these reported values for organic carbon in the LpF and the assumption that each nitrogen is associated with at most five carbons (e.g., pyridine), then, on the average, at least half of the organic carbon in the LpF is in ONCs.

Nonosmotic Dissolved Gas Dialysis (NOGD)

Microporous fluorinated polymeric membranes were originally developed by W.L. Gore and Associates, Inc. (Elkton, MD); fabrication into tubular membranes for commercial use (as vascular grafts) was accomplished in 1974. These membranes are manufactured by a proprietary process from polytetrafluoroethene (Teflon) film to yield a microporous (heterogeneous) hydrophobic membrane.

[‡]The composite water contained equal volumes of eight of the waters; Paraho was excluded from the composite and from the calculations because of its extremely high solute concentration.

Table 1. Organic Kjeldahl nitrogen (OKN), nonpolar organic nitrogen (NPON), nonvolatile organic nitrogen (NVON), and nonpolar/nonvolatile organic nitrogen [(NP&NV)ON] values for nine oil shale process waters and a composite.

Process water	OKN	rds (%)	NPON	rsd (%)	NVON	rsd (%)	(NP&NV)ON[a]
Paraho	4299	1.8	645	5.7	4839	1.1	5072
Composite	652	1.0	311	1.6	766	1.2	860
150-Ton	541	3.4	295	2.7	587	3.7	671
S-55	372	0.9	172	0.5	414	1.5	569
TOSCO HSP	305	1.2	236	1.9	470	1.9	484
Geokinetics	194	3.4	133	3.2	242	4.1	245
Oxy-6 RW	183	3.0	159	1.7	218	0.5	208
Omega-9	112	0.9	81	2.0	100	2.9	203
Oxy-6 GC	21	1.4	79	1.2	30	17.9	133
Rio Blanco sour	14	4.8	21	2.9	17	2.3	66
Average[b]	671		na[c]		769		850
Average[d]	218		147		na		na

[a]See Fig. 2.

[b]Mean for nine waters, excluding Composite.

[c]Not applicable; Paraho not used in Composite.

[d]Mean for eight waters, excluding Composite and Paraho.

Although its effective pore size is about 2.0 μm, the membrane's extreme hydrophobicity prevents the passage of liquid water (i.e., osmosis cannot occur). Therefore, the passage of nonvolatile aqueous solutes is also prevented. Gases, however, can rapidly permeate by diffusion through large, gas-filled pores, as opposed to solvation in the membrane matrix itself—the process that occurs with nonporous (homogeneous) membranes such as silicone elastomer.[14]

For the preferential separation of ammonia from ONCs in an aqueous matrix, the pH is increased to 10.5 so that dissolved ammonia gas is favored over ammonium ion. Samples are placed in tubular microporous Teflon membranes, which are then sealed. The dialysis solution, external to the Teflon membrane, is acidified to protonate ammonia permeating the membrane; this maintains the concentration gradient of ammonia across the membrane, a condition necessary for driving the permeation process. The dialyzed sample can then be analyzed for total-N. The resulting estimate of organic-N is a direct measure of "nonvolatile" organic-N (NVON). As a tool for quantitatively separating ammonia from organic-N, NOGD relies on the greater "volatility" of ammonia (under the conditions of the dialysis process) compared with the ONCs.

The reproducibility of NOGD was assessed with triplicate determinations of NVON for each of 10 dialyzed samples of composite water. The mean NVON concentration was 763 mg/L, and the rsd was 1.95%. This value agrees remarkably well with the average NVON value of 769 mg/L obtained for the nine constituent oil shale wastewaters (Table 1).

The NVON data for each of the nine retort waters and the composite are listed along with the respective OKN values in Table 1. For all but one of the waters (TOSCO HSP), the NVON values ranged from 89% to 143% of the respective OKN values, with rsd values less than 5% (excluding Oxy-6 gas condensate). The average NVON value for the waters was 768 mg/L, compared with 766 mg/L for another sample of composite water. The average OKN value was 671 mg/L. Correlation analysis of the NVON and OKN values gave a correlation coefficient of 1.000.

Using the dissolved organic carbon values for these waters[15] and their NVON values, and assuming that each nitrogen is associated with at most five carbons, we find that, on the average, more than half of the organic carbon is in ONCs. This agrees with the analogous calculations using the OKN and NPON values. The extremely high correlation of NVON and OKN strongly supports at least one of

two possibilities: (1) the major classes of ONCs that are removed during dialysis comprise only a small portion of the number of nitrogenous compounds in retort waters, and (2) some of the same compounds removed during dialysis are also lost during the predistillation step in Kjeldahl analysis.

Combined RPF/NOGD

The sequential application of the two separation methods can yield a more accurate estimate of the actual organic-N concentration than either method separately. The methods were combined by first separating the sample into polar and nonpolar fractions using the RPF procedure. The NPON was determined directly on the LpF, and the HpF was analyzed for NVON (using NOGD) to yield a measure of polar/nonvolatile organic-N, P(NVON). This procedure is conceptually diagrammed in Fig. 2. The sum of these two measurements, (NP&NV)ON, is a more comprehensive measure of organic-N, assuming that NPON and NVON are not identical subsets.

The values obtained by this combined method for nine oil shale wastewaters are listed in Table 1. From Fig. 2, it can be inferred that these values cannot be less than either NPON or NVON (if they comprised identical sets), yet they must be less than the sum of NPON and NVON (if they comprised nonintersecting sets). The results were either equal to or greater than the values obtained by any of the other three methods (NPON, NVON, or OKN). In addition, from the DOC values for these waters[15] and the assumption that each nitrogen is associated with at most five carbon atoms, then on the average, nearly three-fourths of the organic carbon was associated with ONCs. This is a significantly larger percentage than similar calculations using the NPON, NVON, or OKN values and reflects the improved recovery of organic-N by the combined method. Its major disadvantage is the compounding of error.

With either the RPF or NOGD procedure, approximately 40 samples can be fractionated or dialyzed and analyzed in triplicate within 8 hours; each fractionation requires only 5 minutes, each dialysis 20 minutes, and each replicate C/CL determination only 90 seconds. In contrast, 5 hours are required to analyze three samples (in triplicate) by the Kjeldahl method with a 12-place digestion/distillation unit and automated titration.

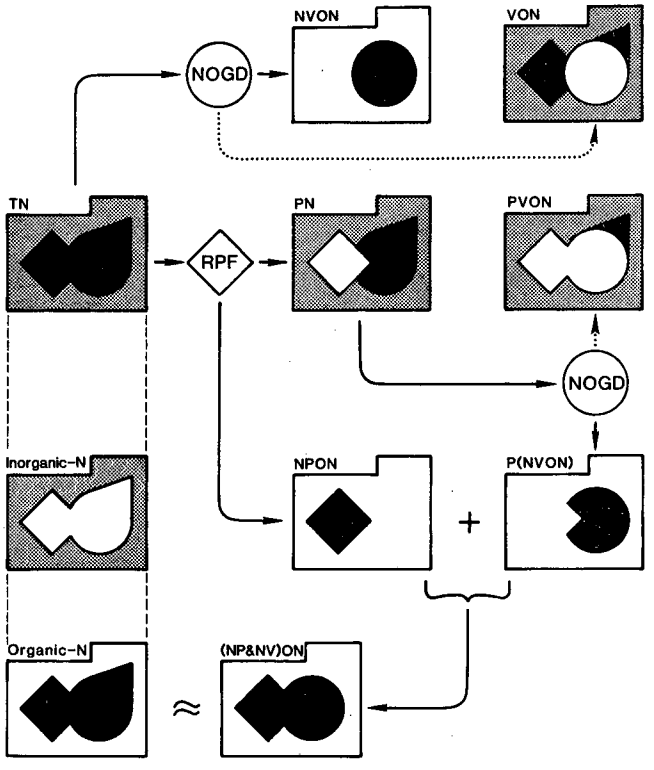

Figure 2. Conceptualized flow chart of organic-N estimation in oil shale retort water by sequential application of two methods for removing ammonia (reverse-phase fractionation, RPF; and nonosmotic dissolved-gas dialysis, NOGD). Labels refer to combined black and stippled regions (except for PVON and VON, which refer only to the black regions; stippled area refers to inorganic-N). Total-N (TN) comprises inorganic- and organic-N. Application of NOGD separates volatile-N from nonvolatile organic-N (NVON; region bounded by circle). Application of RPF separates polar-N (PN) from nonpolar organic-N (NPON; region bounded by diamond). Application of NOGD to the PN fraction yields polar-nonvolatile organic-N, P(NVON); the volatile fraction (polar-volatile organic-N; PVON) is lost (short dotted line). Adding the values obtained for NPON and P(NVON) gives a measure of (NP&NV)ON (i.e., organic-N that comprises either NPON or NVON); intersection of the circle and diamond represents organic-N that is both nonpolar *and* nonvolatile. (NP&NV)ON is an estimate of the true organic-N value.
(XBL 8411-4767)

PLANNED ACTIVITIES FOR FY 1985

In FY 1984, three rapid methods for determining organic nitrogen were compared with the standard Kjeldahl method. These methods involved two different principles for separating ammonia from organonitrogen solutes. The organic-N was then quantified as total-N by the rapid method of combustion/chemiluminescence. These methods were evaluated for oil shale wastewaters. In FY 1985, these methods will be more extensively evaluated for use in waste-treatment and environmental-fate research to assess the removal and disposition of organonitrogen compounds.

REFERENCES

1. Hawthorne, S.B. and Sievers, R.E. (1984), "Emission of Organic Air Pollutants from Shale Oil Wastewaters," *Environ. Sci. Technol. 18*, p. 483.
2. Leenheer, J.A., Noyes, T.I., and Stuber, H.A. (1982), "Determination of Polar Organic Solutes in Oil-Shale Retort Water," *Environ. Sci. Technol. 16*, p. 714.
3. Pellizzari, E.D., *et al.* (1979), "Identification of Organic Components in Aqueous Effluents from Energy-Related Processes," in *Measurement of Organic Pollutants in Water and Wastewater*, C.E. Van Hall, Ed.; American Society for Testing and Materials, Denver, CA; ASTM STP 686, p. 256.
4. Raphaelian, L.A. and Harrison, W. (1981), *Organic Constituents in Process Water from the In-Situ Retorting of Oil from Oil-Shale Kerogen*, Argonne National Laboratory report ANL/PAG-5.
5. Richard, J.J. and Junk, G.A. (1984), "Steam Distillation, Solvent Extraction and Ion Exchange for Determining Polar Organics in Shale Process Waters," *Anal. Chem. 56*, p. 1625.
6. Sievers, R.E., Conditt, M.K., and Stanley, J.S. (1981), "Speciation of Organic Compounds and Trace Elements in Oil Shale Wastewaters," in *Environmental Speciation and Monitoring Needs for Trace Metal-Containing Substances from Energy-Related Processes*, National Bureau of Standards, Gaithersburg, MD, NBS Special Publications No. 618, p. 93.
7. Stuber, H.A. and Leenheer, J.A. (1983), "Selective Concentration of Aromatic Bases from Water with a Resin Adsorbent," *Anal. Chem. 55*, p. 111.
8. Daughton, C.G., Ed.(1984), *A Manual of Analytical Methods for Wastewaters*, 2nd ed., Appendix A, LBL-17421 (available from the National Technical Information Service as NTIS DE84015967).
9. Jones, B.M., Harris, G.J., Thomas, J.F., and Daughton, C.G. (1984), "Quantification of Total and Organic Nitrogen in Oil Shale Wastewaters," in *Applied Science Division FY 1983 Annual Report, Environmental Research Program Chapter*, LBL-17073, p. 4–31.
10. Jones, B.M., Harris, G.J., and Daughton, C.G. (1984), "Nitrogen: Kjeldahl and Combustion/Chemiluminescence," in *A Manual of Analytical Methods for Wastewaters*, 2nd ed., C.G. Daughton, Ed.; LBL-17421, Chapter V (NTIS DE84015967).
11. Daughton, C.G., Jones, B.M., and Sakaji, R.H. (1984), "Rapid Fractionation of Aqueous Samples by Reverse-Phase Partitioning," in *A Manual of Analytical Methods for Wastewaters*, 2nd ed., C.G. Daughton, Ed., LBL-17421, Chapter I (NTIS DE84015967).
12. Daughton, C.G. and Sakaji, R.H. (1984), "Separation of Ammonia from Organic Nitrogen Using Tubular Microporous Polytetrafluoroethene Membranes: Nonosmotic Dissolved-Gas Dialysis," in *A Manual of Analytical Methods for Wastewaters*, 2nd ed., C.G. Daughton, Ed., LBL-17421, Chapter II (NTIS DE84015967).
13. Healy, J.B., Jr., Jones, B.M., Langlois, G.W., and Daughton, C.G. (1983), "Biotreatment of Oil Shale Wastewaters," in *Sixteenth Oil Shale Symposium Proceedings*, J.H. Gary, Ed., Colorado School of Mines, Golden, CO, p. 498.
14. Yasuda, H. and Peterlin, A. (1973), "Diffusive and Bulk Flow Transport in Polymers," *J. Appl. Polym. Sci. 17*, p. 433.
15. Langlois, G.W., Jones, B.M., Sakaji, R.H., and Daughton, C.G. (1984), "Quantitation of Carbon in Oil Shale Process Wastewaters: Coulometry Coupled with UV-Peroxydisulfate and High-Temperature Oxidation," *J. Test. Eval. 12*, p. 227.

Removal of Ammonia from Wastewaters Using Tubular Microporous Polytetrafluoroethene Membranes*

R.H. Sakaji, J.F. Thomas, and C.G. Daughton[†]

A membrane separation process for separating dissolved ammonia from wastewaters[1] is being studied as an alternative to conventional ammonia removal techniques (gas stripping, ion exchange, biological oxidation). Wastewater is pumped through a tubular, microporous polytetrafluoroethene (Teflon) membrane submerged in an acid solution. This membrane prevents the contact of two miscible solutions, while allowing the selective transport of dissolved ammonia through the membrane. The process is termed "nonosmotic dissolved-gas dialysis" (NOGD). Although it is similar to dialysis, liquid water does not permeate the membrane (i.e., osmosis does not occur). This process is also being used to selectively separate ammonia from organic nitrogen so that organic-N can be quantified by a rapid method selective only for total-N (see preceding article by Daughton *et al.*).

Synthetic, selectively porous polymeric membranes have been used for many types of separation processes. These include micro- and ultra-filtration, reverse osmosis, gas-phase separation, and dialysis. The selective transport of solutes through polymeric membranes is driven by a concentration or pressure gradient normal to the membrane surface. Dialysis, for example, is driven by a concentration gradient; water diffuses from a solution of lower solute concentration to a more concentrated solution, while solutes flow in the opposite direction. These processes effect separations by one of two mechanisms: (1) selectively passing smaller solutes or particles, while retaining those that are larger (the molecular or particle size cut-offs differ for each process, depending on the nominal pore size of the membrane—from the nanometer range for dialysis to the micrometer range for microfiltration); or (2) selectively transporting those molecules that have a higher rate of permeation within the matrix of the membrane itself (e.g., membrane separation of gaseous mixtures).

*This work was supported by the Assistant Secretary for Fossil Energy, Office of Oil Shale, Division of Oil, Gas, and Shale Technology of the U.S. Department of Energy under Contract No. DE-AC03-76SF00098.

†Sanitary Engineering and Environmental Health Research Laboratory, University of California (Berkeley), Richmond, CA.

None of these membranes, however, can separate dissolved ammonia from an aqueous sample and its associated solutes, because each of them also passes water and low-molecular-weight organic compounds or passes water while retaining most of the solutes. The process reported here uses a new type of membrane to prevent the passage of water while allowing selected solutes to diffuse through the membrane.

ACCOMPLISHMENTS DURING FY 1984

Microporous fluorinated polymeric membranes were developed by W.L. Gore and Associates, Inc. (Elkton, MD); fabrication into tubular membranes for commercial use (as vascular grafts) was accomplished in 1974. The membranes are manufactured by a proprietary process (possibly involving controlled stretching or expanding) of polytetrafluoroethene film (PTFE or polytef; homopolymer of CF_2 units made under a variety of trade names such as Teflon and Fluon) to yield a microporous hydrophobic membrane. The porous structure of the wall of a sample of Gore-Tex microporous PTFE tubing is shown in the scanning electron micrographs in Fig. 1. Strands of PTFE bridge fissures and run parallel to the centerline of the tubing; the fissures are aligned around the circumference of the tubing. As these micrographs show, the pores are not hollow cylinders (such as those in polycarbonate membrane filters) that run through the tubing wall; rather, the bridges of PTFE themselves act like a sieve through which the permeants must pass.

Tubular, microporous PTFE membranes have several qualities that lend themselves to degassing aqueous samples for chemical analysis: (1) relatively large pore size (2.0 or 3.5 μm) and porosity (50%), allowing high permeation rates; (2) flexibility, which allows for ease of coiling; (3) availability in a variety of internal diameters; (4) high ratio of membrane surface area to contained volume; (5) adaptability to continuous-flow applications; (6) extreme chemical inertness and thermal stability; and (7) extreme hydrophobicity (water is unable to displace air from the voids in the membrane unless a water-miscible organic solvent is first used to "wet" the surface; the solvent displaces air from the pores and allows water to then enter the pores). Even though these tubular membranes have rather large pore sizes, their hydrophobicity blocks the passage of liquid water; this means that the passage of nonvolatile solutes is also prevented. Gases, however, can rapidly permeate, because the process involves diffusion through large pores as opposed to solvation in the membrane matrix itself.

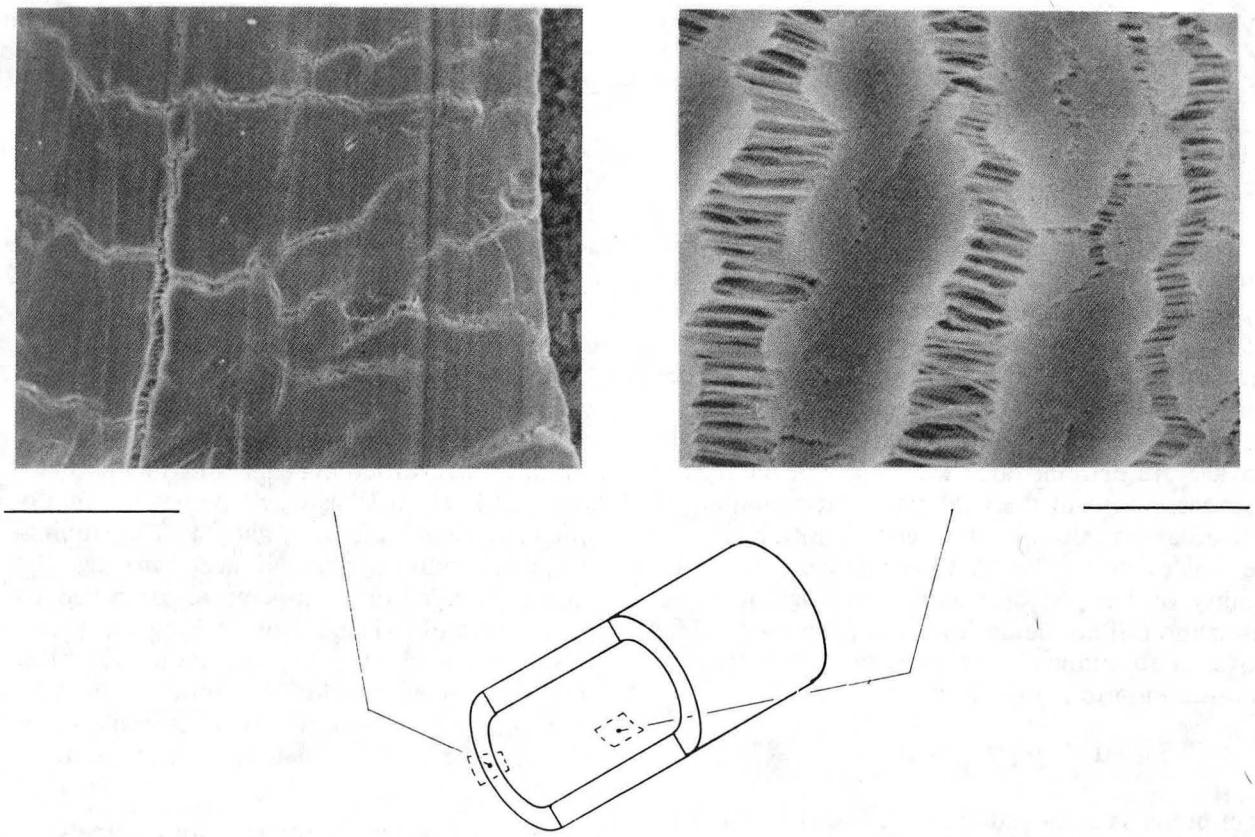

Figure 1. Isometric cutaway of 1-mm i.d. microporous PTFE tubing (0.4-mm wall thickness). Scanning electron micrographs correspond to, left, cross-sectional slice of membrane wall and, right, inner wall surface. In left-hand SEM, the curvature at right edge corresponds to the inner membrane wall. Left bar = 100 μm; right bar = 10 μm. (XBB 846-4306)

Wastewater in the tubular membrane is exposed to the pore spaces that run through the membrane matrix. Ammonia volatilizes from the sample into the pore space and diffuses to the opposite side of the membrane. For the mass transport of dissolved gases to occur, a concentration gradient must be maintained between the inner and outer walls of the membrane. Thus, as ammonia diffuses through the membrane, it must be rapidly removed from the outer surface to maintain the steepest possible concentration gradient. This is most easily accomplished by submerging the membrane in an acid solution. The ammonia permeant then dissolves in this acid solution and reacts with a proton to yield ammonium ion; this ammonium ion solution is termed the "dialysate." This process minimizes the concentration of ammonia external to the membrane. Degassing could also be accomplished by surrounding the membrane with a heated gaseous phase, but significant quantities of water and associated organic material would also volatilize through the membrane. An aqueous solution of high-boiling acid, such as sulfuric acid, simplifies recovery of ammonia (as ammonium sulfate) and minimizes the escape of other materials.

For wastewater treatment, a likely design would use microporous PTFE tubing in a jacketed flow-through apparatus so the acid solution can flow in a direction opposite (i.e., countercurrent) to that of the wastewater. The wastewater could flow on either the inner or outer side of the tubing, and the acid solution would pass on the opposite side. The bulk flow of the wastewater and acid solution would be tangential to the membrane surface, and the dissolved gases would diffuse in a direction normal to the membrane surface. The surface area of membrane required for a specified degree of ammonia removal would be determined by the rate of wastewater generation in the retort process. By adjusting process variables (e.g., temperature or wastewater pH), the rates of removal can be optimized to accommodate variations in wastewater flow.

Variables that affect the permeation rate of ammonia through the tubing are (1) temperature and pH of both the sample and dialysate, (2) thickness of the membrane walls, (3) internal diameter (as it affects the surface-area:volume ratio), (4) degree of anisotropy (i.e., the gradient of transport properties through the membrane), and (5) the pressure across the membrane. Increased temperature lowers the solubility of ammonia in the wastewater, decreases the pK_a of the ammonia–ammonium ion reaction (causing a shift in the equilibrium to favor the formation of dissolved ammonia gas), and increases the diffusivity.

The effects of temperature and pH on ammonia removal were demonstrated during the development of a process used in the analytical determination of nonvolatile organic nitrogen concentration in oil shale wastewaters.[2] At elevated temperatures, the solubility of NH_3 is decreased, favoring the rapid volatilization of ammonia from the wastewater. The removal of ammonia also requires the dissociation of ammonium ion to ammonia gas:

$$NH_4^+ \rightleftarrows NH_3^+ + H^+ \quad .$$

As ammonia is removed from the wastewater, this reaction is pulled to the right, producing a proton and dissolved ammonia gas. If the wastewater pH is sufficiently below the pK of this reaction (e.g., 9.3 at 25°C), then the ionized, nonvolatile ammonium form will predominate. The buffering capacity of the water must therefore be sufficient to maintain the alkaline conditions that favor the formation of ammonia over ammonium ion. In addition to lowering the solubility of the deprotonated ammonia species, increased temperature shifts the equilibrium of the dissociation reaction to the right (for any set pH). These two effects act synergistically to promote the degassing of free ammonia.

Once the pH and temperature are optimized, the physical process of transporting the dissolved ammonia from the wastewater to the dialysate becomes important. The resistance to mass transfer in the acidic dialysate can be assumed to be negligible, since the reaction of ammonia to ammonium ion in the dialysate is very fast. There would be a steep gradient of ammonia concentration between the inner membrane wall and the dialysate. Mass transfer would therefore be limited by one of the following steps: (1) diffusion of ammonia from the bulk wastewater to the inner wall of the membrane, (2) transfer through the liquid-gas interface into the pore space, (3) diffusion through the pore space, or (4) passage through the gas-liquid interface at the external membrane wall.

Experimental work on this separation process began with continuous-flow experiments on two oil shale wastewater samples and an ammonium hydroxide solution. Samples of PTFE tubing (1-mm i.d. with a 0.4-mm wall thickness) were obtained from Michael R. Davis of W.L. Gore and Associates. The retort waters were pressure-filtered through 0.4-μm pore-diameter membrane filters to remove particulates. The two retort waters were Oxy-6 (Occidental Oil Shale, Inc., Logan Wash Site, Colorado; Burn #6) and Paraho (Development Engineering, Inc., Anvil Points, Colorado). The ammonium hydroxide solution was prepared in a 1-*N* NaOH solution. The waters were pumped through three different lengths of membranes (52.3, 61.4, and 11 cm), using a peristaltic pump with silicone-rubber tubes. The PTFE tubing was wrapped around a stainless steel wire cage that was then submerged in a temperature-controlled 1-*N* sulfuric acid bath. The silicone tubing from the pump was submerged in a water bath to preheat the influent wastewater; for the ammonium hydroxide solution, the silicone tubing was replaced with a 131-cm length of coiled 0.17-cm o.d. stainless steel tubing.

Retort water samples were analyzed for ammonia by phenate colorimetry.[3] Ammonia removal from the ammonium hydroxide samples was quantified by direct analysis for total nitrogen by combustion/chemiluminesence (C/CL)[4]; use of the C/CL method on the retort water samples would have yielded a measure of total nitrogen.

Samples of Oxy-6 retort water were treated in continuous-flow mode at two temperatures. Since flow rate and PTFE tubing length determine the residence time of the wastewater, the liquid hourly space velocity (LHSV; volumetric flow rate divided by the reactor volume) was used to compare the results of studies done at different flow rates. At 50°C with an LHSV of 0.20 min^{-1}, ammonia removal was 93%. When the temperature was increased to 88°C and the LHSV increased to 2.08 min^{-1}, the ammonia removal was 82%. This increase in LHSV lowered the mean residence time by an order of magnitude, but the efficiency of removal dropped by only 12%. The increased temperature did not sufficiently decrease the ammonia solubility to fully offset the effect of increased LHSV. The significance of changing the LHSV was demonstrated on an ammonium hydroxide solution at 30°C. Increasing the LHSV fivefold decreased the removal efficiency by almost half. As the LHSV was increased from 0.56 to 2.56 min^{-1}, the removal of ammonia decreased from 95% to 48%.

Studies done with Paraho retort water indicate that the degassing of retort waters is a complex process. Both physical and chemical factors play a role in ammonia removal. When treated under conditions similar to those used for Oxy-6 retort water, Paraho retort water could not be degassed as efficiently. Since Paraho has an ammoniac-N concentration of nearly 25,000 mg/L, the total-nitrogen values for the treated effluent indicated that a significant quantity of ammonia remained in the effluent at the low LHSV of 0.11 min^{-1} (see Table 1). Effluent samples indicated that the pH had dropped below 7.0. In contrast, in Oxy-6 retort water after treatment, the pH remained above 8.0. This was probably due to the stronger carbonate buffering system of Oxy-6 retort water. The titration of bicarbonate to carbonic acid requires one proton. Therefore, if the molar ratio of NH_4^+ to inorganic-C is greater than one, the buffering provided by the bicarbonate will be consumed by the production of acid from the deprotonation of ammonium ion to ammonia. Titration of the buffering system will cause the pH to drop, preventing the formation of ammonia gas. The difficulty of degassing Paraho retort water was probably associated with this chemical problem since the molar ratio of NH_4^+-N to inorganic-C was 69 (at 30°C). In contrast, the molar ratio for Oxy-6 retort water was 0.66. The higher pH maintained by the carbonate buffering system favored formation of ammonia gas over ammonium ion. The efficiency of the degassing process could therefore be maintained throughout the course of treating Oxy-6 retort water, but not for Paraho.

To compensate for the low carbonate concentration of Paraho retort water, its pH was elevated with a buffer. The water was diluted with an equal volume of 2 *M* sodium carbonate solution, and the LHSV was increased to 0.35 min^{-1}. This increased the efficiency of ammonia removal (Table 1); the concentration of total-N in the effluent was reduced to 25% of the effluent total-N concentration obtained from the unbuffered water. The total-N remaining in the effluent was almost equal to the nonvolatile organic-N concentration (4,839 mg/L).[5]

Table 1. Effect of buffering on removal of ammonia from Paraho retort water by NOGD.

Sample	Liquid hourly space velocity (min^{-1})	Temperature (°C)	Total nitrogen concentration (mg/L)	
			Influent	Effluent
Unbuffered	0.11	86	33,729	20,913
Buffered	0.35	88	32,168	4,932

From these preliminary studies, it is apparent that three physical variables (temperature, pH, and LHSV) affect the efficiency of this nonosmotic dialysis process. Other factors such as the chemical composition (e.g., pH and alkalinity) of the wastewater also play a role in determining the efficiency of ammonia removal.

PLANNED ACTIVITIES FOR FY 1985

Currently, PTFE tubing is relatively expensive (several dollars per foot); this is partly because of its limited commercial availability. Only two other problems would be anticipated in applying the PTFE-NOGD process to oil shale wastewaters: (1) deposition of tarry materials on the inner walls of the membrane and (2) the low physical strength of the membrane. The latter may necessitate operation at lower pressures (with a maximum of about 13 psi), which in turn would limit the length of tubing that could be used. Biofouling during operation at low temperature and fouling by tarry materials also need to be investigated as possible operational limitations. These questions will be addressed in future experiments. In addition, the feasibility of treating other ammonia-containing wastewaters will be investigated.

REFERENCES

1. Daughton, C.G. and Sakaji, R.H. (1984), "Removal of Ammonia from Wastewaters Using Tubular Microporous Polytetrafluoroethene Membranes: Nonosmotic Dissolved-Gas Dialysis," Lawrence Berkeley Laboratory report LBID-925.
2. Daughton, C.G. and Sakaji, R.H. (1984), "Separation of Ammonia from Organic Nitrogen Using Tubular Microporous Polytetrafluoroethene Membranes: Nonosmotic Dissolved-Gas Dialysis," in *A Manual of Analytical Methods for Wastewaters*, 2nd ed., C.G. Daughton, Ed., LBL-17421, Chapter II (available from the National Technical Information Service as NTIS DE84015967).
3. Daughton, C.G., Cantor, J., Jones, B.M., and Sakaji, R.H. (1984), "Ammonia: Colorimetric and Titrimetric Quantitation," in *A Manual of*

Analytical Methods for Wastewaters, 2nd ed., C.G. Daughton, Ed., LBL-17421, Chapter IV (NTIS DE84015967).
4. Jones, B.M., Harris, G.J., and Daughton, C.G. (1984), "Nitrogen: Kjeldahl and Combustion/ Chemiluminesence," in *A Manual of Analytical Methods for Wastewaters*, 2nd ed., C.G. Daughton, Ed., LBL-17421, Chapter V (NTIS DE84015967).
5. Daughton, C.G., Ed. (1984), *A Manual of Analytical Methods for Wastewaters*, 2nd ed., Appendix A; LBL-17421 (NTIS DE84015967).

Identification and Correlation of Volatile Components in Retort Wastewaters*

L. Hunter, P. Persoff, J.F. Thomas, and C.G. Daughton[†]

A major problem in the commercialization of the oil shale resources of Colorado, Utah, and Wyoming is the development of environmentally acceptable practices for the disposal of the two major by-products of the surface retorting process: retorted (spent) shale and cogenerated retort wastewater. Spent shale would be disposed and compacted in layered "lifts" at on-site dumpsites. To achieve the desired degree of compaction for the physical stability of the lifts, it is necessary to wet the spent shale to an optimal water content of about 15%. The limited water resources of the oil shale region would necessitate the use of process wastewaters to supply at least a portion of this moisturizing water. A potential advantage of this disposal strategy (called codisposal) is that it would eliminate the problem of disposing of contaminated wastewater. For this codisposal scheme to be acceptable, however, it must meet a number of criteria for minimizing its negative environmental effects on a local and regional basis. Our area of interest is the evaluation of the volatile emissions that may occur during the dumping, compacting, and weathering of the codisposed materials. With no pretreatment of the wastewater, these emissions would comprise large quantities of ammonia and a wide variety of organic compounds. Our primary goals are to identify the mechanisms that control the release of volatile compounds, to identify some of the components that could contribute to the hazardous or malodorous nature of these emissions, and to quantify the release of volatile compounds to the atmosphere.

*This work was supported by the Assistant Secretary for Fossil Energy, Office of Oil Shale, Division of Oil, Gas, and Shale Technology of the U.S. Department of Energy under Contract No. DE-AC03-76SF00098.

[†]Sanitary Engineering and Environmental Health Research Laboratory, University of California (Berkeley), Richmond, CA 94804.

ACCOMPLISHMENTS DURING FY 1984

Headspace analyses were carried out on the various wastewater and reference mixture samples by placing the samples in sealed vials at 65°C and withdrawing a portion of the headspace with a gas-tight syringe for analysis by capillary gas chromatography. The samples were analyzed on a 30-m fused-silica Carbowax column, programmed from 30°C to 220°C at 4°C/minute. Peaks were detected either with a flame ionization detector (FID) or with a nitrogen-sensitive flame thermionic detector (FTD). Peak correlations between samples were based on a statistical comparison of their retention indices, using an in-house computer program, Chromscan. Retention indices were calculated using two nitrogen heterocyclic compounds, pyridine and quinoline, as reference points with index values of 100 and 200, respectively.[1]

FID/FTD Comparison of Headspace Components

Because of their malodorous and potentially hazardous properties, volatile nitrogen-containing compounds (especially nitrogen heterocycles) have been the main focus of our attention. To determine the extent of their presence in volatile emissions from oil shale wastewaters, we have compared headspace chromatograms, using two detectors: a flame ionization detector (FID) and a flame thermionic detector (FTD), which has greatly enhanced sensitivity to nitrogen-containing compounds. In a survey of seven different wastewater samples (Oxy-6 gas condensate, Oxy-6 retort water, Omega-9, Paraho, TOSCO HSP, Geokinetics, and Rio Blanco sour) a major portion of the component peaks was shown to comprise nitrogenous compounds. A typical example, the FID/FTD comparison for Omega-9 (at equivalent attenuations), is shown in Fig. 1. Most of the peaks in the FID chromatogram can be matched

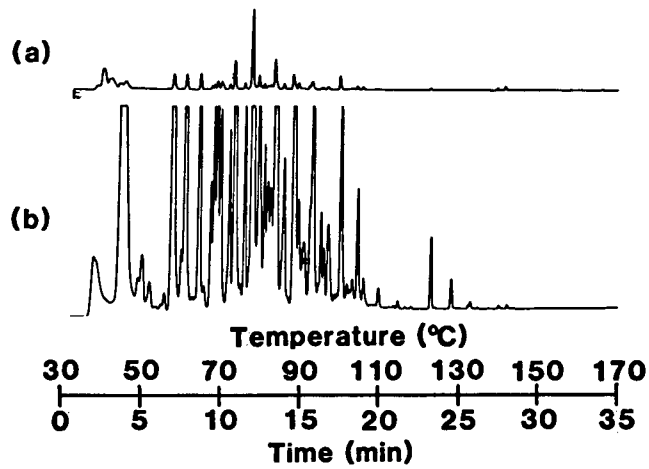

Figure 1. Omega-9 headspace (65°C for 30 min). Comparison chromatograms using different detectors: (a) flame ionization detector (FID) and (b) nitrogen-sensitive flame thermionic detector (FTD). (XBL 8411-4908)

with the much larger peaks, which are presumably nitrogen-containing, in the FTD chromatogram.

Peak Correlations in Seven Wastewaters

A recurring problem in working with waste products from oil shale processing is determining what constitutes a suitable, representative material on which the expenditure of a large amount of research time can be justified. All of the available wastewater (and spent shale) samples are derived from atypical sources such as pilot runs, simulations, and lab-scale retorts. This has been unavoidable since full-scale plants have yet to be operated. Selection of waste samples that are relevant to the future development of an oil shale industry has always been difficult. In this regard, selection of suitable wastewater samples has been of special concern in our investigation of volatile headspace components that might constitute a pollution hazard at oil shale dumpsites.

In our chromatographic examination of seven of these wastewaters (previous section), we have noted a general similarity in the peak patterns, suggesting the presence of many common volatile components (each not necessarily present in the same relative amounts). If this inference could be substantiated, it would indicate that the selection of wastewaters for volatilization studies might not be so critical. A statistical comparison of the headspace chromatograms from the seven wastewaters was therefore carried out to locate peaks in common. Each water was analyzed in triplicate using the FTD detector, and the retention index was computed for each peak. Each peak in one of the samples was compared simultaneously in a series of analysis of variance (anovas) with the nearest retention-index peak in each of the other waters. To assess peak uniqueness and to strengthen peak correlations, the program also checked for possible overlapping correlations, resulting, for example, from two very closely emerging peaks, by extending the anova to include the two nearest-neighbor peaks in the comparison chromatograms. In no instance did this result in any additional (cross) correlations. The seven-water comparison produced 22 correlated peaks that were statistically common to all the headspace samples. These are shown graphically in Fig. 2 (shaded peaks), using the Oxy-6 gas condensate chromatogram as an example. These common nitrogen-containing peaks constituted a majority (55% in Oxy-6 GC) of the total number of detected nitrogen-containing compounds in every water sample. These observations suggest that the selection of a "typical" wastewater sample may not be critical for headspace investigations, except where the relative amounts of the nitrogen-containing volatile components are an important consideration.

Identification of Wastewater Headspace Components Using a Reference Mixture

Neat Reference Mixture

An attempt was made to identify nitrogen heterocycles in wastewater samples by correlating wastewater headspace chromatograms with headspace chromatograms from a neat mixture of 17 reference compounds [Table 1; Fig. 2(b)]. Surprisingly, despite the presence in the reference mixture of many alkylpyridines known to be frequent constituents of oil shale wastewaters,[2] our computer comparison program produced few correlations. Since excellent correlations were obtained when like samples were compared (e.g., different series of reference mixture runs or even wastewater runs), the difficulty appeared to be due to a matrix effect resulting from the great complexity of the wastewater solutes. The wastewater solutes were able to sufficiently modify the properties of the Carbowax capillary column temporarily to produce small but statistically significant changes in component retention behavior relative to the reference samples. In support of this hypothesis, even reference compounds added to the wastewater could not be correlated with the same components in the reference mixture. Further support was adduced from the effect of sample-size reduction on peak correlations. With the relatively simple reference mixture the effect was slight; eight out of ten peaks correlated in a high- versus low-

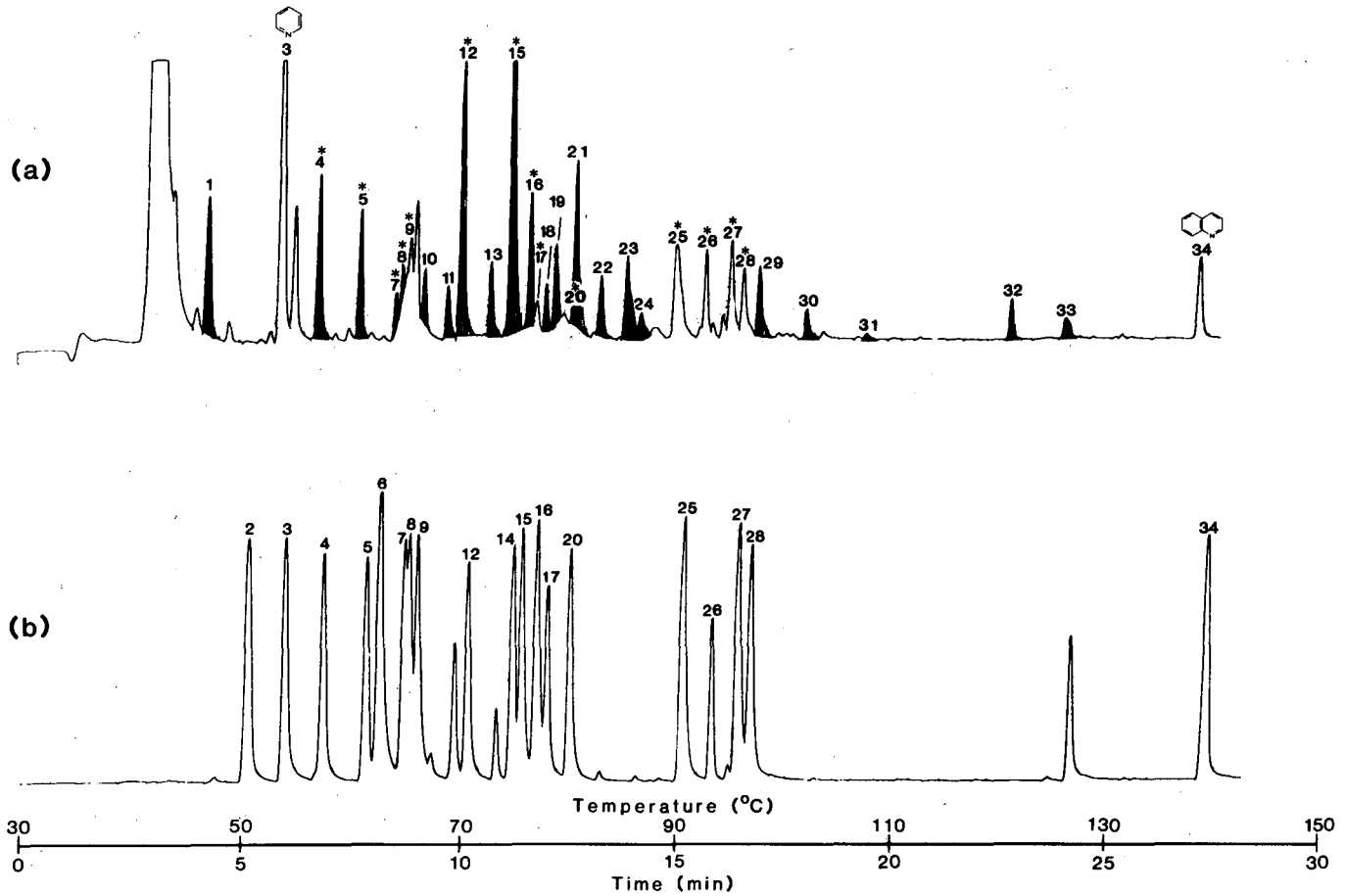

Figure 2. FTD headspace (65°C) chromatograms: (a) Oxy-6 gas condensate; asterisks indicate identified compounds (see Table 1), and shaded peaks indicate compounds common to all seven wastewaters. (b) Neat reference mixture (see Table 1 for compound identification). (XBL 849-4045A)

level (1 to 0.01) comparison. With the complex wastewater headspace, on the other hand, none of nine peaks in a similar comparison were correlated. Presumably, the smaller sample loading had a reduced effect on the Carbowax capillary column that was sufficient to significantly change its retention characteristics vis-a-vis the larger sample. Unfortunately, while these observations provide an insight into the retention behavior of the capillary Carbowax column, operation at lower sample levels does not appear to be a practical solution to the correlation problem, since many peaks become too small to detect above background level.

Reference Mixture Prepared in Wastewater

Preparation of the reference mixture in the same medium present in the wastewater samples, namely the wastewater itself, should minimize sample differences and their effect on peak retention-time behavior. The same series of 17 reference compounds was added to a sample of Oxy-6 gas condensate. Sufficient amount of each reference was added to "swamp" any nearby wastewater headspace peak that might or might not be identical. Triplicate analyses were run, and the computed retention indices for the reference compounds and the unknown wastewater headspace peaks statistically compared. The results (Table 1) showed a much improved correlation. Fourteen of the 17 reference compounds, including all the methyl- and ethyl-pyridine isomers, were correlated with wastewater peaks. Furthermore, since seven of the correlated peaks were among the 22 peaks found to be common to the seven wastewater samples (see above), these compounds (all pyridines) may be presumed to be present in all the waters: 2- and 3- methyl; 2-, 3-, and 4-ethyl; 2,4-dimethyl; and 2,6-dimethyl.

Table 1. Identification of headspace peaks in Oxy-6 gas condensate.

Peak No.	Reference compound	Mean retention index (s)	Identified in Oxy-6 gas condensate
2	1-Methylpyrrole	95.89 (0.087)	nd[a]
3	--Pyridine--	--100--	na[b]
4	2-Methylpyridine	104.08 (0.005)	+
5	2,6-Dimethylpyridine	108.56 (0.094)	+
6	2-Methylpyrazine	109.82 (0.061)	+
7	2-Ethylpyridine	112.46 (0.140)	+
8	3-Methylpyridine	113.23 (0.136)	+
9	4-Methylpyridine	113.83 (0.090)	+
12	2,4-Dimethylpyridine	119.23 (0.140)	+
14	2-*n*-Propylpyridine	123.86 (0.090)	nd
15	3-Ethylpyridine	124.63 (0.139)	+
16	4-Ethylpyridine	126.83 (0.147)	+
17	1,2,5-Trimethylpyridine	127.57 (0.195)	+
20	5-Ethyl-2-methylpyridine	130.27 (0.288)	+
25	4-*t*-Butylpyridine	142.46 (0.104)	+
26	Pyrrole	145.79 (0.123)	+
27	3-Ethyl-4-methylpyridine	148.53 (0.104)	+
28	4-Ethyl-3-methylpyridine	149.93 (0.106)	+
34	--Quinoline--	--200--	na

[a]nd = not detected.

[b]na = not applicable; added as index marker.

PLANNED ACTIVITIES FOR FY 1985

Headspace analysis of retort waters will be continued and extended to investigate retort-water/spent-shale mixtures designed to simulate codisposal of these waste products. The identification and quantification of individual volatile components will continue to be focused on the heterocyclic nitrogenous compounds that are the major contributors to the malodorous and possibly hazardous nature of volatile emissions from the codisposal process.

REFERENCES

1. Novotny, M., Kump, R., Merli, F., and Todd, L.J. (1980), "Capillary Gas Chromatography/Mass Spectrometric Determination of Nitrogen Aromatic Compounds in Complex Mixtures," *Anal. Chem. 52*, p. 406.
2. Hawthorne, S.B. and Sievers, R.E. (1984), "Emission of Organic Air Pollutants from Shale Oil Wastewaters," *Environ. Sci. Technol. 18*, p. 490.

Removal of Nitrogen Heterocycles from Water by Sorption to Spent Oil Shale*

P. Persoff, L. Hunter, E.R. Blatchley, J.F. Thomas, and C.G. Daughton[†]

Mixing two waste streams from oil shale processing (i.e., spent shale and retort water) for waste disposal is called "codisposal." Codisposed wastes contain volatile solutes originating in the wastewater, notably nitrogen heterocycles (NHCs; see accompanying article by Daughton *et al.*), and are planned to be disposed in the environment at elevated temperatures. A large fraction of these solutes may be lost to the atmosphere by volatilization.[1] Both volatilization of solutes from warm codisposed wastes (in the short term) and leaching from codisposed wastes (in the long term) are strongly influenced by the equilibration of the compounds between the solid and liquid phases.[2] Because NHCs volatilized from codisposed wastes would generate nuisance odors and present a potential occupational health problem, the removal of these compounds by their sorption onto spent shale was studied.

*This work was supported by the Assistant Secretary for Fossil Energy, Office of Oil Shale, Division of Oil, Gas, and Shale Technology of the U.S. Department of Energy under Contract No. DE-AC03-76SF00098.

[†]Sanitary Engineering and Environmental Health Research Laboratory, University of California (Berkeley), Richmond, CA.

ACCOMPLISHMENTS DURING FY 1984

Sorption was studied for five NHCs and five spent oil shales from various commercial and experimental retorting processes. These studies showed that spent shales containing significant amounts of char (i.e., the organic residue remaining from the pyrolytic retorting process) could remove these NHCs from aqueous solution. In contrast, spent shales that were fully burned (combusted shales) did not remove significant amounts of the NHCs.

A solution of five NHCs in water was prepared (see Table 1) and stored at 4°C. Each of these compounds had been identified in Oxy-6 retort water,[3,4] and one (2-ethylpyridine) had been identified in each of seven retort waters analyzed (see preceding report by Hunter *et al.*). Portions of this solution were shaken with various amounts of spent shale in 50-mL polycarbonate centrifuge tubes for 24 hours at ambient temperature (23° ± 0.5°C). Two blanks

Table 1. Nitrogen heterocycles (NHC) used in spent-shale sorption study.

NHC compound	Initial concentration (mg/L)	Fraction extracted[a]	pK_a[b]	Boiling point (°C)
Pyridine	118	0.294	5.2	115.5
2-Ethylpyridine	38	0.773	5.9	148.6
5-Ethyl-2-methylpyridine	37	0.849	n.a.[c]	176.7–177.8
4-Ethyl-3-methylpyridine	37	0.892	n.a.	192–193
Quinoline	22	0.740	4.8	243.3

[a]Fraction of solute extracted from aqueous phase after partitioning for 8 minutes with an equal volume of *n*-pentane.

[b]Data from Ref. 8.

[c]Not available; pK_a values for other ethyl-methylpyridine isomers are 3.6–6.5.

(one shaken and one static) with no spent shale were also carried through the procedure. Other blanks, each containing distilled water and one of each of the five spent shales, determined that none of the NHC analytes was leached from the spent shale in detectable amounts. After shaking, the solid spent shale was separated from the supernatant liquid by centrifugation for 3 minutes. Centrifugation was used, rather than filtration, to minimize sample handling and possible solute loss via volatilization. The supernatant liquid was removed from the centrifuge tubes by pipetting into preweighed vials and then made alkaline (pH > 12) by dropwise addition of 6 *N* NaOH. This ensured that the nitrogen bases were in their neutral deprotonated forms. The amount of dilution resulting from this step (approximately 1%) was determined by weighing the vial before and after base addition. Ten milliliters of the basified supernatant liquid was then extracted by shaking for 8 minutes in a 60-mL separatory funnel with an equal volume of *n*-pentane. Time-course studies had shown that 8 minutes of shaking was sufficient to reach 99% equilibration between the two phases. Extractions were done on the original aqueous solution of heterocycles (also made basic) to determine the proportion extracted by this procedure; these data are shown in Table 1. The concentration of each solute remaining in the aqueous phase after sorption could thereby be calculated from the concentration in the organic phase.

The concentrations of the five solutes in the organic phase were determined by gas-liquid chromatography (HP-5880A) on a 6-m × 2-mm i.d. stainless steel packed column (10% SP 2100 on 80–100 mesh Supelcoport) with quantitation by FID (flame ionization detector) area response. Temperature was maintained at 40°C for 2 minutes, then linearly increased at 30°C per minute to 130°C, followed by 10°C per minute to 240°C. Calibration curves for each of the five compounds were determined from injections of standard solutions in *n*-pentane; correlation of FID response with the mass of compound injected was linear (coefficient of determination > 0.995) for each compound. The amount of solute that partitioned to the solid phase was calculated by subtracting the remaining from the initial aqueous-phase concentrations.

In retorting, raw shale is heated in an oxygen-free environment. Kerogen present in the raw shale is pyrolyzed to offgas and syncrude, leaving a residue of char on the spent-shale particles. If the spent shale is subsequently heated in air (combusted), the char is burned and the spent shale is relatively or almost totally char-free. This is intentionally done in some processes to provide heat for the retorting process. Of the five spent shales studied, three had been fully combusted (L-2, Lurgi cyclone, and TOSCO HSP), one had been partially combusted (Paraho), and one had only been retorted (TOSCO II). The combusted spent shales were tan to light gray, while the Paraho and TOSCO II were black. Removal of NHCs by sorption from aqueous solution onto the fully combusted spent shales was too small to detect. Significant removals were observed, however, for the Paraho and TOSCO II spent shales (see Figs. 1 and 2).

Linear adsorption isotherms were adequate to express the equilibria between the aqueous and sorbed forms of the compounds (Figs. 1 and 2). Of the two methyl-ethylpyridine isomers, 4-ethyl-3-methylpyridine is more polar than 5-ethyl-2-methylpyridine, because of the dipole moment established by separation of the alkyl groups and the

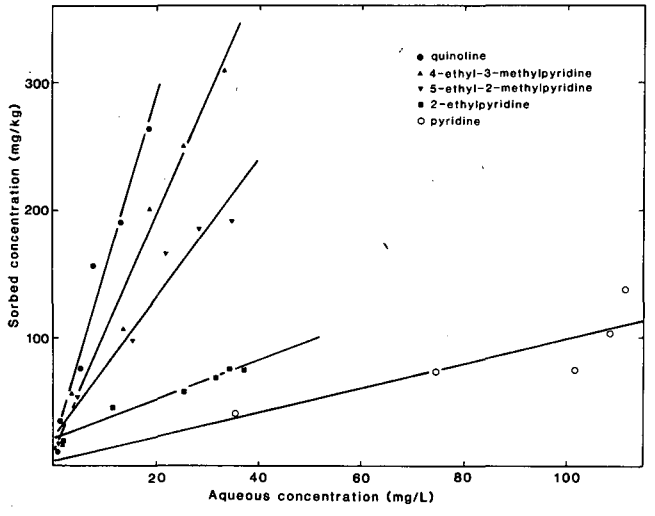

Figure 1. Adsorption isotherms for five nitrogen heterocycles on Paraho spent shale. (XBL 8411-4931)

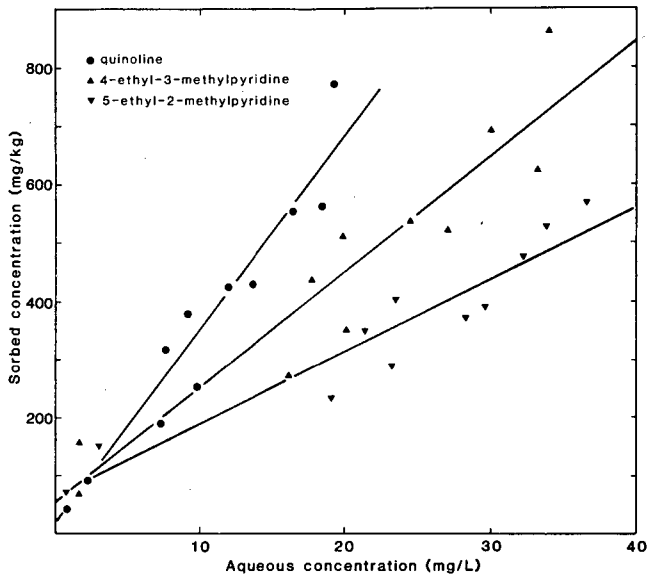

Figure 2. Adsorption isotherms for three nitrogen heterocycles on TOSCO II spent shale. (XBL 8411-4932)

electronegative nitrogen. This was evidenced by its greater tailing in the chromatographic separations. The lack of shielding for the nitrogen in 4-ethyl-3-methylpyridine leads to greater hydrogen bonding (higher boiling point) and explains why it was more strongly adsorbed than 5-ethyl-2-methylpyridine (Figs. 1 and 2).

The sorption isotherm data shown in Figs. 1 and 2 are needed to predict transport of NHCs through, and from, waste-shale disposal piles. A model commonly used to predict volatilization from soil considers the soil as a one-dimensional column with zero concentration at the atmosphere-soil interface.[2,5–7] Diffusional mobility of a solute through the soil is characterized by the "effective diffusivity," which is an average of the molecular diffusivity in the solid, liquid, and gas phases, weighted by the fraction of molecules in each phase and corrected for tortuosity in each phase. Therefore, liquid-vapor equilibrium data and adsorption isotherm data are needed to calculate the effective diffusivity.[2,5–7] A further requirement for using this model of volatilization is that the adsorption isotherm be linear.

Solutes that partition to the gas phase would be most mobile, and those that partition to the solid phase would be least mobile. The findings presented here suggest that TOSCO II and Paraho spent shales retain NHCs strongly enough to sharply reduce atmospheric emissions. For the other, fully-combusted, spent shales, a large fraction of the NHCs present in moisturizing water could volatilize to the atmosphere. Combusting the spent shale releases heat that can be transferred to the raw shale to bring it to pyrolysis temperature. If this strategy is not used, then an external heat source is required. The economics of oil shale development may therefore impel the use of retorting technologies in which spent shale is combusted. This retorting strategy would lead to greater release of NHCs to the environment, because the resulting spent shales would not impede the volatilization process in the codisposed wastes.

PLANNED ACTIVITIES FOR FY 1985

Vapor-liquid equilibrium data for N-heterocycles will be obtained experimentally, and the volatilization model will be modified to include the effects of intraparticle mass-transfer resistance, which is expected to be significant in spent shale disposal. Codisposal of oil shale wastes will be simulated at bench scale to verify the model.

REFERENCES

1. Persoff, P., Hunter, L., Daughton, C.G., and Thomas, J.F. (1984), "Prediction of Atmospheric Emissions Resulting from Codisposal of Oil Shale Wastes," in *Applied Science Division 1983 Annual Report, Environmental Research Program Chapter*, p. 4–38; LBL-17073.
2. Jury, W.A., Grover, R., Spencer, W.F., and Farmer, W.J. (1980), "Modeling Vapor Losses of Soil-Incorporated Triallate," *Soil Sci. Soc. Amer. J. 44*, p. 445.
3. Leenheer, J.A., Noyes, T.I., and Stuber, H.A. (1982), "Determination of Polar Organic Solutes in Oil-Shale Retort Water," *Environ. Sci. Technol. 16*, p. 714.
4. Hunter, L., Persoff, P., and Daughton, C.G. (1984), *Identification and Correlation of Volatile Components in Retort Wastewaters.* Lawrence Berkeley Laboratory Report LBID-966.
5. Lyman, W.J., Reehl, W.F., and Rosenblatt, D.H., Eds. (1982), *Handbook of Chemical Property Estimation Methods*, McGraw-Hill Book Co., New York, Chap. 17.
6. Mayer, R., Letey, J., and Farmer, W.J. (1974), "Models for Predicting Volatilization of Soil-Incorporated Pesticides," *Soil Sci. Soc. Amer. Proc. 38*, p. 563.
7. Jury, W.A., Spencer, W.F., and Farmer, W.J. (1983), "Behavior Assessment Model for Trace Organics in Soil: I. Model Description," *J. Environ. Qual. 12* (4), p. 558.
8. Perrin, D.D. (1965), *Dissociation Constants of Organic Bases in Aqueous Solution*, Butterworths, London.

Temporal and Spatial Scales in a Heated and in a Reacting Turbulent Boundary Layer*

R.K. Cheng, L. Talbot, and F. Robben

Combustion of premixed fuel-lean mixtures embedded in a turbulent boundary layer over a strongly heated wall is a special case in the study of turbulence-combustion interactions. This configuration is also pertinent to many practical combustion situations. In most other configurations, such as turbulent premixed flames stabilized by a rod or at the rim of a tube, the Damkholer number is large (i.e., the chemical reaction rate compared to the turbulent mixing rate is small); in a reacting boundary layer, however, the Damkholer number is much smaller because of the reduction in the chemical reaction rate associated with lean mixtures. Previous measurements[1] have suggested that the combustion reactions take place in a region thicker than the laminar flame thickness, such that the thin wrinkled laminar flame analogy[2] (fast-chemistry assumption) would not be applicable for this flow. Therefore, this configuration provides an opportunity for studying turbulent combustion in a fuel-lean situation for which the numerical models would have to incorporate finite-rate chemistry.

The overall objective of this program is to characterize experimentally the flow field of this reacting turbulent boundary layer, using laser diagnostics techniques. To study the effects of combustion in the classical fluid-mechanics flow field, the nonreacting isothermal and heated wall boundary layers under similar flow conditions are also considered. Previous measurements include the velocity of two components, using the laser Doppler anemometry (LDA) technique,[1] and the density, using Rayleigh scattering.[3] These qualitative data are compared with the qualitative features of the thermal and flame structures shown in high-speed schlieren movies.

*This work was supported by the Director, Office of Energy Research, Office of Basic Energy Sciences, Chemical Sciences Division of the U.S. Department of Energy under Contract No. DE-AC03-76SF00098.

ACCOMPLISHMENTS DURING FY 1984

The two-point Rayleigh technique[4] for measuring joint density statistics at two points separated by an adjustable distance is used to study the temporal and spatial scales in the heated and in the reacting layers. The experimental conditions are a free-stream velocity, U_∞, of 10.5 m/sec, a wall temperature, T_w, of 1000 K, and an ethylene/air equivalence ratio of 0.35.

For the heated layer, measurements of the density cross correlation coefficient at two points separated in three orthogonal directions—$R(\Delta x)$, $R(\Delta y)$, and $R(\Delta z)$—have been completed. Here, Δx, Δy, and Δz represent the separation distances in, respectively, the axial direction, x; the transverse direction normal to the heated wall, y; and the spanwise direction parallel to the wall, z. For the reacting layer, data are thus far available only for separation in the spanwise direction, z. Measurements of $R(\Delta x)$ and $R(\Delta y)$ are currently being undertaken. The separation distances range from 0.0 to 16.0 mm for Δz, 2.0 to 1.0 mm for Δy and 2.0 to 50.0 mm for Δx. Also, measured for the heated layer are the space-time double correlations, $R(T,\Delta x,\Delta y)$ where T is the time delay between the data at the two points separated by Δx and Δy. A space-time correlation coutour can be deduced from these data to show the general orientations of the thermal structures. These data will be compared with similar data to be obtained for the reacting layer.

The spatial correlation $R(\Delta z)$ deduced at the point of maximum root-mean-square density fluctuation within the heated and reacting layers are compared in Fig. 1. It is apparent that $R(\Delta z)$ for the heated layer drops more rapidly with increasing Δz than that for the reacting layer. This means that the spanwise length scale of the reacting layer is larger than that for the heated layer, possibly because of combustion-induced expansion. The length scales obtained by integrating the two curves are 4.4 mm for the reacting layer and 2.0 mm for the heated layer.

The analysis of the space-time double correlation for the heated layer has yet to be completed. Preliminary spatial correlations indicate that the axial length scale is much larger than both the transverse and the spanwise length scales. Therefore, the thermal structures have a very high aspect ratio.

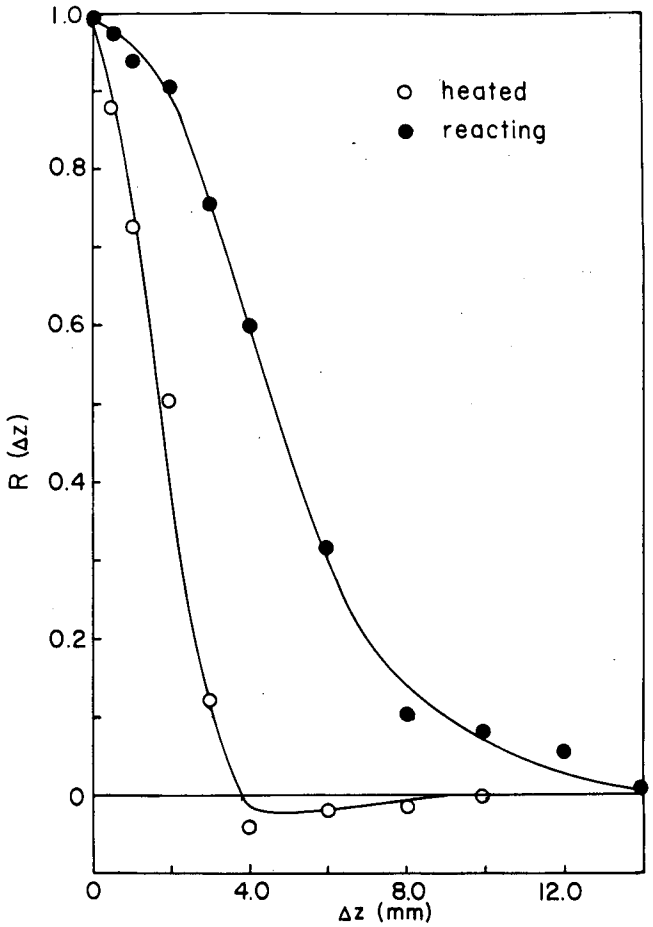

Figure 1. Comparison of the spanwise spatial correlation $R(\Delta z)$ within the heated and the reacting turbulent boundary layers. Data are shown at the position of maximum density fluctuation: for the heated layer, at y = 3.0 mm; for the reacting layer, at y = 9.0 mm. (XBL 851-1026)

Also, the fairly high correlation coefficient of $R(T, \Delta x, \Delta y)$ when Δx is large and $\Delta y \approx 4.0$ mm seems to demonstrate that the thermal structures are oblique to the wall, as shown on the schlieren movies. The optimum delay time T_0 (i.e., the value of T at which $R(T\Delta x, \Delta y)$ shows a maximum) tends to increase with increasing Δx. This is consistent with a convection velocity for the thermal structures. The complete analysis of the space-time double correlation coefficient will determine this convection velocity, which can be compared with the convection velocity of the turbulent structures reported in many studies of isothermal turbulent boundary layers.

PLANNED ACTIVITIES FOR FY 1985

The study of the reacting turbulent boundary layer, using the two-point Rayleigh scattering technique, will be completed. The data are expected to provide the spatial scales, the space-time double correlations, the joint probability density function, the convection velocity, and the general orientation of the flame structures in the reacting layer.

The technique for measuring joint statistics of velocity at two points in space will be developed for studying the reacting turbulent boundary layer. The velocity measurements will complement the present density data. Also, the space-time correlations of velocity are already available for the isothermal turbulent boundary layer. Similar study of the heated and the reacting layers will provide further insight into the effects of combustion in this flow.

REFERENCES

1. Cheng, R.K., and Ng, T.T. (1985), "Conditional Reynolds Stress in a Strongly Heated Turbulent Boundary Layer with Premixed Combustion," to appear in *Physics of Fluids.*
2. Bray, K.N.C., Libby P.A., Masuya, G., and Moss, J.B. (1981), "Turbulent Production in Premixed Turbulent Flames," *Combust. Science Technol. 25*, p. 127.
3. Ng, T.T., Cheng, R.K., Robben, F., and Talbot, L. (1982), "Combustion Turbulence Interaction in the Turbulent Boundary Layer Over a Hot Surface," *Nineteenth Symposium (International) on Combustion*, The Combustion Institute, Pittsburgh, PA, p. 359.
4. Namazian, M., Talbot, L., Robben, F., and Cheng, R.K. (1983), "Two-Point Rayleigh Scattering Measurements in a V-Shaped Turbulent Flame," in *Nineteenth Symposium (International) on Combustion,* The Combustion Institute, p. 487.

Interpretation of Conditional Statistics in Open, Oblique Premixed Turbulent Flames*

R.K. Cheng, I.G. Shepherd, L. Talbot, and F. Robben

The objective of this program is to study the velocity statistics of turbulent premixed flames. The overall goal is to gain better physical understanding of turbulent combustion processes and to aid in the development of numerical models capable of predicting these phenomena. Because of the highly complex nature of the flow field in a practical combustion system, it is important to study the interactions of turbulence with combustion in very simplified systems. The configuration chosen for this study is the rod-stabilized premixed V-shaped flame propagating in a low-Reynolds-number turbulent flow generated by a grid or perforated plate.

ACCOMPLISHMENTS DURING FY 1984

Although most experimental premixed turbulent flames, including the V-shaped flames studied here, are at the very least two-dimensional,[1,2] recent developments in the modeling of such flames have been mostly confined to one dimension.[3] Comparison of the experiment with theory often requires selection of the flame coordinate and consequent transformation of the experimental measurements. Since the results of the transformation are very sensitive to the orientation of the flame coordinate, a consistent and unambiguous definition of the flame coordinate is sought. In FY 1984, we developed a means to establish the flame coordinate for V-shaped flames, using two-component conditional velocity data.[1,2] The conditional velocities are transformed for comparison with some of the predictions of the turbulent combustion model developed by Bray *et al.*[3]

Two methane-air and two ethylene-air flames were studied. The approach-flow velocity was 5.5 m/sec, with turbulence intensity varying from 5% to 8%. The velocity statistics were measured with a two-color laser Doppler anemometry (LDA) system.[1,2] Conditional data were deduced from these measurements by a conditional analysis method.[1]

When the overall time-averaged mean turbulent flame thickness is large compared to the laminar flame thickness, the velocity statistics within the flame brush can be described by an intermittency model that relates the the mean, the root mean square (rms), and covariance to their corresponding conditioned values in the reactants and in the products by using an intermittency factor. This intermittency factor, Ω, which can also be determined experimentally, represents the probability of the products. Therefore, $\Omega = 0$ in the reactant zone and $\Omega = 1$ in the product zone.

For example, the mean velocity vector is decomposed into two conditioned vectors, one corresponding to the reactants and the other to the products (Fig. 1). The difference in the two vectors, ΔU, is the relative velocity between the reactant and the product zones. The direction normal to ΔU describes a surface where the tangential component of the conditioned mean velocities is constant. This surface is the proposed flame coordinate for data transformation. It is the most logical choice because then changes in velocity occur only in the normal component, as in the one-dimensional model.

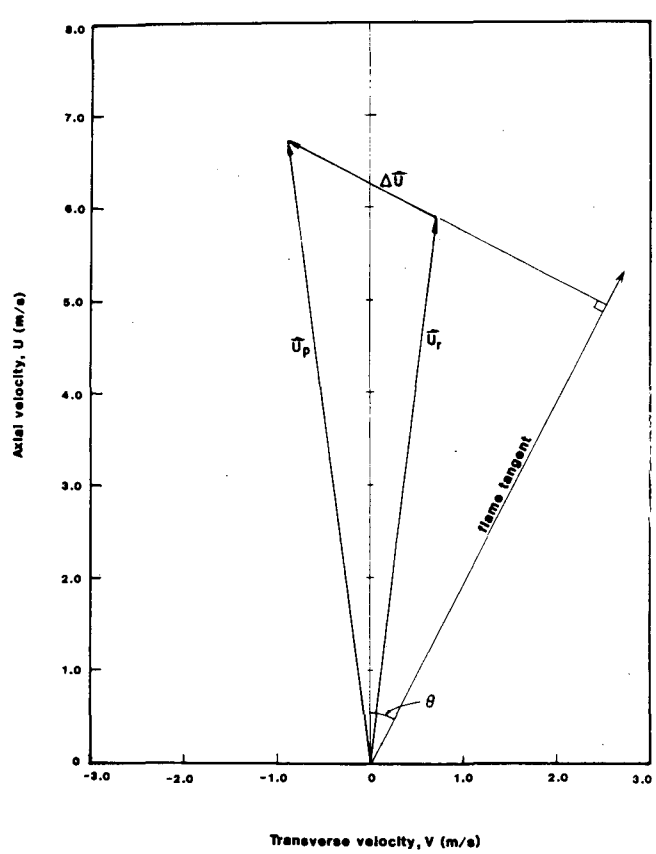

Figure 1. Comparison of the conditional mean velocity vectors in the reactants, U_r, and in the products, U_p, obtained at the center of the flame brush of an ethylene-air V-shaped turbulent flame. (XBL 851-978)

*This work was supported by the Director, Office of Energy Research, Office of Basic Energy Sciences, Chemical Sciences Division of the U.S. Department of Energy under Contract No. DE-AC03-76SF00098.

The transformed mean velocities normal and tangential to the flame orientation are shown in Fig. 2. After the transformation, the normal component shows significant changes within the flame brush (region between 13 and 20 mm) compared to only a slight change in the tangential component. Both the normal and tangential rms velocities (not shown) increase within the products, indicating that the assumption of unchanged tangential rms fluctuation used in some current models may be unjustified.

The most significant result is that after transformation, the unconditioned covariance is an order of magnitude lower than the value before transformation. This result lends support to the modeling assumption that production of turbulence by Reynolds stress in a premixed turbulent flame is not significant.

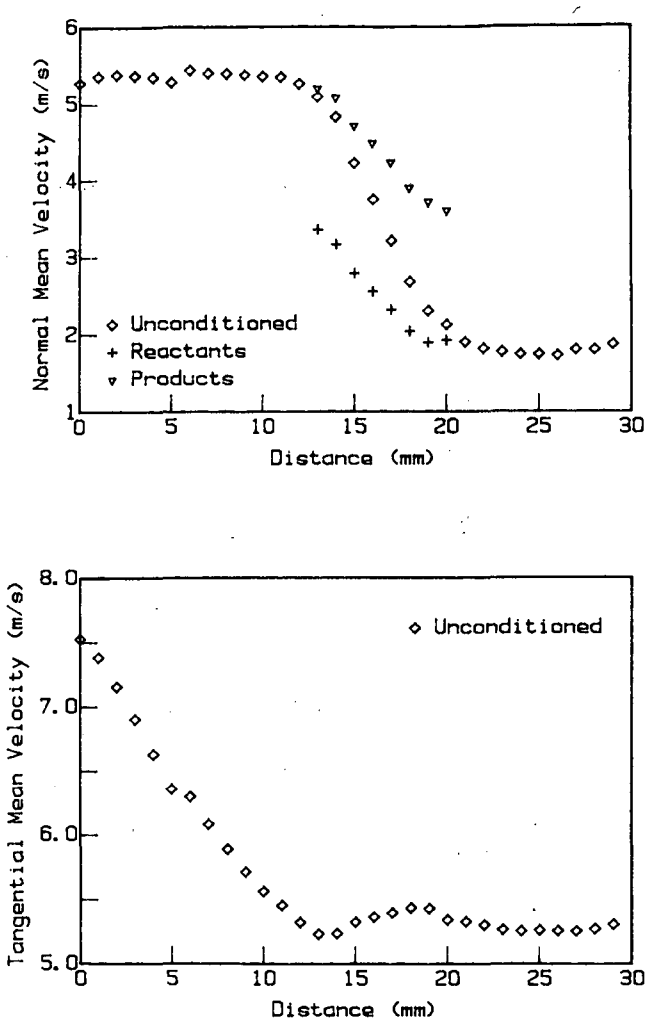

Figure 2. Profiles of velocity components normal and tangential to the turbulent flame brush at 50.0 mm above the flame stabilizer rod. (XBL 851-977)

The transformed velocity normal to the flame coordinate is used to compute the parameters appearing in the 1-D model by Bray *et al.*[3] In this model, a parameter, κ_3, is used to relate the difference in the mean conditioned velocities $\overline{U}_p$ and $\overline{U}_r$ to the increase in the conditioned turbulence fluctuations, $\overline{u'^2p}$ and $\overline{u'^2r}$:

$$\overline{u'^2p} - \overline{u'^2r} = \kappa_3 (\overline{U}_p - \overline{U}_r)^2 \quad .$$

For their calculation, a value of $\kappa_3 \approx 0.1$ is selected. The values of κ_3 deduced from the experimental results are listed in Table 1. In general, the comparison with the model is satisfactory.

Other modeling parameters that can be determined from the experimental data include I, the Favre averaged unconditioned turbulence intensity; F, the turbulent scalar transport; and the fluxes for the scalar, K, and turbulence, L. Experimentally determined values of the parameters I, F, K, and L for an ethylene flame are shown in Fig. 3 as functions of the progress variable $\tilde{c}$, which is related to the mean density and hence distance across the flame brush. Agreement for I and F has been found with previous results of Moss[4] and Shepherd and Moss,[5] though there are no available data for K and L to compare with present results.

PLANNED ACTIVITIES FOR FY 1985

An experimental study of the density and velocity statistics of a turbulent premixed flame in a large Bunsen-type burner will be initiated. Construction of this Bunsen burner has been completed. It is much larger than the ordinary laboratory model (5.0 cm diameter), and the turbulent flame is stabilized by pilot flames fitted at the burner exit. Incident turbulence is generated by a perforated plate placed 5.0 cm upstream of the exit. Conditioned and unconditioned measurements of velocity statistics are planned. The results will be compared with those obtained from the V-shaped flame to investigate whether the geometry of the burner plays a significant role in determining the flame turbulence.

Table 1. Values of κ_3 at flame brush center.

	x (mm)				
No.	20.0	30.0	40.0	50.0	60.0
1		0.015	0.053	0.061	0.060
2	0.009	0.034	0.070	0.102	0.060
3		−0.003	0.004	0.004	0.001
4	−0.011	0.002	0.027	0.052	0.072

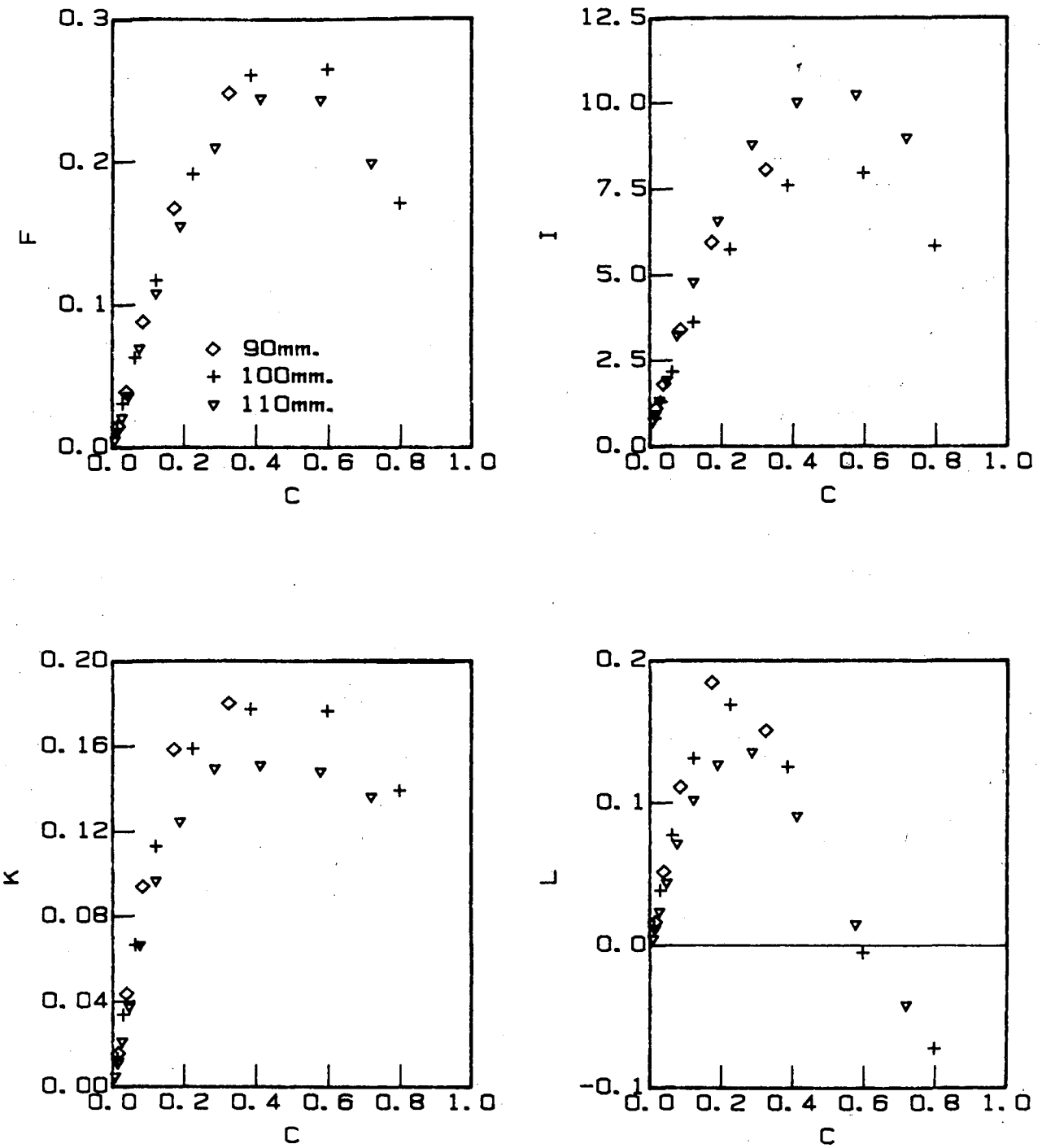

Figure 3. Experimentally determined values of the modeling parameters *F, I, K,* and *L* proposed by Bray *et al.*[3] Data are shown for profiles obtained at 40, 50, and 60 mm above the flame stabilizer. (XBL 851-976)

REFERENCES

1. Cheng, R.K., Talbot, L. and Robben, F. (1984), "Conditional Velocity Statistics in Premixed CH_4-Air and C_2H_4-Air Turbulent Flames," presented at the 20th Symposium (International) on Combustion, Ann Arbor, MI, Aug. 12–17, 1984.
2. Cheng, R.K. (1984), "Conditional Sampling of Turbulence Intensities and Reynolds Stress in Premixed Flames," *Combust. Sci. Technol. 41*, p. 109.
3. Bray, K.N.C., Libby, P.A., Masuya, G., and Moss, J.B. (1981), "Turbulent Production in Premixed Turbulent Flames," *Combust. Sci. Technol. 25*, p. 127.
4. Moss, J.B. (1980), "Simultaneous Measurements of Concentration and Velocity in an Open Premixed Turbulent Flame," *Combust. Sci. Technol. 22*, p. 115.
5. Shepherd, I.G., and Moss, J.B. (1982), "Measurements of Conditioned Velocities in a Turbulent Premixed Flame," *AIAA J. 22*, p. 556.

Characterization of Density Fluctuations in a Premixed Turbulent V-Shaped Flame*

M. Namazian, I.G. Shepherd, and L. Talbot

This program has the broad aim of understanding some of the fundamental processes which occur during premixed gaseous combustion. The characteristic scales of scalar variables, such as temperature and density, in open premixed turbulent flames is the object of current experimental[1,2] and theoretical[3,4] interest. In these flames, the "thin flame" approximation is well-founded, and radical but realistic simplifications can be made to theoretical models which then provide directly testable predictions.

Two-point Rayleigh scattering data has been obtained from a turbulent V-shaped, premixed flame and compared with the predictions of two models: an extension of the Bray-Moss-Libby (BML) model[3] and a wrinkled laminar flame model (WLF).[4] The BML model describes turbulent premixed combustion by idealized probability density functions (pdf) of a progress variable, c, where $c = 0$ in the unburnt gas and $c = 1$ in the burnt gas. A generalized description has been specialized to a one-point, two-time formulation from which may be derived[3] expressions for the autocorrelation, power spectrum, and flame-front passage times for the scalar variable, c. These results are compared with experimental values. A somewhat simpler description, the WLF model, considers the pdf of the position of a laminar flame within the turbulent flame brush. Cross correlations and length scales have been derived and compared with empirical data.

ACCOMPLISHMENTS DURING FY 1984

Figure 1 shows a schematic diagram of the coaxial combustor used in this study. The premixed gases of air and fuel (ethylene or methane) flow through the center jet and are surrounded by an outer coaxial air jet at the same velocity. The inner and outer diameters are 5.1 cm and 10.2 cm, respectively. Grids or perforated plates generate a range of turbulence intensities (5%–10%) in the approach flow, and the flame is stabilized on a 1-mm-diameter

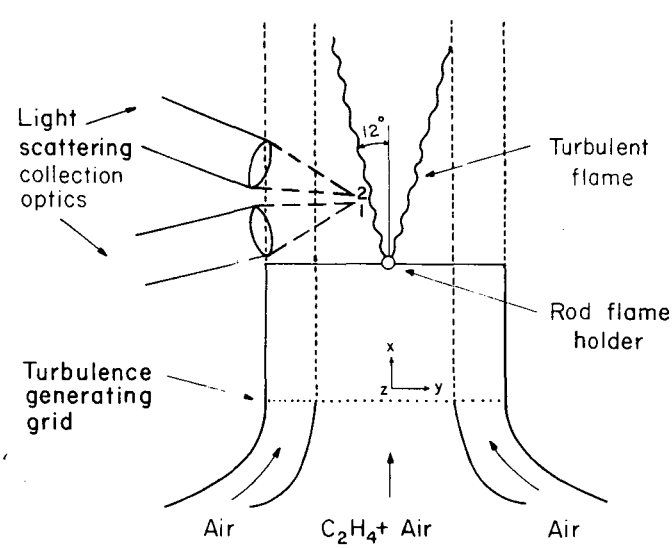

Figure 1. Schematic of the experimental apparatus for two-point Rayleigh scattering measurements.
(XBL 823-8761)

*This work was supported by the Air Force Office of Scientific Research under Contract No. AFOSR F 44620-76-C-0083. Additional equipment and facility support were provided by the Chemical Sciences Division of the U.S. Department of Energy under Contract No. DE-AC03-76SF00098.

rod 50 mm above the turbulence generation source. With this setup and the method described in Ref. 2, gas density was measured at different locations downstream of the flameholder at equivalence ratios of 0.6 and 0.8 with approach-flow mean velocities of 5 m/sec and 7 m/sec. Table 1 summarizes the experimental conditions of the eight flames studied.

The flames were characterized by the turbulent flame-brush thickness, which was obtained from the mean density profile by the maximum gradient method (Fig. 2). Increases in the equivalence ratio increase the laminar burning velocity and the burnt gas temperature and generally have a more significant effect on the flame thickness than approach-flow velocity or inlet turbulence.

The single-point experimental results from which may be derived the temporal characteristics of the scalar field compare very well with the predictions of the BML model. For example, in Fig. 3, the experimental and theoretical normalized power spectra are compared at points in the center of the flame brush. Good agreement was also obtained for the mean passage times and autocorrelation.

The WLF model provides predictions for spatial features of the flames. Nondimensionalizing the flame density profile by the turbulent flame thickness (cf. Fig. 2), all the data may be collapsed onto a simple error function plot. This is compared with the equivalent modeled Gaussian distribution for the instantaneous flame position in Fig. 4. Further comparisons for the cross correlations and density length scales indicate that this representation models the measured values well.

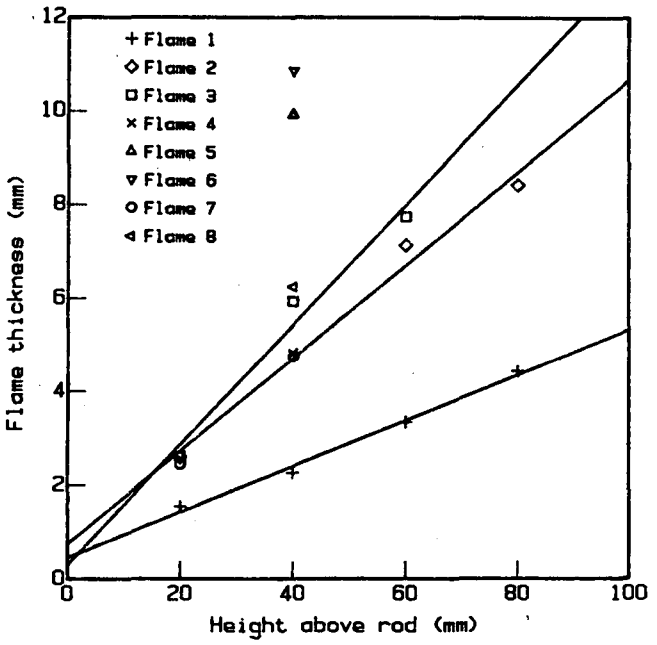

Figure 2. Variation of turbulent flame thickness with height above flameholder. Lines are least-mean-square fits for flames 1, 2, and 3. (XBL 8412-5380)

Table 1. Summary of experimental conditions for the eight flames studied.

Flame no.	Equivalence ratio	U_∞ (m/sec)	Turbulence source	u'/U_∞	Axial measurement location (mm)	Fuel
1	0.6	7	grid	5%	20, 40, 60, and 80	C_2H_4
2	0.6	7	plate 1	8%	20, 60, and 80	C_2H_4
3	0.8	7	grid	5%	20 and 40	C_2H_4
4	0.6	5	plate 1	8%	40	C_2H_4
5	0.8	5	plate 1	8%	40	C_2H_4
6	0.6	7	plate 2	10%	40	C_2H_4
7	0.6	7	plate 1	8%	20 and 40	CH_4
8	0.8	7	plate 1	8%	20 and 40	CH_4

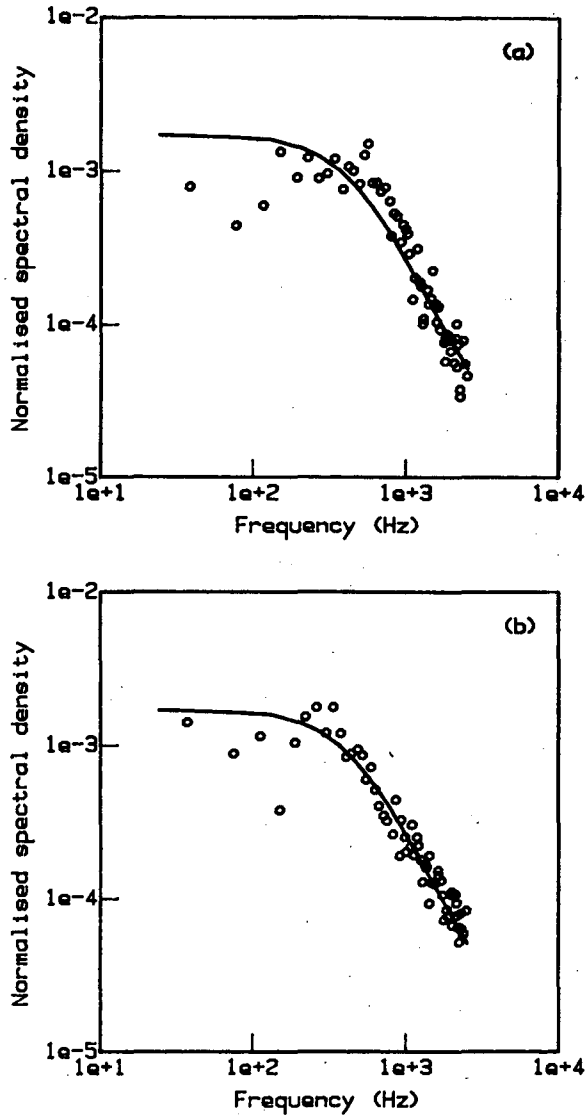

Figure 3. Normalized power spectra of density fluctuations. Height above rod: (a) 60 mm; (b) 40 mm. Lines from BML model.[2] (XBL 8412-5381)

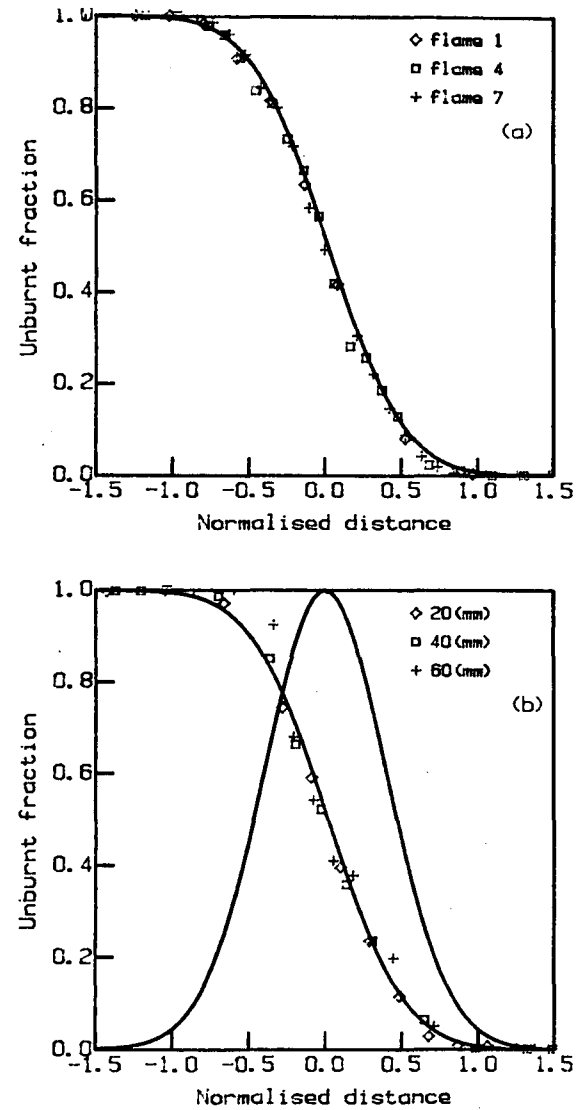

Figure 4. Normalized mean density profiles for (a) three flames at 40 mm height above flameholder and (b) flame 3 at three heights above holder. (XBL 8412-5382)

PLANNED ACTIVITIES FOR FY 1985

The success of the current results encourages the development of the theoretical models and the widening of the experimental base. During the coming year, the Linear Array Rayleigh Scattering (LARS) system will become available and will constitute a significant extension of the two-point Rayleigh measurements. It will also provide information on structural features of these flames that are not available with current techniques.

REFERENCES

1. Shepherd, I.G. and Moss, J.B. (1983), *Combust. Sci. Technol. 33*, p. 231.
2. Namazian, M., Talbot, L., Robben, F., and Cheng, R.K. (1983), "Two-Point Rayleigh Scattering Measurements in a V-Shaped Turbulent Flame," in *Nineteenth Symposium (International) on Combustion,* The Combustion Institute, Pittsburgh, PA, p. 487.
3. Bray, K.N.C., Libby, P.A., and Moss, J.B.

(1984), paper to appear in *Combustion Science and Technology.*
4. Namazian, M., Talbot, L., and Robben, F. (1984), "Density Fluctuations in Premixed Turbulent Flames," presented at the Twentieth Symposium (International) on Combustion, University of Michigan, Ann Arbor, August; LBL-17466.

Premixed Flame Stabilization on a Bluff Body*

J.R. Hertzberg, M. Namazian, L. Talbot, and F. Robben

In order to study the effects of fluid mechanics on combustion, the structure of a turbulent premixed flame stabilized on a bluff-body flameholder has been observed using laser tomography for flame visualization and Rayleigh scattering for single-point measurements of density. The region near the flameholder is the focus of this work.

ACCOMPLISHMENTS DURING FY 1984

The combustor configuration for the laminar, premixed V-shaped flame consisted of a 5-cm-diameter open jet of an ethylene-air mixture and a rod flameholder transverse to the flow, as described in other articles in this annual report. Turbulence was generated by a wire grid of 1-mm elements and 5-mm spacing, placed 50 mm upstream of the flameholder.

A laser-illuminated tomographic technique was used to visualize the flame front.[1] The premixed, combustible mixture was seeded with a translucent light-scattering aerosol of silicone oil droplets that evaporate and burn at the flame front; the disappearance of the droplets thus marks the flame front. By illuminating the flow with a sheet of light from an argon ion laser, sufficient light is scattered from the aerosol to be photographed with a high-speed movie camera.

Figure 1 is an example of the results obtained with this setup. It shows a sequence of frames from a 16-mm film in which the flame is blown off the flameholder as the equivalence ratio is reduced. The flow is from bottom to top at 5 m/sec. The flame forms the sides of the central dark area, and the flameholder is in the center at the bottom of the frame. The outer boundaries of the bright region delineate the interface between the seeded jet flow and a shielding annular coflow.

The film in its entirety shows that blowoff can be interpreted as the result of a perturbation on an unstable system. During the film, the flame twice attained the state of initial instability shown in the ninth frame of Fig. 1 and restabilized itself before being completely blown off as pictured. Note that, in the twelfth frame, some burned gas remains in the recirculating region behind the flameholder. It is unknown whether flame persists at the sides of this region because the tomographic technique cannot distinguish between a flame and a simple interface between fresh and burned gas.

Point measurements of density using laser Rayleigh scattering[2] have been made near the flameholder. Figure 2 compares mean density profiles (solid lines) and root-mean-square (rms) density fluctuations (dashed lines) for two flames at two axial locations. Distances are measured from the center of the flameholder. The top two profiles are taken in a very lean flame, with an equivalence ratio of $\phi = 0.5$. This is close to blowoff, which occurs at $\phi = 0.47$. Note the presence of fluctuations in the burned gases, both close to the flameholder and further downstream. In the slightly richer flame, $\phi = 0.6$, these fluctuations in density are absent.

PLANNED ACTIVITIES FOR FY 1985

Laser Doppler velocimetry measurements will be made in order to map the flow characteristics of the flameholder region in the well-stabilized and near-blowoff cases. Ionization probe measurements will also be made to determine the flame stand-off distance and how it changes with equivalence ratio.

*This work was supported by the Air Force Office of Scientific Research under Contract No. AFOSR F 49620-80-C-0065 through the U.S. Department of Energy under Contract No. DE-AC03-76SF00098.

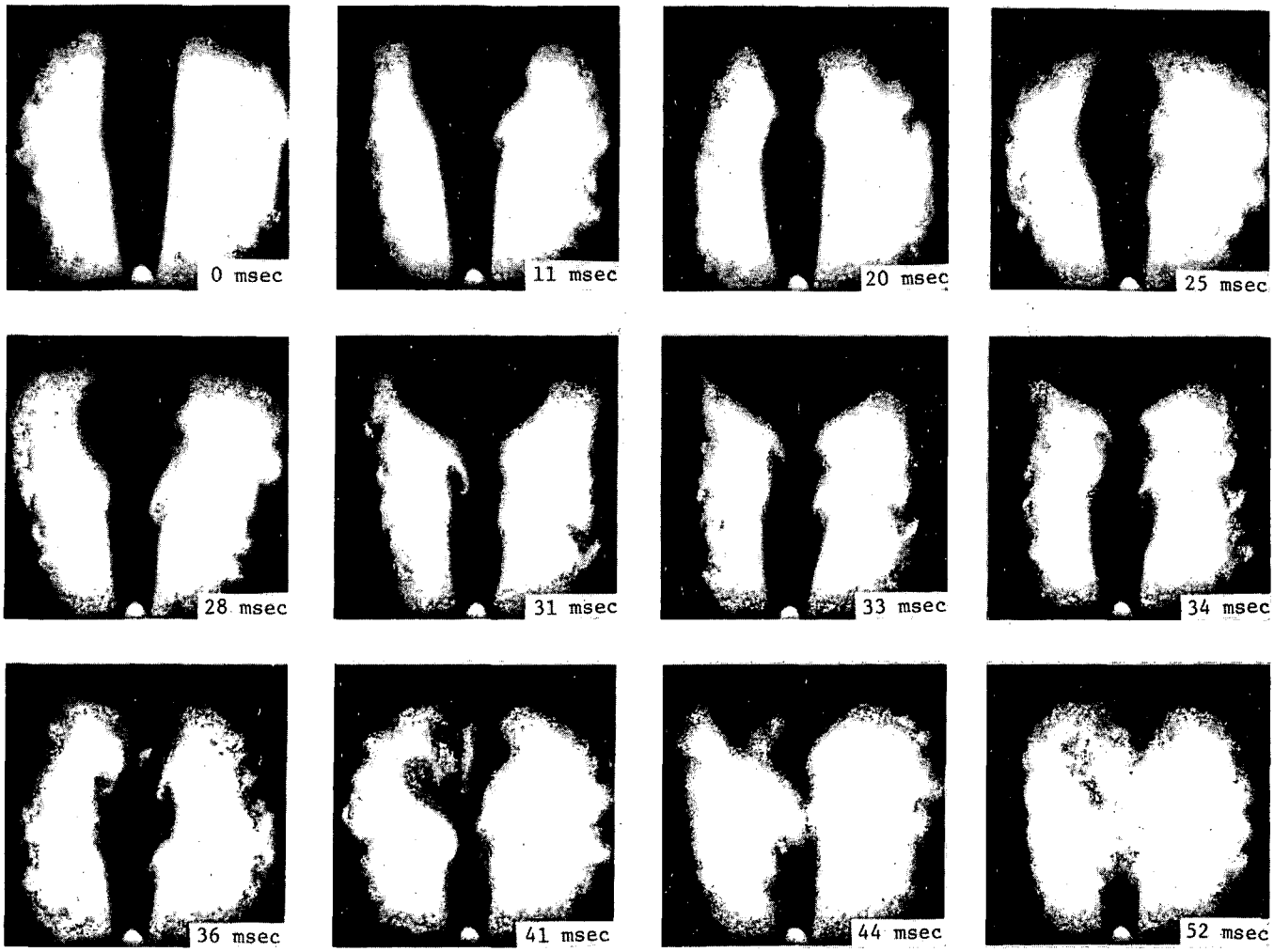

Figure 1. Laser tomographic images of premixed rod-stabilized flame (sides of central dark area). Sequence taken from a 16-mm film showing blowoff caused by decrease in equivalence ratio. Velocity = 1 m/sec. (XBB 8412-9413)

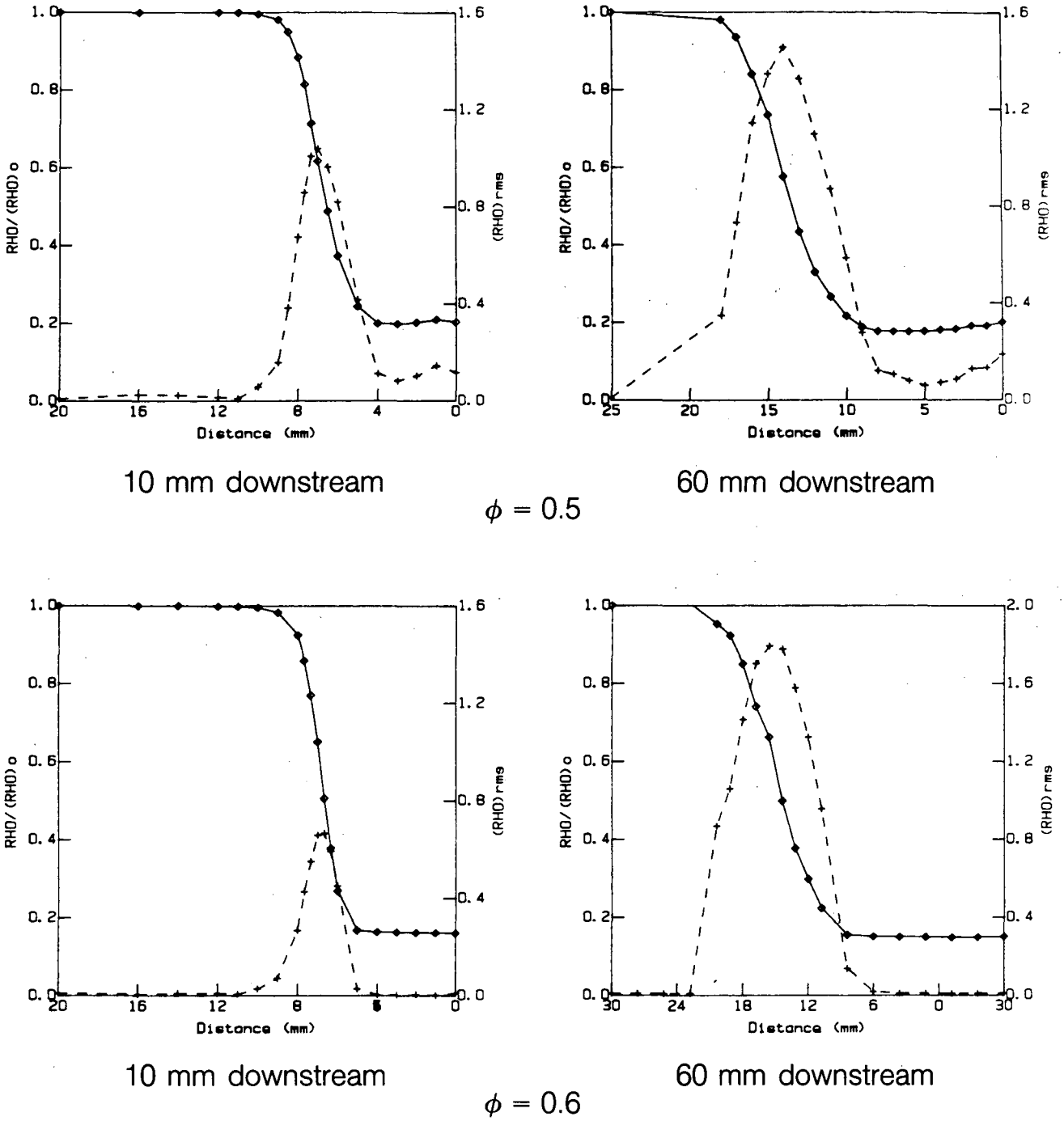

Figure 2. Density measurements using Rayleigh scattering. Solid lines are mean density profiles; dashed lines are root-mean-square density fluctuation profiles. Distances measured from center of flameholder. (XBL 8412-5240)

REFERENCES

1. Hertzberg, J.R., Namazian, M., and Talbot, L. (1984), "A Laser Tomographic Study of a Laminar Flame in a Kármán Vortex Street," *Combust. Sci. Technol. 38*, p. 205.
2. Namazian, M., Talbot, L., Robben, F., and Cheng, R.K. (1982), "Two-Point Rayleigh Scattering Measurements in a V-Shaped Flame," in *19th Symposium (International) on Combustion*, The Combustion Institute, Pittsburgh, PA, p. 487.

Numerical Simulation of Turbulent Combustion*

M. Pindera, F. Robben, and L. Talbot

The object of this investigation is to develop a deterministic numerical model of premixed turbulent flame for studying flame-turbulence interaction processes. The configuration to be modeled is the rod-stabilized V-shaped flame for which experimental statistical data for density and velocity are available.[1] The technique employed in this model is the vortex dynamic method developed by Chorin.[2] Compared to the statistical modeling approach used in many investigations, where the turbulent flame speed and the changes in the flame turbulence are often used as input parameters, the vortex dynamics model for turbulent premixed flames, when developed, will be capable of predicting these parameters in addition to predicting the evolution of the turbulent flame brush to give the turbulent flame thickness.

ACCOMPLISHMENTS DURING FY 1984

A computer program simulating the turbulent V-shaped flame has been developed, and test runs are being made on VAX computers at LBL. Flow conditions for the numerical study are based on the experimental conditions of a free-stream velocity equal to 5.5 m/sec and an incident turbulence level of 5%. The two-dimensional turbulent velocity field is modeled as a composite of rotational and irrotational (potential) components. The irrotational component is the uniform flow (i.e., equal to the mean free-stream velocity), while the rotational part is introduced by inserting discrete vortex elements upstream of the flame. These elements are convected downstream by the uniform flow. The combined strength of the elements simulates a turbulence intensity of 5% with integral length scales of 0.005 m.

Since the Reynolds number of the turbulent flow is low, the flame can be treated as a smooth, wrinkled, continuous interface separating burned combustion products from unburned reactants. In the calculations, the interface is composed of a number of short, straight line segments. This interface moves in two fractional steps: first, it propagates in the direction normal to itself at a specified flame speed, then it is advected by the motion of the gas.

Exothermicity is accounted for by placing volume sources along the front. The magnitude of the sources depends on the laminar flame speed and the density ratio, both of which are functions of mixture composition. Modification of the flame speed by flame stretching (fractional change of the flame surface areas with time) can also be considered, as has been shown by various analytical studies, e.g., Matalon and Matkowsky[3] or Pelce and Clavin.[4] The baroclinic effects across the flame are accounted for by generating vorticity along the front, as shown by Hayes.[5]

PLANNED ACTIVITIES FOR FY 1985

Continuation of the test runs is planned for the early part of FY 1985. This will be followed by full-scale simulations on the IBM 3380 and the Cray X-MP E machines at Sandia National Laboratory.

REFERENCES

1. Cheng, R.K., Talbot, L., and Robben, F. (1984), "Conditional Velocity Statistics in Premixed CH_4-Air and C_2H_4-Air Turbulent Flames," to appear in proceedings of the 20th Symposium (International) on Combustion, The Combustion Institute.
2. Chorin, A.J. (1973), *J. Fluid Mechanics 57*, p. 785.
3. Matalon, M. and Matkowsky, B.J. (1982), *J. Fluid Mechanics.*
4. Pelce, P. and Clavin, P. (1983), *J. Phys. Lettres 44*, p. 1.
5. Hayes, W.D. (1957), *J. Fluid Mechanics 2*, p. 595.

*This work was supported by the Director, Office of Energy Research, Office of Basic Energy Sciences, Chemical Sciences Division of the U.S. Department of Energy under Contract No. DE-AC03-76SF00098.

Coal Slurry Ignition in a Diesel Engine Simulator*

D.D. Brehob, F. Robben, R.F. Sawyer, and P.M. Sherman[†]

Diesels used in transportation consume approximately 7.5% of the nation's oil supply. One-third of the fuel is burned in low- to medium-speed engines. A huge fuel savings could be realized if distillate-burning engines could be converted to burning coal. Extensive research and development of engines burning coal dust was carried out in Germany from 1930 to 1944.[1] The Germans were interested in finding an economical fuel and achieving independence from foreign oil supplies.

Most of the U.S. work on engines fueled by solids has been conducted using coal-slurry fuels. Slurries are preferred over coal dust for storage, handling, and safety reasons. Pulverized coal has been slurried with diesel fuel, methanol, and water, with coal mass loadings from 10% to 60%. The diesel fuel and methanol carriers aid in the ignition and help sustain the coal combustion. However, these carriers greatly increase the cost of the slurry. Thus, there may be insufficient economic incentive to overcome the injection, combustion, fuel stability, fuel storage, wear, and lubrication problems associated with the introduction of coal particles. Coal/water slurry is the least expensive alternative. However, it is more difficult to ignite and more difficult to completely burn than the other slurries.

It is the goal of this project to determine the conditions (temperature and pressure) under which the three slurries ignite, compared to diesel fuel. In addition, high-speed movies of the combustion events of the different fuels are to be examined.

ACCOMPLISHMENTS DURING FY 1984

Before experiments in the engine, the injection system was tested in a pressurized bomb outside the engine (Fig. 1). Backlighted shadowgraphs were used to analyze the spray penetration distance, cone angle, and droplet size[‡] as functions of nozzle diameter, nozzle opening pressure, fuel type, and the rack setting on the injection pump (i.e., the quantity of fuel injected). The degree of atomization was found to increase as nozzle diameter decreased. A nozzle orifice of not less than 0.33 mm was sufficient for injecting slurries with infrequent occurrence of blockage at the tip. Nozzle opening pressures of 200 atm and moderate rack settings gave the best atomization. Higher opening pressures were not possible because the sacless nozzle tips could not withstand the stresses.

The square-piston test facility is shown in Fig. 2 and has been described by Robben.[2] The salient features are the square cross-section "cylinder" and piston that permit optical access, the single injection and single combustion nature of the experiments, the ability to vary the inlet air temperature and pressure, and the ability to preheat the engine block. The fuels used in this study were provided by the Bartlesville Energy Technology Center. A description of the fuels is contained in Table 1.

The facility is equipped with an LSI-11 microcomputer with an analog-digital converter for data acquisition. Cylinder pressure is recorded each one-half crank angle degree (CAD). Injection line pressure is recorded by oscillogram. Inlet air conditions and injection parameters are also recorded. The complete engine control and data acquisition system is shown schematically in Figs. 3(a) and (3)b. The photodetector and proximity detector will be added in FY 1985, as discussed below.

Ignition (without combustion-assisting techniques such as pilot injection or a glow plug) has been achieved for all of the test fuels. Figure 4 shows the results of ignition delay for all the fuels versus injection timing. The air temperatures in Figs. 4(a)–(c) are calculated from a computer code

Table 1. Description of fuels.

Reference fuel: Diesel No. 2 (40 cetane)
Test fuels: 45% coal/55% water
Test fuels: 45% coal/55% methanol
Test fuels: 45% coal/55% Diesel No. 2
Coal diameter: 5 micrometers mean, maximum of 40 micrometers
Coal type: Pittsburgh seam HVA bituminous cleaned by the Otisca Process (0.7% ash)
Enthalpy of reaction (coal alone): 32.5 MJ/kg

*This work was supported by the Assistant Secretary for Fossil Energy, Office of Advanced Energy Conversion Systems, Heat Engines Program, U.S. Department of Energy under Contract No. DE-AC03-76SF00098.

[†]On leave from the Department of Aerospace Engineering, University of Michigan, Ann Arbor.

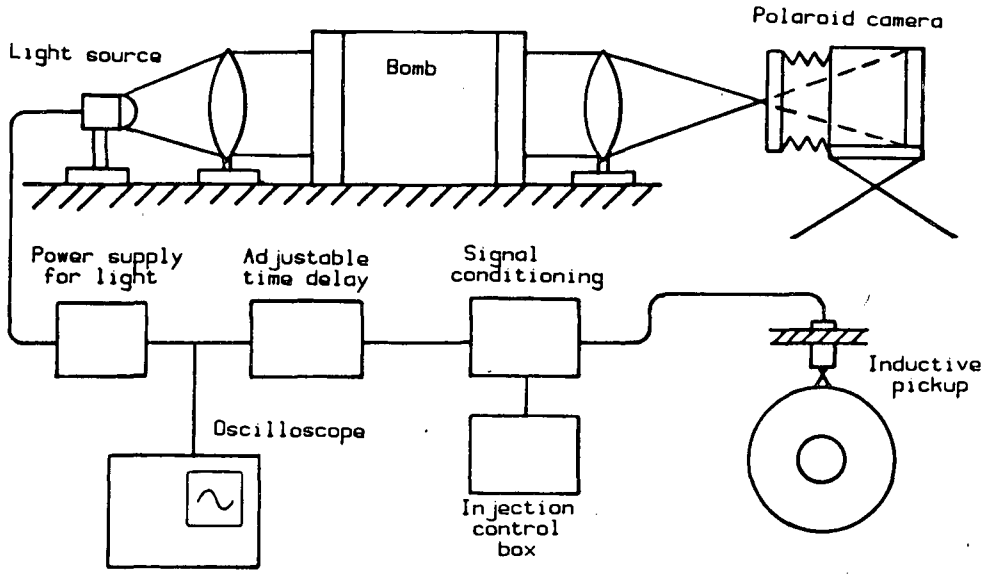

Figure 1. Backlighted shadow photographic setup. (XBL 8412-5423)

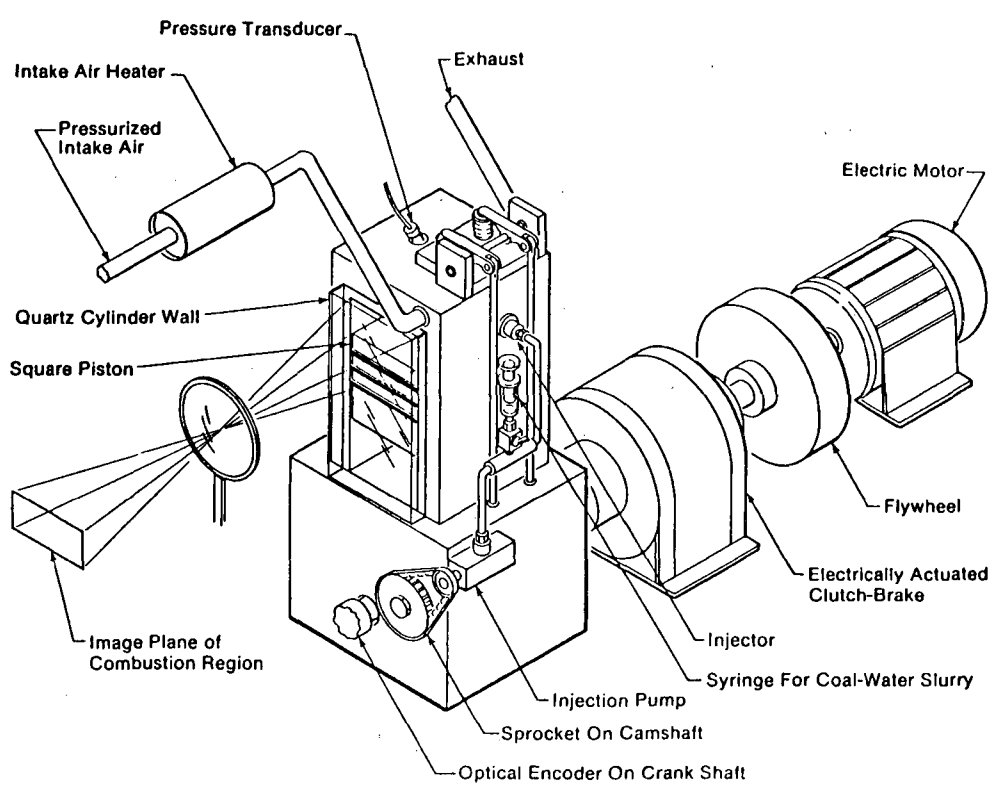

Figure 2. Single-cycle, square-piston diesel engine simulator. (XBL 8412-5422)

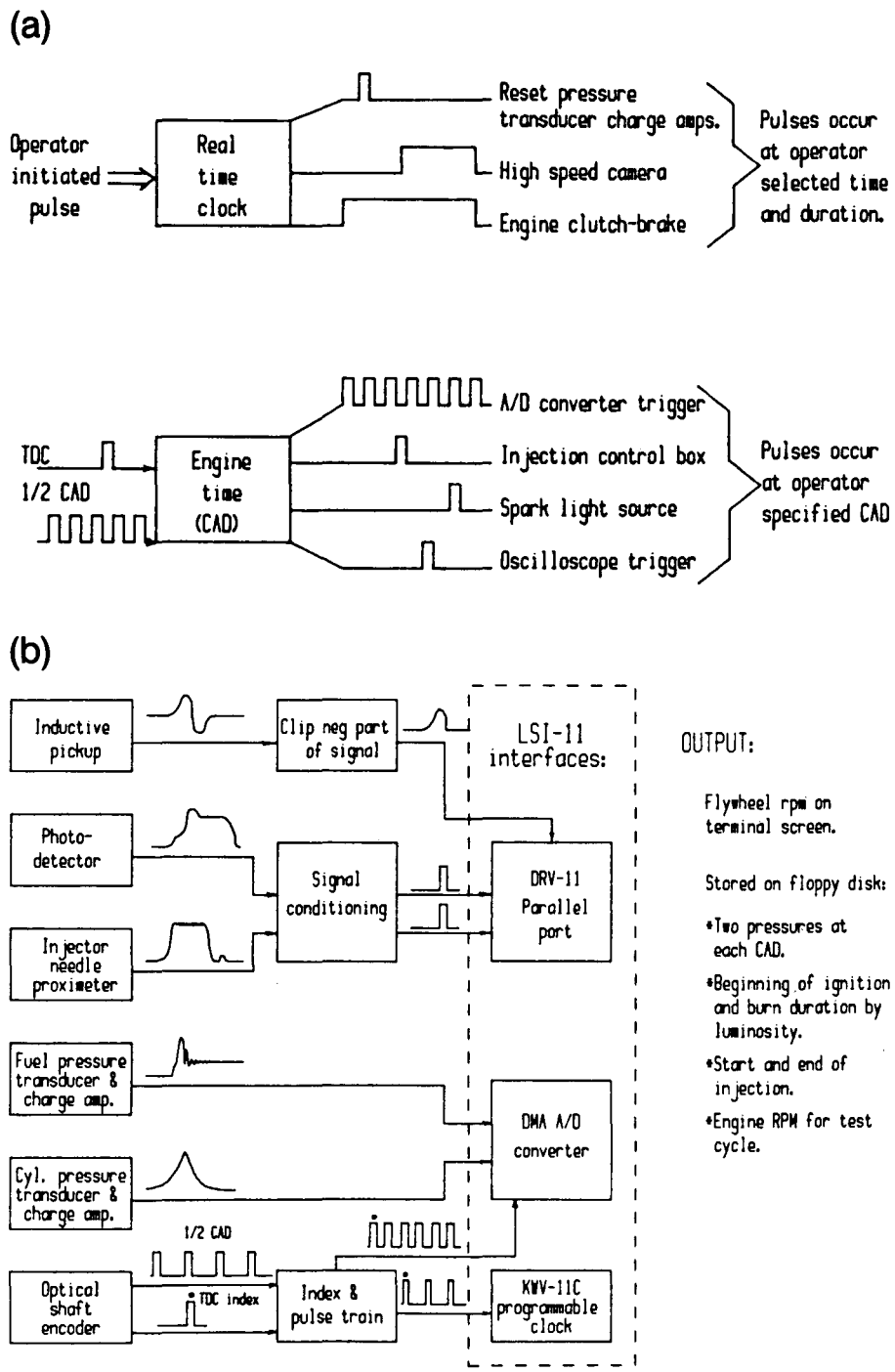

Figure 3. (a) Engine control electronics and (b) LSI-11 data acquisition system.
(XBL 8412-5425)

developed to simulate the engine cycle without combustion but including change in specific heat, mass leakage, and heat transfer effects. The following conclusions can be made about the ignition conditions:

(1) Because of heat transfer to cold cylinder walls and leakage, the inlet air temperature needs to be higher than 400 K to ignite.

(2) Coal/water slurry does not ignite unless inlet air temperatures are higher than 525 K.

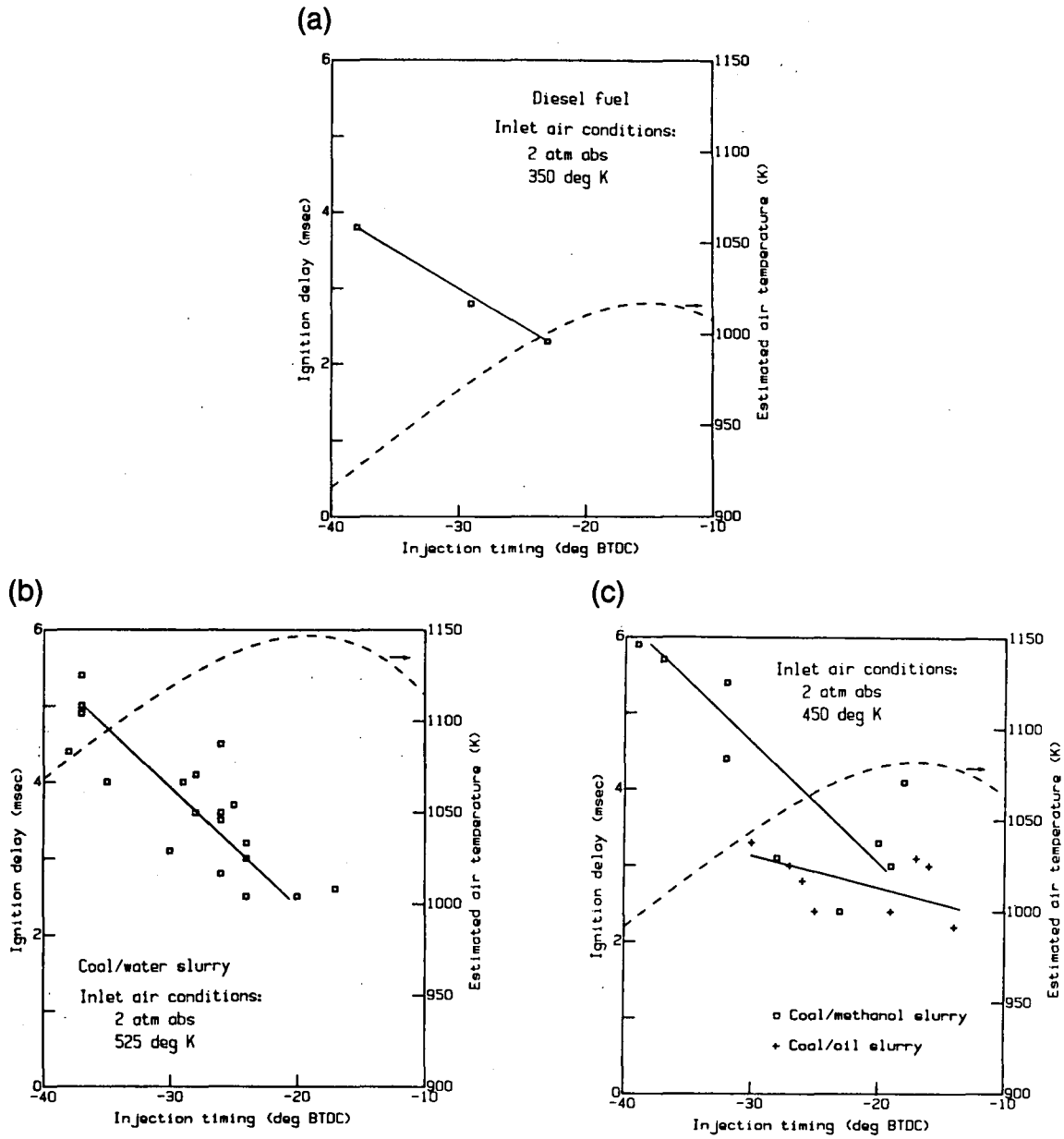

Figure 4. Ignition delay vs. injection timing for (a) diesel fuel; (b) coal/water slurry; and (c) coal/oil and coal/methanol. (XBL 8412-5424)

(3) The coal/methanol and coal/oil slurries readily ignite at an inlet air temperature of 450 K. (Attempts to burn at lower temperatures have not been made.)

The high-speed movies provided the following information:

(1) The burn duration of the fuels is as expected. The coal/water slurry extinguishes rapidly, followed by coal/methanol, then coal/oil. The pure diesel is luminous the longest, approximately 90 CAD.

(2) In nearly all cases, ignition is initially observed near the injector. The flame then spreads throughout the entire chamber. The smaller droplets, which are volatile and consequently burn more readily, do not penetrate across the chamber (i.e., away from the injector) as far as the larger particles do.

PLANNED ACTIVITIES FOR FY 1985

The data acquisition system of the facility is to be upgraded as indicated in Fig. 3(b). The two transducers to be installed are a proximity detector ("proximeter") to provide injector needle lift information and a photodetector to measure luminosity from combustion, thereby indicating initiation and termination of combustion. With these additional data, it will be possible to compare ignition delay from pressure measurements and from combustion luminosity measurements. Also, the start of injection can be known more precisely. The rate of fuel addition can be computed from the digitized injection line pressure measurement.

It is planned to do a more extensive comparison of the fuels and to define the ignition conditions more comprehensively. In addition, neat methanol fuel will be evaluated in this test matrix. A computer code to evaluate the rate of energy release on the basis of the cylinder pressure will be developed.

REFERENCES

1. Soehngen, E.E. (1976), *Development of Coal-Burning Diesel Engine in Germany,* Energy Research and Development Administration Report FE/WAPO/3387-1.
2. Robben, F. (1983), *Coal-Fueled Diesel Engines,* Society of Atuomotive Engineers Paper No. 831747.

Molecular Beam Studies of Ignition Chemistry*

D. Lucas and N.J. Brown

Identification of the principal elementary reaction steps that occur during ignition of hydrocarbon-oxygen mixtures and determination of the corresponding rate coefficients are required to achieve an understanding of ignition. Ignition chemistry is thought to be dominated by the reactions of radical species such as O, OH, and H. To study reactions of these and other species, we have designed and are constructing a molecular beam mass spectrometer (MBMS) system that can be interfaced to a heated flow reactor or a constant-volume cell. This apparatus will allow us to measure reaction rates and product distributions, both of which are necessary to understand the complex set of reactions that lead to combustion.

ACCOMPLISHMENTS DURING FY 1984

A schematic diagram of the molecular beam mass spectrometer being assembled is shown in Fig. 1. The design relies on experience gained from studying the flash photolysis ignition of NO_2- doped CH_4/O_2 mixtures.[1] The system has been designed to achieve high pumping speeds in all three stages while retaining a source-to-detector distance of 19 cm. The detector stage is turbomolecular-pumped and contains all-metal seals to reduce background contamination. The in-line design improves ionization efficiency and facilitates alignment. Modular construction reduces costs and permits a variety of experiments to be interfaced readily. A variable-speed chopper and a simple extension tube to increase the path length allows more precise time-of-flight measurements to be made when desired.

The detector train is adaptable to either photon counting or analog measurements, and both can be computer-controlled by a DEC LSI-11 or Micro PDP-11 microcomputer. Photon counting is accomplished by detecting pulses from the particle multiplier tube with a Pacific AD6 amplifier/ discriminator, which are electronically gated into the signal or background channel of a Bira dual scaler-timer located in a CAMAC crate. Analog signals are

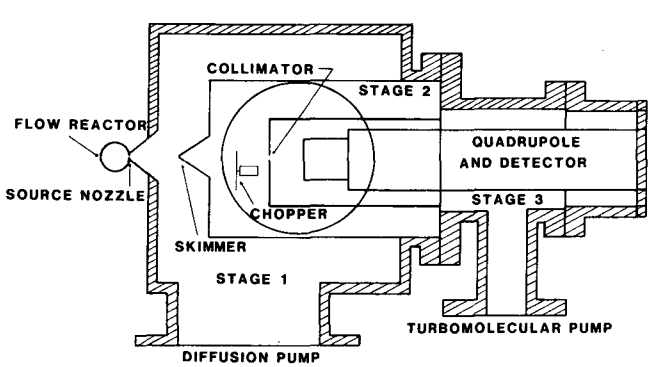

Figure 1. Schematic diagram of the molecular beam mass spectrometer coupled to a flow reactor. (XBL 8412-5475)

*This work was supported by the Director, Office of Energy Research, Office of Basic Energy Sciences, Chemical Sciences Division of the U.S. Department of Energy under Contract No. DE-AC03-76SF00098.

processed with a Lecroy 8210 10-bit, 4-channel analog-to-digital converter with internal buffer memory.

The spectrometer will be coupled to either a heated flow reactor or a constant-volume cell. The flow reactor will have a conical sampling orifice located in the side wall to reduce perturbations produced by an end-wall configuration. Nichrome strip heaters will permit operation up to 1000 K. Ignition will be studied by using the constant-volume cell in conjunction with a Lambda Physik EMG 200 excimer laser. The quartz cell will be equipped with a piezotron pressure transducer and a fill/purge port.

Preliminary measurements with a 0.2-mm source orifice and a source pressure of 750 torr have been made. The working pressures for the three stages are 2×10^{-4}, 2×10^{-5}, and 5×10^{-8} torr, respectively. The Mach number for this beam is in excess of 10.0. Results using a prototype of the flow reactor with a 0.5-mm orifice drilled in the side wall and a source pressure of 15 torr indicate a supersonic beam is formed with a Mach number of ~2.5.

PLANNED ACTIVITIES FOR FY 1985

Construction of the molecular beam mass spectrometer will be completed. Research on elementary reactions and ignition phenomena will be conducted using this system in conjunction with a heated flow reactor and an excimer laser.

REFERENCE

1. Lucas, D., Peterson, R., Brown, N.J., and Oppenheim, A.K. (1984), "Molecular Beam Mass Spectrometer Sampling of Flash Ignited Combustion," presented at the 20th Symposium (International) on Combustion, Ann Arbor, MI, Aug. 12–17, LBL-17222.

The Measurement of Combustion-Generated Pollutants with TALMS*

D. Lucas and N.J. Brown

In order to understand sulfur and nitrogen combustion chemistry, assess control technologies, and evaluate the relationship between source emissions and acid deposition, it is important to be able to measure these compounds quantitatively under combustion and exhaust-stack conditions. Sulfur can be present in gaseous, liquid, and solid fuels. Although the amount of sulfur in gaseous fuels is quite low, it can account for as much as 10% of the mass of coal. Measurements of the combustion products of fuels with known sulfur contents indicate that sulfur dioxide is the major sulfur-containing species. Nitrogen compounds have two sources: (1) nitrogen-containing molecules in the fuel and (2) the products of high temperature reactions with atmospheric nitrogen molecules. Our research is directed toward the development and understanding of spectroscopic techniques useful for measuring sulfur and nitrogen oxides in combustion environments.

*This work was supported by the Director, Office of Energy Research, Office of Basic Energy Sciences, Chemical Sciences Division of the U.S. Department of Energy under Contract No. DE-AC03-76SF00098.

ACCOMPLISHMENTS DURING FY 1984

Tunable Atomic Line Molecular Spectroscopy (TALMS) has been applied to the measurement of SO_2 in the postflame region of atmospheric pressure, premixed methane/air stoichiometric flames doped with SO_2.[1] This nonintrusive line-of-sight absorption technique is sensitive and very selective. The TALMS technique is based upon the Zeeman effect, which allows for magnetic tuning of an atomic line into resonance with a molecular absorption.[2] The technique has been successfully applied to the detection of small molecules that exhibit sharp rotational structure[3] and to SO_2 detection under ambient conditions.[4] The TALMS results we report for SO_2 measurements are the first for a triatomic molecule in combustion mixtures.

The dependence of the TALMS signal strength on magnetic field for SO_2 differential absorption has been measured at 300 K and 1500 K. Maximum sensitivity occurs at a magnetic field strength of 14.5 kG. Data obtained at 1500 K show the same dependence of signal strength on magnetic field as that obtained at 300 K, indicating that the same transition is measured in the flame system as under ambient conditions.

The sensitivity of the TALMS technique varies with the temperature of the sample. For a 7-cm path length at 1 atmosphere, the minimum detectable concentration is ~40 ppm at 300 K, and ~2000 ppm at 1500 K. The determination at room tem-

perature was made in the quartz cell using mixtures of SO_2 in nitrogen, and the high temperature value was determined in the flame. The response of the TALM spectrometer to varying SO_2 concentrations in the flame system is shown in Fig. 1. The TALMS signal is linear for SO_2 concentrations below 20,000 ppm in the 7-cm-diameter burner.

Ultraviolet spectra of SO_2 were taken at various temperatures in a heated quartz cell for SO_2/N_2 mixtures of fixed concentration and in the postflame region of the SO_2-doped methane/air flame to determine the cause of the lowered sensitivity. The discrete absorption features gradually broaden as the temperature increases, and the underlying continuum becomes even more absorbing when corrected for density differences. The ultraviolet spectrum of SO_2 at 1500 K, taken in the postflame region, shows continuing broadening, with no evidence of absorption by other species. The resolution in these spectra is on the order of 0.2 nm, much coarser than the resolution in the TALMS apparatus, which is <0.003 nm. The broadening of the absorption features is largely due to redistribution of the rotational level populations at the elevated temperatures, with the particular transition probed by the zinc line

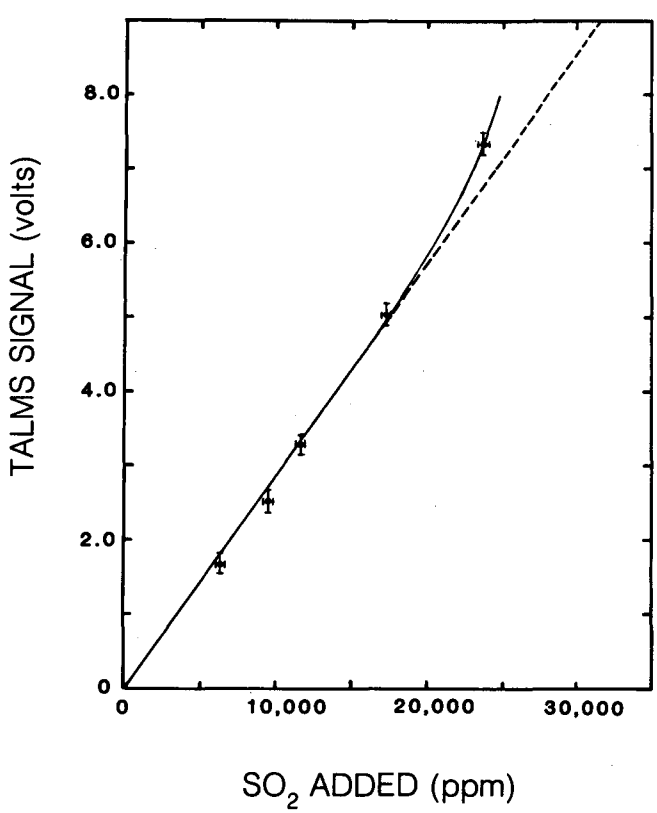

Figure 1. TALMS signal as a function of SO_2 added to a 7-cm flat-flame burner. (XBL 847-2821)

in the TALMS experiment suffering a corresponding loss of population in the initial state. Pressure broadening due to the presence of other species may also contribute to the loss of sensitivity noted under postflame conditions, but the steady broadening noted as temperature increased from 300 K to 800 K in the cell experiments where only N_2 and SO_2 were present indicates that the loss of sensitivity is dominated by rotational redistribution. Also, the magnetic field dependence of the TALMS signal indicates no significant perturbation of the energy levels at the higher temperatures.

The ultraviolet absorbance at approximately the same wavelength as the TALMS experiments is linear to concentrations as high as 30,000 ppm. This indicates that the nonlinearity in the TALMS signal is not attributable to self absorption or deviations from Beer's law under low resolution conditions. Assuming that a single rotational state is involved in the TALMS measurement, a 75 K decrease in the postflame temperature can account for the deviation observed at the high SO_2 concentration. We have measured postflame temperature drops of ~60 K when SO_2 is added, but our uncoated thermocouple measurements are not reliable in this flame system. However, results of other researchers indicate that a temperature change of this magnitude is not unreasonable.

We have measured nitric oxide (NO) in the postflame region with a sealed cadmium lamp emitting at 214.4 nm. The use of natural-abundance Cd results in a broadening of the emission line by the hyperfine structure of the odd isotopes, resulting in a lowered sensitivity. To improve the sensitivity, we have constructed a lamp similiar to the unsealed lamp described previously,[1] but with a new anode configuration consisting of a pure isotope of ^{114}Cd electrodeposited onto a stainless steel screw. Results indicate that less than 0.01 g of Cd is needed to construct a lamp with a lifetime in excess of 8 hours.

The TALMS technique is well suited for measurements in combustion environments. The selectivity of the technique (because of the high resolution of the light source) reduces interferences to those molecules that have a differential absorption at the same wavelength as the molecule being measured. Any interference of this type can be detected by measuring the TALMS absorption as a function of magnetic field strength and can often be eliminated or reduced by changing the magnetic field strength. For example, NO can be detected using the Zn line at 213.8 nm, but the maximum signal occurs at 20 kG, with no significant differential absorbance at <15 kG, while the SO_2 maximum differential absorbance occurs at 14.5 kG. Most molecules,

including NO, also have sufficient differential absorbance at more than one wavelength coincident with an available light source, reducing the chance of an undetected interference.

In summary, the range of concentrations that can be measured by the TALMS technique make it an attractive method for measuring SO_2 and NO in combustion exhausts at utility sites where the emission levels must be monitored.

PLANNED ACTIVITIES FOR FY 1985

Research on measuring SO_2 and NO was completed during FY 1984.

REFERENCES

1. Lucas, D., and Brown, N.J. (1984), "Measurement of Sulfur Dioxide in the Post-Combustion Environment," presented at the 20th Symposium (International) on Combustion, Ann Arbor, MI, Aug. 12–17, 1984, LBL-17274.
2. Koizumi, H., Hadeishi, T., and McLaughlin, R. (1979), "A New Technique for the Determination of Isotopic Species Using Zeeman Scanning of an Atomic Line," *Appl. Phys. Lett. 34*, p. 277.
3. Koizumi, H., Hadeishi, T., and McLaughlin, R. (1979), "Detection of Small Molecules by Magnetically Tuned Frequency-Modulated Atomic Line Sources," *Appl. Phys. Lett. 34*, p. 382.
4. Koizumi, H., Hadeishi,T., and McLaughlin, R. (1981), "A New Technique for the Determination of SO_2 by a Zeeman Shifted Atomic Line," *Spectrochim. Acta 36B*, p. 483.

Combustion Characteristics of Unvented Space Heaters*

T. Lionel, R.J. Martin, and N.J. Brown

Energy conservation can be achieved in the home environment by modifications of ventilation, insulation, and heating. The use of space heaters in residences has become more popular as the cost of central heating systems has increased. Kerosene heaters offer a truly portable alternative to electric, natural gas, and oil-fired heaters; however, their unvented design necessitates consideration of the effects of combustion emissions in the indoor environment. The rate of air infiltration is closely coupled to emission levels in affecting the indoor air quality.

Descriptions of the emissions produced by kerosene heaters have involved three types of experiments: laboratory studies characterizing exhaust concentrations,[1] environmental chamber studies,[2–4] and field studies in houses.[5–7] The indoor air pollutants carbon monoxide (CO), sulfur dioxide (SO_2), oxides of nitrogen ($NO_x = NO_2 + NO$), carbon dioxide (CO_2), unburned hydrocarbons, and particulates have been detected.

The purposes of this research are (1) to acquire a better understanding of the combustion occurring in unvented kerosene heaters and thereby contribute to design improvements; (2) to determine exhaust-gas composition as a function of heater type and heater operating conditions; and (3) to determine whether differences exist between chamber studies of the heaters and combustion studies. A paper describing the research is in press.[8]

We have investigated three different (prototypical) heaters, of radiant, convective, and multistage designs. All heaters have a wick (first section) to introduce kerosene to the primary combustion chamber (second section), where much of the combustion occurs. The third section mixes the products of combustion, allowing increased residence time before exhausting the products to the environment.

ACCOMPLISHMENTS DURING FY 1984

An exhaust and sampling system was modified to completely mix the products of combustion while producing no effect upon the kerosene heaters. Samples were withdrawn through quartz probes and filtered heated Teflon lines to a gas chromatograph (measuring CO_2, CO, O_2, N_2, and hydrocarbons), a chemiluminescence analyzer (for oxides of nitrogen), a pulsed fluorescent SO_2 analyzer, or a nondispersive infrared analyzer (for CO). Additional diagnostic

*This work was supported by the Assistant Secretary for Conservation and Renewable Energy, Office of Energy Systems Research, Energy Conversion and Utilization Technologies Division of the U.S. Department of Energy under Contract No. DE-AC03-76SF00098.

information was obtained about the following physical parameters: temperature, pressure, fuel consumption, and exhaust-flow velocity. A schematic diagram of the experimental apparatus is shown in Fig. 1.

Two types of experiments were performed to acquire an understanding of the combustion in the three heaters. In the first type, composition and temperature were measured at different spatial locations in the heater to determine the progress of combustion as a function of axial position. In the second type, composition, temperature, pressure, and exhaust-gas mass flow rate were measured in the exhaust manifold to ascertain the effect of heater type and heater operating conditions on exhaust-gas composition.

Composition and temperature were measured as a function of axial position within the multistage heater to determine the progress of combustion. These positions and the data collected for this profile are shown in Fig. 2 and Table 1, respectively. Combustion occurs from the region directly above the wick up into the third section of the heater. Measurements of composition and temperature indicate that significant quantities of CO and hydrocarbons are found in the flame zone but are almost fully oxidized to CO_2 before exiting the third section. Nitrogen dioxide is present in the second section but is not detectable above the flame zone, where NO predominates.

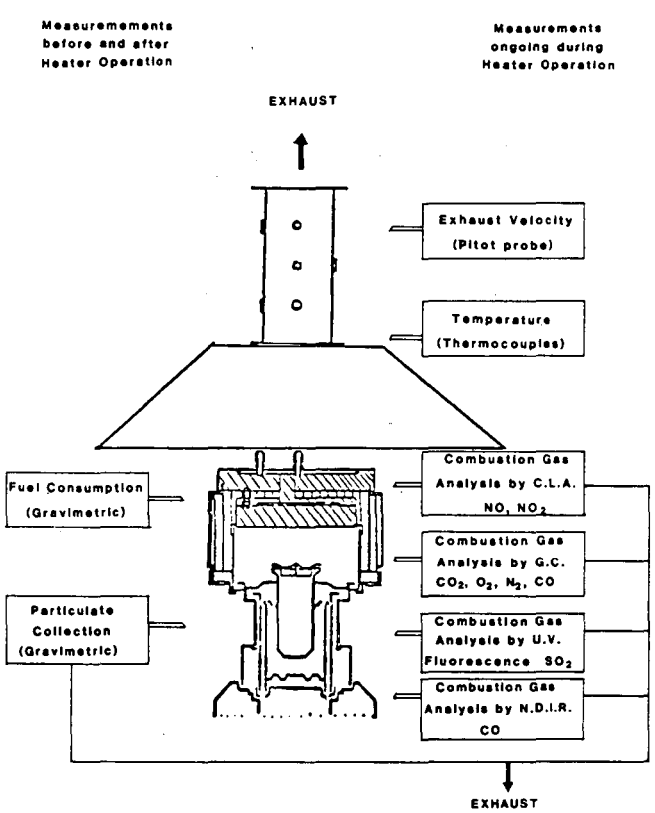

Figure 1. Experimental apparatus for measuring combustion products of unvented space heaters. (XBL 851-969)

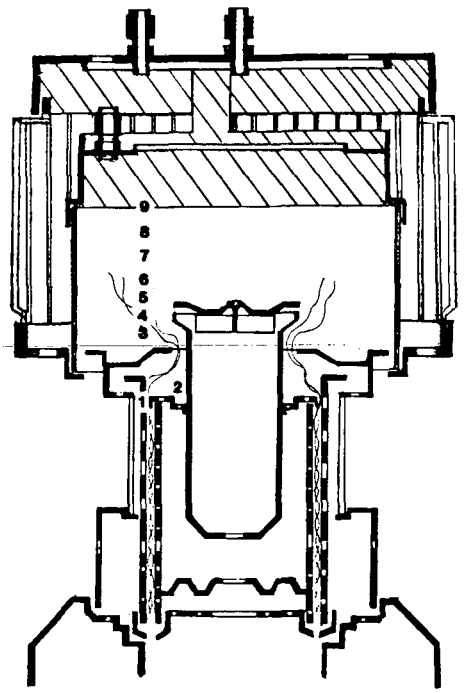

Figure 2. Axial probing positions in the multistage heater. (XBL 851-970)

Product composition, fuel consumption rate, temperature, pressure, and exhaust-stream mass flow rate were measured in the exhaust manifold to ascertain the effect of heater type and heater operating conditions on exhaust-gas composition. Prior to conducting experiments to determine the effect of operating parameters on final gas composition, measurements were performed to verify the reproducibility of the heater combustion and to determine the uniformity of conditions in the sampling manifold. Radial profiles of temperature, velocity, and composition measurements indicated that the exhaust gases were uniformly mixed. Velocity and temperature profiles were typical of turbulent flow in circular ducts. The fuel consumption of the heaters was sensitive to wick height, wick age, and volume of fuel in the tank. Heater design strongly influenced emission concentrations. The multistage heater had the smallest concentration of CO and intermediate concentrations of NO_x. The radiant heater had the largest concentrations of CO and smallest NO_x concentrations. The convective heater had the greatest NO_x concentrations. These data are detailed in Tables 2 and 3. Results were compared with chamber and other

Table 1. Axial profile of emission products in multistage heater.

Position[a] (cm)	ϕ[b]	Hydro-carbons (%)	CO_2 (%)	O_2 (%)	N_2 (%)	CO (%)	NO_x (ppm)	NO_2 (ppm)	NO (ppm)	Temp (K)
1		0.114	~5.19	~10.0	~65.1	~0.366	16.9	8.5	8.4	
2	2.64	0.0016	5.23	13.4	75.4	0.019	21.8	13.5	8.2	1080
3[c]	14.1	N.D.[d]	0.98	19.1	75.7	0.016	1.5	0.1	1.4	1210
4		0.0201	12.0	2.77	77.9	1.40	18.8	2.1	16.6	1330
5	2.20	N.D.	6.40	11.6	77.3	0.049				
6	1.99	N.D.	7.06	10.9	76.8	N.D.	11.9	1.6	10.2	
7	2.02	N.D.	7.04	11.2	77.9	N.D.	10.0	N.D.	10.2	
8	1.92	N.D.	7.18	10.4	75.6	N.D.	12.6	2.0	10.5	
9	1.84	N.D	7.56	9.94	76.0	N.D.				

[a]See Fig. 2.

[b](Air/fuel)/(air/fuel)$_{stoichiometric}$, estimated from measured O_2 and N_2 and assuming complete combustion.

[c]Outside of flame contour, in flow of dilution air.

[d]Not detectable.

Table 2. Comparison of heaters.

Heater[a]	Fuel consumption (kJ/hr)	ϕ	CO_2[b] (μg/kJ)	CO_2[b] (%)	Temperature[b] (K)
Radiant	8,040	12.8	85,000	(1.11)	390
	8,160	13.8	81,000	(1.05)	400
Convective	11,300	10.5	78,000	(1.37)	440
	11,600	11.1	76,000	(1.29)	430
Multistage	14,800	10.1	72,000	(1.41)	470
	14,600	10.2	75,000	(1.40)	450
	16,000	10.3	77,000	(1.39)	460

[a]All measurements performed with wick in high position.

[b]Measured in exhaust; CO_2 emission rate (μg/kJ) determined from exhaust flow rate.

Table 3. Comparison of heaters.

Heater[a]	Fuel consumption (kJ/hr)	Emissions[b] CO (μg/kJ)	CO (ppm)	NO (μg/kJ)	NO (ppm)	NO_2 (μg/kJ)	NO_2 (ppm)
Radiant	8,160	130	(29.3)	1.7	(0.4)	5.6	(0.8)
Convective	11,600	8.0	(2.2)	16.3	(4.2)	5.6	(0.9)
Multistage	14,800	4.6	(1.4)	6.0	(1.7)	m.e.[c]	m.e.
	14,600			5.7	(1.6)	5.6	(1.0)
	14,600	2.4	(0.7)	7.5	(2.1)	4.3	(0.8)

[a]All measurements performed with wick in high position.

[b]Measured in exhaust. Emission rate (μg/kJ) calculated from measured concentration and fuel consumption rate.

[c]Measurement error.

laboratory studies performed by other investigators, and agreement among the various studies was found to be quite satisfactory.

PLANNED ACTIVITIES FOR FY 1985

Experiments are currently under way to further characterize the emission of noxious combustion products such as aldehydes, peroxides, and oxidized sulfur species.

REFERENCES

1. Yamanaka, S., Hirose, H., and Takada, S. (1979), "Nitrogen Oxides Emissions from Domestic Kerosene-Fired and Gas-Fired Appliances," *Atmos. Environ. 13*, p. 407.
2. Kweller, E.R., and Cuthrell, W. (1980), "Ventilated Room Combustion Test Results for Three Portable Kerosene Heaters," unpublished report prepared for the U.S. Consumer Product Safety Commission, Washington, D.C.
3. Leaderer, B.P. (1982), "Air Pollutant Emissions from Kerosene Space Heaters," *Science 218*, p. 1113.
4. Traynor, G.W., *et al.* (1983), "Pollutant Emissions from Portable Kerosene-Fired Space Heaters," *Environ. Sci. Technol. 17*, p. 369.
5. Clarkson, S.G., Tom, B.L., Babcock, A.J., and Mehkeri, K.A. (1984), "Results of Testing Unvented Kerosene Heaters in a House: Gas Emissions, Surface Temperatures and Fuel Consumption Rates," presented at the 77th Annual Meeting of the Air Pollution Control Association, San Francisco, CA, June 1984.
6. Leaderer, B.P., Stolwijk, J.A.J., Zagraniski, R.T., and Qing-Shan, M. (1984), "A Field Study of Indoor Air Contaminant Levels Associated with Unvented Combustion Sources," presented at the 77th Annual Meeting of the Air Pollution Control Association, San Francisco, CA, June 1984.
7. Yamanaka, S. (1984), "Decay Rates of Nitrogen Oxides in a Typical Japanese Living Room," *Environ. Sci. Technol. 18*, p. 566.
8. Lionel, T., Martin, R.J., Brown, N.J. (1985), "A Comparative Study of Combustion in Kerosene Heaters," *Environ. Sci. Technol.*, in press.

Theoretical Combustion Chemistry*

N.J. Brown, O.M. Rashed, and A. Edlin

Bimolecular radical shuffling reactions in the gas phase represent an important class of elementary processes in complex systems, particularly combustion. The bimolecular reaction between H_2 and OH, which produces H_2O and H, is extremely important in combustion systems. In hydrogen/oxygen flame systems, this reaction[1] appears to be the principal source of water production at temperatures above 700 K to temperatures prior to the onset of partial equilibrium. The reaction is also the main source of water[2] in typical hydrocarbon-air flames at atmospheric pressure. Because of its importance, the H_2 + OH reaction has been the object of extensive theoretical and experimental study. We have recently investigated this reaction, using both statistical and dynamical approaches.[3–4]

ACCOMPLISHMENTS DURING FY 1984

We have performed a quasi-classical molecular dynamics study of the $H_2 + OH \rightarrow H_2O + H$ reaction with a modified potential energy surface. We have attempted to understand the role that the system's initial energy distribution plays in influencing reactivity. We have also computed a series of reaction cross sections necessary to determine the thermal rate coefficient at 1200 and 2000 K. We have placed special emphasis on determining the effect of reagent rotation on reactivity, and have also examined the influence of reagent vibration and translational temperature.

The methods of quasi-classical dynamics used in this study are similar to other treatments of four-atom systems.[5] The particular formalism used here incorporates three approximations: (1) the use of the Rashed-Brown modification to the Schatz-Elgersma[6] analytical fit to the Walsh-Dunning[7] potential surface; (2) the treatment of the dynamics with classical mechanics; and (3) the use of Monte Carlo averaging techniques to sample the phase space of the H_2 + OH system.

We have investigated reactivity in the H_2-OH system as a function of the initial translational temperature and the vibrational and rotational energies of H_2 and OH. The range of translational temperatures investigated was between 300 and 4000 K, with emphasis placed upon 1200 and 2000 K. The initial value of the rotational quantum number was in the range 0–6 for H_2 and 0–7 for OH. The initial values of the vibrational quantum number for both molecules was 0–4. The barrier for reaction is 6.1 kcal/mol, and the exoergicity is 15.1 kcal/mol.

Reactivity increases monotonically with translational temperature, and the sharpest increase occurs between 300 and 2000 K. At 2000 K, the average kinetic energy is approximately equal to the barrier height. The influence of translational energy in enhancing reactivity is consistent with the character of an exoergic reaction. According to Hammond's postulate,[8] the transition state should be more similar to reactants than to products since the reaction is exoergic; this is observed for the HHOH system and is responsible for its strong dependence on translational energy.

Rotational excitation of either H_2 or OH or both suppresses reactivity. For cases when one and only one molecule has initial rotational energy, reactivity is suppressed in proportion to the rotational energy of that molecule. For example, when the initial rotational quantum number of H_2 increases from $j = 0$ to $j = 4$—corresponding to a gain of approximately 3 kcal/mol rotational energy—the percentage suppression of reactivity that occurs is about 55%. The percentage suppression is the same for rotationally exciting OH by the same amount of energy. This is illustrated in Figs. 1 and 2 for ensembles at 1200 and 2000 K, respectively. The same percentage suppression is found for both values of the translational temperature. Thus there is no correlation between rotational suppression and translational temperature. If the rotational energy of one molecule is fixed and that of the other molecule is allowed to increase, reactivity is suppressed in proportion to the increasing rotational energy. The percentage decrease in reactivity is independent of the amount of fixed rotational energy of the other molecule, and it thus appears that the rotational motions of both molecules are uncorrelated. The major effect of reagent rotation is to reduce the probability of achieving the proper H_2-OH orientation required for reaction.

The effect of reagent vibrational excitation in either or both molecules was determined at 1200 and 2000 K (Figs. 3 and 4). Vibrational excitation of H_2 has little effect upon reactivity for ensembles at 1200 K with vibrational states $v < 4$. An increase in reactivity is observed at $v = 4$. For ensembles at 2000 K, a monotonic increase in reaction cross section occurs with increasing H_2 vibrational energy. The motion

*This work was supported by the Director, Office of Energy Research, Office of Basic Energy Sciences, Chemical Sciences Division of the U.S. Department of Energy under Contract No. DE-AC03-76SF00098.

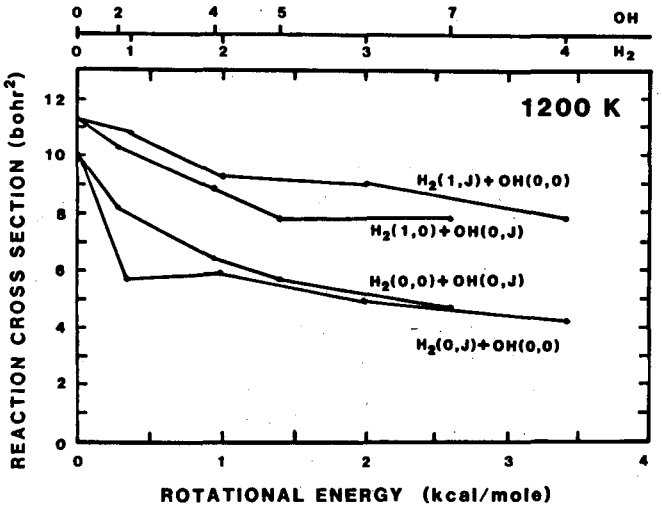

Figure 1. Plot of the reaction cross section as a function of the rotational energy for the H_2 + OH ensembles at 1200 K. The units of the reaction cross section are square bohrs and those for rotational energy are kcal/mol. Both molecules are in the ground vibrational state.
(XBL 851-917)

associated with the H_2 bond is coupled to the reaction coordinate motion, with the result that the vibrational excitation influences reactivity. Vibrational excitation of OH between $v = 0$ and $v = 4$ produces negligible change in the reaction cross section. The OH bond acts as a spectator during the reaction and does not contribute energy to crossing the barrier.

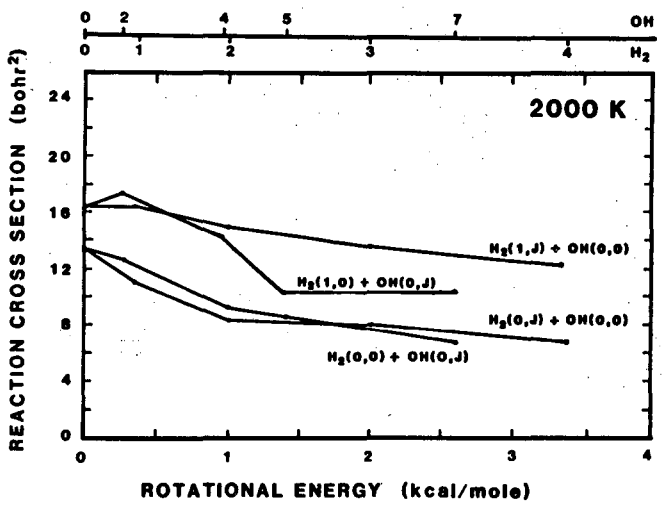

Figure 2. Plot of the reaction cross section as a function of the rotational energy for the ensembles at 2000 K. The units of the reaction cross section are square bohrs and those for rotational energy are kcal/mol. Both molecules are in the ground vibrational state. (XBL 851-919)

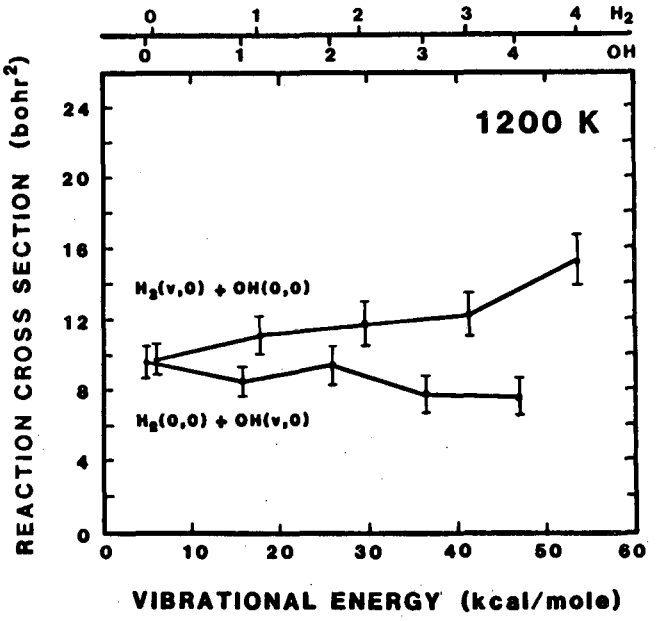

Figure 3. Plot of the reaction cross section as a function of the vibrational energy for the ensembles at 1200 K. The units of the reaction cross section are square bohrs and those for vibrational energy are kcal/mol. Both molecules are in the ground rotational state. (XBL 851-920)

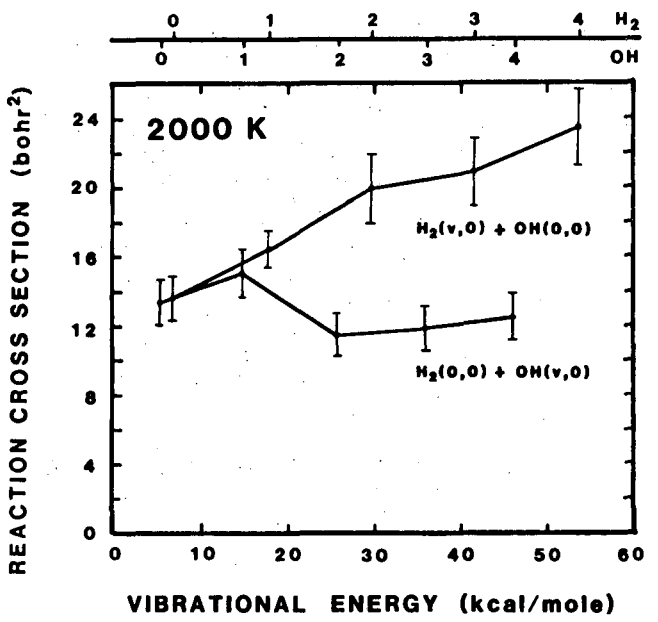

Figure 4. Plot of the reaction cross section as a function of the vibrational energy for the ensembles at 2000 K. The units of the reaction cross section are square bohrs and those of vibrational energy are kcal/mol. Both molecules are in ground rotational state. (XBL 851-918)

The reaction cross sections evaluated at 1200 and 2000 K were used to compute values of the thermal rate coefficient at each temperature. The cross section for each vibrational-rotational state was multiplied by the statistical weight of the state, and the contributions from all significantly populated states were summed to yield k, the thermal rate coefficient. The following values were obtained:

Temperature (K)	k(cm^3/mol·sec)
1200	9.4×10^{12}
2000	1.8×10^{13}

The computed value compares favorably with experimentally[9] determined values at 2000 K. The agreement at 1200 K is less satisfactory since the computed value appears to be too large. The agreement between theory and experiment at both temperatures, however, indicates that the potential surface is a reasonable representation of the HHOH potential energy.

We have also calculated the thermal rate coefficients for the $H_2 + OH \rightarrow H_2O + H$ reaction and all isotopes obtained by adding one or two deuterium atoms over the temperature range 200 K to 4000 K. Calculations were performed microcanonically, taking full account of angular momentum conservation, following the technique developed by Miller.[10] Tunneling corrections using a generalized Eckart potential were performed by convolving the tunneling correction into the rotational and vibrational number of states. Transition-state geometries and frequencies were those determined from the *ab initio* results of Walsh and Dunning[7] and the fitted potential of Schatz and Elgersma.[6]

Although considerable analysis remains to be accomplished, preliminary results indicate that tunneling had a significant effect on the low-temperature rate coefficients. Rate coefficients determined from the transition-state properties of the *ab initio* surface were larger than those determined from the fitted surface. Calculated isotope effects were compared with the experimentally determined values of Ravishankara *et al.*,[9] and the agreement was satisfactory.

Work was initiated, in collaboration with Dr. James A. Miller of Sandia National Laboratory, on a determination of rate coefficients for the HCN + O reaction. This reaction has a number of product channels, and branching ratios will be computed for channels yielding CN + OH, H + NCO, and NH + CO. Direct count, angular momentum conservation, and tunneling corrections will be applied to microcanonical transition-state theory.

PLANNED ACTIVITIES FOR FY 1985

Energy transfer in reactive and nonreactive H_2 + OH collisions will be analyzed in detail. Energy transfer is being investigated as a function of the initial translational temperature and the rotational and vibrational energy of each molecule. The average energy transferred per collision to each degree of freedom will be computed. Final energy transfer distributions associated with energy transfer into the various degrees of freedom will be determined. Correlation coefficients, which provide a measure of the relationship between two energy transfer quantities in a single collision, will be computed. Thermal rate coefficients for H_2 + OH will be determined with quasi-classical dynamics at temperatures where good experimental results are available.

A dynamics study of the isotopically substituted reactants in the HHOH system will be undertaken, and results will be compared with experiment and statistical calculations. The results of the transition-state calculations for the HHOH system, including direct state count, angular momentum conservation, and tunneling, will be analyzed. Thermal rate coefficients will be determined with quasi-classical dynamics at temperatures below 1200 K. Extensive Monte Carlo averaging over all initial states of the two molecules will be used to determine the thermal rate coefficient.

Work will continue on the HCN + O reactions. Rate coefficients will be computed in several ways: canonically, microcanonically, microcanonically with angular momentum conservation, and microcanonically with angular momentum conservation and tunneling corrections.

A long review paper on the use of theoretical chemical kinetics in combustion science will be written over the summer. After that, we hope to initiate work on formaldehyde decomposition and investigate the non-Arrhenius behavior of the CO + OH reaction.

REFERENCES

1. Brown, N.J., *et al.* (1978), "Low Pressure Hydrogen/Oxygen Flame Studies," *Combustion and Flame 33*, p. 151.
2. Warnatz, J. (1984), "Rate Coefficients in the C/H/O System," in *Combustion Chemistry*, William C. Gardiner, Jr., Ed., Springer-Verlag, New York, p. 197.
3. Rashed, O. and Brown, N.J. (1984), "A Molecular Dynamics Study of the Reaction: H_2 + OH $\rightarrow$ H_2O + H," accepted for publication in *Journal of Chemical Physics*, LBL-18531.

4. Brown, N.J. and Edlin, A.S. (1985), "Transition State Calculations of the Thermal Rate of the $H_2 + OH \rightarrow H_2O + H$ Reaction, Including Isotope Effects, Tunneling, and Angular Momentum Conservation," to be published.

5. Brown, N.J. and Miller, J.A. (1984), "Collisional Energy Transfer in the Low-Pressure-Limit Unimolecular Dissociation of HO_2," *J. Chem. Phys. 80*, p. 5568.

6. Schatz, G.C. and Elgersma, H. (1980), "A Quasi-Classical Trajectory Study of Product Vibrational Distributions in the $OH + H_2 \rightarrow H_2O + H$ Reaction," *Chem. Phys. Lett. 73*, p. 21.

7. Walsh, S.P. and Dunning, T.H. (1980), "A Theoretical Study of the Potential Energy Surface for $OH + H_2$," *J. Chem. Phys. 72*, p. 1303.

8. Hammond, G.S. (1955), "A Correlation of Reaction Rates," *J. Amer. Chem. Soc. 55*, p. 334.

9. Ravishankara, A.S., Nicovich, J.M., Thompson, R.L., and Tully, F.P. (1981). "Kinetic Study of the Reaction of OH with H_2 and D_2 from 250 to 1050 K," *J. Phys. Chem. 85*, p. 2498.

10. Miller, W.H. (1979), "Tunneling Correction to Unimolecular Rate Constants with Application to Formaldehyde," *J. Amer. Chem. Soc. 101*, p. 6810.

Lean-Limit Combustion Processes*

R.F. Sawyer and D. Dunn-Rankin

Operation of homogeneous-charge, reciprocating internal combustion engines under lean conditions promises improved efficiency, reduced emissions, and broadened fuel tolerance. Important fundamental processes impeding the realization of these advantages include ignition of lean mixtures, flame propagation, flame interactions with walls, and quenching of combustion during expansion. Lean-limit combustion is being studied using square-piston engine facilities that allow the observation of combustion events under conditions simulating engine operation. Constant-volume combustion chambers allow more detailed investigation of combustion processes with well-controlled conditions.

ACCOMPLISHMENTS DURING FY 1984

An experimental study of the combustion of lean premixed gases in a square cross-section enclosure fitted with a reciprocating piston[1] revealed flame-front instabilities. The formation of these "tulip-shaped" flames is a well-known phenomenon associated with nonsteady flame propagation in closed tubes and ducts. The qualitative features of such flames have been documented by various investigators for more than 60 years[2,3] but an explanation of the phenomenon has eluded researchers. Several hypotheses about the cause of this flame folding include spontaneous instability of the flame front, reflection of flame-generated pressure waves from the closed end impinging on the flame front, and the interaction of flame-driven fluid circulation with the flame. Flame-driven flows have been measured using laser Doppler anemometry (LDA) and flame development recorded using high-speed schlieren cinematography.[4]

The experimental apparatus (Fig. 1) consists of a laser Doppler anemometer, a high-speed schlieren cinematographic system, a combustion chamber, a spark ignition source, a gas-mixing device, and a data-logging computer. A two-point igniter is situated near one end wall of the chamber (Fig. 2). A 4-watt argon ion laser operated at 514 nm is used in the LDA system. The LDA probe is formed with a beam splitter of 50 mm fixed separation and a lens of 250 mm focal length arranged to measure axial velocity. The two beams are frequency-shifted by Bragg cells to remove directional ambiguity.

The ignition source simultaneously initiates combustion and triggers the data acquisition system. The analog LDA output is digitized at 30 kHz. Measurements are taken along the central axis of the chamber in 10-mm increments from $x = 20$ mm to $x = 140$ mm. The flame is photographed from two perpendicular planes to remove the ambiguity that arises from line-of-sight integration inherent in the schlieren technique. Flame trajectories are shown in Fig. 3.

*This work was supported by the Assistant Secretary for Conservation and Renewable Energy, Office of Energy Systems Research, Energy Conversion and Utilization Technologies Division of the U.S. Department of Energy under Contract No. DE-AC03-76SF00098.

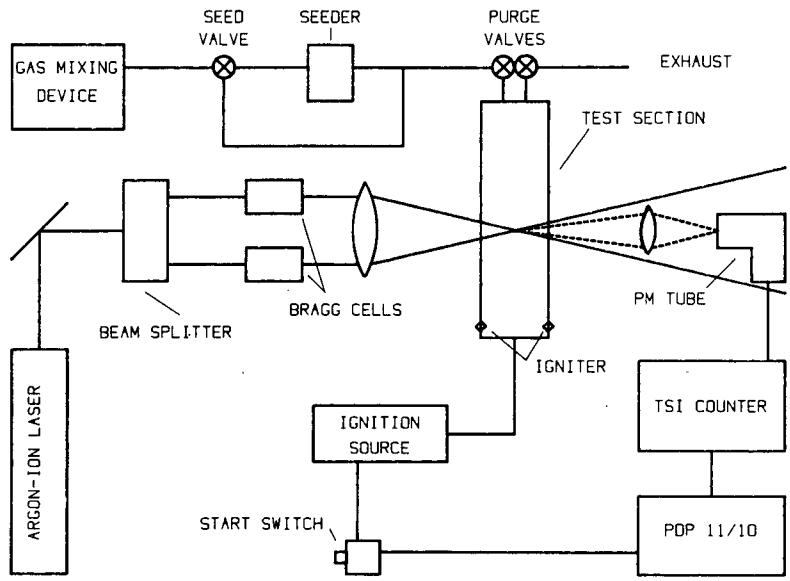

Figure 1. Schematic of experimental apparatus for the study of unsteady flame propagation in premixed gases. (XBL 851-1064)

Measures of centerline velocities provide a time history of the flow velocity of both the unburned reactants in front of the flame and the product gases behind the flame (Fig. 4). For the first 15 msec, the unburned gas velocity decreases linearly from a maximum at the flame to zero at the end wall. At 20 msec the unburned gas velocity drops to a small constant value of about 1 m/sec, the velocity just ahead of the flame becomes negative, and the tulip-shaped flame begins to form. A flow reversal occurs in the burned gas, beginning at approximately 45 msec. A small vortex in the burned gas is noticeable at $x = 50$ mm for times greater than 40 msec. The results suggest that the instability and "tulip" flame formation is the result of unburned gas flow induced by the flame propagation.

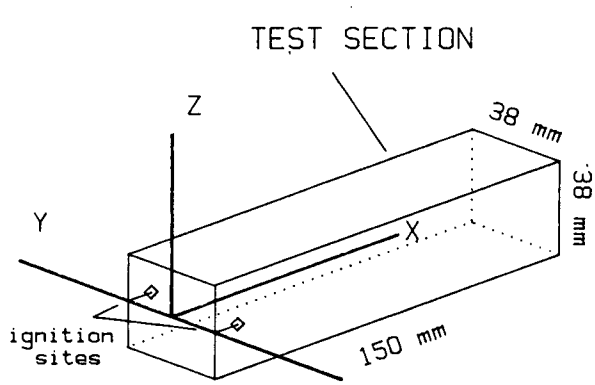

Figure 2. Combustion chamber showing location of spark igniters. (XBL 851-1063)

PLANNED ACTIVITIES FOR FY 1985

Off-centerline velocities will be measured, allowing mapping of the entire flow field and detailed characterization of the flame-induced flows responsible for the observed flame instability. Comparison with a theoretical fluid mechanical model will be made.

Lean-limit flame propagation experiments using the crank-driven compression-expansion apparatus (CE-2) will be resumed. These experiments will be extended to compression ratios higher than the 8:1

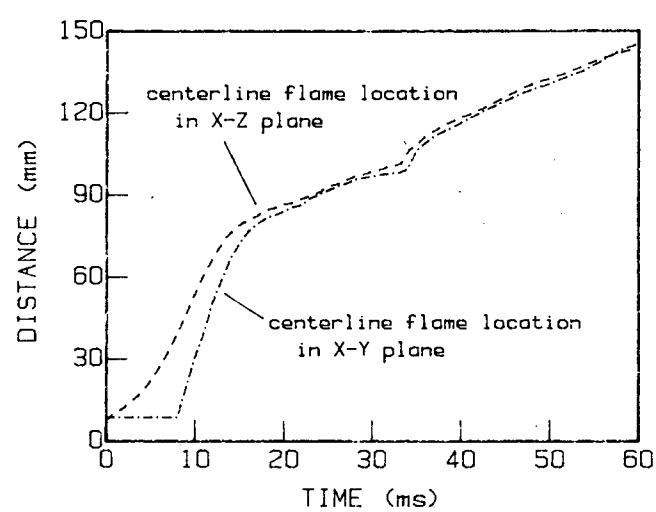

Figure 3. Centerline flame trajectory from two orthogonal directions. (XBL 851-1065)

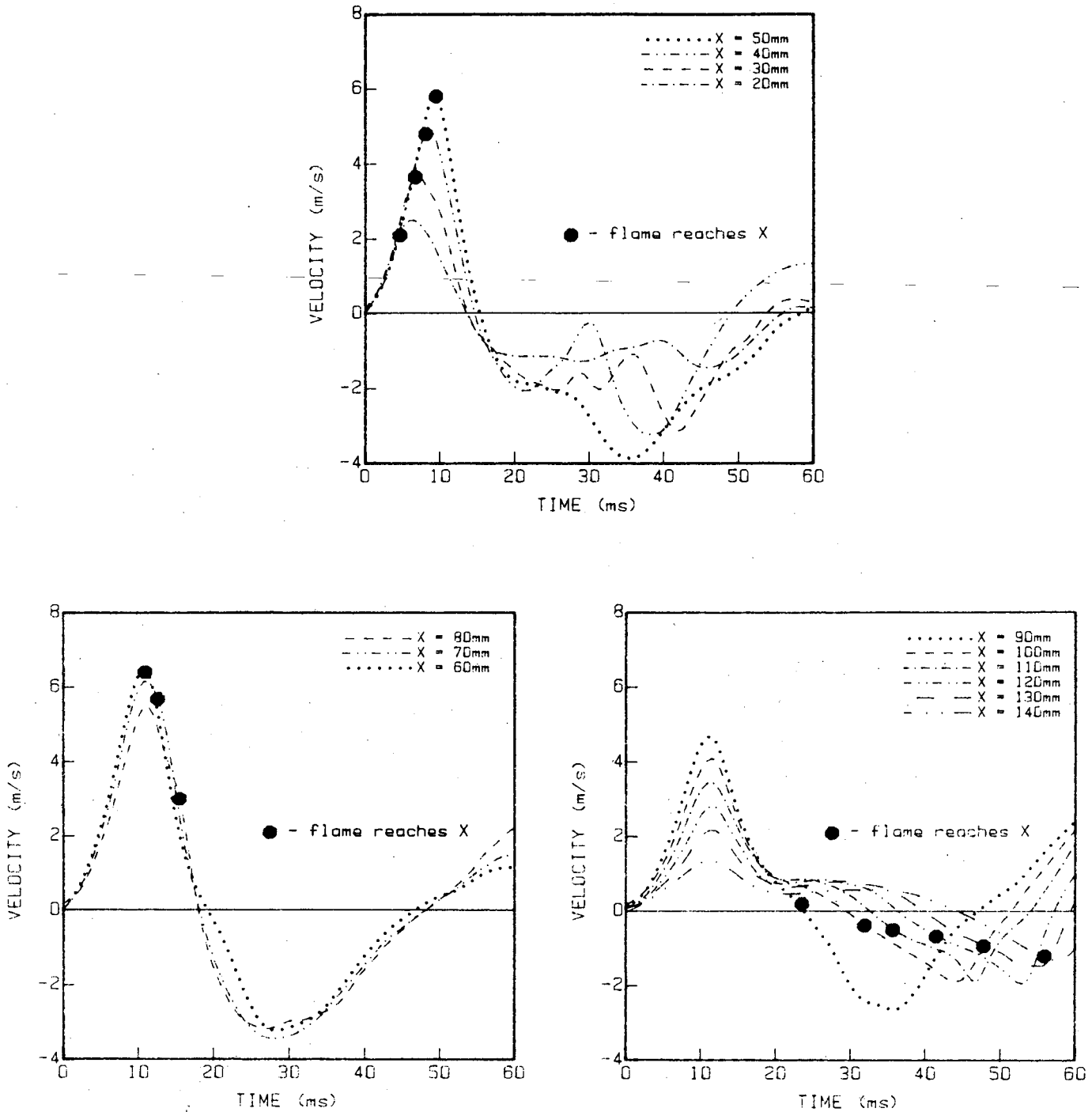

Figure 4. Centerline velocity histories for measurement locations along the duct. (XBL 851-1066)

ratio of the earlier work. Information on lean-limit combustion processes under conditions characteristic of design-goal lean combustion engines will be obtained. The crank-driven CE-2 facility recently has been modified to allow operation at compression ratios up to 22:1.

REFERENCES

1. Steinhert, W., Dunn-Rankin, D., and Sawyer, R.F. (1982), *Influence of Chamber Length and Equivalence Ratio on Flame Propagation in a Constant Volume Duct,* Western States

Section/The Combustion Institute Paper No. 82-52 and LBL-14965.
2. Ellis, O.C. de C. (1928), "Flame Movement in Gaseous Explosive Mixtures (Part 7), *Fuel: a Journal of Fuel Science* 7, p. 502.
3. Guenoche, H. (1964), "Flame Propagation in Tubes and Closed Vessels," in Non-Steady Flame Propagation, G.H. Markstein, Ed., Pergamon Press, New York.
4. Dunn-Rankin, D., Cheng, R.K., and Sawyer, R.F. (1984), "LDA Study of Non-Steady Flame Propagation in a Constant Volume Duct," to be published in *Advances in Laser Doppler Anemometry.*

Fluid Mechanics of Combustion*

C.-C. Hsaio, S.-L. Yuan, A.J. Chorin, and A.K. Oppenheim

Our work is based principally on numerical modeling techniques we developed in the course of our previous studies, as described in the FY 1982 annual report.[1] The major effort has been directed toward the investigation of the mechanism of turbulent combustion systems under a variety of conditions encountered in engineering practice.

ACCOMPLISHMENTS DURING FY 1984

The solutions we obtained this year pertained to two fundamental cases: (1) turbulent flames stabilized behind a rear-facing step in a configuration typical of the so-called dump combustor, and (2) initiation of turbulent flame in the wake behind a cylinder in a configuration typical of the classical bluff-body flameholder. They are reported here for each case in turn.

Turbulent Flame Behind a Step

The technique we developed previously has been refined to permit modeling of more complicated geometrical configurations and reprogrammed for a Cray computer. This provided us with an ability to take into account more practical details of the flow field, as well as to generate a sample of data sufficiently large to obtain their stochastic interpretation. In order to demonstrate the utility of these improvements, we have treated first the case studied in earlier work, namely, turbulent combustion in a tunnel.[2]

A sample of the results we obtained is depicted in Fig. 1, showing, from top to bottom, the inflamed vorticity vector field, the corresponding average axial velocity profiles, and the root-mean-square of axial velocity fluctuations. A complete set of results was included in a paper presented at the 20th Symposium (International) on Combustion.[3]

Inflammation of a Turbulent Wake

Following our study of a turbulent jet reported last year,[4,5] we carried out an investigation of the formation and inflammation of a turbulent wake. We selected for this purpose the flow field past a cylinder—the classical case of the so-called von Kármán street.

This time, the results were expressed not only in terms of the vorticity vector field, as we have done before, but also in the form of streamlines,† streaklines,‡ and particle paths.§ For illustration, they are displayed here in Fig. 2, which, besides these four types of records evaluated for inert flow, includes also a vorticity vector field associated with combustion.

PLANNED ACTIVITIES FOR FY 1985

In continuation of our studies, we intend to pursue the numerical modeling analysis in two phases:

(1) Computation of flow systems of different geometrical configurations; this is to include symmetric damp combustors of different expansion ratios (width of channel to that of inlet duct), rectangular cavities at the channel wall of different aspect

*This work was supported by the Office of Energy Research, Office of Basic Energy Sciences, Engineering, Mathematics, and Geosciences Division of the U.S. Department of Energy under Contract No. DE-AC03-76SF00098, and by NASA-Lewis Research Center under Grant NAG 3-131.

†Curves tangent at a given instant of time to the velocity vector.

‡Loci of points indicating at a given instant the location of all the particles which passed through some specified fixed points in the flow field, corresponding to a snapshot photograph of the so-called passive particles (a dye introduced at fixed points across the field) after a sufficiently long time interval to have the flow field fully earmarked.

§Trajectories of some fixed fluid particles.

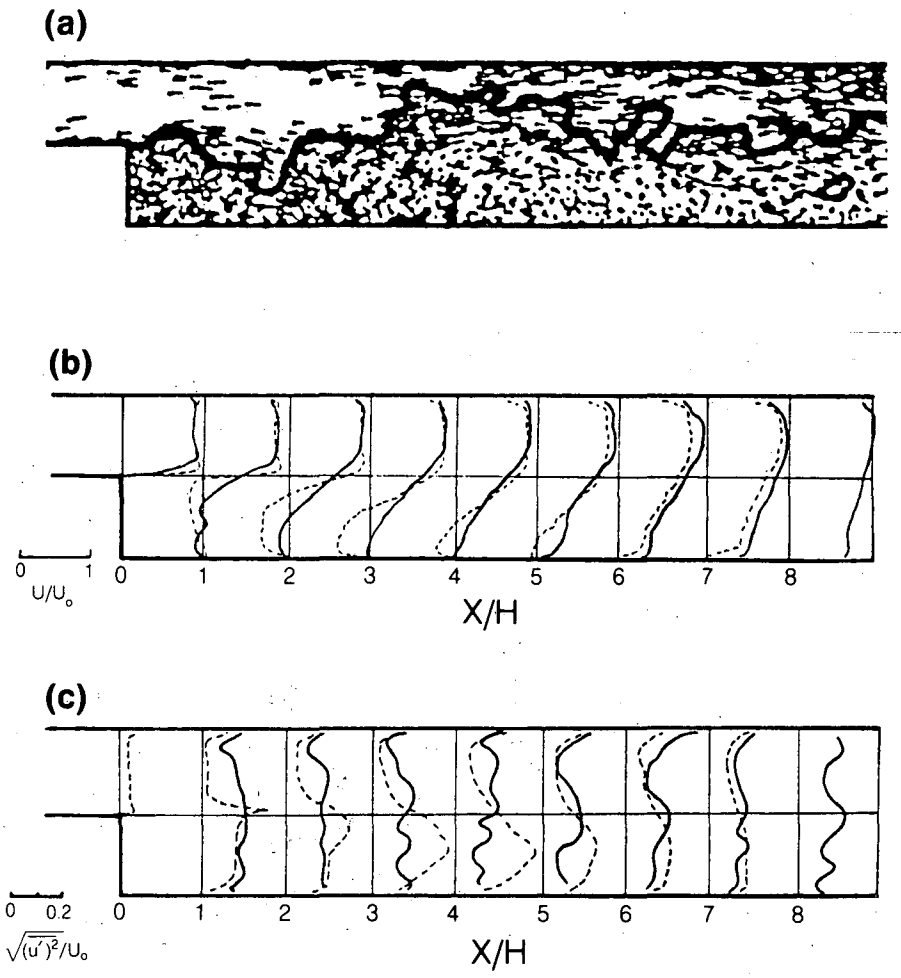

Figure 1. (a) Inflamed vorticity vector field in channel flow behind a step, with (b) concomitant profiles of average velocity component in the axial direction and (c) the corresponding root-mean-square of axial velocity fluctuations.
(XBL 851-9914)

ratios (length to depth), barriers on the side of a channel of different relative heights, as well as symmetric barriers forming orifices of different sizes in channel flow.

(2) Computation of flame-generated flows in an enclosure, a problem of particular significance with respect to internal combustion engines. We propose to start by treating the problem of a flame initiated at the midpoint of the short side in an oblong rectangle. The analysis is to be based on the *projection method* developed by Chorin[6] for the solution of the Navier-Stokes equations at low Reynolds numbers; the flame is considered as a Stefan-like interface propagating at a prescribed normal velocity in an incompressible medium consisting of two components of different density: the unburnt and the burnt gas, one being transformed into the other by crossing the flame.

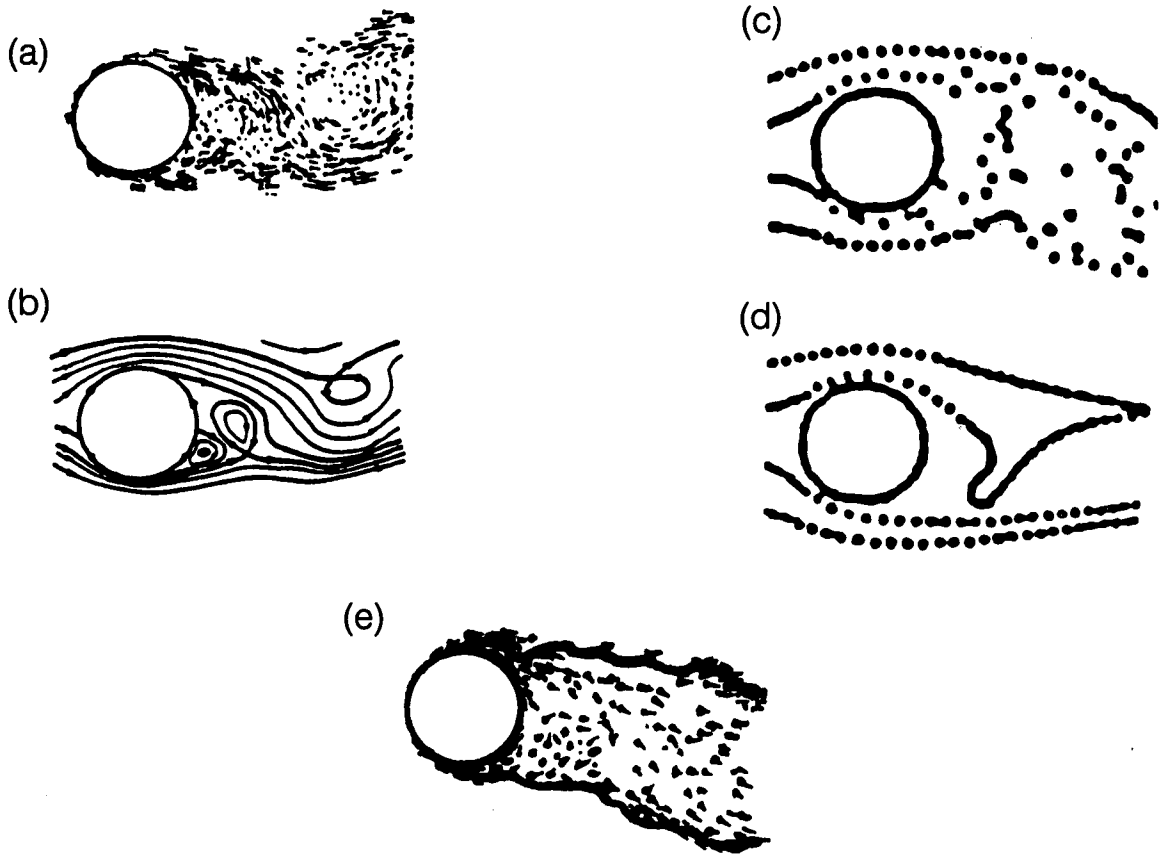

Figure 2. Turbulent flow in the wake of a cylinder, expressed respectively in terms of (a) the inert vorticity vector field, (b) streamlines, (c) streaklines, (d) particle paths, and (e) the inflamed vorticity vector field.
(XBL 852-1089)

REFERENCES

1. Ghoniem, A.F., Chorin, A.J., and Oppenheim, A.K. (1983), "Numerical Modeling of Turbulent Combustion," *Energy and Environment Division, FY 1982 Annual Report, Environmental Research Program*, LBL-15298, p. 4-55.
2. Ghoniem, A.F., Chorin, A.J., and Oppenheim, A.K. (1982), "Numerical Modelling of Turbulent Flow in a Combustion Tunnel," *Phil. Trans. Roy. Soc. London A304*, p. 303.
3. Hsiao, C.-C., Ghoniem, A.F., Chorin, A.J., and Oppenheim, A.K. (1984), "Numerical Simulation of a Turbulent Flame Behind a Rearward-Facing Step," to be published in the Proceedings of the 20th Symposium (International) on Combustion.
4. Ghoniem, A.F., Chorin, A.J., Hsaio, C.-C., and Oppenheim, A.K. (1984), "Fluid Mechanics of Combustion," *Applied Science Division, FY 1983 Annual Report, Environmental Research Program*, LBL-17073, p. 4-53.
5. Ghoniem, A.F., Chen, D.-Y., and Oppenheim, A.K. (1984), "Formation and Inflammation of a Turbulent Jet," American Institute of Aeronautics and Astronautics Paper 84–0572, 10 pp.
6. Chorin, A.J. (1968), "Numerical Solution of the Navier-Stokes Equations," *Mathematics of Computation 22* (104), p. 745.

Controlled Combustion*

N.J. Brown, C.F. Edwards, M. Forsha, K. Hom, D. Lucas, A.K. Oppenheim, T. Parker, R.B. Peterson, R.F. Sawyer, and H.E. Stewart

The main objective of this program is to attain fundamental understanding of the chemical and physical processes that govern the evolution of exothermic energy in combustion systems, especially at their initial stages, as well as the effects of its deposition in the reacting medium. Basic problems one faces in this connection and the methodology adopted for their solution were described in the FY 1982 annual report.[1] The concepts put forth there were brought up to date in a paper focusing upon the problem of knock in internal combustion engines[2] and their background enhanced by the publication of two papers based on our earlier work.[3,4] Major emphasis is placed on investigating specifically the life history of active radicals and the role they play in the development and sustenance of the exothermic process of combustion, as revealed in particular by the concomitant temperature profile.

ACCOMPLISHMENTS DURING FY 1984

As before, the principal effort was directed toward the investigation of ignition processes. Last year, our work consisted of the following three phases:

(1) Measurements made with the molecular beam spectrometer.
(2) Tests of plasma jet ignition in a single-pulse machine.
(3) Experimental studies of high-temperature liquid-fuel jet ignition.

Progress made in each of these phases is reported here in turn.

Molecular Beam Spectrometry

Studies of flash-ignited combustion of mixtures of methane, oxygen, argon, and nitrogen dioxide in a constant-volume reactor have been concluded.[5–8] Temperature measurements of the photolysis and combustion events, obtained with a time-of-flight technique, indicate that the gas sampled by the source cone is representative of the reacting medium. The temperatures measured appear quite reasonable, as confirmed by calculations based on the use of the flash lamp output, absorption coefficient of NO_2, and the gas dynamic properties of the molecular beam.

All significant stable reactants and products were measured with a time resolution on the order of 100 microseconds. Mass signals were normalized to those of inert components in order to compensate for changes in beam intensity caused by the rapidly changing source conditions. Pressure traces recorded simultaneously were used to correlate mass signals, significantly reducing thereby the transient effect of time-dependent noise associated with experimental disturbances.

The results show that the primary sensitization mechanism of NO_2 is different from shock-heated mixtures of the same reactants, and that a chain reaction involving both NO_2 and CH_4 is necessary to rationalize measured induction times. We intend to investigate this mechanism further by the use of an excimer laser, which can provide oxygen atoms in a single electronic state, and by the photolysis of N_2O, yielding N_2 and O.

Concomitantly with the flash-ignited combustion studies, we have developed a novel technique based on the use of electron impact fluorescence to measure species concentration histories in the course of transient combustion events. The basic concept is described schematically in Fig. 1. The molecular beam is crossed with an electron beam, while light emission due to fluorescence, thus induced, is sensed at right angles to both beams by a photomultiplier tube. The technique offers the advantages of good

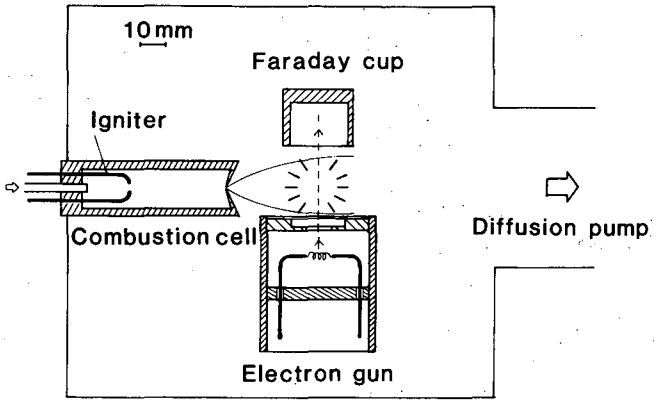

Figure 1. Schematic diagram of the apparatus for electron-impact fluorescence measurement.
(XBL 8412-5330)

*This work was supported by the Office of Energy Research, Office of Basic Energy Sciences, Engineering, Mathematics, and Geosciences Division of the U.S. Department of Energy under Contract No. DE-AC03-76SF00098, by the National Science Foundation under Grant CPE-8115163, and by NASA–Lewis Research Center under Grant NAG 3-137.

time resolution, high species selectivity and sensitivity, and low equipment cost.

Steady-state experiments were conducted to obtain fluorescence spectra of pure gases, namely CO, CO_2, CH_4, O_2, N_2, and Ar. The wavelength yielding the strongest signal was then selected for each species, and a narrow band around it was subsequently used in transient experiments to obtain the time-resolved concentration histories. We use for this purpose a 1/2.6/10.4 mixture of methane, oxygen, and argon initiated by a spark discharge at an initial pressure of 350 torr and room temperature. Concentration histories obtained under such conditions for CO_2, CO, CH_4, O_2, and Ar were in good agreement with the measurements we made previously with the mass spectrometer.

Plasma Jet Ignition

A photographic study of ignition and flame propagation processes was conducted using plasma ignitors in an optical-access engine. The performance of two types of jet ignitors, one using quartz and the other a paraffin liner, as well as that of a high-energy spark-gap discharge, was compared with that of a conventional spark plug.

For each ignitor, basic features of ignition and combustion at the lean limit were revealed. A standard spark permitted lean operation down to an equivalence ratio of ~0.7 after which misignition occurred. Plasma-jet ignitors provided an extension of the lean limit to ~0.5 in equivalence ratio. In this case, the lean limitation was shown to take the form of either extinction of the flame kernel or too slow a flame propagation rate. The plasma jet with paraffin liner exhibited the best performance, igniting mixtures as lean as ~0.4 in equivalence ratio. Performance characteristics of this ignitor demonstrated that it may yield substantial benefits by the improvements it is capable of imparting to the chemical kinetic and fluid dynamic processes of ignition.

In a previous study, we investigated the performance of a number of plasma ignition systems in a CFR† engine.[9] We found that, for moderately lean air/fuel mixtures, the power, emissions, and efficiency were relatively independent of the type of ignitor used. As the fuel content in the charge was diminished, engine operation with a conventional spark gap became limited by the onset of misfire. Plasma-jet ignitors, on the other hand, allowed lean operation to be extended past the misfire limit of the spark gap down to an equivalence ratio of ~0.6. Furthermore, the nature of the lean limit for the plasma jet was distinctly different. As the relative air content was augmented, the power and efficiency of the plasma-jet-ignited engine decreased monotonically, approaching zero at an equivalence ratio of 0.53. This difference in behavior led us to conclude that the lean limitation of the plasma jet was by partial burn or extinction rather than by misignition. Moreover, we found a substantial improvement in the performance of the plasma-jet-ignited engine when it was operated at relatively low air/fuel ratios. We attributed this to the ability of the plasma jet to penetrate into the fresh mixture and impregnate a sizable portion of it with active ignition sources.

In subsequent studies made this year,[10] schlieren cinematographic records were obtained of the process of plasma ignition in a square-piston, optical-access engine. The piston was 86 mm on a side and ran unlubricated between two stainless steel walls and two quartz windows. Compression sealing was provided by three graphite "ring" assemblies in the piston. The piston area and stroke, as well as clearance height, were identical to those of a conventional CFR engine. Overhead intake and exhaust valves driven by the engine camshaft were employed. Ports were provided for a piezoelectric pressure transducer, as well as for the plasma ignitor.

The test section was mounted upon the base of a CLR‡ engine (Fig. 2), providing the crank and connecting rod for piston motion, as well as cams for the valves. Coupled to the CLR was an electromagnetic clutch/brake unit allowing the engine to be driven by a synchronous motor and flywheel. Data acquisition and engine control were accomplished by means of a DEC PDP 11/03 minicomputer and programmable digital timer. Synchronization of the engine with the control electronics was achieved by the use of an optical shaft encoder that provided information on piston position at intervals of one-half crank angle degree.

Schlieren photographs of combustion initiated by a plasma-jet ignitor fitted with a paraffin liner are shown in Fig. 3 for a propane/air mixture at an equivalence ratio of 0.5. Concomitant pressure histories are displayed on the accompanying diagram, the engine monitoring and firing pressures being denoted by P_m and P_f respectively. The difference between the two curves at any time provides a measurement of the amount of exothermic energy evolved by the combustion process. The photographic sequence depicts the flame initiation and travel during a 140° interval following the ignitor discharge.

†Committee for Fuel Research.

‡Committee for Lubrication Research.

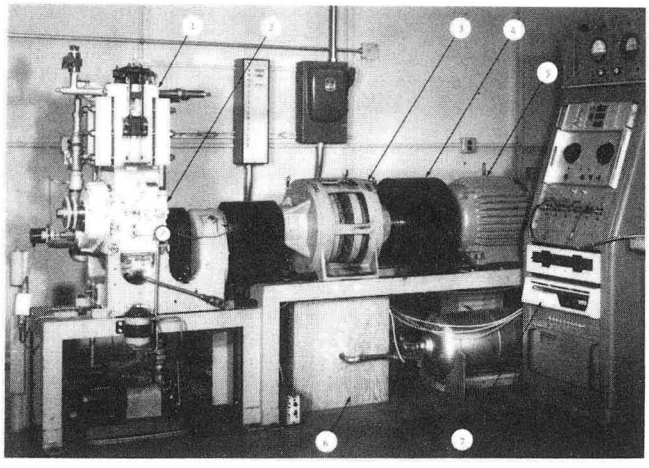

Figure 2. The single-pulse machine. (1) test section; (2) base of CLR engine; (3) electromagnetic clutch/brake unit; (4) flywheel; (5) synchronous drive-motor; (6) chamber for fuel/air mixture; (7) computerized electronic control system. (XBB 8412-9532)

As demonstrated by these records, the paraffin-lined injector was able to ignite and inflame the combustion chamber in its entirety—an achievement which neither the high-energy spark nor the quartz-lined plasma-jet ignitor could attain—although most of the burning took place in the course of the expansion stroke.

Spray Ignition

Ignition of fuel sprays is at the heart of the operation of diesel engines. The induction period (the time between the start of injection and the beginning of the exothermic process of combustion) occupies a prominent portion of the working cycle. It is with this concept in mind that we became involved in the study of the fundamental features of spray ignition, as reported in last year's annual report.[11]

Of particular interest in this respect was the dependence of the induction period upon the temperature of the spray, especially when it was at a level of thermodynamically supercritical conditions for the fuel. Experiments conducted for this purpose involved the use of a stainless-steel cylindrical chamber located in a high-temperature oven, both provided with quartz windows for optical insight in the axial direction of the radially injected spray. The process of spray formation followed by ignition was recorded by high-speed schlieren cinematography in combination with measurements of needle motion and chamber pressure. Pure *n*-dodecane, whose critical conditions are 386°C and 17.9 atm, was used as fuel, whereas its spray and the air in the chamber were maintained at the same pressure and temperature level. An example of experimental records is given by Fig. 4, obtained at an initial temperature of 600°C and a pressure of 28.2 atm.

Our results indicate a practically insignificant dependence of the induction period, τ, on pressure, whereas the effect of the temperature, T, is exponential in nature, so that it could be correlated in terms of the following Arrhenius relationship:

$$\tau = A \exp(T_a/T)$$

where $A = 2.69 \times 10^{-8}$ sec and $T_a = 9032$ K.

PLANNED ACTIVITIES FOR FY 1985

Next objectives for each of the three phases of our research on controlled combustion are as follows:

(1) Measure, by molecular beam spectrometry, the temperature and species concentration profiles of a plasma jet.
(2) Examine, by high-speed laser schlieren cinematography, the transient processes associated with the formation of a plasma jet.
(3) Investigate, using the recently constructed shock tube, the characteristic features of high-temperature fuel-spray ignition.

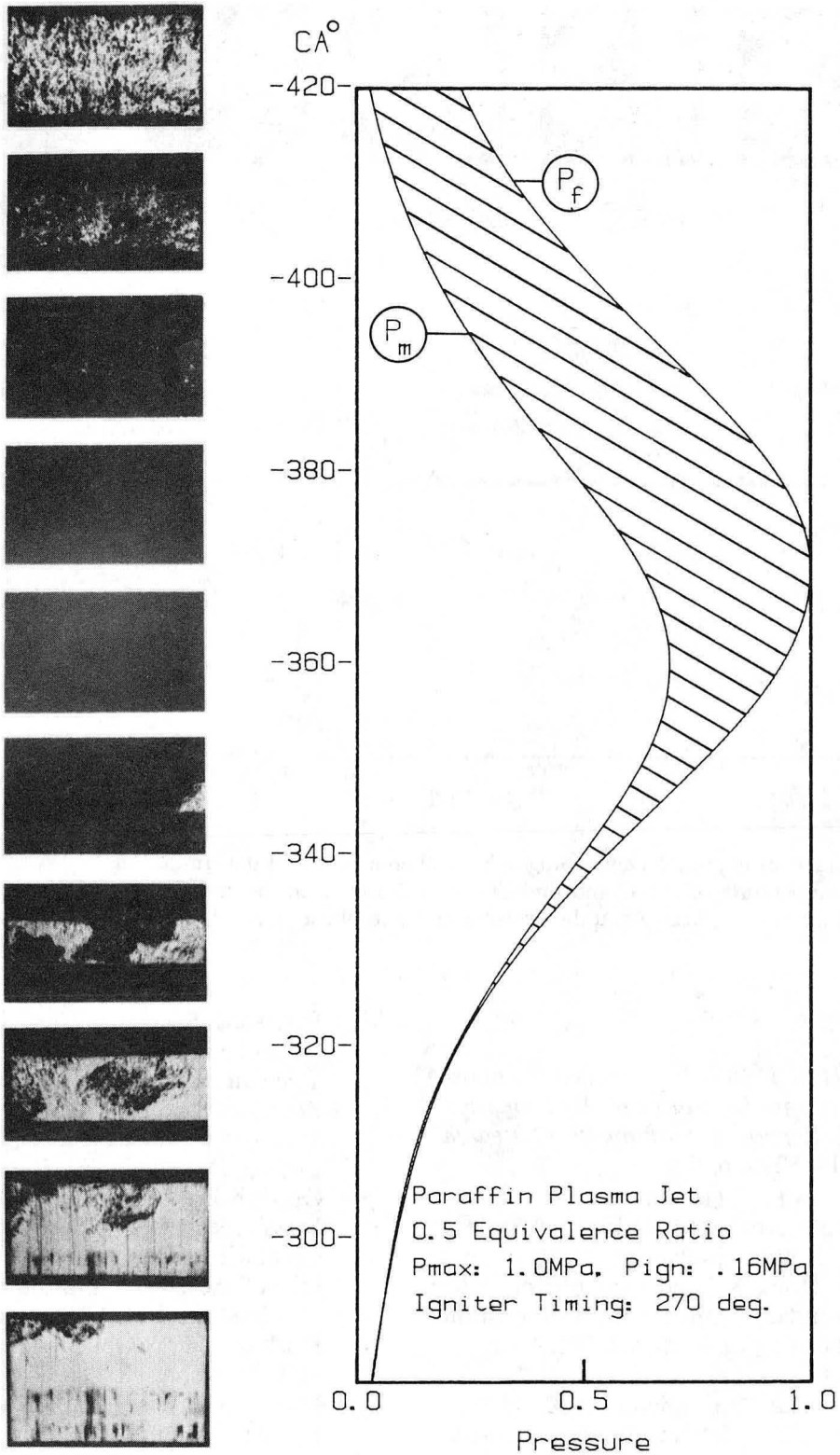

Figure 3. Extracts of high-speed cinematographic schlieren record of combustion initiated in the single-pulse machine by a paraffin-lined plasma jet ignitor, and the concomitant pressure transducer records.
(XBB 840-9534A)

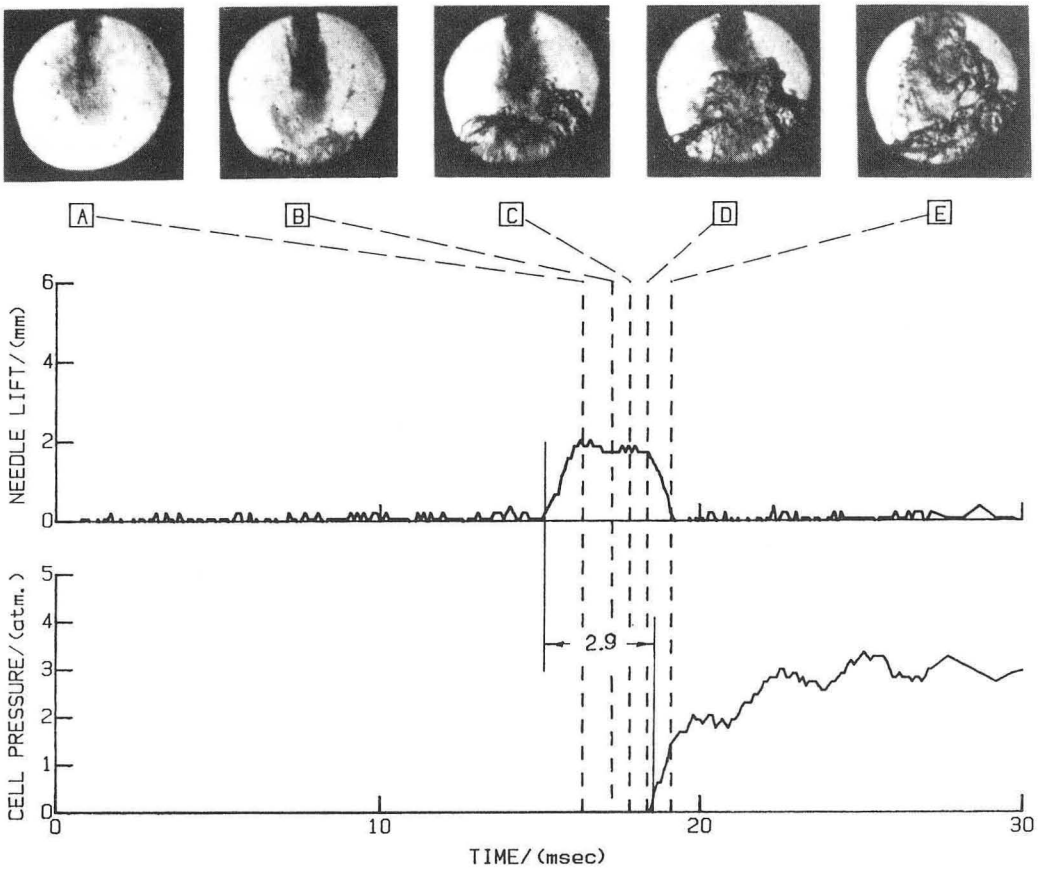

Figure 4. Extracts of high-speed cinematographic schlieren record of the ignition of a spray of *n*-dodecane at an initial temperature of 600°C and pressure of 28.2 atm, with the concomitant transducer records of the motion of the injector needle and the pressure in the combustion cell. (XBB 8412-9362A)

REFERENCES

1. Brown, N.J. *et al.* (1983), "Controlled Combustion," *Energy and Environment Division, FY 1982 Annual Report, Environmental Research Program*, LBL-15298, p. 4-59.
2. Oppenheim, A.K. (1984), "The Knock Syndrome—Its Cures and Its Victims," Society of Automative Engineers Paper 841339, 10 pp.
3. Vaneveld, L., Hom, K., and Oppenheim, A.K. (1984), "Secondary Effects in Combustion Instabilities Leading to Flashback," *AIAA J. 22*, (1), p. 81.
4. Cheng, R.K., and Oppenheim, A.K. (1984), "Autoignition in Methane-Hydrogen Mixtures," *Combust. Flame 58*, (2), p. 125.
5. Lucas, D., Peterson, R., Hurlbut, F.C., and Oppenheim, A.K. (1984), "Effects of Transient Combustion Phenomena on Molecular Beam Sampling," *J. Phys. Chem. 88*, p. 4585, LBL-15799.
6. Peterson, R., Lucas, D., Hurlbut, F.C., and Oppenheim, A.K. (1984), "Molecular Beam Overrun in Sampling of Transient Combustion Processes," *J. Phys. Chem. 88*, p. 4746, LBL-16713.
7. Lucas, D., Peterson, R., Brown, N.J., and Oppenheim, A.K. (1984), "Molecular Beam Mass Spectrometer Sampling of Flash-Ignited Combustion," to be published in the proceedings of the 20th Symposium (International) on Combustion, LBL-17222.
8. Hurlbut, F.C., Oppenheim, A.K., Lucas, D., and Peterson, R. (1984), "Molecular Beam Mass Analysis of Transient Combustion Events," presented at the 14th International Symposium on Rarified Gas Dynamics, Tsukuba, Japan, July 1984.
9. Edwards, C.F., and Oppenheim, A.K. (1983), "A Comparative Study of Plasma Ignition Systems," Society of Automotive Engineers Paper 830479, 12 pp.

10. Edwards, D.F., and Oppenheim, A.K. (1985), "A Photographic Study of Plasma Ignition Systems," presented at the Society of Automotive Engineers International Congress, Detroit, Feb. 15–March 1, 1985.

11. Brown, N.J., et al. (1984), "Controlled Combustion," *Applied Science Division FY 1983 Annual Report, Environmental Research Program*, LBL-17073, p. 4-67.

Fire Modeling*

P. Pagni and C. Okoh

The overall goal of this project is to develop physical and mathematical models of the detailed combustion phenomena that control a fire's growth within a compartment and its subsequent propagation throughout a structure. During this grant period, the emphasis has been on flame radiation and its most important and least known parameter, f_v, the soot volume fraction within the flame, defined as the volume occupied by soot per unit of flame volume. Previous reports have described a multiwavelength laser extinction technique for *in situ* measurement of the local flame's f_v. The full Mie theory, Lee and Tien optical properties, and a two-parameter size distribution are assumed. Alternative simplifying assumptions have been shown to significantly overestimate f_v.

ACCOMPLISHMENTS IN FY 1984

The soot particles have mean diameters, d, $\sim$50 nm, and concentrations, N_o, $\sim 10^9$ cm^{-3}. The mean free path of the gas, λ, is $\sim$500 nm, so the particle Knudsen number is $Kn \equiv \lambda/d \approx 10$, and the flow field around the soot particle is free molecular. This produces strong convective coupling with the gas, i.e., the effective heat transfer coefficient, h, is $\sim 10^5$ W/m^2 K. The soot temperature, T_s, is locked to the gas temperature within $+0/-5$ K, with the larger negative range due to particle radiative emission. Surface reactions involving CO_2, H_2O, OH, and C_2H_2 all appear to have insignificant effects on T_s. A separate consequence of the high Knudsen number is the need to include thermophoretic forces in particle trajectory calculations.

Since the particle temperature is the gas temperature, the sooty gas can be treated as a single radiating medium and the free flow boundary layer equations can be solved, explicitly including radiation. The nonadiabatic flame temperatures (K) from these calculations at 4 cm downstream of the leading edge are shown of Table 1. Only toluene, cyclohexene, and polymethylmethacrylate (PMMA), show significant nonadiabatic effects on the flame temperature at these small scales. The 60-K drop for PMMA is due to radiant emission from the pyrolyzing flue surface, while the 80-K drop for toluene and the 20-K drop for cyclohexene are due to soot emission. The remaining fuels show less than 10-K drops due to radiation, indicating that at this scale in air, radiative effects can be neglected in calculating these flow fields. This is supported by the small amount of carbon converted to soot for these fuels as shown in the third row in Table 1. A comparison of measured and calculated temperature profiles across the boundary layer is shown in Fig. 1. The experimental temperatures have been corrected for radiation losses from the bead. The peak measured temperature, T_{bead}, and the corrected values, T_{exper}, are also given in Table 1.

In addition, calculated velocity fields were used to estimate the time rate of change of the soot volume fraction along particle trajectories, f_v. The data were fit with:

$$\dot{f}_v \approx \overline{u}\,\frac{\Delta f_v}{\Delta s} = A_{\exp}(-E/R\overline{T})\,\overline{Y}_f^a\,\overline{f}_v^b \quad ,$$

where s is the displacement on a trajectory, u is velocity, Y_f is fuel mass fraction, their overbars indicate mean values with respect to Δs, and E and A are parameters given in Table 1. Toluene was so sooty that complete attenuation occurred and data were limited to a short region too close to the leading edge to permit determination of E and A. Good linearity for $a = 1$ and $b = 0$ is shown for two sample fuels in Fig. 2.

PLANNED ACTIVITIES FOR 1985

In the next grant period, existing forced flow and f_v data will be analyzed. We will explore perturba-

*This work was supported by the Center for Fire Research, National Bureau of Standards, under Grant No. NB 80 NAGE 6839-3, through the U.S. Department of Energy under Contract No. DE-AC03-76SF00098.

Table 1. Flame temperatures (K) and soot parameters.

	Toluene	Cyclohexene	Octane	Cyclohexane	Heptane	PMMA
T_{fl}	2266	2287	2225	2242	2203	2075
T_{ad}	2343	2307	2233	2249	2208	2131
%C to soot	15	3.3	1.5	1.0	0.5	1.0
T_{exper}	2077	2077	2047	2044	2009	1943
T_{bead}	1972	1972	1946	1943	1913	1856
E (kcal/mole)	—	50.2	52.9	54.8	59.4	53.5
A (GHz)	—	0.15	0.26	0.37	1.1	0.8

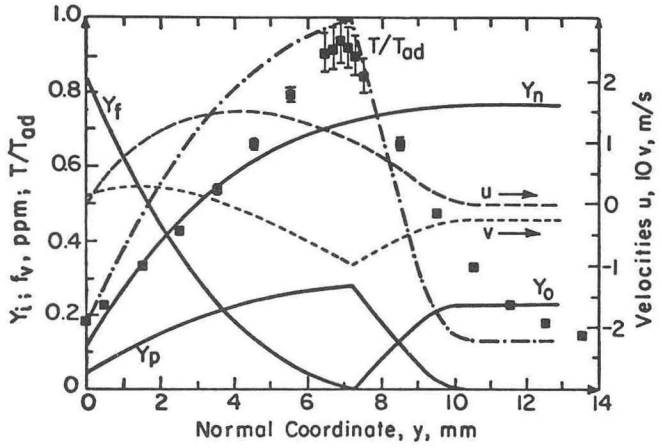

Figure 1. Calculated n-heptane/air free-flow boundary layer profiles at x = 4 cm for the x and y velocities, u and v; the fuel (Y_f), oxygen (Y_o), product (Y_p), and inert (Y_n) mass fractions; and T/T_{ad} calculated (— · — · —) and experimental (■), with $T_{adiabatic}$ = 2250 K.

(XBL 847-7184)

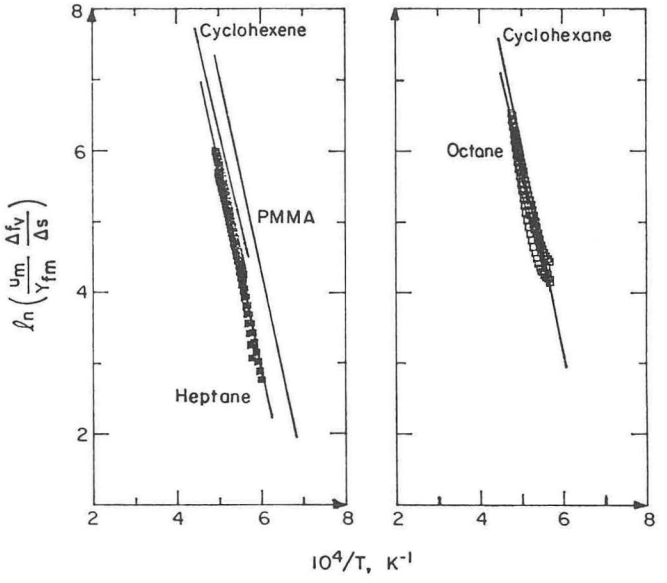

Figure 2. An Arrhenius correlation of soot generation rates for n-heptane, cyclohexene, PMMA, iso-octane and cyclohexane. Sample data are given only for n-heptane and iso-octane for clarity. Note that calculated temperatures are used; experimental temperatures give E's (kcal/mole) smaller by half. (XBL 874-7185)

tion methods incorporating radiation, finite chemical kinetics, and Le ≠ 1 effects in calculations of combusting boundary layers during Dr. Howard Baum's stay at UC Berkeley as Springer Professor of Mechanical Engineering during Spring Semester, 1985.

REFERENCES

1. Pagni, P.J. (1984), "Materials Fire Properties and Test Methods," in *Proceedings of the Seventh Joint Meeting, United States–Japan Natural Resources Panel on Fire Research and Safety*, 24–28 October 1983, Washington, DC, National Bureau of Standards.
2. Mao, C-P., Fernandez-Pello, A.C., and Pagni, P.J. (1984), "Mixed Convective Burning of a Fuel Surface with Arbitrary Inclination," *J. Heat Transfer, Trans. ASME, Series C, 106*, pp. 304–309.
3. Beier, R.A., Pagni, P.J., and Okoh, C.I. (1984), "Soot and Radiation in Combusting Boundary Layers," *Comb. Sci. Tech. 39*, pp. 131–169.
4. Alvares, N., Foote, K., and Pagni, P.J. (1984), "Forced Ventilation Enclosure Fires," *Combust. Sci. Tech. 39*, pp. 55–81.
5. Pagni, P.J., and Okoh, C.I. (1984), "Soot Generation within Radiating Diffusion Flames," presented at the Twentieth Symposium (International) on Combustion, Ann Arbor, MI, August 12–17, 1984; LBL-17391.

The Use of High-Strength Concrete and Mortars in Combustion Environments*

R.B. Williamson, and A.I. Rashed

The overall goal of this project is to examine the use of high-strength concretes and mortars for application in combustion environments such as furnaces or boilers for coal gasification and similar processes requiring high pressure and temperature. Reported here are the results of an investigation on the high-temperature performance of a mortar of different strengths incorporating 0%, 8%, and 16% levels of condensed silica fume (CSF). The experiments were carried out to compare the performance of different strength-level mortars with different CSF contents. Generally speaking, it was found that low-strength mortar with CSF is less susceptible to strength loss after exposure to high temperature than mortar without CSF. On the other hand, high-strength mortar with CSF seems to be more sensitive to high temperature than high-strength mortar without CSF since the former retains only 65% of its room-temperature strength after heating to 320°C, compared with regular high-strength mortar, which retains 95% of its room temperature strength.

Though it was found that there may be a practical problem with using high-strength CSF concrete in a high-temperature environment, the loss of strength in high-strength CSF concrete upon heating may prove very important to our gaining insight into the fundamental mechanisms of strengthening concrete with CSF. An explanation is hypothesized on the observed behavior of high-strength CSF concrete, leading to the following theory for one of the ways in which CSF strengthens portland cement paste. It is speculated that CSF toughens the portlandite in high-strength paste, but after heating to 320°, the CSF particles, now converted to calcium silicate hydrate, lose their ability to toughen the portlandite.

ACCOMPLISHMENTS DURING FY 1984

In order to investigate the effects of high temperature on mortar specimens containing CSF, a matrix of nine mixes was prepared with three levels of strength. A portland cement meeting the criteria for both ASTM Types I and II was used. Condensed silica fume with 82% of its material finer than 1 micrometer and 36% finer than 0.2 micrometer was added to six of the mortar mixes in either 8% or 16% proportions by weight. The fine aggregate was sandstone with a fineness modulus of 2.93. A combination water reducer and retarder (Zeecon R-40, SG = 1.212) and a superplasticizer (Mighty 150) were used to achieve workable mixes. The mortar mixes investigated in this study are of three strengths: high, medium, and low. For each of these three categories, three mortar mixes containing three different CSF contents (0%, 8%, and 16%) were prepared. The mixing procedure was performed according to ASTM Standard C-109 76.

The effects of temperature on the compressive strengths of the various mixes are shown in Figs. 1–3. These figures form the basis for describing the results of our project. Figure 1 shows the effect of temperature on the compressive strength of the three mixes of mortar without CSF. Note that they all lose less than 10% of their room temperature strength at 320°C, with the high-strength mortar losing approximately 5% of its room-temperature strength. The effect of temperature on the compressive strength of the three mixes of mortar with 8% CSF are shown in Fig. 2, and similar curves for the

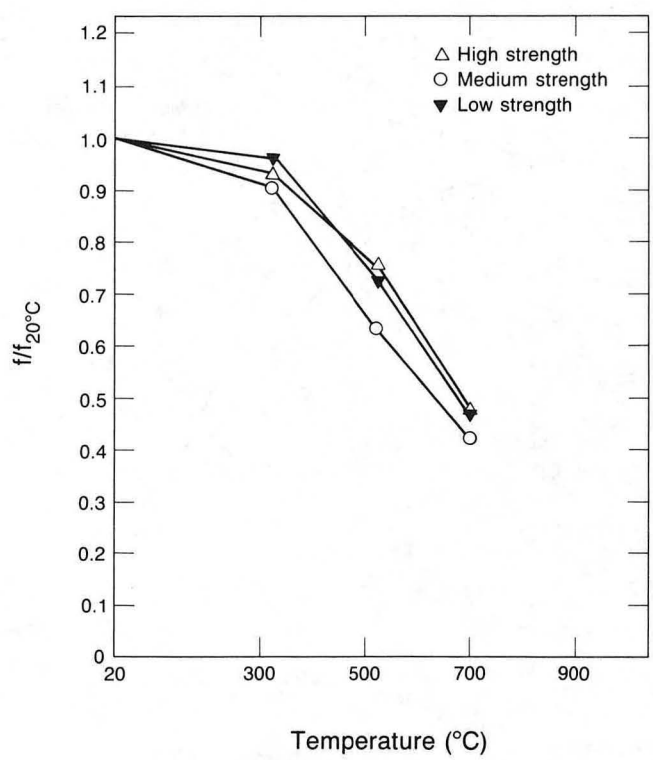

Figure 1. Effect of temperature on the compressive strength of different strength-level mortars with 0% condensed silica fume (CSF). (XBL 852-7031)

*This work was supported by the Director's Fund through the U.S. Department of Energy under Contract No. DE-ACO3-76SF00098.

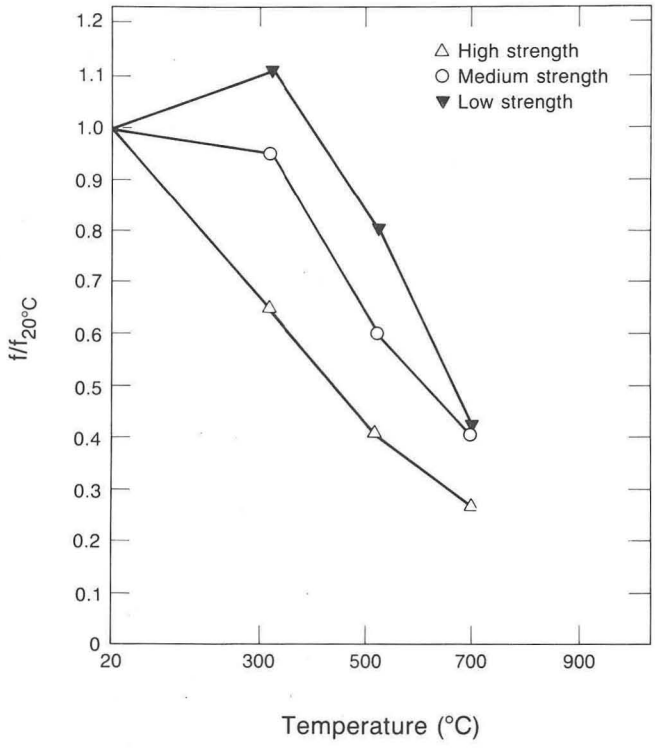

Figure 2. Effect of temperature on the compressive strength of different strength-level mortars with 8% CSF. (XBL 852-7030)

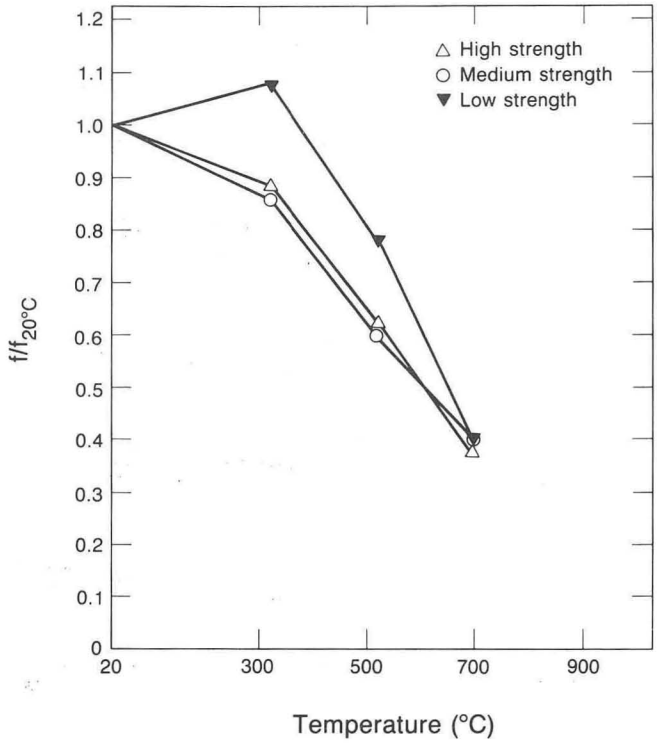

Figure 3. Effect of temperature on the compressive strength of different strength-level mortars with 16% CSF. (XBL 852-7029)

mortar with 16% CSF are shown in Fig. 3. At 320°C, the strength of the "low strength" mortar with 16% CSF increases by 12%, the one with 8% CSF increases by 8%, and the one without CSF decreases by approximately 4%. At 520°C, however, the strength decreases for all three mixes, but the mortar with 16% CSF is still performing best. At 700°C, the difference in relative strength is small (3%), and the strength loss of all three mixes is relatively high. On the other hand, it can be seen from Fig. 3 that the loss of strength for high-strength mortar with 16% CSF is very high, even at low temperatures, when compared with mortar without CSF. (At 320°C, the loss of strength for mortar with 16% CSF was 35% and for mortar without CSF, 4%; at 700°C, the loss of strength for mortar with 16% CSF was 73%, and for mortar without CSF, 52%).

A further observation is that the "relative strength"/temperature curves of all the mortar mixes without CSF are almost the same, while the "relative strength"/temperature curves of the mortar mixes with 16% CSF shown in Fig. 3 vary significantly. Generally speaking, low-strength mortar with CSF is less susceptible to loss of strength with heating than mortar without CSF. On the other hand, high-strength mortar with CSF seems to be more sensitive to high temperature than high-strength mortar without CSF.

The relative strength data as well as the effects of temperature exposure on the modulus of elasticity are given in Table 1. From this table, it can be seen that there is always a decrease in the modulus of elasticity after heating and cooling. A further observation that can be inferred from the table is that mortar with 16% CSF has a lower relative elastic modulus when exposed to high temperature than mortar without CSF. At 700°C, the stress-strain curves of all the mixes flatten, and the E/E_0 ratios for all mixes become close.

The mortar with 8% CSF can be regarded as portraying a "transition" zone between low and high mortar strengths. Condensed silica fume is often added to concrete in that proportion to gain better economy and some improvement in placement qualities. At that level of addition, it can be considered a cement replacement product, and it is to represent that use of the CSF addition to concrete that the 8% CSF mix proportion was included in this study.

Because of the high-temperature behavior of high-strength CSF concrete, as shown in Fig. 3, practical problems may arise when using this material. However, this loss of strength upon heating may prove to be very important in giving us an insight into the fundamental mechanisms of strengthening concrete with CSF, and these studies have provided

Table 1. The relative strength of the mortar and the modulus of elasticity when exposed to different temperature levels.

	Mortar mix (strength and % CSF)								
	Low			Medium			High		
Temp.	0%	8%	16%	0%	8%	16%	0%	8%	16%
20°C	*Average strength (f_o) in psi*								
	5900	5400	4800	11000	11000	8800	16300	14400	17500
	Average modulus of elasticity, E_o								
	2.97	2.65	2.515	3.18	2.87	2.35	7.3	3.23	3.25
320°C	*Strength in % of f_o*								
	96.1	108.0	112.0	90.6	86.2	95.2	94.7	89.1	65.0
	Modulus of elasticity in % of E_o								
	66.8	63.6	49.7	83.9	65.8	44.9	57.0	58.0	37.4
520°C	*Strength in % of f_o*								
	72.7	78.0	80.7	63.0	58.1	60.0	75.0	61.0	42.3
	Modulus of elasticity in % of E_o								
	25.0	21.2	24.1	32.5	31.0	22.3	20.0	22.1	18.0
700°C	*Strength in % of f_o*								
	45.5	40.0	42.5	42.3	35.0	40.0	48.0	37.02	27.3
	Modulus of elasticity in % of E_o								
	8.0	5.0	6.9	12.0	9.4	11.3	9.0	8.4	6.0

us with an important clue into the microstructure of CSF concrete.

These experiments have led us to hypothesize an explanation for the observed behavior of high-strength CSF concrete, and from that to a theory on one of the ways in which CSF strengthens portland cement paste. One of the special characteristics of CSF is that it is divided into very small particles, which are almost perfectly spherical. Figure 4 shows two scanning electron micrographs (SEM) of a portlandite (calcium hydroxide) fracture surface from one of the high-strength mortar specimens containing 16% CSF. The micrographs were taken at room temperature, and the specimen had no history of heating. It is apparent in Figs. 4(a) and 4(b) that the CSF particles have been incorporated into the portlandite crystal in its initial growth. Williamson[1] reviewed the literature, which shows that portlandite crystals, particularly the large ones, grow in the very early portions of the curing process. It is therefore hypothesized here that the CSF particles visible in Fig. 4 are actually calcium silicate hydrate (CSH) pseudomorphs of the original CSF particles. They are thus like the pseudomorphs of the original cement grains that are found in portland cement paste.[2] It is further hypothesized that these CSF pseudomorphs actually increase the fracture toughness of the CSF concrete by changing the fracture characteristics of the large portlandite crystals in the cement paste. This is like the toughening of glassy polymers by the addition of very fine elastomeric particles. The actual mechanism of CSF toughening of portlandite may be either by inducing some plastic deformation in the surrounding portlan-

(a)

(b)

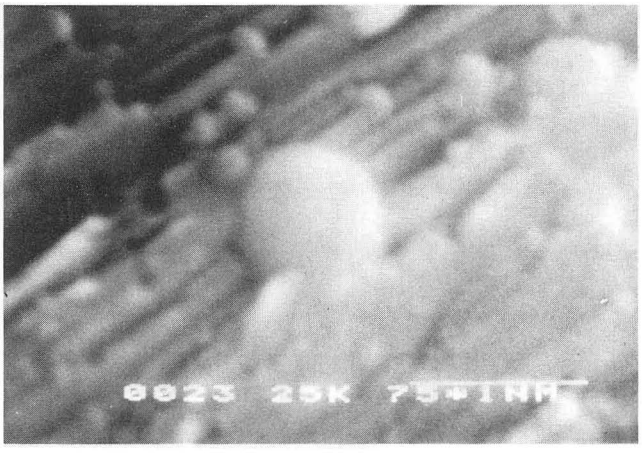

Figure 4. Scanning electron micrographs (SEM) of a portlandite fracture surface from a high-strength mortar specimen with 16% CSF at room temperature.

[(a) XBB 851-745; (b) XBB 851-746]

dite or by increasing the area of the fracture surface.

One of the important aspects of this hypothesized strengthening mechanism of CSF-modified concrete is that it can be used to explain the observed loss of strength shown in Fig. 3. When the CSF pseudomorphs embedded in the portlandite are heated to 320°C, they become debonded from the surrounding brittle portlandite crystal, and thus their toughening effect is lost. The debonding process may only be due to differential thermal expansion, although there may also be some dehydration of the CSH.

According to Schneider,[3] the loss of concrete strength with temperature is due to differential thermal expansion between the cement paste and the aggregate as well as to physical and chemical changes. Using differential thermal analysis (DTA) for concrete based on ordinary portland cement, Schneider concluded that the following reactions occur when concrete is heated:

Temperature	Event
100°C	Loss of free water
180°C	Breakdown of gel (first stage of dehydration)
500°C	Decomposition of portlandite
700°C	Beginning of decomposition of CHS phases

Schneider writes that, in the range 100°C to 300°C, the dehydration of the capillary system occurs simultaneously with a stepwise decomposition of the CSH materials in the paste. At approximately 490°C, the decomposition of the calcium hydroxide into calcium oxide and water takes place. At 780°C, Schneider recorded another stage of CSH decomposition, and, from an x-ray analysis, he showed that beta-C_2S was formed at the same time.

In Schneider's analysis, the embedded CSH particles in the portlandite would have been partially decomposed at 320°C, and the mechanism proposed here is thus consistent with his studies. The resulting portlandite crystals would be weaker than in pastes without CSF since they would now be filled with small voids, which would allow easy fracture.

It is well known that portlandite crystals in pastes can be as large as 50 cement grains in diameter, and Williamson[2] noted that this represents an important contribution to the early strength of portland cement pastes. Williamson[2] hypothesized that at later ages, particularly after several years, these same large portlandite crystals act as flaws which weaken the paste. This approach is taken here, except that the inclusion of the CSF in the portlandite modifies its fracture characteristics, and thus the strength of the paste can be increased.

PLANNED ACTIVITIES FOR FY 1985

The results reported here suggest that further effort should be undertaken to better comprehend the microstructure of the CSF concrete and how it alters upon heating. Such an understanding might lead us to find a temperature at which the microstructure of the CSF concrete does not deteriorate.

REFERENCES

1. Williamson, R.B. (1972), "Solidification of Portland Cement," *Progress in Materials Science 15*, p. 189.
2. Williamson, R.B. (1969), "Crystal Multiplication without Nucleation," *Science 164*, p. 149.
3. Schneider, U. (1982), "Verhalten von Beton bei hohen Temperaturen" ("Behavior of Reinforced Concrete at High Temperatures"), Deutscher Ausschuss für Stahlbeton, No. 337.

Reaction of Ferrous Nitrosyl Chelates with Sulfite and Bisulfite Ions*

D. Littlejohn and S.G. Chang

The motivation for the investigation of this reaction has been to develop a technique for the simultaneous desulfurization and denitrification of flue gases. Flue gases contain sulfur dioxide and nitrogen oxides, primarily as nitric oxide (NO). While sulfur dioxide will readily dissolve in water to form sulfite or bisulfite ions, nitric oxide has low solubility and is difficult to remove without additives such as ferrous chelates. Reports of the reaction[1-5] of ferrous nitrosyl chelates with sulfite and bisulfite ions have indicated that it is complicated, but have not provided a complete understanding of the reaction process. There are contradictions in the literature as to what the reaction products are, as well as what the kinetic behavior is. A clear understanding of this reaction is needed for the design and development of efficient flue-gas scrubbing systems.

ACCOMPLISHMENTS DURING FY 1984

We have studied this reaction, using several different chelates bound to the Fe(II) ions. The chelates were citrate, iminodiacetic acid (IDA), nitrilotriacetic acid (NTA), and ethylenediaminetetraacetic acid (EDTA). Studies of the kinetics of the reaction and of the reaction products were made over a pH range of 2 to 10. The observed reaction products were Fe(III), SO_4^{2-}, $S_2O_6^{2-}$, N_2O, N_2, and hydroxylamine disulfonate (HADS). The HADS can further react to produce other nitrogen-sulfur compounds such as hydroxylamine monosulfonate (HAMS), aminetrisulfonate (ATS), and aminedisulfonate (ADS).[6] The product distribution and the rate of reaction are affected by the solution pH and the reactant concentrations.

The reaction kinetics were studied by using the visible absorption of the ferrous chelates to observe their disappearance in the presence of sulfite and bisulfite ions. The rate equation obtained is:

$$\frac{d[\mathrm{Fe(II)(L)NO}]}{dt} = k_1[\mathrm{HSO_3^-}] + k_2[\mathrm{SO_3^{2-}}][\mathrm{Fe(II)(L)NO}]$$

For L = NTA at 25°C and pH 3 to 8,

$$k_1 = 1.2 \times 10^{-5}\ \mathrm{sec}^{-1}\ ,$$

and

$$k_2 = 0.13\ M^{-1}\ \mathrm{sec}^{-1}$$

for $10^{-4}\ M < [\mathrm{Fe(II)(NTA)NO}] < 10^{-3}\ M$ and $10^{-2}\ M < [\mathrm{S(IV)}] < 10^{-1}\ M$.

For L = EDTA at 25°C and pH 4 to 8,

$$k_1 = 5.6 \times 10^{-5}\ \mathrm{sec}^{-1}$$

and

$$k_2 = 0.175\ M^{-1}\ \mathrm{sec}^{-1}\ .$$

At 55°C and pH 4 to 8,

$$k_1 = 9.0 \times 10^{-5}\ \mathrm{sec}^{-1}$$

and

$$k_2 = 0.60\ M^{-1}\ \mathrm{sec}^{-1}\ .$$

These values are valid for $10^{-4}\ M < [\mathrm{Fe(II)(EDTA)NO}] < 10^{-3}\ M$ and $10^{-3}\ M < [\mathrm{S(IV)}] < 10^{-1}\ M$.

Figure 1 illustrates the pH dependence of the Fe(II)(NTA)NO reaction.

A number of methods were used in the product determinations. Measurements of N_2O and N_2 were done by gas chromatography. The 1,10 phenanthroline method was used to determine Fe(II) concentrations. Laser Raman spectroscopy was used to observe many of the anions in solution, including SO_4^{2-}, $S_2O_6^{2-}$, and HADS. Determinations for HADS were also made colorimetrically by oxidation to nitrosodisulfonate, which has an absorption maximum at 545 nm. Figure 2 shows the dependence of N_2O and N_2 on the $[SO_3^{2-}]$:[Fe(II)(NTA)NO] ratio, on the Fe(II)(NTA)NO concentration, and on pH.

*This work was supported by the Assistant Secretary for Fossil Energy, Office of Coal Utilization Systems, U.S. Department of Energy under Contract No. DE-AC03-76SF00098 through the Pittsburgh Energy Technology Center, Pittsburgh, PA.

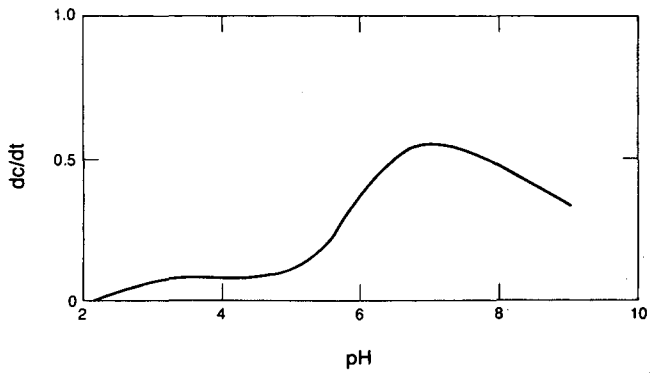

Figure 1. Dependence of reaction rate (*dc/dt*) of Fe(II)(NTA)NO + S(IV) on pH. (XBL 8501-6906)

To explain the kinetic behavior and reaction products observed, we have developed the reaction mechanism listed in Table 1. In most cases, SO_3^{2-} and HSO_3^- can be used interchangeably, so only SO_3^{2-} is listed. HSO_3^- is written where this is not the case. The production of other nitrogen-sulfur compounds[7–9] and N_2 are not included in this mechanism. Significant production of N_2 occurs only at very high pH, and the amount produced is always less than N_2O. Production of N_2 may occur as a result of the decomposition of $(NO)_2SO_3^{2-}$ in the presence of Fe(II).

Table 1. Reaction mechanism of ferrous nitrosyl chelates with sulfite and bisulfite ions.

$Fe(II)(L)NO = Fe(II)(L) + NO$	(1)
$NO + SO_3^{2-} \rightarrow (NO)SO_3^{2-}$	(2)
$NO + NOSO_3^{2-} \rightarrow (NO)_2SO_3^{2-}$	(3)
$(NO)_2SO_3^{2-} \rightarrow N_2O + SO_4^{2-}$	(4)
$Fe(II)(L)NO + SO_3^{2-} = Fe(II)(L)NOSO_3^{2-}$	(5)
$Fe(II)(L)NOSO_3^{2-} + Fe(II)(L)NO \rightarrow Fe(II)(L) + Fe(II)(L)(NO)_2SO_3^{2-}$	(6)
$Fe(II)(L)(NO)_2SO_3^{2-} = Fe(II)(L) + (NO)_2SO_3^{2-}$	(7)
$Fe(II)(L) + Fe(II)(L)(NO)_2SO_3^{2-} \rightarrow 2\ Fe(III)(L) + N_2O_2^{2-} + SO_3^{2-}$	(8)
$2\ Fe(II)(L)NOSO_3^{2-} \rightarrow 2\ Fe(II)(L) + {}^-ON(SO_3^-)_2 + NO^-$	(9)
$Fe(II)(L)NOSO_3^{2-} + Fe(II)(L)NO \rightarrow 2\ Fe(II)(L) + NOSO_3^- + NO^-$	(10)
$HSO_3^- + NOSO_3^- \rightarrow HON(SO_3^-)_2$	(11)
$NO^- + H_2O = HNO \sim + \sim OH^-$	(12)
$2\ HNO \rightarrow H_2N_2O_2$	(13)
$2NO^- \rightarrow N_2O_2^{2-}$	(14)
$H_2N_2O_2 \rightarrow N_2O + H_2O$	(15)
$N_2O_2^{2-} + H^+ \rightarrow N_2O + OH^-$	(16)
$Fe(III)(L) + HSO_3^- \rightarrow Fe(II)(L) + SO_3^- + H^+$	(17)
$2SO_3^- \rightarrow S_2O_6^{2-}$	(18)
$Fe(III)(L) + SO_3^- + OH^- \rightarrow Fe(II)(L) + SO_4^{2-} + H^+$	(19)

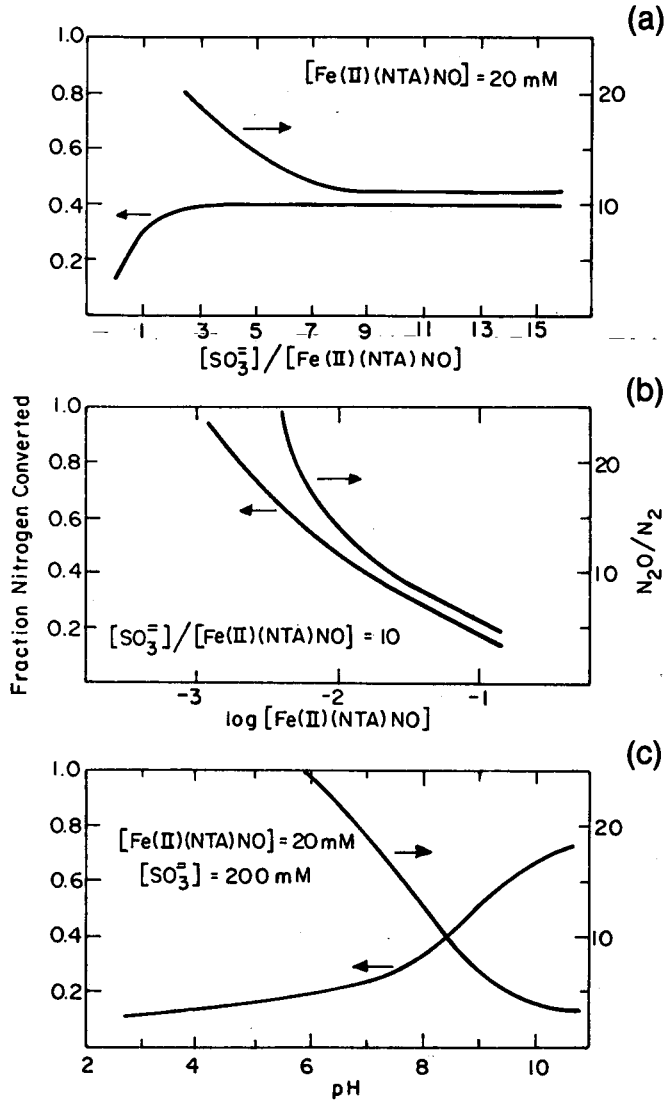

Figure 2. (a) Effect of $[SO_3^{2-}]$:[Fe(II)(NTA)NO] on production of N_2O and N_2; (b) effect of Fe(II)(NTA)NO concentration on production of N_2O and N_2; (c) effect of pH on production of N_2O and N_2. The fraction of nitrogen converted into N_2 and N_2O is indicated on the left axes, and the N_2O:N_2 ratio is indicated on the right axes.

(XBL 846-7006)

PLANNED ACTIVITIES FOR FY 1985

The iron–nitrogen oxyanion–sulfur oxyanion chemistry is very complicated. A number of reaction systems must be investigated to obtain a better understanding of the chemistry of solutions containing these compounds. We plan to study the kinetics of the NO + SO_3^{2-} and HSO_3^- over a range of pH conditions and the reaction between $(NO)_2SO_3^{2-}$ and Fe(II). The reaction between other transition metal nitrosyls and SO_3^{2-} and HSO_3^- may also be studied.

REFERENCES

1. Teramoto, M., *et al.* (1978), "Absorption of Dilute Nitric Monoxide in Aqueous Solutions of Fe(II)-EDTA and Mixed Solutions of Fe(II)-EDTA and Na_2SO_3," *J. Chem. Eng. Japan 11*, p. 450.
2. Sada, E., Kumazawa, H., Kudo, I., and Kondo, T. (1980), "Individual and Simultaneous Absorption of Dilute NO and SO_2 in Aqueous Slurries of $MgSO_3$ with Fe^{II}-EDTA," *Ind. Eng. Chem. Process Des. Dev. 19*, p. 377.
3. Miyadera, T., Kawai, M., Hirasawa, S., and Miyajima, K. (1982), "The Rate of Reaction between Fe^{II}(edta)NO and Sodium Sulfite," *Nippon Kagaku Kaishi*, 1982, p. 1818.
4. Sada, E., Kumazawa, H., Takada, Y. (1984), "Chemical Reactions Accompanying Absorption of NO into Aqueous Mixed Solutions of Fe^{II}-edta and Na_2SO_3," *Ind. Eng. Chem. 23*, p. 60.
5. Narita E. *et al.* (1984), "Formation of Hydroxylamidobis (sulfate) ion by the Absorption of NO in Aqueous Solutions of Na_2SO_2 Containing Fe(II)-edta Complex," *Ind. Eng. Chem. Prod. Res. Dev. 23*, p. 262.
6. Chang, S.G., Littlejohn, D., and Lin, N.H. (1982), "Kinetics of Reactions in Wet Flue Gas Simultaneous Desulfurization and Denitrification System," in *Flue Gas Desulfurization*, ACS Symposium Series No. 188, p. 127; American Chemical Society, Washington, D.C.
7. Oblath, S.B., Markowitz, S.S., Novakov, T., and Chang, S.G., (1982), "Kinetics of the Initial Reaction of Nitrite Ion in Bisulfite Solutions," *J. Phys. Chem. 86*, p. 4853.
8. Oblath, S.B., Markowitz, S.S., Novakov, T., and Chang, S.G. (1981), "Kinetics of the Formation of Hydroxylamine Disulfonate by Reaction of Nitrite with Sulfites," *J. Phys. Chem. 85*, p. 2567.
9. Oblath, S.B., Markowitz, S.S., Novakov, T., and Chang, S.G. (1983), "Reaction of Nitrite Ion with Hydroxylamine-N-Sulfonate in Aqueous Solution," *Inorg. Chem. 22*, p. 579.

Effect of Citrate Buffer Additive on Absorption of Nitric Oxide by Ferrous Chelates*

E. Griffiths and S.G. Chang

In a wet flue-gas simultaneous denitrification and desulfurization system to which ferrous chelates have been added in the scrubbing liquor to promote the solubility of nitric oxide (NO), nitrosyl ferrous chelates are formed.[1-3] The reaction between the complexed NO and $HSO_3^-/SO_3^=$ ions is too slow to affect significantly the rate of absorption of sulfur dioxide.[4] One must, instead, depend upon the buffering capacity of the solution for absorbing SO_2 and upon subsequent reactions for removing it from the solution. Since the pH of the solution in the scrubber is advantageously kept in the range 5–7, and since the acid constants of chelates commonly used for complexation with ferrous ion, such as nitrilotriacetic acid (NTA), ethylenediaminetetraacetic acid (EDTA), and iminodiacetic acid (IDA), cannot provide buffering in this pH range, the soluble buffering must be provided by adding some other base to the scrubbing solution. There has been substantial commercial experience with scrubbing SO_2 from stack gas with a solution containing a soluble base. Sodium citrate, for example, is a base that has been employed in the citrate process developed by the U.S. Bureau of Mines. This is a regenerable flue-gas desulfurization process in which the dissolved SO_2 is reacted with hydrogen sulfide (H_2S) to form elemental sulfur. It has also been demonstrated in our laboratory that H_2S can reduce NO in the nitrosyl ferrous chelates and regenerate ferrous chelate catalysts. The development, therefore, of a regenerable flue-gas denitrification and desulfurization process, based on the addition of both ferrous chelates and H_2S in a wet scrubber and with sodium citrate as a buffer, appears very promising. With this approach, a salable form of sulfur is produced, and costs may be reduced as a result.

ACCOMPLISHMENTS DURING FY 1984

We have determined the equilibrium constants of NO with Fe(II)citrate and Fe(II)IDA as a function of pH and temperature. We have also studied the effect of citrate ions on the absorption capacity of NO by Fe(II)EDTA, Fe(II)NTA, and Fe(II)IDA. Nitric oxide absorption studies and polarographic results indicate a previously unrecognized mixed ligand complex, Fe(II)(cit)(IDA), which has a larger stability constant for NO than either Fe(II)(cit) or Fe(II)(IDA) alone at 25°C.

Equilibrium Measurements

Aqueous solutions of the ferrous chelates were prepared under O_2-free conditions. The concentration of ferrous ion was 10^{-2} *M*, and the concentration of chelate was 10^{-1} *M*. The solutions were adjusted to the desired pH by NaOH and the desired ionic strength, 1 *M*, by Na_2SO_4. The NO (obtained from the Matheson Co.) was a mixture of 2.55% NO in N_2 with NO_2 impurity of less than 255 ppm; this NO was further diluted to 1000 ppm by adding N_2. The experiments proceeded by bubbling a mixture of NO and N_2 of known NO concentration through a NaOH solution to absorb any NO_2 impurity in the gas and then through the ferrous chelate solution. The NO concentration in the outlet gas was measured with a Thermoelectron model 14A chemiluminescent NO_x analyzer. The gas flow rates were 600–810 mL min^{-1}. Equilibrium was attained when the NO concentration in the outlet gas became equal to that of the inlet gas.[5,6] The experiments were performed at 25°C and 55°C.

Polarographic Measurements

The ferrous chelates, 10^{-2} *M*, and the nitrosyl complexes were prepared on a vacuum line.[7] Sodium sulfate was employed to keep the ionic strength 1 *M* and as supporting electrolyte. All solutions contained 0.001% Triton X-100 as a maximum suppressor. Samples of the solution were transferred to a polarographic cell, and the polarograms were recorded on a PAR model 174A polarographic analyzer. A dropping Hg electrode was used with a drop time of approximately 2 seconds A constant stream of nitrogen was passed over the solution to prevent oxidation of the ferrous chelates. An H-type cell with saturated calomel electrode was used, and all measurements were made at 25°C.

The equilibrium constants of Fe(II)(cit^{3-})NO were determined to be 4.9×10^4 M^{-1} at 25°C and 1.3×10^4 M^{-1} at 55°C in the pH range 4–6.5. The absorption of NO increased linearly until at pH $\approx$ 8.5, it leveled out and the equilibrium constants became 2.1×10^5 M^{-1} at 25°C and 1.15×10^5 M^{-1} at 55°C. Studies of ratio dependency showed that, for every mole of ferrous ion, only 1 mole of citrate ions was bound to it. So the primary absorb-

*This work was supported by the Assistant Secretary for Fossil Energy, Office of Coal Utilization Systems, U.S. Department of Energy under Contract No. DE-AC03-76SF00098 through the Pittsburgh Energy Technology Center, Pittsburgh, PA.

ing species must have been Fe(II)(cit^{3-}) when 4 < pH < 6.5, and Fe(II)(cit^{3-})OH$^-$ at pH > 6.5.

The equilibrium constants of Fe(II)(IDA^{1-})$_n$NO were 2.05×10^5 M^{-1} at 25°C and 5×10^4 M^{-1} at 55°C. Ratio-dependent studies showed n equal to one. At pH > 8, the absorption of NO decreased, which may be attributed to the formation of a new complex, Fe(II)(IDA^{2-})$_x$, where x is undetermined.

When 0.1 M citrate ions were added to a solution of 0.01 M Fe(II)IDA^{1-}, the equilibrium constant became that of Fe(II)(cit^{3-})NO in the pH range 4–5.2. At pH > 5.2, the equilibrium constant increased with increasing pH, similar to the behavior observed for Fe(II)(cit^{3-})(OH)NO, although the latter only occurred at pH ≥ 6.5 . The formation of Fe(II)(cit^{3-})(OH)NO complex could not account for the strong absorption of NO. It is proposed that a mixed chelate, such as Fe(II)(cit^{3-})(IDA^{1-})NO, is formed at 25°C. Experiments were performed at pH > 7.5 to see if the absorption of NO would change when the second hydrogen ion of IDA was ionized. Precipitation occurred, whereas the Fe(II)(cit^{3-})(OH)NO complex was soluble up to pH 9.5. At 55°C, the absorption of NO was that of Fe(II)(cit^{3-})(OH)NO at high pH.

Polarography was employed to confirm that the mixed ligand chelate complex, Fe(II)(cit)(IDA), occurred at pH > 5.2. In addition, it was employed to show that only Fe(II)(cit) formed at pH < 5.2 when IDA was present in the mixed chelate system.

Figure 1 shows the half-wave potentials of the ferrous chelates as a function of pH. The anodic wave for Fe(II)(IDA) occurs at much more positive potential than that of Fe(II)(cit), with a slope of 36 mV per pH unit. The half-wave potential for Fe(II)(cit) is a linear function of pH, the relation being:

$$E_{1/2} = 0.217 - 0.063\,(\mathrm{pH}) \quad ; \qquad (1)$$

when the pH < 6.5. At pH > 6.5, the slope becomes 33 mV per pH unit, which is due to the oxidation of the new species, Fe(II)(cit)(OH)$^{8-10}$ When ferrous ion is in solution with equal amounts of citrate and IDA, the $E_{1/2}$ is the same as that of Fe(II)(cit) at pH < 5.2:

$$E_{1/2} = 0.212 - 0.062\,(\mathrm{pH}) \quad ; \qquad (2)$$

At pH > 5.6, the half-wave potentials are more positive than those of Fe(II)(cit). This indicates a new species that binds ferrous ion more strongly and has a slope of 60 mV per pH unit. In the pH range 5.2–5.6, we observed the transition from one oxidizable species to another. We attribute this new species to Fe(II)(cit)(IDA).

Figure 2 gives further evidence for the mixed ligand complex. The polarograms of Fe(II)(cit)(IDA)NO and Fe(II)(cit)NO are recorded at pH 6. The half-wave potentials of their characteristic cathodic waves[11] are −0.76 V and −0.785 V,

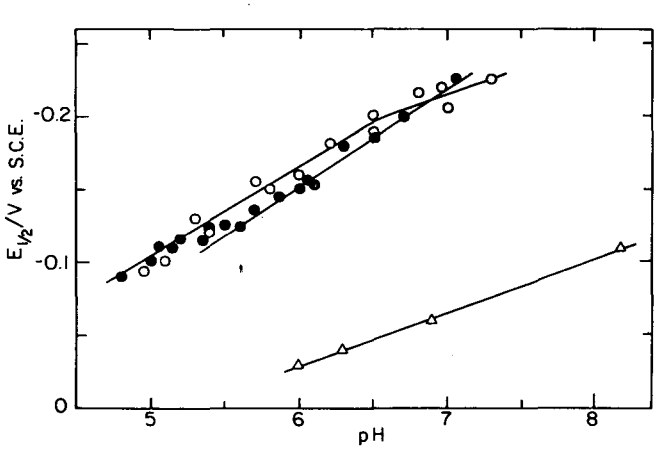

Figure 1. The half-wave potentials of Fe(II)(IDA) (triangles), Fe(II)(cit) (open circles), and Fe(II)(IDA) with citrate buffer (filled circles), as a function of pH at 25°C. (XBL 845-6995)

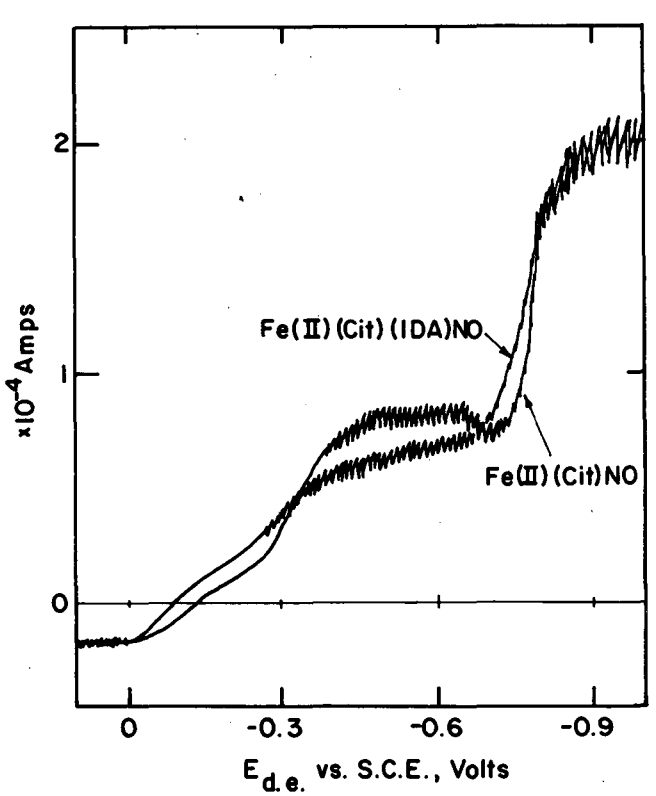

Figure 2. The polarograms of Fe(II)(IDA)(cit)NO and Fe(II)(cit)NO at pH 6 and 25°C. (XBL 845-6996)

respectively. The abrupt change in the waves indicates a multi-electron process. In analogy to a similar system, Fe(II)(EDTA)NO, investigated by linear scanning voltammetry,[12] the electrode reaction can be described by:

$$[Fe(II)(cit)NO]^{1-} + 2e + H^+ \rightarrow$$

$$[Fe(II)(cit)HNO^-]^{2-} \quad (3)$$

$$[Fe(II)(cit)HNO^-]^{2-} + H^+ \rightarrow$$

$$[Fe(II)(cit)NHOH]^{-1} \quad (4)$$

$$[Fe(II)(cit)NHOH]^{1-} + e + H^+ \rightarrow$$

$$[Fe(II)(cit)]^{1-} + NH^2OH \quad (5)$$

Effectively, citrate ions acted as a masking agent, decreasing the value of the stability constant of Fe(II)IDA. This new stability constant is referred to as a conditional stability constant.[13]

In the presence of 0.1 *M* citrate ions, the absorption of NO by Fe(II)NTA decreased when pH > 5 at 25° and 55°C. This is due to the decrease in the concentration of Fe(II)NTA available, because of the reduced stability constant. The absorption of NO by Fe(II)EDTA at 25° and 55°C was unaffected by the addition of 0.1 *M* citrate ions, because the conditional stability constant was still large.

This study showed that, depending on which ferrous chelate is in the solution, the addition of citrate ions could enhance NO absorption [Fe(II)(IDA^{1-})], decrease it [Fe(II)(NTA)], or have no effect [Fe(II)EDTA].

PLANNED ACTIVITIES FOR FY 1985

Work is continuing on the investigation of ferrous nitrosyl chelates. New chelates and chelate mixtures will be studied.

REFERENCES

1. Yaverbaum, L.H. (1979), *Nitrogen Oxide Control and Removal, Recent Developments,* Noyes Data Corporation, Park Ridge, NJ.
2. Martin, A.E., Ed. (1981), *Emission Control Technology for Industrial Boilers,* Noyes Data Corporation, Park Ridge, NJ.
3. Chang, S.G., Littlejohn, D., and Lin. N.H. (1982), "Kinetics of Reactions in a Wet Flue Gas Simultaneous Desulfurization and Denitrification System," in *Flue Gas Desulfurization,* ACS Symposium Series 188, American Chemical Society, Washington, DC.
4. Chang, S.G., Littlejohn, D., and Griffiths, E. (1982), "The Reaction of Ferrous Nitrosyl Complexes with Sulfite and Bisulfite Ions," *Energy and Environment Division FY 1982 Annual Report: Environmental Research Program,* LBL-15298, p. 4-88.
5. Hishinuma, Y., *et al.* (1979), "Reversible Binding of NO to Fe(II)(EDTA)," *Bull. Chem. Soc. Japan 52,* p. 2863.
6. Lin, N.H., Littlejohn., and Chang., S.G. (1982), "The Thermodynamics and Kinetics of the Coordination of NO to Fe^{2+}(NTA) in Aqueous Solutions, *I & EC Process Res. Dev. 21,* p. 725.
7. Littlejohn, D., and Chang, S.G. (1982), "A Kinetic Study of Ferrous Nitrosyl Complexes," *J. Phys. Chem. 86* (4), p. 537.
8. Lingane, J.L. (1946), "Polarographic Investigation of Oxalate, Citrate and Tartrate Complexes of Ferric and Ferrous Iron," *J. Am. Chem. Soc. 68,* p. 2448.
9. Meites, L. (1951), "Polarographic Studies of Metal Complexes. V. The Cadmium(II), Zinc(II) and Iron(III) Citrates," *J. Am. Chem. Soc. 73,* p. 3727.
10. Hamm, R.E., Schull, C.M., and Grant, D.M. (1954), "Citrate Complexes with Iron(II) and Iron(III)," *J. Am. Chem. Soc. 76,* p. 2111.
11. Uchiyama, S., Nozaki, K., and Muto, G. (1977), "A Basic Study on the Determination of Nitrogen Oxides with Iron(II)-NTA Complex Absorbent. I. Formation of the Iron(II) Nitric Oxide-NTA Complex from Nitrous Acid and the Iron(II)-NTA Complex," *Bunseki Kagaku, 26,* p. 219.
12. Uchiyama, S. and Muto, G. (1981), "Dependence of pH and Chelate Ligand on the Electroreduction Mechanism of a Nitrosyl-Aminopolycarbonato-Ferrous Complex in Weakly Acidic Media," *J. Electroanal. Chem. 127,* p. 275.
13. Ringbom, A. (1963), *Complexation in Analytical Chemistry,* Wiley-Interscience, New York.

Photoreduction of Ferric Chelates*

S.G. Chang and E. Griffiths

Untreated flue gases from coal-fired power plants contain substantial amounts of sulfur dioxide (SO_2) and nitric oxide (NO). A number of control strategies to reduce the concentrations of these pollutants to acceptable levels are being developed. One promising technique is to add ferrous chelate catalysts to flue-gas scrubbing liquors; this substantially increases both the solubility of NO and the reaction rates of NO with bisulfite (HSO_3^-) and sulfite ($SO_3^=$). Under these conditions, the efficiency of removing NO and SO_2 in a flue-gas wet scrubber can be improved. However, ferrous chelates in scrubbing liquors are subject to oxidation by residual oxygen. In addition, the reaction of nitrosyl ferrous chelates with $SO_3^=/HSO_3^-$ forms ferric chelates, which are inactive.[1] To be economically attractive, a scrubbing solution must be cost-effectively regenerable with little or no loss of active ingredients. One of several methods we are investigating to accomplish this is photoreduction of ferric chelates in scrubbing liquors to regenerate the desired ferrous chelates.

ACCOMPLISHMENTS DURING FY 1984

The quantum efficiency of photoreduction of Fe(III)(EDTA), Fe(III)(citrate), Fe(III)(oxalate), and mixtures of these complexes has been determined at the 458, 488, and 514 nm Ar^+ laser lines and at 350 nm by a 200-W high-pressure Hg arc light source (Table 1). These quantum efficiencies are calculated from the number of ferrous ions produced as a result of photolysis divided by the number of photons absorbed by ferric chelates during irradiation. The concentration of ferrous ion was determined by colorimetric analysis at 630, 570, and 590 nm for Fe(II)(EDTA)NO, Fe(II)(citrate)NO, and Fe(II)(oxalate)NO, respectively, all three being produced as a result of the coordination of ferrous chelates with NO. Nitric oxide was added into the system either before or after the solutions were irradiated to determine whether NO has an effect on the chemistry of photolysis of ferric chelates.

Ferric chelate solutions were prepared such that the initial concentration of ferric ion was 7.2×10^{-4} *M* and the ligand concentrations varied from 2.16×10^{-3} to 0.1 *M*. The pH of the solutions was adjusted to 5.9 by adding NaOH and the ionic strength to 1 *M* by Na_2SO_4. The ferric chelate solution was transferred to a specially designed quartz cell. The cell has a path length of 10 cm, a volume capacity of 500 cc, and a magnetic stirring bar. The solutions were degassed and one atmosphere of NO was added to the cell as the solutions were being agitated vigorously to ensure thorough mixing. When NO was added after photolysis, an atmosphere of inert Ar gas was introduced into the system over the solution prior to irradiation. The solutions were

Table 1. Quantum efficiency of photoreduction of ferric chelates.

	Φ (molecules · photon^{-1})			
	350 nm	458 nm	488 nm	514 nm
Fe(III)(oxalate)	0.92[a]	1.27[a]		
	0.398	1.12		
		0.368		
Fe(III)(EDTA)	0.064	0.0127	0.0047	0.00118
	0.065[b]		0.0053[a]	
Fe(III)(citrate)				
[citrate] = 0.1 *M*	0.335	0.247	0.199	
	0.356[a]		0.167[a]	
[citrate] = 10^{-2} *M*	0.677			
	0.583[a]			
[citrate] = 2 m*M*	0.793		0.0706	
	0.736[a]			
Fe(III)(EDTA) with citrate [EDTA] = 2 m*M*; [citrate] = 0.1 *M*	0.177		0.028	
	0.186[a]		0.017[a]	
[citrate] = 10^{-2} *M*	0.123		0.018	
	0.176[a]			
[citrate] = 2 m*M*	0.089		0.009	
	0.161[a]			
Fe(III)(EDTA) with oxalate [EDTA] = 2 m*M*; [oxalate] = 0.1 *M*	0.159		0.008	
	0.176[a]			

[a]Nitric oxide was added after photolysis.

[b]From Ref. 2.

*This work was supported by the Assistant Secretary for Fossil Energy, Office of Coal Utilization Systems, U.S. Department of Energy under Contract No. DE-AC03-76SF00098 through the Pittsburgh Energy Technology Center, Pittsburgh, PA.

then irradiated at a selected wavelength. Ultraviolet and visible spectra of the solutions were recorded before and after photolysis on a Cary 219 spectrophotometer.

Table 1 shows that the quantum efficiency is greater at shorter wavelengths for all ferric chelates investigated and that Fe(III)(oxalate) has the largest quantum efficiency for the wavelengths studied, followed by Fe(III)(citrate) and Fe(III)(EDTA). The quantum efficiency of Fe(III)(EDTA) is enhanced when citrate ion or oxalate ion is present and increases with increasing citrate ion concentration. Polarography showed that this was due to the distribution of ferric ion between the ligands. The quantum efficiency of Fe(III)(EDTA) is independent of the EDTA concentration, whereas the quantum efficiency of Fe(III)(citrate) was found to be linearly dependent on the citrate ion concentration at 488 nm and inversely dependent at 350 nm.

Preliminary results showed that one molecule of EDTA was destroyed for every two molecules of ferric ion reduced. This was determined by adding an equivalent amount of ferrous ion to the excess EDTA in the photolyzed solution. Then the increase in concentration of the Fe(II)(EDTA)NO complex was measured, and from this, the amount of EDTA destroyed could be calculated.

In addition, formaldehyde was detected as one of the products of photolysis. Therefore, the mechanism for Fe(III)(EDTA) and Fe(III)(oxalate) photoreduction is one that has been proposed before.[2–4] Fe(III)(citrate) is seen to behave differently. More than one molecule of citrate was destroyed for every one molecule of ferric ion reduced. Also, no formaldehyde was detected in the reaction products. It had been found earlier that a reaction of the primary radicals with the solvent molecules of Fe(III)(citrate) occurs.[5] This could account for the linear dependence of the quantum efficiency on the citrate ion concentration at 488 nm. At 350 nm, photooxidation of the ferrous ions may be occurring, as has been proposed before for both 254 and 350 nm.[6,7]

The NO was found to have no effect on the chemistry of photolysis of Fe(III)EDTA or Fe(III)(citrate) solutions. It did, however, have a large effect on the quantum yields determined for Fe(III)(oxalate). This is because photoreduction is occurring so rapidly that the concentration of Fe(II)(oxalate)(NO) builds up quickly and begins to absorb most of the incident light intensity.

A bench-scale scrubbing column was set up and connected to a Thermoelectron model 14A chemiluminescent NO_x analyzer. The experimental setup and procedure have been described elsewhere.[8] A solution of 10^{-2} *M* Fe(II)(oxalate) and 2×10^{-2} *M* $SO_3^{=}$ was prepared under O_2-free conditions at pH 7.5 and ionic strength 1 *M*. Nitric oxide was bubbled through the solution in the column, and the concentration of unabsorbed NO gas was measured by the NO_x analyzer and recorded (Fig. 1). A 200-W high-pressure Hg arc light source was set up facing the column in order to photolyze the solution and record the change in absorption of NO. Figure 1 shows the initial absorption of NO at point *a* due to Fe(II)(oxalate) forming the nitrosyl complex. At *b*, after the light source was turned on, the absorption of NO increases until it reaches a steady state. The photoreduction of Fe(III)(oxalate) must therefore be as fast as the reaction of the nitrosyl ferrous oxalate with $SO_3^{=}/HSO_3^{-}$. At *c*, the light is switched off and the absorption of NO decreases as the Fe(II)(oxalate) becomes both saturated with NO and oxidized due to the reaction with $SO_3^{=}/HSO_3^{-}$; the process is repeated at *d* and *e*. The large increase in absorption at *d* may be attributed to the photoreduction of Fe(III)(oxalate), the concentration of which having built up considerably during the time from *c* to *d*, 50 minutes.

This experiment illustrates the applicability of light irradiation on a scrubbing column as a method of keeping the catalyst, ferrous chelate, in the reduced form. The photon flux used was 2.0×10^{18} photons sec^{-1}.

PLANNED ACTIVITIES FOR FY 1985

We are in the process of preparing these results for publication. The photosensitivity of other fer-

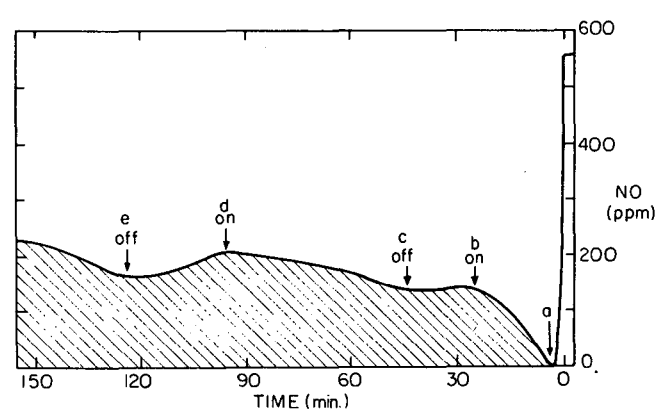

Figure 1. A chart recording of the absorption of NO in a bench-scale scrubbing column by Fe(II)(oxalate) and a $SO_3^{=}/HSO_3^{-}$ solution on exposure to a 200-W, high-pressure Hg arc light source. The conditions of the experiment were $[Fe(II)(oxalate)]_0 = 10^{-2}$ *M*, and $[S(IV)] = 2 \times 10^{-2}$ *M* and [NO] = 560 ppm. (XBL 8410-8242)

rous chelate systems may be studied in the coming year.

REFERENCES

1. Sada, E., *et al.* (1984), "Chemical Reactions Accompanying Absorption of NO into Aqueous Mixed Solutions of Fe(II)-edta and Na_2SO_3," *Ind. Eng. Chem. Fundam. 23*, p. 60.
2. Carey, J.H., and Langford, C.H. (1973), "Photodecomposition of Fe(III) Aminopolycarboxylates," *Can. J. Chem. 51*, p. 3665.
3. Parker, C.A. (1953), "A New Sensitive Chemical Actinometer. I. Some Trials with Potassium Ferrioxalate," *Proc. Roy. Soc. Ser. A. 220*, p. 104.
4. Hatchard, C.G., and Parker, C.A. (1956), "A New Sensitive Chemical Actinometer. II. Potassium Ferrioxalate as a Standard Chemical Actinometer," *Proc. Roy. Soc. Ser. A. 235*, p. 518.
5. Arzhankov, S.I., and Poznyak, A.L. (1974), "ESR Spectra of Free Radicals Formed During Low Temperature Photolysis of Complex Ions of Iron(III)-Citric Acid," *Zhur. Prik. Spektroskopii 21* (4), p. 754.
6. David, P.G. (1972), "Photoreduction of Iron(III) Chloride in Aqueous Media," *J. Chem. Soc. Chem. Comm.*, p. 1294.
7. Langford, C.H., and Carey, J.H. (1975), "Outer Sphere Oxidations of Alcohols and Formic Acid by Charge Transfer Excited States of Iron(III) Species," *Can. J. Chem. 53*, p. 2436.
8. Hishinuma, Y., *et al.* (1979), "Reversible Binding of NO to Fe(II)(EDTA)," *Bull. Chem. Soc. Japan, 52*, p. 2863.

Investigation of the Synergistic Effect of Metal Ions on S(IV) Oxidation by Laser Raman Spectroscopy, Using a High-Pressure, Rapid-Mixing Flow System*

S. Wolfgang and S.G. Chang

Sulfur dioxide, an undesirable byproduct of coal combustion contributing to acid rain formation, can be removed from stack gases via aqueous lime/limestone scrubbing processes, where a key reaction is the oxidation of bisulfite ion by oxygen, i.e.:

$$2HSO_3^- + O_2 \rightarrow 2SO_4^{2-} + 2H^+ \qquad (1)$$

A number of metal ions, most notably Mn^{2+} and Cu^{2+}, catalyze reaction (1), and a synergistic effect is demonstrated by Mn^{2+} and Fe^{3+}. Since lime/limestone scrubbers contain a myriad of metal ions, a complete understanding of the kinetics and mechanism of this synergistic effect is warranted.

*This work was supported by the Assistant Secretary for Fossil Energy, Office of Coal Utilization Systems, U.S. Department of Energy under Contract No. DE-AC03-76SF00098 through the Pittsburgh Energy Technology Center, Pittsburgh, PA.

ACCOMPLISHMENTS DURING FY 1984

We have set up a high-pressure, rapid-mixing flow system for kinetic study of the synergistic effect of flue-gas desulfurization (FGD) impurities on S(IV) oxidation under some realistic lime/limestone FGD conditions. The materials of this system were chosen so that it can be operated safely up to a pressure of 1500 psi and also avoid contamination of the solution by impurities from these materials. Virtually all components of the flow system are made from stainless steel, the exceptions being the flowmeter glass tubes and the quartz observation tube. All valves and fittings are gold-plated, the feed tank and flexible hoses are Teflon-lined, and the mixer body is Rulon (Teflon with glass fibers).

In operation, solutions of O_2 and HSO_3^- are driven to the mixer by O_2 and N_2 pressure, respectively. The scattering of an incident Ar ion laser beam by the reaction medium is monitored via the quartz tube located downstream from the mixer. The entire Raman spectrum can be scanned. The monochromator can also be tuned to observe the growth or decay of a species at its characteristic scattering frequency. In stopped-flow mode, reactions with half-lives longer than 1 minute can be monitored. Continuous-flow conditions can be used for faster reactions or to obtain spectra of intermediates.

Reaction (1) was studied under five sets of conditions:

(1) No catalyst.

(2) Mn^{2+} added to the HSO_3^- feed tank.
(3) Mn^{2+} and Fe^{2+} added to the HSO_3^- feed tank.
(4) Mn^{2+} and Fe^{2+} added to the HSO_3^- feed tank; Fe^{3+} added to the O_2 feed tank.
(5) Fe^{3+} added to the O_2 feed tank.

All studies were done at room temperature, 22° ± 1°C, and at pH 4.2–4.5, except when Fe^{3+} was present. In the latter instance, while the pH of the HSO_3^- feed tank was 4.2–4.5, the pH in the O_2 feed tank was 2.8 to prevent precipitation of $Fe(OH)_3$.

The rate data are summarized in Table 1. In all cases, the reaction is independent of both O_2 concentration and pH. With an excess of HSO_3^-, there is virtually no change in the rate of formation of SO_4^{2-}

Table 1. Concentration and rate data for the S(IV) oxidation reaction, with and without metal ion catalysts.

	Concentration (*M*)						
pH	$[HSO_3^-]$	$[O_2]$	$[Mn^{2+}]$	$[Fe^{3+}]$	$[Fe^{2+}]$	Rate (sec^{-1})	Corrected rate (sec^{-1})
4.4	0.125	0.0320				0.15	0.15
	0.121	0.0235				0.37	0.37
	0.140	0.0200				0.28	0.28
	0.130	0.0157				0.20	0.20
3.6	0.239	0.0062				0.33	0.33
4.0	0.119	0.0234	2.33×10^{-4}			0.65	0.45[a]
4.5	0.136	0.0193	$2.66\ 10^{-4}$			0.94	0.71[a]
	0.196	0.00853	3.84×10^{-4}			1.0	0.68[a]
	0.0804	0.0293	1.58×10^{-4}			0.48	0.33[a]
4.2	0.117	0.0234	7.10×10^{-4}			1.21	1.01[a]
	0.0768	0.0308	4.68×10^{-4}			0.534	0.38[a]
4.2/2.8	0.119	0.0228	7.34×10^{-4}		1.24×10^{-6}	1.44	0.35[a,b]
	0.129	0.0219	7.94×10^{-4}	4.0×10^{-7}	1.36×10^{-6}	0.62	—[c]
	0.022	0.043	1.34×10^{-4}	7.8×10^{-7}	0.227×10^{-6}	0.030	—[c]
	0.012	0.045	7.12×10^{-5}	8.2×10^{-7}	$0.121 - 10^{-6}$	0.012	—[c]
	0.125	0.043		4.3×10^{-7}		0.25	0.03[a]

[a]Assuming rate law for noncatalyzed reaction is $[HSO_3^-]^1 \times k$ = rate.
[b]Assuming rate law for Mn^{2+}-catalyzed reaction is; rate = $k[HSO_3^-]^1\ [Mn^{2+}]^{1/2}$.
[c]Insufficient data on $Fe^{3+/2+}$-catalyzed reaction to correct rates.

until essentially all of the O_2 is consumed, at which time the reaction rate drops abruptly to an immeasurable value. Figure 1 is typical reaction curve, showing the growth of SO_4^{2-}. Also, over the course of the reaction, the pH drops about 2 units, i.e., the H concentration increases 100-fold, indicating that H^+ is one of the products. Although the range of HSO_3^- concentrations studied is rather too narrow to make an unequivocal determination of the reaction's order, in the absence of catalyst the reaction is at least first order in HSO_3^-, but probably not as high as second order (Fig. 2). The formation of twice as much SO_4^{2-} as the initial amount of O_2 confirms our stoichiometry for the reaction and suggests that there are no products of HSO_3^- oxidation other than SO_4^{2-} when no catalyst is present.

When a catalyst is present, however, the concentration of sulfate formed at the end of the run is always less than twice the initial concentration of dissolved O_2. This result indicates that a reaction other than SO_4^{2-} formation is taking place, one that consumes O_2. Some $S_2O_6^{2-}$ forms when the catalyst is added (Fig. 3), but not enough to account for the discrepancy between $[HSO_3^-]_i$ and $[SO_4^{2-}]_f$. With Mn^{2+}, the rate of SO_4^{2-} formation is somewhat faster than when no catalyst is present. The Mn^{2+}-catalyzed rates can be extracted from the raw rate data by assuming that the noncatalyzed rate law is first order with respect to the HSO_3^- concentration. The corrected rate data suggest that, in the presence of Mn^{2+} the reaction is half order in Mn^{2+} (i.e., $[Mn^{2+}]^{1/2}$) and first order in HSO_3^- (Fig. 4).

Iron was added as either Fe^{2+} or a combination of Fe^{2+} and Fe^{3+}. With Fe^{2+} and Mn^{2+}, the rate of formation of SO_4^{2-} is faster than with Mn^{2+} alone. However, preliminary results indicate that when

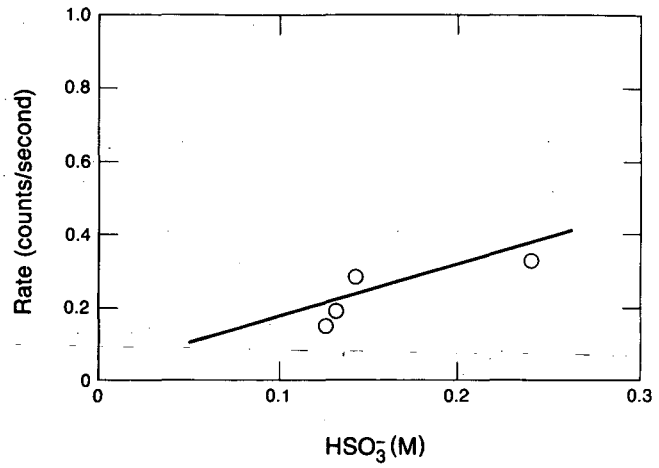

Figure 2. Relative rate of reaction (1) as a function of $[HSO_3^-]$ in the absence of metal ions. (XBL 8501-6903)

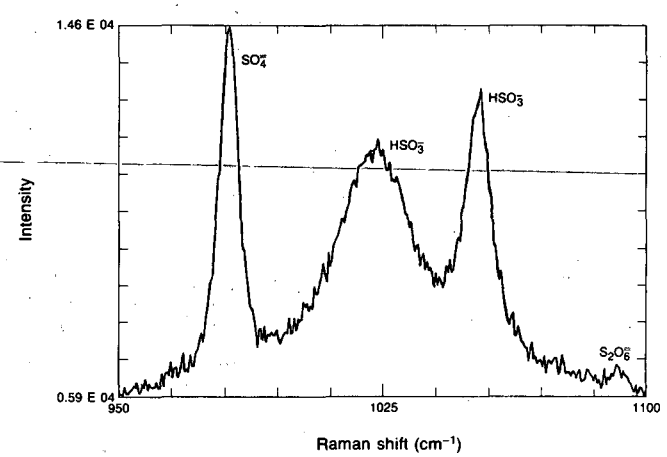

Figure 3. Raman spectrum of the reaction mixture in the presence of Mn^{2+} and Fe^{2+}. (XBL 8501-6902)

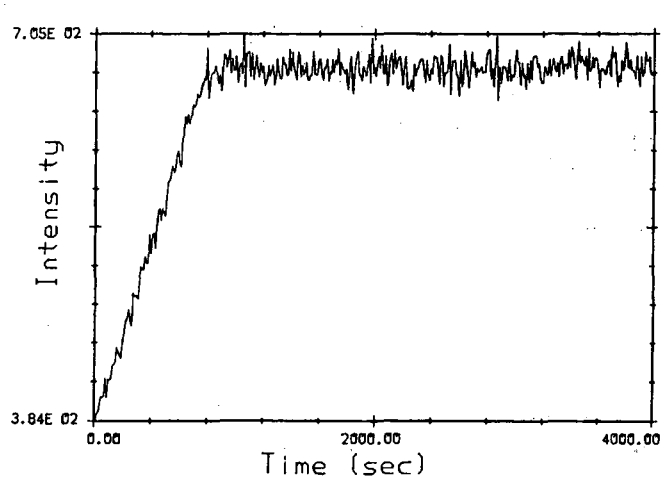

Figure 1. Raman spectrum of the build-up of SO_4^{2-}, taken at 982 cm^{-1}. (XBL 8412-5246)

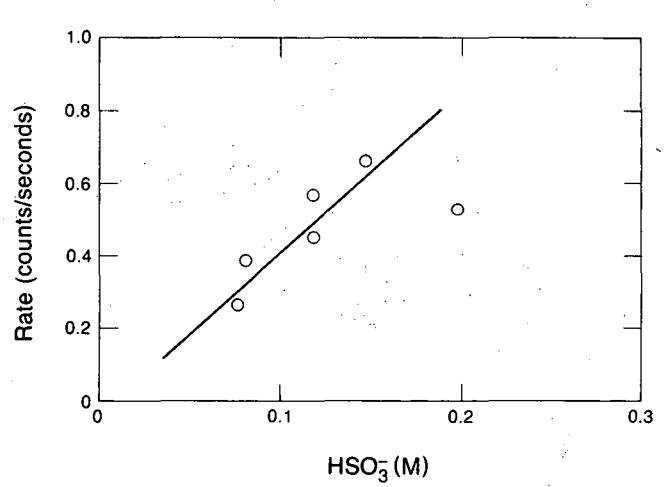

Figure 4. Relative rate of reaction (1) as a function of $[HSO_3^-]$ in the presence of Mn^{2+}. (XBL 8501-6905)

Mn^{2+}, Fe^{2+}, and Fe^{3+} are present, the rate of reaction is slower than when only Mn^{2+} and Fe^{2+} are present.

PLANNED ACTIVITIES FOR FY 1985

Future work will include confirmation of the preliminary experimental results obtained so far and the study of mass and charge balance (using an inert standard), and the dependence of the reaction on pH over the pH range 3–8 (using inert buffers), reactant concentration, ionic strength, and FGD impurities. Attempts will be made to detect intermediates at various given reaction times, using a continuous-flow system, and to identify side reactions that may be responsible for additional oxygen consumption when catalysts are present. The objective of these various experiments is elucidate reaction rate laws for S(IV) oxidation under realistic wet lime/limestone FGD conditions so that a comprehensive computer model simulating the FGD process can be developed.

A Study of Ferrous Ion on Chelex 100 for Nitric Oxide Absorption and Subsequent Reactivity with Oxygen*

K. Brodbeck and S.G. Chang

Amino-carboxylic acids will chelate with Fe^{2+} ion to form a complex that is highly reactive towards aqueous nitric oxide.[1,2] It has been proposed to use such ferrous chelates to remove NO from industrial power-plant flue gases. Chelex 100, a carboxylic cationic exchange resin, is an ideal candidate for use in the first phase of the scrubbing process. Chelex 100 will chelate with Fe^{2+} and, being a solid, is easily separated from waste liquors.

We have examined the effectiveness of Fe(II)Chelex 100 as a nitric oxide scrubbing agent and have determined its absorption capacity at various temperatures. This chelate can react with O_2 present in industrial flue gases to form an Fe(III)Chelex 100. Rates of oxidation of both Fe(II)Chelex 100 and Fe(II)Chelex 100·NO have been explored and modeled, allowing one to predict their durability in industrial applications.

ACCOMPLISHMENTS DURING FY 1984

Equilibrium measurements were performed using aqueous solutions containing Chelex 100 (2:1 ratio of mass to H_2O volume) that had been purged with N_2 to remove oxygen. Ferrous ion was then added to the solution to yield an effective concentration of 10^{-1} *M*. The experiments proceeded by bubbling a mixture of NO and N_2 of known NO concentration through the ferrous-Chelex 100 solution. The NO concentration in the outlet gas was measured with a Thermoelectron model 14A chemiluminescent NO_x analyzer. When equilibrium was attained, the NO concentration in the outlet gas became equal to that of the inlet gas. The experiments were performed at 25°C, 40°C, and 55°C.

For kinetic measurements, solutions containing Fe(II)Chelex 100 or Fe(II)Chelex 100·NO were prepared in an O_2-free environment. These reagents were added to a reactor containing water and saturated with O_2 at 25°C. Oxygen depletion was monitored using a YSI model 57 O_2 probe. Concentrations of NO_2^- and free Fe^{3+} were monitored as a function of time by pumping the aqueous phase through a Cary 219 spectrophotometer. All other kinetic rates were calculated from their theoretical relationship to O_2 consumption and NO_2^- formation.

The equilibrium equation is:

$$K_{eq} = \frac{k_1}{k_{-1}} = \frac{[\text{Fe(II)Chelex 100}\cdot\text{NO}]}{[\text{NO}][\text{Fe(II)Chelex 100}]} \quad . \qquad (1)$$

Measurable values can be substituted into this equation to yield:

$$K_{eq} = \frac{n}{(\text{H}\cdot\chi)(\text{Fe(II)Chelex 100} - n)} \quad . \qquad (2)$$

where n = the moles of NO absorbed by the column; H = Henry's constant, $H(T)$; χ = mole fraction NO in flue gas; and Fe(II)Chelex 100 = moles of Fe(II) initially added to the column solution (saturated on the Chelex 100). The equilibrium constants for the coordination of NO to Fe(II)Chelex 100 were calculated as a function of temperature, using Eq. (2), and are shown in Fig. 1. Thermodynamic properties for

*This work was supported by the Assistant Secretary for Fossil Energy, Office of Coal Utilization Systems, U.S. Department of Energy under Contract No. DE-AC03-76SF00098 through the Pittsburgh Energy Technology Center, Pittsburgh, PA.

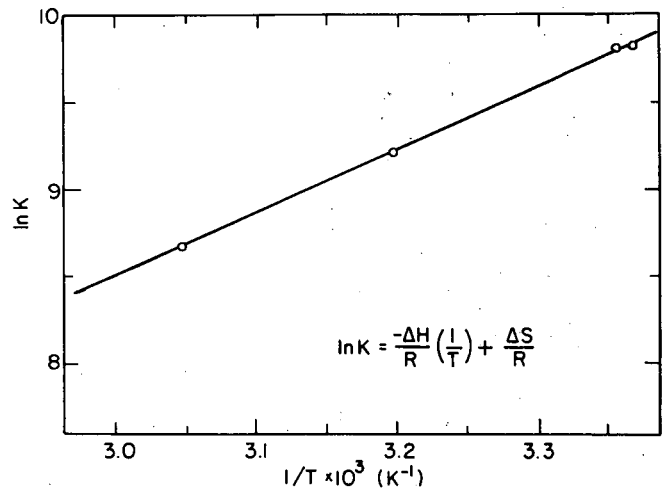

Figure 1. Van't Hoff plot of equilibrium constants for the coordination of NO to Fe(II)Chelex 100. (XBL 8412-6136)

the formation of the nitrosyl complex were derived from equilibrium data. The calculated values are $\Delta H = -7.320$ cal/mol and $\Delta S = -5.05$ cal/mol.

Oxygen will oxidize Fe(II)Chelex 100 as follows:

$$\text{Fe(II)Chelex 100} + \frac{1}{2}\,O_2 \xrightarrow{k_{exp}} \text{Fe(II)Chelex 100} + \text{other products} \tag{3}$$

The oxidation rate of Fe(II)(Chelex 100) is governed by both kinetic reaction rates and mass transfer limitations. The homogeneous case was first studied to yield the intrinsic rate; this was then extended to incorporate the heterogeneous particle to yield the global rate.

The intrinsic rate expression for the depletion of O_2 in a solution containing Fe(II)Chelex 100, at an ionic strength of 0.02 and 25°C is:

$$-\frac{d[O_2]}{dt} = 2.21 \times 10^5\,[\text{Fe(II)Chelex 100}] \times [O_2][OH^-]^{0.37}\,(M\cdot\text{min}^{-1}) \quad . \tag{4}$$

And, at an ionic strength of 0.20 and 25°C, it is:

$$-\frac{d[O_2]}{dt} = 5.69 \times 10^5\,[\text{Fe(II)Chelex 100}] \times [O_2][OH^-]^{0.39}\,(M\cdot\text{min}^{-1}) \quad . \tag{5}$$

Both of these expressions will hold for a pH range of 3.0 to 6.3. Figure 2 shows the degree of Fe(II)–Chelex 100 bonding as a function of pH. The oxidation of free Fe(II) in solution is extremely slow,[3] so it does not contribute greatly to the disappearance of oxygen.

The following is a derivation of a diffusion model required in the calculation of the global rate of oxidation.

For derivation of the global rate of oxidation, the Fe(II) concentration is assumed to be uniform throughout the particle upon saturation. Bonding sites deactivate upon reaction with O_2. Therefore, as time progresses, deeper penetration into the pellet is required before reactions can occur. The differential equation governing diffusion in the Chelex 100 pellets is as follows:[4]

$$\frac{D_{eff}}{r^2}\cdot\frac{d}{dr}\left(r^2\frac{d[O_2]}{dr}\right) = k_{exp}[O_2] \tag{6}$$

where D_{eff} is the effective diffusivity in Chelex 100, k_{exp} is the intrinsic first order rate constant, and r is the radial coordinate. The boundary conditions for this process are: (a) $[O_2] = [O_2]^*$ at $r = R(1 - \alpha)$ and (b) $d[O_2]/dr = 0$ at $r = 0$. Here, α is the fraction of deactivated ferrous sites (reaction extent), R is the particle radius, and $[O_2]^*$ is the oxygen concentration at the tailing edge of the deactivated region. The solution to Eq. (6), using these boundary conditions, is:

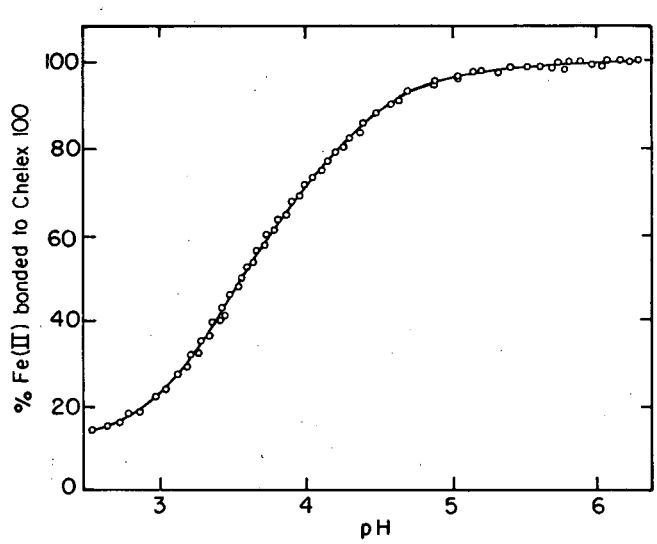

Figure 2. Percent of Fe(II) bonded to Chelex 100 as a function of pH. (XBL 8412-6135)

$$\frac{[O_2]}{[O_2]^*} = \left(\frac{R(1-\alpha)}{r}\right)$$

$$\times \frac{\sinh\sqrt{k_{exp}/D_{eff}}\cdot r}{\sinh\sqrt{k_{exp}/D_{eff}}\cdot R(1-\alpha)} \quad . \tag{7}$$

We define the Thiele modulus as:

$$\phi p = R(1-\alpha)\sqrt{\frac{k_{exp}}{D_{eff}}} \quad . \tag{8}$$

The oxygen concentration profile is then:

$$[O_2] = [O_2]^* \left(\frac{R(1-\alpha)}{r}\right) \frac{\sinh[\phi p r/R(1-\alpha)]}{\sinh\phi p} \quad . \tag{9}$$

The $[O_2]^*$ term will be omitted later, using a mass balance over the deactivated region of the pellet.

The reaction rate inside the pellet is equal to the rate of diffusion of O_2 into the pellet:

Rate =

$$\frac{-4\pi r^2 D_{eff}\, d[O_2]}{dr}\Big|_{r=R(1-\alpha)} \text{ (mols/time)} \quad . \tag{10}$$

Combining equations (9) and (10) yields:

$$\left(\frac{d[O_2]}{dr}\right)_{r=R(1-\alpha)}$$

$$= \frac{[O_2]^*\phi p}{R(1-\alpha)}\left(\frac{1}{\tanh\phi p} - \frac{1}{\phi p}\right) \quad . \tag{11}$$

The mass balance over the deactivated region $[R > r > R(1-\alpha)]$, from the equation of continuity, is:

$$D_{eff}\left(\frac{1}{r^2}\frac{d}{dr}(r^2 d[O_2]/dr)\right) = 0 \quad . \tag{12}$$

Integrating twice and combining Eq. (10) and (11) yields:

$$[O_2]^* = [O_2]_s \Big/ \left[1 + \phi p\alpha\left(\frac{1}{\tanh\phi p} - \frac{1}{\phi p}\right)\right] ,$$

where $[O_2]_s$ is the concentration of O_2 in the bulk and at the pellet surface in a well-mixed reactor.

We can now express the rate in terms of the bulk O_2 concentration:

$$-\frac{d[O_2]}{dt} = \text{Rate} =$$

$$\frac{4\pi R(1-\alpha)\, D_{eff}[O_2]_s \phi p \left(\frac{1}{\tanh\phi p} - \frac{1}{\phi p}\right)}{\left[1 + \phi p\alpha\left(\frac{1}{\tanh\phi p} - \frac{1}{\phi p}\right)\right]} \tag{13}$$

Use of an effectiveness factor will define the degree of mass transfer limitation incorporated into the global rate. The effectiveness factor is simply the ratio of global to intrinsic rates ($0 < \eta < 1$):

$$\eta = \frac{\text{observed rate (global)}}{\text{rate as if } [O_2] = [O_2]_s \text{ everywhere in pellet}}$$

$$\eta = \frac{3(1-\alpha)^3}{\phi p}\,\frac{\left(\frac{1}{\tanh\phi p} - \frac{1}{\phi p}\right)}{\left[1 + \phi p\alpha\left(\frac{1}{\tanh\phi p} - \frac{1}{\phi p}\right)\right]} \tag{14}$$

Because the effectiveness factor is a function of the reaction extent, as the reaction proceeds the effect of deactivation shows the reaction extent. Using the above model, the diffusivity for O_2 in swollen Chelex 100 at 25°C was determined to be:

$$D_{eff} = (7.8 \pm 0.53) \times 10^{-7}\ \text{cm}^2/\text{sec} \quad .$$

As expected, this value is somewhat less than D_{eff} for O_2 in H_2O at 25°C.

Fe(II)Chelex 100 ·NO can also react with oxygen, as follows:

Fe(II)Chelex100·NO

$$+ O_2 \rightarrow \text{Fe(III)Chelex100}$$

$$+ NO_2^- + \text{other products} \quad . \tag{15}$$

Because the reaction is slow, mass transfer does not limit the reaction rate. This rate is on the order of 1 mg O_2/L/min at pH 5, T = 25°C, μ = 0.02, and O_2 concentration of 8.0 mg O_2/L.

Nitric oxide oxidizes to the same extent as the ferrous ion, forming NO_2^- as a product. Over an

extended period of time, NO_2^- oxidizes further, forming NO_3^-.

The oxidation of Fe(II)Chelex 100·NO is much slower than Fe(II)Chelex 100 under the same conditions, indicating that the absorbed NO inhibits deactivation of the catalyst to a certain extent.

PLANNED ACTIVITIES FOR FY 1985

We plan to investigate more of the properties of the Fe(II)Chelex 100·NO system. We are also interested in the reaction of the Fe(II)Chelex 100·NO complex with sulfite and bisulfite ions. Reduction of the Fe(III)Chelex 100 complex by suitable reducing agents is another potential area of study.

REFERENCES

1. Hishinuma, Y., *et al.* (1979), "Reversible Binding of NO to Fe(II)(EDTA)," *Bull. Chem. Soc. Japan 52*, p. 2863.
2. Lin, N.H., Littlejohn, D., and Chang, S.G. (1982), "Thermodynamics and Kinetics of the Coordination of NO to Fe^{II}NTA in Aqueous Solutions," *I&EC Process Res. Dev. 21*, p. 725.
3. Goto, K. Tamura, H., and Nagayama, M. (1970), "The Mechanism of Oxygenation of Ferrous Ion in Neutral Solution," *Inorg. Chem. 9*, p. 963.
4. Hill, C.G. (1977), *Chemical Engineering Kinetics and Reactor Design*, Wiley & Sons, New York.

Quantitative Determination of Nitrogen Sulfonates in Flue-Gas Liquors*

D. Littlejohn and S.G. Chang

Nitrogen sulfonate compounds have been found to occur in a number of aqueous reaction systems containing oxyanions of nitrogen and sulfur.[1-3] They are readily produced by the reaction of bisulfite ion and nitrite ion,[1] as shown in Fig. 1. Hydroxylamine disulfonate (HADS) is the product of this reaction. It can hydrolyze in acid solution to produce hydroxylamine monosulfonate (HAMS), which, in turn, can hydrolyze to produce hydroxylamine (HA). If excess bisulfite ion is present, HADS can react with it to produce aminetrisulfonate (ATS). ATS will hydrolyze to aminedisulfonate (ADS), which can hydrolyze to sulfamic acid (SA). Hydroxylamine is a hazardous compound; while the toxicity of the other compounds is unknown, they can generate hydroxylamine under appropriate conditions.

Scrubber systems designed for the simultaneous denitrification and desulfurization of coal-fired power-plant flue gases could potentially generate these nitrogen sulfonates. Consequently, accurate methods are needed to determine the presence, and concentrations, of these compounds.

*This work was supported by the Assistant Secretary for Fossil Energy, Office of Coal Utilization Systems, U.S. Department of Energy under Contract No. DE-AC03-76SF00098 through the Pittsburgh Energy Technology Center, Pittsburgh, PA.

ACCOMPLISHMENTS DURING FY 1984

We have found two techniques that can successfully be used in determinations of nitrogen sulfonate compounds. Both techniques require only a small amount of sample and allow simple, rapid, and simultaneous determination of these compounds.

One technique is laser Raman spectroscopy (LRS). In LRS, the sample is illuminated with a laser, and the Raman-scattered light from the compounds in the sample is analyzed by a double monochromator and detected by a photomultiplier tube. The scattered light from each Raman-active compound is shifted by a characteristic amount from the illuminating light. Figure 1 shows Raman spectra of the nitrogen sulfonates along with the sulfate ion reference peak at 980 cm^{-1}. The spectra can be quantified by adding a known amount of a reference compound, such as ClO_4^-, to the sample and comparing peak heights. The peak heights must be corrected for the relative scattering efficiencies of the compounds (Table 1). LRS also permits the use of solid samples, although quantitation is more difficult. The major drawback of LRS is that the analysis time can become excessively long for sample concentrations below $\sim 1-10 \times 10^{-3}$ *M*.

The other technique we have used is ion chromatography (IC). IC analysis utilizes a column containing an ion exchange resin to separate ions. The retention time of an ion will depend on a number of factors, including resin type, eluent concentration, and charge and structure of the ion. Using a Dionex 2010i ion chromatograph with a conductivity detector, we can make determinations of HADS, HAMS, ADS, and SA. Hydroxylamine is

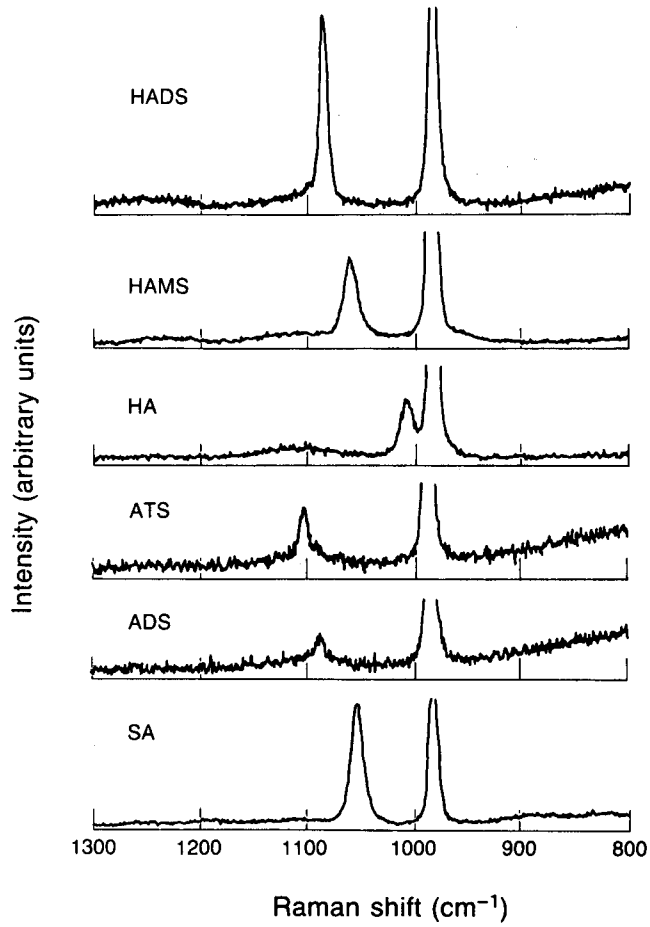

Figure 1. Raman spectra of (from top to bottom) HADS, HAMS, HA, ATS, ADS, and SA, along with $SO_4^{=}$ reference peak at 980 cm^{-1}. (XBL 8501-6904)

Table 1. Raman shifts and relative intensities of six nitrogen sulfonates.

	Raman shift (cm^{-1})	Relative molar intensity[a]
HADS	700	0.13
	1084	1.43
HAMS	760	0.075
	1058	0.48
ATS	1097	1.80
ADS	1084	1.02
HA (pH < 7)	1004	0.21
HA (pH > 9)	918	0.09
SA (pH > 3)	1049	0.41

[a]SO_4^{2-} at 981 cm^{-1} = 1.000.

positively charged and requires different conditions for separation. ATS has a 3- charge and is strongly retained by the columns used in these analyses. It can be determined by first measuring the ADS in solution by IC, then acidifying the solution sufficiently to hydrolyze the ATS to ADS and measuring the increase in ADS concentration. ADS hydrolyzes more slowly than ATS, so there should be little conversion to SA. The measurements are quantified by running nitrogen sulfonate standards under the same conditions as the samples. Figure 2 shows a composite ion chromatogram of the compounds. The upper trace shows ADS and HADS, using an AG4 column and 18 m*M* $CO_3^{=}$ eluent at a 1.5 mL/min flow rate. More rapidly eluted ions such as

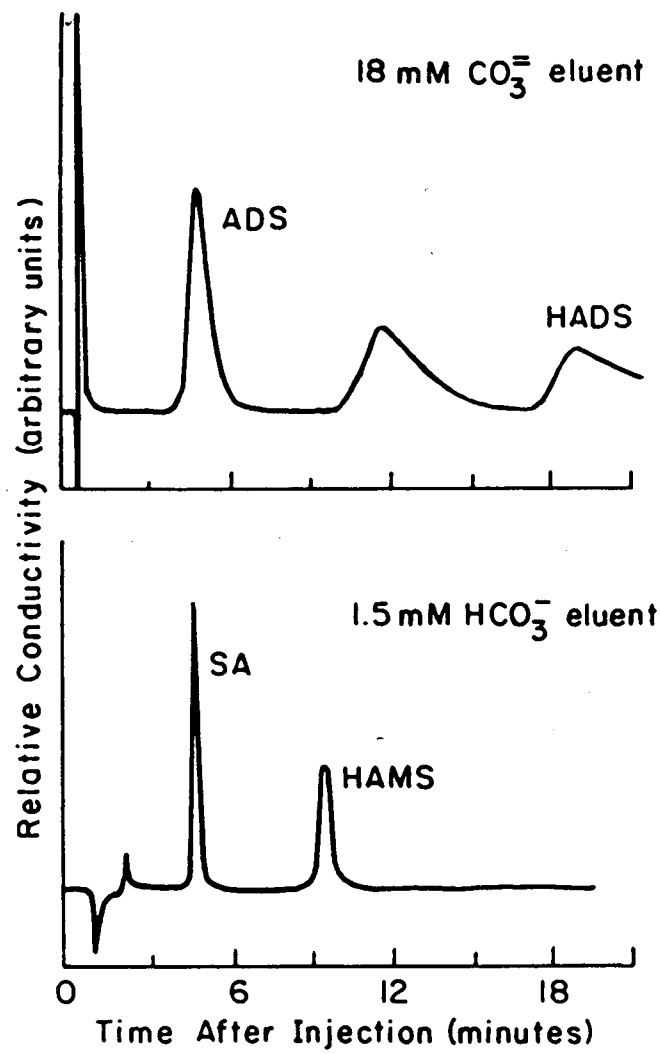

Figure 2. Ion chromatograms of ADS and HADS with 18 m*M* $CO_3^{=}$ eluent (upper trace) and SA and HAMS with 1.5 m*M* HCO_3^{-} eluent (lower trace). (XBL 8412-6139)

NO_3^- and $SO_4^=$ come out together shortly after injection. The lower trace shows SA and HAMS using an AS4 column and 1.5 m*M* HCO_3^- eluent at a 2 mL/min flow rate. By running samples at these two conditions, we can obtain measurements of these four compounds, as well as many simple anions.

PLANNED ACTIVITIES FOR FY 1985

We plan to continue developing LRS and IC techniques to investigate other compounds that may occur in reaction systems containing nitrogen oxyanions and sulfur oxyanions. Measurement of nitrogen sulfonates by these techniques will allow the study of the kinetics of reactions involving these compounds. Use of a different column-detector combination on the IC will allow determination of transition metal ions, which would permit study of oxidation-reduction reactions involving these ions.

REFERENCES

1. Oblath, S.B., Markowitz, S.S., Novakov, T., and Chang, S.G. (1982), "Kinetics of the Initial Reaction of Nitrite Ion in Bisulfite Solutions," *J. Phys. Chem. 86*, p. 4853.
2. Oblath, S.B., Markowitz, S.S., Novakov, T., and Chang, S.G. (1981), "Kinetics of the Formation of Hydroxylamine Disulfonate by Reaction of Nitrite with Sulfites," *J. Phys. Chem. 85*, p. 2567.
3. Oblath, S.B., Markowitz, S.S., Novakov, T., and Chang, S.G. (1983), "Reaction of Nitrite Ion with Hydroxylamine-N-Sulfonate in Aqueous Solution," *Inorg. Chem. 22*, p. 579.
4. Chang, S.G., Littlejohn, D., and Lin, N.H. (1982), "Kinetics of Reactions in a Wet Flue Gas Simultaneous Desulfurization and Denitrification System," ACS Symposium Series No. 188, American Chemical Society, Washington, DC, p. 127.

TOXICOLOGY STUDIES OF BIOLOGICAL SYSTEMS

Free Radicals in Mitochondrial Membranes*

R.J. Mehlhorn, J. Maguire, and L. Packer

"Active oxygen" species, including the free radicals superoxide and perhaps hydroxyl, appear to play major roles in the degradation of aerobic biological cells. Since most metabolic processes occur under oxygen, active-oxygen reactions impose significant limitations on the overall efficiencies of most biological processes. For example, the repair of oxygen-radical damage probably represents a major energy drain on photosynthetic organisms and is likely to be partially responsible for the poor overall efficiencies of solar energy conversion by plants. Moreover, active-oxygen damage may be responsible for damage that cannot be repaired over a prolonged period of time, an idea that has been promoted in the "free-radical theory of aging." Since degradation of biological cells is a crucial aspect of many energy and environmental processes, this project is concerned with the study of fundamental free-radical reactions in a major and representative aerobic biological environment—the mammalian mitochondrion, the respiratory energy source for aerobic cells. The release of free-radical molecules from the membrane, a process that promotes oxidative damage and may contribute substantially to mammalian aging, is also being studied.

This project also seeks to determine how the asymmetric structure of the inner mitochondrial membrane is related to the energy conversion of respiratory substrates to ion gradients and ATP synthesis. Our approach uses stable free-radical (nitroxide) spin probes to specifically probe aqueous and membrane domains. Concentrations of membrane-permeable hydrophobic ions sensitive to electrical potentials, or of weak acids and amines sensitive to pH gradients, are measured with electron spin resonance (ESR) instrumentation and then related to electrochemical gradients. A novel aspect of our approach is that the intracellular population of the spin probes is distinguished from the extracellular population by treating the cells with paramagnetic line-broadening reagents whose charge characteristics are such that they cannot cross the cell membranes and thus broaden only the extracellular spin signals.[1]

A sensitive method for detecting free radicals is to observe the decay of an ESR signal of a "stable" free radical. Nitroxides are stable with respect to dismutation, i.e., in reactions with each other, but they react rapidly with most other radicals, such as thiyls or carbon-centered radicals. We monitor the loss of nitroxide spectra and relate it to reactions of the nitroxide radicals with lipid and thiyl radicals, reactions whose products are nonparamagnetic molecules. Oxidation of hydroxylamines, derived from nitroxides by one-electron reduction, is being used to infer concentrations of superoxide radicals. This assay is based on the fact that nitroxides are readily formed when superoxide abstracts a hydrogen atom from these hydroxylamines.[2] Supportive evidence for free-radical formation is being sought with the complementary ESR technique of spin trapping.[3]

ACCOMPLISHMENTS DURING FY 1984

During the past year, the following accomplishments were made:

(a) A methodology for detecting free-radical reactions with nitroxides was described.[4]

(b) Iron deficiency was investigated with respect to its effect on NADH† and succinate oxidase.[5]

(c) Electrical surface potentials and transmembrane electrochemical gradients were studied in inner mitochondrial membranes.

(d) The interaction of metal ions, metalloids, and metal ion complexes with membranes was reviewed.[6]

(e) The production of superoxide radicals by purified mitochondrial electron transport complex II (succinate dehydrogenase) was demonstrated and its assembly was characterized by analyzing gene products of *B. subtilis* mutants.[7]

(f) A spin-trapping procedure was used to characterize the occurrence of thiyl radicals in mitochondria.

(g) The current understanding of how free radicals contribute to mammalian aging was reviewed.[8]

*This work was supported by the National Institutes of Health (Grant AG-04818) through the U.S. Department of Energy under Contract No. DE-AC03-76SF00098 and by the National Foundation for Cancer Research.

†NADH - nicotinamide adenine dinucleotide hydrogenate.

(h) A new, more stable nitrone spin trap, using a carbon-13 methyl group rather than the usual alpha-hydrogen as a reporter group was synthesized.

Each of these accomplishments is described more fully below.

(a) *A procedure for detecting free-radical species* in biological environments was described.[4] The method consists of monitoring the loss of ESR signal in a free-radical-generating environment such as the respiring mitochondrial membrane and characterizing the reaction products, primarily by chromatographic methods. The significance of this assay is that it allows for the detection of free-radical reactions within the membrane interior. We have noted that lipid spin probes that are deeply imbedded in the mitochondrial membrane, e.g., the stearic acid nitroxides, suffer a very slow spin signal loss relative to aqueous spin probes unless free-radical processes are initiated within the membrane; they are thus especially effective for the detection of free-radical reactions in these domains. On the other hand, the occurrence of free-radical processes in the aqueous mitochondrial regions is amenable to study with conventional nitrone spin traps, although the resulting adducts are so unstable that they do not accumulate significantly and therefore require high concentrations of spin-trapping agents to elicit an ESR-detectable signal.

(b) *The effect of iron deficiency* on the concentration of iron-containing enzymes in the mitochondrial membrane has been studied.[5] Two systems of respiratory enzymes—NADH- and succinate-ubiquinone oxidoreductase—lost about 30% activity as a result of iron deficiency. The loss of enzyme activity could be ascribed to a decrease in enzyme concentration and not to altered kinetics. The study showed that the limited availability of iron leads to a reduced content of at least some of the membrane proteins that require iron for their function but no decrease in non-iron proteins.

(c) The development of *electrical surface potentials at mitochondrial interfaces* has been investigated. The first stage of this research consisted of characterizing the permeability of our nitroxide probes used for these measurements. It had been suggested by Rottenberg *et al.* that the Cat_n probes used for such studies were too permeable to be useful for surface potential work.[9] We have found that the probes do indeed cross the inner mitochondrial membrane at an appreciable rate at room temperature. A biophysics senior honors thesis describing this work has been written by Grant Hartzog. The research is continuing with the development of rapid mixing facilities to perform short-term measurements of bioenergetic phenomena. We have pursued preliminary measurements of surface potentials with rapid measurement techniques under conditions of minimal probe internalization and have observed that there are small but measurable surface potential changes induced at the outer surface upon energization with ATP, as originally reported by our laboratory. We will also exploit our recent discovery that the spin of nitroxides located outside mitochondria and at the outer surface of the membrane can be very effectively and rapidly eliminated by illuminating the mitochondria with a mixture of FMN[‡] and EDTA,[§] a highly effective photochemical system for nitroxide reduction.[10]

(d) The literature on *metal and metalloid effects on biological membranes* has been reviewed.[6] In part, this work was motivated by a recognition that transition metal ions like copper and iron may play a critical role in promoting metabolically initiated free-radical chains by participating in Fenton reactions. The production of hydrogen peroxide by mitochondria, microsomes, peroxisomes, and certain cytoplasmic enzymes is well-documented.[11] In view of the considerable destructive potential of the hydroxyl radical, and the possibility that the Fenton reaction could be a source of these radicals in biological environments, there is now a great interest in evaluating the possibility that "free iron," i.e., iron with an available coordinating site for binding hydrogen peroxide,[12] exists in aerobic cells. In particular, our efforts have turned toward the detection of iron in mitochondria, and those assays are in progress. Preliminary indications are that iron release from membranes occurs as a function of acidity and low reducing potentials. These conditions arise in ischemia and are likely to be important in disease and aging. We have recently succeeded in observing hydroxyl radicals in mitochondria without adding powerful pro-oxidants like ascorbate and iron and are in the process of correlating spin trapping of the hydroxyl radical with iron assays, lipid peroxidation and loss of energy coupling.

(e) Data on *a new potential source of free radicals in mitochondria* has been obtained. There is great interest in cellular mechanisms of free-radical production. One principal source of radicals is known to be the mitochondrion. We have obtained data that purified complex II (succinate dehydrogenase) can liberate superoxide radicals in the absence of ubiquinone. Succinate dehydrogenase is a membrane-bound enzyme that is bound to the inner membrane of mitochondria and to the inner side of

[‡]FMN = flavin mononucleotide, or riboflavin 5'-phosphate.

[§]EDTA = ethylenediaminetetraacetic acid.

the membrane of aerobic bacteria. It is composed of two subunits and contains flavin adenine dinucleotide (FAD) and three iron-sulfur clusters. This enzyme is one of the Krebs cycle enzymes within the respiratory chain and was first isolated in a partially purified form over two decades ago. The technology for understanding how this enzyme is assembled and where the constituents of the subunits are located was not available until genetic manipulations became possible.[7]

Previous publications about mitochondrial superoxide production had claimed that no superoxide release occurred from mitochondrial membranes that had been depleted of ubiquinone and that repletion of ubiquinone restored the superoxide production.[13] Our studies with the purified enzyme have clearly shown that succinate dehydrogenase *in vitro* is a significant one-electron reductant of molecular oxygen and, more important, that the oxygen is reduced in the absence of quinones. These findings provide new insight into the problem of determining how and where oxygen is reduced in aerobic systems. The results may be relevant to oxidative damage mechanisms, but thus far we have not been able to convince ourselves that a similar phenomenon will occur when the enzyme is functioning in the intact mitochondrial membrane. It is certainly conceivable that the site of superoxide generation in the isolated enzyme complex will be masked in the intact membrane, e.g., by ubiquinone.

We have obtained *new evidence on how the mitochondrial enzyme succinate dehydrogenase is synthesized.* The study of enzyme assembly is of fundamental interest for learning how biogenesis is controlled, but it is also of interest for free-radical research because deficiencies in protein assembly could cause the catalysis of errant free-radical reactions. The isolation of mutants of *B. subtilis* that are deficient in the synthesis of specific components of succinate dehydrogenase has prompted us to seek low-temperature ESR information about how this enzyme is assembled in the membrane. We have observed that this enzyme has its iron-sulfur cluster assembled before attachment to the membrane. Importantly, the iron-sulfur complex remains freely soluble in the cytoplasm in the mutant bacterium, whereas it becomes membrane-bound in the normal bacterium.

(f) Two ESR techniques have been devised for *detecting the occurrence of thiyl radicals* during oxidative cellular free-radical reactions. One is the decay of piperidine nitroxides to secondary amines in a process that involves the direct coupling of a thiyl and nitroxide radical. Another is the observation of spin adducts of the thiyl with nitrone spin traps. Figure 1 shows examples of the ESR spectra we have obtained.

Using these assays, we have made the startling observation that hydroxyl radicals are produced in a reaction system that is devoid of transition-metal ions like copper and iron. We have suggested that such a process may explain the hitherto unresolved puzzle of the toxicity of the superoxide radical.

(g) We have written a critical *review of the free radical theory of aging* in collaboration with Gregory Cole.[8] The purpose of this review was twofold: to compile the data that appear to support or contradict the theory, and to identify research directions most likely to make a significant impact on aging research. One immediate objective was to identify critical research areas that can benefit from our ESR approach to free-radical detection.

(h) We have performed exploratory syntheses of new *nitrone spin traps for detecting free radicals* with better sensitivity than has been realized in the past. One approach has been to devise a spin trap that becomes a fully shielded nitroxide upon reacting with reactive radicals, yet retains the diagnostic value of a nuclear spin that reports on the nature of the radical. To this end, we have performed an initial synthesis to attach a C-13 methyl group to the widely used 2,2-dimethyl pyrroline-N-oxide (DMPO) spin trap. The position of the nuclear spin-labeled methyl group ensures that the ESR signal from spin adducts of this radical trap will give information diagnostic of the trapped species. The yield of this reaction was too low to permit purification of the product, but we had enough product in the reaction mixture to determine that the new spin trap could be used for the specific detection of hydroxyl radicals. A larger-scale synthesis is in progress.

PLANNED ACTIVITIES FOR FY 1985

The research projects described above have opened promising insights into mitochondrial free-radical processes and will be continued. A major shift in emphasis will be on intramitochondrial free-radical detection, since the asymmetric organization of the membrane is likely to affect the distribution of free radicals in the internal and external aqueous compartments. We will complete the measurements of surface potentials and transmembrane electrochemical gradients because these data are useful for estimating the chemical potentials that promote univalent oxygen reduction to superoxide. Free-radical reactions in the mitochondrial membrane will be measured directly with our approach of combining nitroxide destruction and nitrone spin trapping.

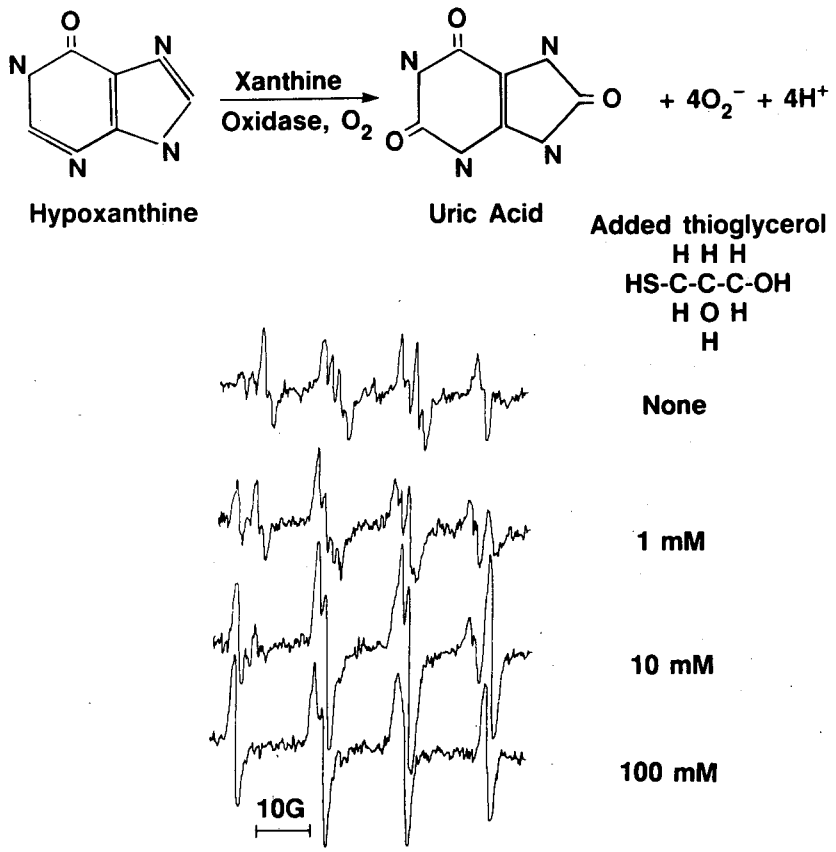

Figure 1. Electron spin resonance spectra of thiyl radicals arising from the abstraction of hydrogen atoms from glutathione by superoxide. Conditions: 100 m*M* DMPO, 30 μg/mL catalase, 75% O_2/25% N_2; 3.5 m*M* hypoxanthine, 37 mU xanthine oxidase, modulation amplitude 1.0 G, gain 3.2 × 10^9, on Varian E109E. (XBL 847-8552)

The new C-13 trap will fully exploited for the measurement of hydroxyl radicals in the mitochondrial system.

We will also measure the release of superoxide radicals from the inner surface of the mitochondrial membrane. This is an important issue for aging research since superoxide from mitochondria may be a primary source of cellular oxidative damage. It has also been suggested that mitochondria may be particularly vulnerable to oxidative damage, an idea that has been embodied in the notion that mitochondria are the pacemakers of mammalian aging. Recent publications have suggested that damaged mitochondrial DNA may be a significant consequence of oxidation. One promising procedure for discerning the appearance of superoxide radicals within the mitochondrial matrix is to allow slowly permeable reduced nitroxides to equilibrate into the matrix space while the sample is maintained under a stream of nitrogen gas, and then to monitor the superoxide-dependent reoxidation of the ESR signal when the sample is subjected to an oxygen gas stream.

A hypothesis of a major pathway for free-radical damage is that transition-metal ions may become "decompartmentalized" during stressful conditions like disease. Such "free" transition-metal ions have the potential to catalyze Fenton reactions, thus producing very destructive hydroxyl radicals. We have begun to examine whether the stress of exercise could induce the release of iron from tissues in a rodent model. Although we observed a significant correlation between nutritional status and endurance among the animals, no evidence was seen for a substantial release of iron under these conditions. However, more careful studies may show that partial release of transition metals can occur with exercise. The significance of the research performed thus far is that it seems to rule out extensive decompartmentalization of iron as a major contributor to the substantial tissue damage that is known to accompany exhaustive exercise.

We will apply the expertise we have gained with determining mitochondrial free iron to study how iron decompartmentalization can occur. We will

also use iron determinations to establish the extent of involvement of this transition-metal ion in catalyzing the Fenton reaction *in vivo*. Work is in progress with two assays: a recently developed and biologically relevant bleomycin procedure that consists of monitoring the degradation of DNA in the presence of this antibiotic,[14] and the more traditional procedure of spectroscopically measuring the concentration of a phenanthroline sulfonate–iron complex.[15]

The mechanism by which complex II generates superoxide radicals will be further elucidated. We seek to learn which specific electron donors within this complex can react with oxygen. One promising avenue being explored is to add free flavins to the complex. It is known that some flavin enzymes readily accept electrons from reduced aqueous flavins. It is possible that reduced flavoproteins can donate electrons to free flavins, and the possibility that free flavins within mitochondria can serve as electron donors to oxygen should not be ignored. Specific experiments to be performed include adding either riboflavin or FMN to ubiquinone-depleted complex II and then monitoring superoxide production upon succinate addition.

REFERENCES

1. Mehlhorn, R.J., and Packer, L. (1983), "Measurements of Volumes and Electrochemical Gradients with Spin Probes in Vesicles," *Methods Enzymol. 88,* p. 751.
2. Rosen, G.M., Finkelstein, E., and Rauckman, E.J. (1982), "A Method for the Detection of Superoxide in Biological Systems," *Arch. Biochem. Biophys. 215,* p. 367.
3. Janzen, E.G. (1980), "A Critical Review of Spin Trapping," in *Free Radicals in Biology,* vol. 4, W.A. Pryor, Ed., Academic Press, New York, pp. 116–154.
4. Mehlhorn, R.J., and Packer, L. (1984), "ESR Spin Destruction Methods for Radical Detection," *Methods Enzymol. 105,* p. 215.
5. Åkrell, B.A.C., Maguire, J.J., Dallman, P.R., and Kearney, E.B. (1985), "Effect of Iron Deficiency on Succinate- and NADH-Ubiquinone Oxidoreductases in Skeletal Muscle Mitochondria," *J. Biol. Chem.* (in press).
6. Mehlhorn, R.J. (1984), *The Interaction of Metals and Metalloids with Biomembranes,* to be published as a Dahlem Workshop Book, Springer-Verlag.
7. Hederstedt, L., Maguire, J.J., Warrig, A.S., and Ohnishi, T. (1984), "Characterization by EPR and Studies of the Localization and Assembly of the Iron-Sulfur Clusters of *Bacillus Subtilis* Succinate Dehydrogenase," submitted for publication to *Journal of Biological Chemistry.*
8. Mehlhorn, R.J. and Cole, G. 1984, "The Free Radical Theory of Aging: A Critical Review," submitted to *Reviews of Oxygen Radicals in Biology and Medicine,* W.A. Pryor, Ed.
9. Hashimoto, K., Angiolillo, P., and Rottenberg, H. (1984), "Membrane Potential and Surface Potential in Mitochondria: Binding of a Cationic Probe, *Biochim. Biophys. Acta 764,* p. 55.
10. Mehlhorn, R.J., and Packer, L. (1982), "Nitroxide Destruction and Flavin-Photosensitized Damage in Inner Mitochondrial Membranes," *Can. J. Chem. 60,* p. 1452.
11. Chance, B., Sies, H., and Boveris, A. (1979), "Hydroperoxide Metabolism in Mammalian Organs," *Physiol. Rev. 59,* p. 527.
12. Graft, E., Mahoney, J.R., Bryant, R.G., and Eaton, J.W. (1984), "Iron-Catalyzed Hydroxyl Radical Formation: Stringent Requirement for Free Iron Coordination Site," *J. Biol. Chem. 259,* p. 3620.
13. Boveris, A., Cadenas, E., and Stoppani, A.O.M. (1976), "Role of Ubiquinone in the Mitochondrial Production of Hydrogen Peroxide," *Biochem. J. 156,* p. 435.
14. Gutteridge, J.M.C., Rowley, D.A., and Halliwell, B. (1981), "Superoxide-Dependent Formation of Hydroxyl Radicals in the Presence of Iron Salts: Detection of Free Iron by Using Bleomycin-Dependent Degradation of DNA," *Biochem. J. 199,* p. 263.
15. Tangeras, A., Flatmark, T., Backstrom, D., and Ehrenberg, A. (1980), "Mitochondrial Iron Not Bound in Heme and Iron-Sulfur Centers," *Biochem. Biophys. Acta 589,* p. 162.

Lake Ecotoxicology Research*

J. Harte, J. Oldfather, C. Blanchard, H. Michaels, M. Turner, and A. Bradman

This project focused on the application of microcosms to study the effects of prolonged darkness on aquatic ecosystems, and on laboratory and field investigations of the effects of acid precipitation on a subalpine western watershed.

ACCOMPLISHMENTS DURING FY 1984

Biological Effects of Prolonged Darkness

This research was an experimental study of the biological consequences of prolonged darkness. It was stimulated both by the asteroid impact hypothesis and by the recent work on "nuclear winter" that one of us (J.H.) coauthored.[1] We used the LBL Microcosm Facility to determine the consequences for the phytoplankton and zooplankton in a freshwater lake of a two-month period of complete darkness, followed by a gradual increase in light level to ambient intensity. The comparison of treatment and control replicates revealed a sharp decline in the phytoplankton populations, followed by a recovery with the return of illumination. Zooplankton populations generally showed no pattern of decline, with some (rotifers) appearing to prosper in the dark. A recently advanced argument against the asteroid impact hypothesis, based on the observation that freshwater life was not impacted severely at the Cretaceous-Tertiary boundary, is thus weakened by our results, which suggest a robustness in these populations.

These results demonstrate that the LBL aquatic microcosm facility can be used to study the effects of severe environmental stress, such as several months of nearly complete darkness, on the survivorship of planktonic populations of freshwater lakes. Comparison of survivorship patterns with the paleontological record across the great extinction boundaries will provide data for evaluating hypotheses that link such stresses to extinction events. Microcosms afford a powerful and unique tool for this purpose because they permit study of realistic segments of ecosystems under environmental conditions that can be manipulated by the investigator.

A paper on this research has been prepared for publication.[2]

The Chronology of Western Watershed Acidification

Our past research has demonstrated that acid deposition is occurring in low-alkalinity watersheds in the Colorado Rockies.[3] A major unresolved question concerns the rate at which this deposition will induce chemical changes in the soils and surface waters of these watersheds. Our current research on this problem coordinates field, laboratory, and mathematical modeling techniques. Aquatic and soil microcosms are essential to the research, and thus the work builds on the microcosm-research experience developed at LBL by our group over the past several years. An innovative aspect of this research is the way in which field-validated microcosms are being used to measure the rate of loss of alkalinity-regeneration capacity in lake sediments and soils at the site. Hydrologic measurements are made to characterize runoff waters and lake and subsurface waters during spring and summer. These field data then allow design of appropriate manipulations of the microcosm to yield the alkalinity-regeneration loss rate. A relatively simple mathematical box model of the watershed is now being constructed to determine the chronology of the acidification process under various assumptions about the acid loading rate.

Soil-runoff interactions are critical to the buffering processes that, at least temporarily, protect from acidification watersheds receiving acid precipitation. We began a series of studies last year to determine whether successive years of snow-melt percolation through soil can be studied in the laboratory with weekly, or even more rapid, acid additions to soil-core microcosms. This goal is possible only if the addition interval does not affect the results. A test of this proved to be positive, demonstrating that the relevant properties of the water-soil interaction are time-compressible. This result, along with a considerable amount of hydrological information obtained in the field at the Rocky Mountain site during the summer of 1984, permits us now to make some predictions about the chronology of the acidification process in the ponds and lakes at the site. A paper will be prepared for publication in 1985 after data analysis is completed.

PLANNED ACTIVITIES FOR FY 1985

Although LBL funding is not available for this research in 1985, the acid precipitation work is proceeding with grants administered by the Univer-

*This work was supported by Director's Program Development Funds through the U.S. Department of Energy under Contract No. DE-AC03-76SF00098.

sity of California, Berkeley. Funding through LBL is being sought for continuation of both the acid precipitation and the extinction research.

REFERENCES

1. Ehrlich, P.R., *et al.* (1983), "Long-Term Biological Consequences of Nuclear War," *Science 222*, p. 1293.
2. Harte, J. and Oldfather, J. (1984), "Effects of Prolonged Darkness on the Pelagic Plankton in a Eutrophic Lake," Energy and Resources Group, University of California, Berkeley.
3. Harte, J., Lockett, G., Schneider, R., Blanchard, C. and Michaels, H. (1985), "Acid Precipitation and Surface Water Vulnerability on the Western Slope of the High Colorado Mountains," accepted for publication in *Journal of Water, Air, and Soil Pollution.*

TRACE ELEMENT ANALYSIS

Survey of Instrumentation for Environmental Monitoring*

M. Quinby-Hunt, R. McLaughlin, G. Morton, and A. Quintanilha

Technological development has resulted in the generation, transformation, and release of large numbers of substances that constitute health and safety hazards to human beings. Accurate measurement of such products is necessary if corrective or preventive actions are to be taken. For 14 years, the Survey of Instrumentation for Environmental Monitoring has been an up-to-date source of critical information on instruments for detecting, measuring, and monitoring substances of environmental concern.

The Survey is of great value to industrial and government groups that must spend considerable time and money investigating and selecting techniques and instruments for obtaining reliable data on environmental problems. It provides extensive information both on specific pollutants (sources, pathways, and approaches to control) and on monitoring instruments (principles of operation, problems, detection limits, and interferents). Detailed descriptions of commercially available instruments are also included.

The Survey is in four volumes: *Radiation, Water, Air*, and *Biomedical Monitoring*.

The *Radiation* volume[1] was published by John Wiley & Sons in April 1983. The instrument notes were completely revised so that the latest information (up to January 1983) could be included for each manufacturer. The published edition contained over 1100 pages.

ACCOMPLISHMENTS DURING FY 1984

The *Water* volume was completely rewritten and submitted to Wiley on 1 July 1984 for publication later in the year. The book consists of four major sections: Inorganics, Organics, Biological Constituents, and Physical Characteristics. Chapter topics include:

Inorganics

Salinity, the major ions, and cyanide
Characteristics of metallic trace elements
Measurement of metallic trace elements
Nutrient species
Dissolved gases
Disinfectants
pH, Alkalinity

Organics

Organic carbon
Synthetic organic chemicals
Pesticides
Halogenated hydrocarbons
Phenolics
Oil and grease

Biological Constituents

Biomass indicators
Coliform bacteria and other microorganisms
Biochemical and chemical oxygen demand

Physical Characteristics

Temperature
Turbidity
Solids
Fibrous materials
Color, taste, and odor
Radiation

Instrument notes were completely revised and expanded to include the latest information (up to May 1984) on instrumentation for environmental monitoring of water.

*This work was supported by the Assistant Secretary for Environment, Office of Health and Environmental Research, Pollutant Characterization and Safety Research Division of the U.S. Department of Energy under Contract No. DE-AC03-76SF00098.

PLANNED ACTIVITIES FOR FY 1985

The *Water* volume will be published in 1985. Contingent on funding, work will begin on rewriting and editing the *Air* volume, with an expected publication date in 1986.

REFERENCE

1. Environmental Instrumentation Survey Group, Lawrence Berkeley Laboratory (1983), *Instrumentation for Environmental Monitoring, Vol. 1, Radiation,* John Wiley & Sons, New York.

Iridium Anomalies at the Cretaceous-Tertiary and Cambrian-Precambrian Boundaries*

F. Asaro, H.V. Michel, W. Alvarez, and L.W. Alvarez

The impact theory[1] predicts that significant enrichments of iridium will be found at the 65-million-year-old Cretaceous-Tertiary (K-T) boundary, wherever it is intact. This article reports on continuing work related to the theory, including its possible extension to other extinction horizons.

ACCOMPLISHMENTS DURING FY 1984

Cretaceous-Tertiary Boundary

A detailed stratigraphic geochemical study has been made of a Canadian K-T boundary section (near the Montana border) deposited on the continent 65 million years (MY) ago. Very pronounced anomalies of iridium and other siderophile elements were found near the base of the lowest Tertiary coal deposit, and, about 2 cm below the Ir, a layer of claystone (called tonstein) occurs that is rich in titanium and rare in nickel. This pattern is typical in the K-T boundary regions identified in continental sections in Montana, about 100 miles away. This study thus extends the identification of the 65-MY-old iridium time horizon—which is very important for precise relative stratigraphic dating—into continental deposits in Canada from previously identified sites in Montana, Wyoming, Colorado, and New Mexico.

There had been an obstacle to the use of the Ir time horizon for such stratigraphic dating. This centered on the discovery of Tertiary (post-Cretaceous) fauna (in a site called Morales I in Montana) stratigraphically below a K-T iridium anomaly found in a site ~190 meters away (called Iridium Hill). If the asteroid theory is correct, Tertiary fauna should be above the Ir, not below. It had been suggested by others[2] that the fauna were debris deposited in a channel dug by an ancient river, and therefore the fauna were stratigraphically "misplaced." To see if this explanation were correct, we made a geochemical study of the exact location (Morales I) where the Tertiary fauna were found, using samples provided by Professor William Clemens of the University of California, Berkeley. We were able to identify the K-T iridium anomaly in that location (see Fig. 1) and found that it was indeed below the Tertiary fauna as expected from the asteroid impact theory. Thus, the last major obstacle to the use of the K-T Ir anomaly for precise relative dating in the Western United States has been removed.

Cambrian-Precambrian Boundary

M.A. Nazarov *et al.*[3] from Moscow State University have reported an iridium anomaly on the Siberian platform (Aldan River, Siberia) associated with the 570-million-year-old boundary between the Cambrian and Precambrian. The authors suggest an extraterrestrial body impacting the earth as one possible reason for the Ir anomaly.

This boundary is particularly important because life as we know it now, with skeletons and complex organs, had its beginning at that time. Also, it has been independently proposed that earlier flat or disc forms of life (Ediacaran fauna) suffered a catastrophe 570 MY ago.

In collaboration with Dr. J. Kirschvink of the California Institute of Technology and M.H. Anders of UC Berkeley, we have made a detailed study of a suite of samples from the Aldan occurrence of the boundary and the region 7.6 m above and below.

*This work was supported by the Director, Office of Energy Research, Office of Basic Energy Sciences, Engineering, Mathematical and Geosciences Division of the U.S. Department of Energy under Contract No. DE-AC03-76SF00098, and the National Aeronautics and Space Administration Ames Research Center under Contract No. A-71683B.

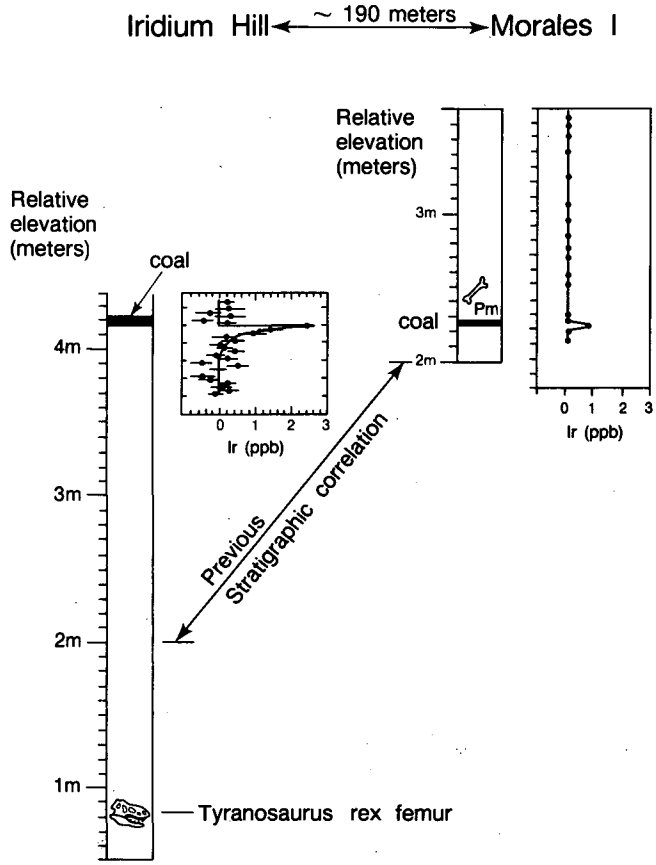

Figure 1. Correlation of Ir anomalies, paleocene fauna, and highest dinosaur fossil in the "Iridium Hill" and "Morales I" sections separated by ~190 m in the Hells Hollow area of Montana (Pm = Paleocene mammals). Relative stratigraphic designations (in meters), made prior to the discovery of the Morales I iridium anomaly are shown to be in error by 1.8 m. Thus, consistent with the impact theory, Paleocene (Tertiary) fauna discovered in Morales I remain above the iridium anomaly, not below it. (XBL 8412-6034)

Our measurements of Ir abundances in rocks from the background regions above and below the boundary and also within ±2 cm of the interface are about a factor of 4 lower than those reported in the previous work (which therefore may have a calibration problem).

In addition, our best value of the ratio of the Ir to Fe abundances is $(19.7 \pm 4.7) \times 10^{-10}$ in the Cambrian, $(24.2 \pm 4.6) \times 10^{-10}$ in the Precambrian, and $(27.2 \pm 5.1) \times 10^{-10}$ within ± 2 cm of the interface. This constancy of the ratio within the measurement statistics suggests that the major source of the iridium is the same in all three regions.

Because all of the Ir abundances that we measured in this suite are comparable to or lower than the average found the earth's crust (25 parts per trillion), and because there is no significant change in the iridium-to-iron ratio at the boundary, it seems likely that the variations in Ir abundances are related not to an impacting bolide but to other terrestrial mechanisms, e.g., variations in the rate of sedimentation or of dissolution of carbonate.

PLANNED ACTIVITIES FOR FY 1985

Construction has begun on a unique coincidence spectrometer capable of measuring iridium at the 50 ppb (parts-per-billion) level at the rate of 100,000 samples per year. This instrument will significantly reduce the time necessary to search for iridium anomalies at other extinction horizons.

REFERENCES

1. Alvarez, L.W., Alvarez, W., Asaro, F., and Michel, H.V., (1980), "Extraterrestrial Cause for the Cretaceous-Tertiary Extinctions," *Science 208*, p. 1095.
2. Smit, J., and van der Kaars, S. (1984), "Terrestrial Extinction at the Cretaceous-Tertiary Boundary Compatible with Catastrophic Extinction Caused by a Large Impact," *Science 223*, p. 1177.
3. Nazarov, M.A., Barsukova, L.D., Kolesov, C.M., and Alekseev, A.S. (1982), abstract in *Proceedings of the Lunar and Planetary Science Meeting* in Houston, Texas, pp. 546–7.

Determination of Hitherto Unknown Sources of New World Obsidians by Precise Elemental Analysis*

F.H. Stross, F. Asaro, and H.V. Michel

Studies of source and artifactual obsidian by sensitive and precise elemental analysis (neutron activation and x-ray fluorescence) have continued with a view to gaining information on the provenience and distribution patterns of this valued material. As before, these studies were carried out on a collaborative basis with other academic institutions, which funded the various projects.

ACCOMPLISHMENTS DURING FY 1984

Texas Project

The University of Texas in San Antonio, represented by Professor T.R. Hester, has for some years collected archaeological material, including obsidian artifacts, from local excavations. These artifacts are of special interest since there are no known significant sources of obsidian in Texas or in its immediate vicinity, and consequently the raw material for the artifacts, or the artifacts themselves, must have traveled over considerable distances. It was found, for instance, that the raw material for a projectile-point base excavated in Uvalde County (in south central Texas), and dated to the seventh or eighth millenium B.C., had come from the state of Queretaro in Mexico, nearly 1000 km distant by straight line.

The composition patterns of substantial numbers of obsidian artifacts from more recent periods were found, in subsequent studies, to fall into several easily distinguishable groups. Attempts are being made to match these patterns with those of obsidian sites in the western U.S., some of which have only recently become known. For example, two of these groups were found to have originated in New Mexico near the Valles Caldera, one source north, and another east, of the Caldera (designated Polvadera Peak and Valles Caldera sources, respectively).

Another composition-defined group of artifacts has led to new insights on the extent of obsidian distribution in prehistoric times. Designated "Escondido Ranch Type" (from the site in Dimmit County where the first specimen of this group was found), it is represented by specimens found in a sizable number of sites in central and southern Texas. Recently, a paper by F.W. Nelson[1] reporting analytical data from a number of obsidian sources in the western U.S. became available. The composition pattern of one of these sources, located near Malad, Idaho, suggested a possible match with the Escondido Ranch Type, and detailed analysis by neutron activation and x-ray fluorescence of samples from that source, generously provided by Dr. Nelson, produced an excellent match. The distances involved—some 2000 km by straight line—and the difficult intervening terrain imply a fairly widespread and highly developed distribution network for obsidian. Moreover, the stratigraphy of the excavations indicates that the artifacts derive from a period extending from the first or second century A.D. to late prehistoric or early historic (Conquest) times, evidence that this route was used more or less steadily over a period of at least a millenium and a half.

Tables 1 and 2 list the compositions of Escondido Ranch Type artifacts and those of the Malad, Idaho obsidian source, as determined by x-ray fluorescence and neutron activation analyses, respectively.

Nicaragua Project

Last year, we reported the results of a project undertaken in collaboration with Professor Payson Sheets of the University of Colorado.[2] The study has been continued; one unassigned chemical group has a similarity in composition to sources in the Guatemalan Highlands. Precise measurements indicated that the source did not correspond to any that had previously been studied. These results, and the development of another unassigned group among artifacts collected in the Petén—whose origin we have designated[2] "Source X"—indicate that there still exist several sources in the Mayan cultural area, probably in the Guatemalan Highlands, that gave rise to appreciably widespread trading but that are still unknown to workers in the field.

PLANNED ACTIVITIES FOR FY 1985

Collaborative research with other academic institutions, relating to the provenience of obsidian, and possibly other rock material, will continue. Specific projects under consideration include the analysis of South American obsidian (Peru and Ecuador), Belize, Guatemala, and the southeastern United States.

*This work was supported by the University of Texas, San Antonio, and the University of Colorado, Boulder, and by the U.S. Department of Energy under Contract No. DE-AC03-76SF00098.

Table 1. Composition of Escondido Ranch Type artifacts (ERT) and Malad, Idaho source samples, by x-ray fluorescence analysis.

Designation	Analysis by	No. of samples	Ba (ppm)	Zr (ppm)	Elemental ratios	
					Rb/Zr	Sr/Zr
ERT	LBL	11	1570 ± 79	106 ± 8	1.228 ± 0.039	0.748 ± 0.029
ERT	R.N. Jack[a]	3		104 ± 8	1.293 ± 0.051	0.690 ± 0.030
Malad source	LBL	2	1520 ± 7	102 ± 4	1.289 ± 0.048	0.715 ± 0.013

[a]Formerly associated with the Department of Earth Sciences, University of California, Berkeley.

Table 2. Composition of Escondido Ranch Type (ERT) artifacts by neutron activation analysis (ppm or %) and comparison with Malad, Idaho, source.

Element	ERT (TEX-22)	Malad source
Al(%)	6.59 ± 0.08	6.59 ± 0.06
Ba	1498 ± 24	1500 ± 25
Ce	64.33 ± 0.98	63.94 ± 0.98
Co	0.50 ± 0.05	0.47 ± 0.06
Cs	2.35 ± 0.06	2.48 ± 0.08
Dy	5.22 ± 0.11	5.15 ± 0.08
Eu	0.589 ± 0.009	0.603 ± 0.006
Fe(%)	0.703 ± 0.011	0.710 ± 0.011
Hf	3.40 ± 0.07	3.47 ± 0.07
K(%)	3.73 ± 0.30	3.88 ± 0.21
La	31.60 ± 0.58	32.84 ± 0.32
Mn	206 ± 3	207 ± 3
Na(%)	2.73 ± 0.03	2.78 ± 0.03
Rb	135 ± 6	134 ± 6
Sb	0.11 ± 0.03	0.17 ± 0.04
Sc	1.971 ± 0.020	1.950 ± 0.020
Sm	4.700 ± 0.047	4.739 ± 0.047
Ta	1.149 ± 0.012	1.174 ± 0.012
Th	21.98 ± 0.22	22.10 ± 0.22
U	5.30 ± 0.05	5.30 ± 0.05
Yb	3.405 ± 0.061	3.405 ± 0.062

REFERENCES

1. Nelson, F.W, Jr. (1984), "Obsidian Studies in the Big Basin," *Contributions of the University of California Archaeological Research Facility No. 45,* R.E. Hughes, Ed., p. 47.
2. Stross, F.H., Asaro, F., and Michel, H.V. (1984), "Building of a Reliable and Generally Useful Data Bank of Mesoamerican Obsidian Sources and Its Application to Ancient Artifacts," *Applied Science Division FY 1983 Annual Report, Environmental Research Program Chapter*, LBL-17073, p. 4-124.

This report was done with support from the Department of Energy. Any conclusions or opinions expressed in this report represent solely those of the author(s) and not necessarily those of The Regents of the University of California, the Lawrence Berkeley Laboratory or the Department of Energy.

Reference to a company or product name does not imply approval or recommendation of the product by the University of California or the U.S. Department of Energy to the exclusion of others that may be suitable.

TECHNICAL INFORMATION DEPARTMENT
LAWRENCE BERKELEY LABORATORY
UNIVERSITY OF CALIFORNIA
BERKELEY, CALIFORNIA 94720